



**Università
degli Studi
di Ferrara**

**DOCTORAL COURSE IN
"SCIENZE DELLA TERRA E DEL MARE"**

CYCLE XXXI

DIRECTOR Prof. Massimo Coltorti

**High-grade burnt lime products: impact of
calcination kinetics on slaking reactivity; sticking
tendency and blocks formation at HT (1300 °C)**

Scientific/Disciplinary Sector (SDS) GEO/06

Candidate

Dott. Gabriele Vola



(signature)

Supervisor

Prof. Giuseppe Cruciani



(signature)

Years 2016/2018

Alla mia famiglia

<u>CONTENTS</u>	pp.	4
Abstract	pp.	10
Riassunto	pp.	11
Abbreviations used in the text	pp.	12
1. <u>INTRODUCTION</u>	pp.	16
1.1 Quicklime reactivity: modelling and prediction	pp.	16
1.1.1 Introduction to the issue	pp.	16
1.1.2 Calcination theory	pp.	18
1.1.3 Limestone decomposition	pp.	18
1.1.4 Kinetics of calcination	pp.	21
1.1.5 Dolomite decomposition	pp.	23
1.2 Calcination process in industrial kilns	pp.	24
1.2.1 Kilns technology and design	pp.	24
1.2.2 Parallel flow regenerative (PFR) kilns	pp.	25
1.2.3 Modelling calcination process in PFR kilns	pp.	26
1.3 Factors affecting the quicklime reactivity	pp.	31
1.3.1 Process and kiln parameters	pp.	31
1.3.2 Intrinsic parameters of carbonate raw materials	pp.	35
1.3.3 Derived parameters of burnt lime products	pp.	51
1.4 Lime agglomeration, blocks formation sticking tendency	pp.	54
1.4.1 Introduction to the issue	pp.	54
1.4.2 Ringing in lime rotary kilns	pp.	57
1.4.3 Factors affecting sintering at high temperature	pp.	57
1.4.4 Solid-state sintering	pp.	59

Contents

1.4.5	Liquid-phase sintering	pp.	63
1.5	Lime Hydration	pp.	65
1.5.1	Chemical reactions	pp.	65
1.5.2	Hydration kinetics	pp.	66
1.5.3	Effects of particle-size, temperature, and agitation	pp.	66
1.5.4	Effects of slaking water composition	pp.	67
1.5.5	Effects of air-slaking and recarbonation	pp.	69
1.6	References	pp.	70
2.	<u>MATERIALS AND EXPERIMENTAL METHODS</u>	pp.	80
2.1	Materials supply	pp.	80
2.1.1	Materials supply for Article no. 1	pp.	80
2.1.2	Materials supply for Article no. 2	pp.	80
2.1.3	Materials supply for Article no. 3	pp.	81
2.1.4	Materials supply for Article no. 4	pp.	82
2.2	Tests and experimental methods	pp.	83
2.2.1	Carbonate rocks and burnt limes nomenclature	pp.	83
2.2.2	Pre-treatments for insoluble residua and clay minerals extraction...	pp.	83
2.2.3	Wavelength Dispersive X-ray Fluorescence Spectroscopy (XRF-WDS)	pp.	85
2.2.4	Inductively Coupled Plasma Mass Spectrometry (ICP-MS)	pp.	86
2.2.5	Elemental Analysis coupled with Isotope Ratio Mass Spectrometry	pp.	86
2.2.6	Carbon-Sulfur (C-S) elemental analysis	pp.	87
2.2.7	BET Specific Surface Area by Nitrogen absorption (BET/N ₂)	pp.	88
2.2.8	Mercury Intrusion Porosimetry (MIP)	pp.	88
2.2.9	Real density by gas pycnometry	pp.	89
2.2.10	X-Ray powder Diffraction analysis (XRD) and clay mineralogy	pp.	90
2.2.11	Quantitative Phase Analysis (QPA) by the Rietveld method	pp.	91

2.2.12 Crystallite-size analysis by Fundamental Parameters method	pp. 92
2.2.13 Synchrotron X-ray powder diffraction at high-temperature	pp. 93
2.2.14 Optical Polarized Microscopy (OPM) and cathodoluminescence (CL)	pp. 94
2.2.15 Quantitative petrography by the Micrite-to-Sparite Ratio (MSR)	pp. 94
2.2.16 Thermogravimetric analysis (TG-DTG) and calcination kinetics	pp. 95
2.2.17 Thermal analysis (TG-DTA)	pp. 95
2.2.18 Scanning Electron Microscopy (SEM-EDS)	pp. 95
2.2.19 Electron Microprobe Analysis (EMPA)	pp. 96
2.2.20 Burning tests on limestone/dolomite lumps at 1050-1150-1250 °C	pp. 97
2.2.21 High Temperature or “Overburning Test” (OT) method	pp. 97
2.2.22 Slaking reactivity test and Available Lime Index (ALI)	pp. 100
2.2.23 Mechanical Degradation (MD) and Drop Tests (DT)	pp. 101
2.3 References	pp. 103
3. <u>RESULTS AND DISCUSSION</u>	pp. 107
3.1 Premise	pp. 107
3.2 Article no. 1: The influence of petrography, mineralogy and chemistry on burnability and reactivity of quicklime produced in Twin Shaft Regenerative (TSR) kilns from Neoproterozoic limestone (Transvaal Supergroup, South Africa)	
3.2.1 Abstract	pp. 108
3.2.2 Introduction	pp. 111
3.2.3 Geological Setting	pp. 113
3.2.4 Economic Significance	pp. 114
3.2.5 Materials and Methods	pp. 115
3.2.6 Results	pp. 116
• <i>Limestone characterization</i>	pp. 116
• <i>Burnt lime characterization</i>	pp. 128

Contents

3.2.7	Discussion	pp.	130
	• <i>Depositional facies and diagenetic features</i>	pp.	130
	• <i>Limestone burnability and quicklime reactivity</i>	pp.	131
3.2.8	Conclusions	pp.	133
3.3	Article no. 2: Impact of rock fabric, thermal behavior, and carbonate decomposition kinetics on quicklime industrial production and slaking reactivity		
3.3.1	Abstract	pp.	136
3.3.2	Introduction	pp.	137
3.3.3	Test Methods	pp.	142
3.3.4	Results	pp.	142
	• <i>Carbonate rocks characterization</i>	pp.	142
	• <i>Thermal analyses and kinetic parameters</i>	pp.	144
	• <i>Burnt limes characterization</i>	pp.	157
3.3.5	Discussion	pp.	158
	• <i>Nabertherm method validation</i>	pp.	155
	• <i>LOI relevance</i>	pp.	159
	• <i>Burnability of carbonate rocks</i>	pp.	159
	• <i>Impact of intrinsic features and derived properties on quicklime reactivity</i>	pp.	163
3.3.6	Conclusions	pp.	166
3.3.7	Acknowledgements	pp.	167
3.3.8	Final remarks	pp.	168
3.4	Article no. 3: Investigation and prediction of lime agglomeration, blocks formation, sticking tendency and occasional melting by the Overburning Test method for industrial quicklime production		
3.4.1	Abstract	pp.	170
3.4.2	Introduction	pp.	171
3.4.3	Test and Experimental Methods	pp.	173

3.4.4	Results	pp. 173
	<ul style="list-style-type: none"> • <i>Carbonate rocks characterization</i> • <i>Insoluble residua and clay minerals characterization</i> • <i>Overburning Test (OT) and Sticking Tendency (ST) classification</i> • <i>Lime blocks characterization</i> 	<ul style="list-style-type: none"> pp. 173 pp. 196 pp. 197 pp. 205
3.4.5	Discussion	pp. 207
	<ul style="list-style-type: none"> • <i>Pressed pellets method (XRF-WDS) validation</i> • <i>Impact of chemical and mineralogical compositions on burnability and ST</i> • <i>Impact of rock fabric and lime microstructure on ST</i> • <i>Impact of capillary moisture and superficial soil dust on ST</i> • <i>Impact of organic compounds on ST</i> • <i>Overburning Test (OT) validation and applications in the lime industry</i> 	<ul style="list-style-type: none"> pp. 207 208 pp. 215 pp. 215 pp. 217 pp. 220
3.4.6	Conclusions	pp. 220
3.5	Article no. 4: Factors affecting early sintering, lowering of slaking reactivity, and overburning tendency of quicklime pebbles burnt at high temperatures (1150-1300°C)	
3.5.1	Abstract	pp. 224
3.5.2	Introduction	pp. 225
3.5.3	Test Methods	pp. 229
3.5.4	Results	pp. 229
	<ul style="list-style-type: none"> • <i>Carbonate rocks characterization</i> • <i>Thermal behavior and calcination kinetics</i> • <i>In-situ High Temperature XRD</i> • <i>Burnt lime characterization</i> • <i>Slaking reactivity</i> 	<ul style="list-style-type: none"> pp. 229 pp. 236 pp. 237 pp. 238 pp. 239
3.5.5	Discussion	pp. 251
	<ul style="list-style-type: none"> • <i>Calcination kinetics and heating behavior by different techniques</i> 	<ul style="list-style-type: none"> pp. 251

Contents

• <i>Sintering and overburning tendency at HT</i>	pp. 252
• <i>Impact of hydration kinetics</i>	pp. 263
• <i>Impact of CaO crystallography, BET SSA, and real density</i>	pp. 263
• <i>Impact of particle size distribution and composition of slaking water</i>	pp. 266
Conclusions	pp. 267
3.6 References	pp. 270

Printed on 12nd February 2019, Dalmine, Bergamo, Italy

Abstract

This dissertation regards results obtained in three years of doctorate research activity dedicated to the study of quicklime products for different industrial applications. The heating behavior or burnability of different carbonate rocks, i.e. high-grade limestones and dolostones, marbles, marly limestones, and other impure carbonates was investigated considering typical aggregate sizes, i.e. from 15-30 mm up to 40-80 mm, and temperatures, i.e. 1050-1300 °C, occurring in a parallel flow regenerative (PFR) kilns. This study was possible thanks to the collaboration between Cimprogetti S.r.l., a company that design lime plants, based in Dalmine (Bergamo), and the Physics and Earth Sciences Department of the University of Ferrara. Raw materials were supplied from several lime producers worldwide. A multidisciplinary analytical approach, including physical-chemical, mineralogical-petrographic, crystallographic, microstructural, and thermal analyses, was performed for solving “critical” issues of industrial interest and scientific relevance. The systematic decreasing of the slaking reactivity between 1050-1250 °C, which is generally associated with the use of solid fuels into the kiln, such as coal and petcoke, was investigated with respect to specific geological rock features and derived burnt lime parameters from the one side. Lime agglomeration, blocks formation and sticking tendency at high temperature, were evaluated to the other. The last topic was studied by means of the so-called “overburning test” invented by Cimprogetti to predict blockages at 1300 °C, which is ideally considered the highest temperature occurring in PFR kilns. Indeed, this dissertation reports four scientific papers recently published, or still under revision/submission, to scientific international peer-reviewed journals. The first article regards the unusual and drastically pronounced sintering or overburning tendency of the South African Neoproterozoic limestone case-study. The second paper is dedicated to the impact of rock fabric, thermal behavior, and carbonate decomposition kinetics on quicklime industrial production and slaking reactivity. The third one regards the prediction of lime agglomeration, blocks formation, sticking tendency and occasional melting occurring by the “overburning test” method, which is industrially adopted for quality control, designing, and commissioning new kilns. Finally, the fourth paper is dedicated to the investigation of factors affecting the early sintering and the lowering of slaking reactivity of limes burnt at high temperatures (1150-1300 °C).

Riassunto

La presente discussione espone i risultati ottenuti nei tre anni di dottorato di ricerca dedicati allo studio di prodotti a base di calce viva per differenti applicazioni industriali. Il comportamento termico, o attitudine alla cottura, di diverse rocce carbonatiche (calcari e dolomie ad alto titolo, marmi, calcari marnosi e altri carbonati impuri), è stato investigato considerando le tipiche frazioni granulometriche (da 15-30 mm, a 40-80 mm) e le tipiche temperature (1050-1300 °C) presenti nei forni rigenerativi a flusso parallelo (PFR). Questo studio è stato possibile grazie alla collaborazione tra Cimoprogetti S.r.l., una società che progetta impianti per la calce con sede a Dalmine (Bergamo) e il Dipartimento di Fisica e Scienze della Terra dell'Università di Ferrara. Al fine di chiarire alcuni argomenti "critici" di rilevante interesse scientifico e industriale, i campioni sono stati caratterizzati con diverse tecniche analitiche, mediante analisi chimico-fisiche, mineralogico-petrografiche, cristallografiche, microstrutturali e termiche. Da un lato è stata investigata la decrescita sistematica della reattività nell'intervallo di temperatura compreso tra 1050–1250 °C, che generalmente è associato all'utilizzo di combustibili solidi nel forno, come il carbone e il petcoke. Dall'altro, è stata determinata la tendenza della calce ad agglomerare, formare blocchi e "incollare" ad alta temperatura. Questo tema è stato investigato mediante il cosiddetto "test di stracottura" inventato da Cimoprogetti per predire la formazione di blocchi nei forni da calce a 1300 °C. Quest'ultima è considerata, infatti, la massima temperatura operativa dei forni PFR. La dissertazione riporta quindi quattro articoli scientifici recentemente pubblicati o tuttora in corso di revisione/sottomissione su riviste scientifiche internazionali sottoposte a processo di peer-review. Il primo articolo riguarda il caso specifico di un calcare sudafricano di età neoarcheana, caratterizzato da un'insolita tendenza precoce a sinterizzare o "stracuocere". Il secondo articolo tratta gli effetti del fabric della roccia, del comportamento termico e delle cinetiche di decomposizione sulla reattività della calce viva per produzioni industriali. Il terzo articolo riguarda la previsione della formazione dei blocchi, la tendenza della calce a incollare e occasionalmente a fondere mediante il "test di stracottura", utilizzato in ambito industriale per il controllo qualità, la progettazione e l'avviamento di nuovi forni. L'ultimo articolo, infine, analizza i fattori che influenzano la sinterizzazione precoce e l'abbassamento della reattività delle calci cotte ad alta temperatura (1150-1300 °C).

Abbreviations used in the text

A: pre-exponential factor of the Arrhenius Equation

AD: air-dried oriented samples (for clay mineralogy)

A_{eq}: Alkali equivalent

ALI: Available Lime Index according to ASTM C25

Ang: Angstrom (equivalent to 0.1 nm or $1 \cdot 10^{-10}$ m)

AR: Alumina Iron ratio (cement modulus)

BSE: Back Scattered Electrons imaging

BET SSA: Specific Surface Area by nitrogen absorption (BET/N₂ method)

BF: Burning Factor (cement modulus)

C_p: heat capacity (TG-DTA analysis)

CL: Cathodoluminescence analysis (by optical microscopy)

C-S: Carbon-Sulphur analysis by infrared technology

CSD: Crystal Size Distribution by optical microscopy

ΔH: Decomposition (calcination) Enthalpy

DDL: Declared Detection Limit

DSC: Differential Scanning Calorimetry

DT: Drop Test

DTA: Differential Thermal Analysis

E_a: (apparent) Activation Energy of the Arrhenius Equation

EA-IRMS: Elemental Analysis coupled with Isotope Ratio Mass Spectrometry

EG: Ethylene Glycol saturated samples (clay mineralogy)

Abbreviations

EMPA: Electron Microprobe Analysis

ESRD: European Synchrotron Radiation Facility (Grenoble, France)

FP: Fundamental Parameter method

FSW: Fuoss-Salymer-Wilson method for reaction kinetics

FWHM: Full Width at Half Maximum (X-ray diffraction pattern peaks)

HR: Heating Rate (either slaking reactivity or thermal analysis)

HT: High Temperature (burning and overburning tests)

HT₅₅₀: Heat Treatment at 550 °C for oriented samples (clay mineralogy)

HT-XRD: in-situ High Temperature X-ray powder Diffraction analysis

ICP-MS: Inductively Coupled Plasma Mass Spectrometry

IR: Insoluble Residue by acid attack

IRMS: Isotopic Ratio Mass Spectrometer

LP: (potential) Liquid Phase (cement modulus)

LOI: Loss On Ignition

LSF: Lime Saturation Factor (cement modulus)

MD: Mechanical Degradation test

MIP: Mercury Intrusion Porosimetry

MHR: Maximum Heating Rate (slaking reactivity)

MSR: Micrite-to-Sparite Ratio (digital images analysis)

ND: Not Determined

NR: Not Reached (generally referred to t_{60})

OPM: Optical Polarized Microscopy, i.e. petrographic analysis

OT: Overburning Test method at 1300 °C

PFR: Parallel Flow Regenerative (kiln)

P.i.: Proprietary Information (not declared by the producer)

PPL: Plane Polarized Light microscopy (petrographic analysis)

RSD: relative standard deviation (crystallite size)

SCM: Shrinking Core Model (calcination and hydration theories)

SEM-EDS: Scanning Electron Microscopy with Energy Dispersive X-ray Spectroscopy

SEM-SE: Scanning Electron Microscopy with Secondary Electrons imaging

ST: Sticking Tendency (according to the Overburning Test method)

T_{max}: Maximum Temperature (slaking test or thermal analysis)

t₆₀: time to reach 60 °C (equivalent to ΔT 40 °C) according to slaking reactivity test

t₅₀: time to reach 50 °C (equivalent to ΔT 30 °C) according to slaking reactivity test

TAST: Total Active Slaking Time according to ASTM c110

TC: Total Carbon

TG: Thermogravimetric analysis

TG-DTG: Thermogravimetric and Differential Thermogravimetric analysis

TOC: Total Organic Carbon

TPD: Tons Per Day (kiln production)

TSR: Twin Shaft Regenerative (kiln)

XPL: Crossed Polarized Light microscopy (petrographic analysis)

XRD: X-ray powder Diffraction (qualitative) analysis

XRD-QPA: X-ray powder Diffraction Quantitative Phase Analysis by Rietveld Method

XRF-WDS: Wavelength-Dispersive X-ray Fluorescence Spectroscopy

1. INTRODUCTION

1.1. Quicklime reactivity: modelling and prediction

1.1.1 Introduction to the issue

The art of lime burning has been practiced since ancient times, but a scientific explanation of calcination process, i.e. the calcination theory, was advanced just on the 18th century. The soft burning process performed in conventional vertical kilns adopting traditional fuels is characterized by low firing temperatures and generally allowed to obtain a highly porous reactive lime. This is the reason why the lime reactivity was not considered a significant criterion for judging quality and suitability of a lime than chemical purity, almost until the industrial revolution. As industrial and chemical technology developed, lime became an increasingly important component in different reactions and processes (Eades and Sandberg, 1970). Reaction rates of commercial limes became a matter of considerable interest with the introduction of the basic oxygen converter steel furnace (König, et al., 1967; Obst, et al., 1970). The use of quicklime instead of limestone and the rapid acceptance of this technology during the 1960s, caused the definitive substitution of open hearth steelmaking furnaces, and created parallel revolution within the lime industry (Limes and Russell, 1970). Furthermore the lime reactivity became a topic of great interest in other industrial sectors such as chemical and mining industries, e.g. acids neutralization and environmental applications, e.g. the flue gas desulfurization. Each sector and country developed different standard methods to evaluate the lime reactivity according to their practice and use. Germans metallurgists evaluated the relationship between the lime reactivity and the slagging time according to the hydrochloric acid coarse grain titration (Wuhrer, 1956; Schlitt and Healy, 1970), which is also known by insiders as “Wülfrath test”. Conversely, Americans developed the so-called “crucible test” in order to more closely simulate basic oxygen furnace atmospheres (Limes and Russell, 1970). Nowadays the lime reactivity in the building sector is evaluated according to the American (ASTM C110, 2016) or European (UNI EN 459-2, 2010) standards tests, which are complementary, and both based on temperature rise, related to a water slaking rate test. A comparison between the ASTM slaking rate test and the German coarse grain titration test proved to be suitable for the determination of the degree of the lime burning (Schlitt and Healy, 1970). Limes and Russell (1970) founded a correlation between the “crucible test”

Chapter 1. Introduction

and the ASTM water reactivity test for commercial lime products. The European water slaking test method UNI EN 459-2 (2010) was adopted for this research activity. It consists in measuring the temperature rise of a milk of lime obtained adding 150 g of powdered ($<200\ \mu\text{m}$) quicklime at time zero into a Dewar thermos containing 600 mL of water at $20\ ^\circ\text{C}$. The water with lime is kept in movement by a stirrer at the speed of 400 rpm. The temperature rise ($\Delta T\ 40\ ^\circ\text{C}$ or t_{60} for high-calcium quicklime, $\Delta T\ 30\ ^\circ\text{C}$ or t_{50} for magnesium-rich or dolomitic quicklime), the maximum slaking temperature (T_{max}) and the Total Active Slaking Time (TAST) are determined. According to the European practice used throughout the lime producers when $t_{60} < 3$ min the reactivity is high ($t_{60} < 1$ min very high), when t_{60} is between 3 and 6 min. the reactivity is medium, and when $t_{60} > 6$ min. the reactivity is low (Fig.1.1a). Moreover, the reactivity can be also reported as $T_{\text{max}}/t_{\text{max}}$ ($^\circ\text{C}/\text{s}$). Another way to represent the reaction rate is plotting the differential curve with respect to the logarithm of the time, and the time at which the highest conversion rate occurred, i.e. the maximum of the conversion rate (Hogewoning et al.; 2008a). Most of the samples exhibit several other maxima in addition to the initial maximum (bi- or multi-modal curves). In principle, the conversion rate maximum with the highest rate values is used in such cases (Fig.1.1b).

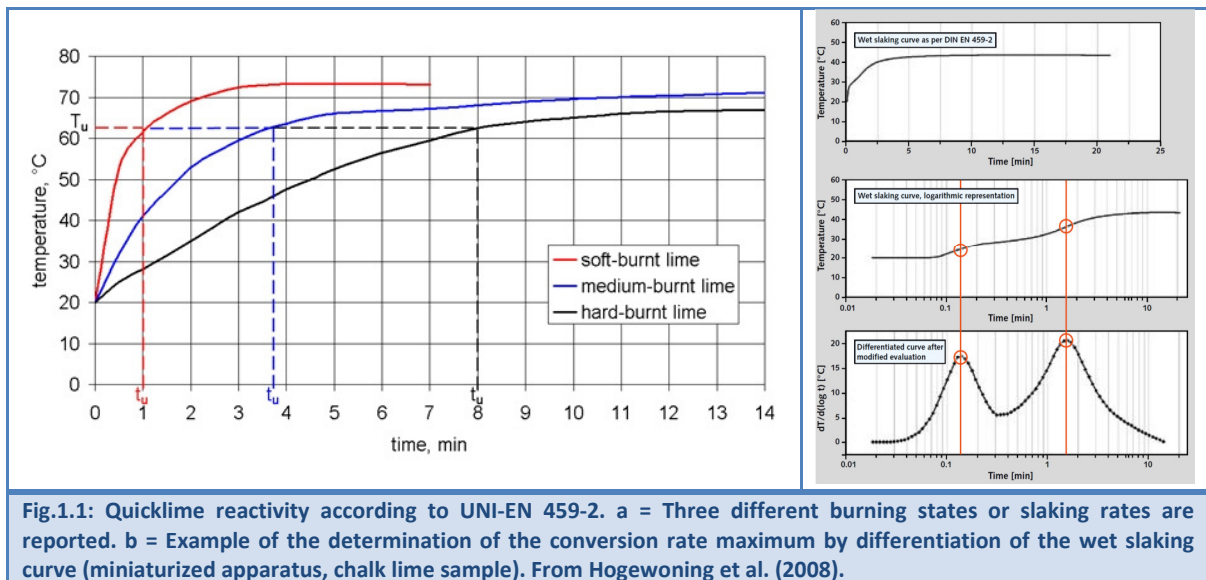


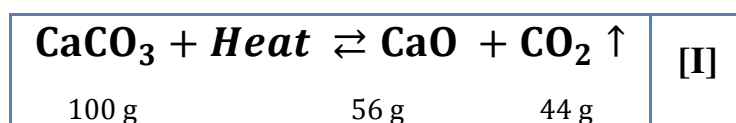
Fig.1.1: Quicklime reactivity according to UNI-EN 459-2. a = Three different burning states or slaking rates are reported. b = Example of the determination of the conversion rate maximum by differentiation of the wet slaking curve (miniaturized apparatus, chalk lime sample). From Hogewoning et al. (2008).

1.1.2 Calcination theory

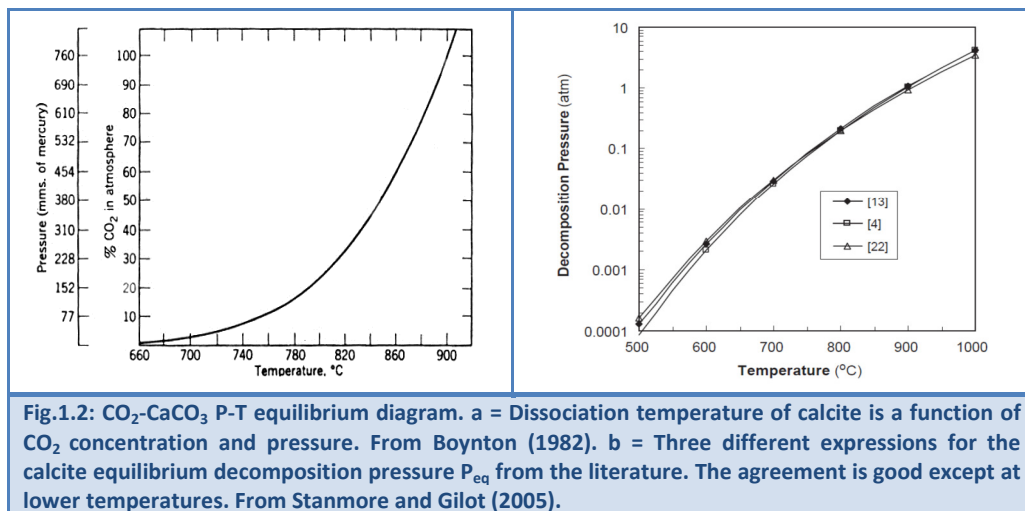
Fundamentals on limestone and dolomite calcination theory are reported by Schiele and Berens (1976), Boynton (1982), and Oates (1998). The term “calcination” refers to the process of thermal decomposition of carbonate rocks or minerals into high-calcium or magnesium-rich quicklime and carbon dioxide. Preferably, “calcination” is used by lime producers, while in the cement sector is mostly adopted the term “decarbonation” with the same meaning (Taylor, 1997, Schorcht et al., 2013). The same process or chemical reaction plays a role in several geological phenomena, i.e. pyrometamorphism on a small scale, subduction, and high-grade metamorphism on a large scale (see references in Rodriguez-Navarro et al., 2009).

1.1.3 Limestone decomposition

Reactions involved in the decomposition of pure limestone are simple. However complications may arise from the contemporary presence of dolomite, which shows different crystallographic features mainly due to diagenetic, and/or metamorphic modifications. Kinetics of decomposition within granular and lump limestones, e.g. industrial grain-sizes or particle fractions, is more complex. Theory of calcination was investigated by several Authors over the years, but all models have had limited validity. Reason is related to the influence of several factors involved in the process, affecting calcination reaction kinetics. Differences in crystallography and microfacies, i.e. intrinsic characteristics of the limestone, coupled with the microstructure of the quicklime, especially in terms of density and specific surface area can have a significant effect. Finally, impurities, which are always present in a natural occurring material, play a role in carbonate decomposition too. Because the above limitations the calcination of a specific carbonate rock have to be determined by practical experiments. This fact is even more evident when the target to achieve is specific quicklime reactivity (see paragraph 1.3 on factors affecting lime reactivity). The **chemical reaction for the thermal decomposition of calcium carbonate**, or more simply **the calcination reaction**, can be written as:



The **dissociation temperature of calcite** is a function of the partial pressure of CO_2 (Fig. 1.2). The reaction will proceed if the partial pressure of CO_2 in the gas above the solid surface is less than the decomposition pressure of the CaCO_3 (Stanmore and Gilot, 2005). It should be noted that the calcination reaction [I] is endothermic, indeed ΔH is negative, and reversible, meaning that the recarbonation is possible under specific constraints (Barker, 1973). The calcite dissociation reaction is favored by higher temperatures, reaching approximately 900°C at 1 atm (corresponding to 760 mm Hg, or 101.3 kPa) for a 100% CO_2 atmosphere. The exact dissociation temperature value is still an open topic in the scientific literature, e.g. Oates (1998) indicates that for many years at the beginning of the 20th century the correct value was considered 898°C , but different Authors between the '70s and the '80s of the last century declared to be 902.5°C (Boynton, 1982). Kiliç (2005) reports an experimental range for calcination temperatures between $682\text{--}691^\circ\text{C}$, up to $944\text{--}961^\circ\text{C}$, for different calcium carbonates. Bes (2006) reports a range 880°C to 920°C at 1 bar from the literature, declaring experiments gave range between $915\text{--}917^\circ\text{C}$ at 1 bar of CO_2 pressure (corresponding to 0.87 atm, or 0.1 MPa). In the same PCO_2 conditions, Silva et al. (2010b) reported a range between $907\text{--}920^\circ\text{C}$ for pure limestones of different geological origin. The **heat of dissociation of limestone** relative to 25°C has variously been reported in the range 695 to 834 kcal/kg of CaO (corresponding to 163 kJ/mol to 196 kJ/mol of CaO) Oates (1998). Boynton (1982) reports an average value of 770 kcal/kg, while Schwarzkopf (1994), which was published subsequently, quotes 754 kcal/kg. Oates (1998) favours a value of 760 kcal/kg (corresponding to 178 kJ/mol).



The expression for the thermodynamic equilibrium decomposition pressure P_{eq} , can be derived by the Arrhenius equation for gas-solid state reactions, considering a shrinking core model (Fig.1.2a). The agreement of plots from three expressions listed in the literature is good except at lower temperatures (Fig.1.2b).

A typical expression for **equilibrium decomposition pressure P_{eq} [II]**, as inferred from thermochemical data, is quoted by Silcox et al. (1989) and subsequently cited by several Authors (Barin, 1989; Garcia-Labiano et al., 2002; Valverde, 2015; Valverde and Medina, 2015). The same equation is reported by Stanmore and Gilot (2005), but the pre-exponential factor is somewhat different, i.e. $4.137 \cdot 10^7$ instead of $4.083 \cdot 10^7$. T is the temperature of the system expressed in Kelvin degree. Results reported by Bes (2006) and Hai Do (2012) are approximated by the correlation [III], which is substantially equivalent to [II], considering the gas constant R is $8.3144598 \text{ J/mol}\cdot\text{K}$.

$P_{eq} = 4.083 \cdot 10^7 e^{\left(-\frac{20474}{T}\right)} \text{ atm}$	[II]
$P_{eq} = 4 \cdot 10^7 e^{\left(-\frac{\Delta H \text{ kJ}}{R \cdot T \text{ mol}}\right)} \text{ bar}$	[III]

The **decomposition enthalpy ΔH (relative to $\sim 900 \text{ }^\circ\text{C}$) is 167 kJ/mol** according to Specht (1993), and Bes (2006) or **168 kJ/mol** according to Cheng and Specht (2006), and Hai Do and Specht (2011). Formation enthalpies of CaCO_3 at 298 K ($\approx 25 \text{ }^\circ\text{C}$) from different Authors, and related decomposition enthalpies of CaCO_3 recalculated at $900 \text{ }^\circ\text{C}$, are reported in Tab.1.1

Tab.1.1 – Decomposition enthalpies of CaCO_3 at $25 \text{ }^\circ\text{C}$ (from Silva et al. 2010b, modified), and related decomposition enthalpies of CaCO_3 recalculated at $900 \text{ }^\circ\text{C}$ considering the contribution of specific heat capacity of elements (between $25\text{-}900 \text{ }^\circ\text{C}$) according to Green and Perry (2007).

References	Enthalpy (kJ/mol) at $25 \text{ }^\circ\text{C}$	Enthalpy (kJ/mol) at $900 \text{ }^\circ\text{C}$
Valverde and Medina (2015)	177.8	168.3
Yan et al. (2010)	177.8	168.3
Rodriguez-Navarro et al. (2009)	177.8	168.3
Stanmore and Gilot (2005)	182.1	172.6
Chai et al. (1992)	178.3 ± 1.2	168.8
Holland et al. (1990)	180.0 ± 1.1	170.5
Berman et al. (1988)	178.2	168.7
Watkinson et al. (1982)	170.0	160.5
Robie et al. (1978)	178.8 ± 1.0	169.3
Helgeson et al. (1976)	179.6	170.1
Schwiete et al. (1956)	176.7	167.2

1.1.4 Kinetics of calcination

The calcination kinetics in the reaction [I] can be calculated by the Arrhenius equation [III], considering spherical particles and a shrinking core model. If the CO₂ partial pressure in the calcination environment, P, is much smaller than P_{eq}, the rate of CaCO₃ conversion is essentially governed by T and can be generally well fitted by an Arrhenius law:

$$k = A \left(-\frac{E}{R \cdot T} \right) \quad \text{[IV]}$$

Where *k* is the **rate coefficient**, and A is the **pre-exponential coefficient** constant. According to Galwey and Brown (2002), Rodriguez-Navarro et al. (2009), and Valverde and Medina (2015) the **apparent activation energy E_a is approximately the decomposition enthalpy change, i.e. E_a ≈ ΔH**, and it can be experimentally determined by means of thermogravimetric analysis (TG), and/or differential scanning calorimetry (DSC). T is the temperatures in degrees Kelvin, and R is the universal gas constant, having a value of 8.314·10 J/mol·K. Taking the natural logarithm of Arrhenius' equation, and rearranging yields:

$$\ln(k) = -\frac{E}{R \cdot T} \cdot \left(\frac{1}{T} \right) + \ln(A) \quad \text{[V]}$$

Equation [V] has the same form as an equation for a straight line, where x is the reciprocal of T. So, when a reaction has a rate constant that obeys Arrhenius' equation, a plot of ln(*k*) versus T⁻¹ gives a straight line, whose gradient and intercept can be used to determine the **activation energy E_a** and the **pre-exponential factor A**. This procedure has become so common in experimental chemical kinetics to define the activation energy for a reaction. The activation energy E_a is defined to be (-R) times the slope of a plot of ln(*k*) vs. (1/T).

$$E \equiv -R \left(\frac{\partial \ln k}{\partial \left(\frac{1}{T} \right)} \right) \quad \text{[VI]}$$

Several theoretical objections had been expressed about the application of the Arrhenius equation to the kinetics of solid state reactions. One is that the energy distribution amongst the immobilized constituents of a crystalline reactant is not represented by the Maxwell-Boltzmann equation (Galway and Brown, 2002). From a practical perspective, values of A and E_a provide convenient comparative measure of reactivity and the temperature coefficient rate. In practice, Arrhenius plots, are often acceptably linear (or approximately linear) and the calculated values of E and A are usually regarded as possessing significances similar to those developed in the theory of homogeneous reactions (Galway and Brown, 2002).

The evaluation of rate constants from thermogravimetric (TG) analysis can be performed according to Fuoss et al. (1964), Ozawa (1965), or Flynn and Wall (1966). All these methods allow extrapolating the (apparent) activation energy E_a from basic thermogravimetric (TG) devices. More sophisticated and accurate thermal analysis by means of Differential Scanning Calorimetry (TG-DSC) or Differential Thermal Analysis (TG-DTA) has been largely adopted to study the calcination kinetics over the years. Recently, a new approach based on the in-situ High Temperature X-ray powder Diffraction analysis (HT-XRD) was performed, as well (Marinoni et al., 2012; Valverde and Medina, 2015; Valverde et al. 2015).

An important review on studies dedicated to thermal decomposition kinetics of calcium carbonate over the last 50 years was performed by Georgieva et al. (2012). According to results obtained from different Authors, kinetics parameters range from 110 to 3800 kJ/mol for the activation energy E_a , and from 10^2 to 10^{157} /s for the pre-exponential or frequency factor A of the Arrhenius equation. Moreover, it changes the algebraic expression of reaction and its-corresponding rate-determining mechanism. Reasons for widely varying values include differences in crystallographic, mineralogical, petrographic, and diagenetic or metamorphic features of the limestone, sample weight, particle-size distribution, and other process parameters, such as isothermal (Halikia et al., 2001), or non-isothermal (Cho et al. 2006) heating conditions, heating rate, CO_2 partial pressure, static or dynamic atmosphere around sample, and atmosphere in the furnace. Finally, the calculation procedure affects kinetics parameters too (Georgieva et al., 2012). This is consistent with the experimental data collected for this dissertation, as well (see Vola et al. 2018 and the related paragraph in Results and Discussion chapter).

1.2. Calcination process in industrial kilns

The calcination process into an industrial kiln can be divided into three main stages or heat zones, described as follow (Schorcht et al., 2013):

1. *Preheating zone*: limestone or dolomite are heated from the ambient temperature up to 800 °C by direct contact with the gases leaving the calcining zone composed mainly of combustion products along with excess air and CO₂ from calcinations.
2. *Burning or calcining zone*: fuel is burned in preheated air from the cooling zone and, depending on the design, in additional combustion air added with the fuel. In this zone temperatures of >900 °C are produced. From 800 to 900 °C the surface of the carbonate stones start the decomposition. At higher temperatures the front of reaction move from the surface into the core of the pebbles. Some residual carbonate could remain at the core, while at the same time external layers have been already sintered.
3. *Cooling zone*: quicklime leaves the calcining zone at temperatures of 900 °C, is cooled by the direct contact with cooling air, part or all of the combustion air, which in return is preheated. Lime leaves this zone at temperatures <100 °C.

1.2.1. Kilns technology and design

A large variety of techniques and kilns design have been used over the years and around the world. Many alternatives at different costs are available with respect to specific applications. Mechanical strength of the limestone before and after burning, and related potential production of fines, input granulometry, output capacity, type of available fuel, final product applications, costs of fuel, investment and operating, and environment impact must be considered when selecting a kiln technique (Schorcht et al., 2013). Six general types of kilns are used in the manufacture of the lime. They are synthetized in Tab.1.2.

Tab.1.2 – Operational parameters for types of lime kilns (Schorcht et al., 2013)

Kiln type	Abbreviation	Output range (t/d)	Range of feed stone size (mm)
Long rotary kiln	LRK	160-1500	2-60
Rotary kiln with preheater	PRK	150-1500	10-60
Parallel Flow Regenerative	PFR	100-600	10-200
Annular shaft kiln	ASK	80-300	10-150
Mixed feed shaft kiln	MFSK	60-200	20-200
Other kilns	OK	10-200	20-250

1.2.2. Parallel flow regenerative (PFR) kilns

The standard PFR kiln is constituted by two circular or rectangular shaft interconnected by a crossover channel (Fig.1.3). Each shaft is subjected to two distinct operation modes: burning and non-burning one. Alternatively, one shaft operates in the burning mode, supplied by fuel and combustion air, and simultaneously the other shaft operates in the non-burning mode. “In burning mode, one shaft is characterized by parallel flow of combustion air/gases and stone, whereas, in non-burning mode the other shaft is characterized by the counter-current flow of off-gases and stone. Combustion air is introduced under pressure at the top of the preheating zone above the stone bed. The complete system is pressurized. The combustion air is preheated by the stone in preheating zone prior to mixing with the fuel. The combustion gases exit burning shaft through a crossover channel into the non-burning shaft. The off-gases transfer heat to the stone during the non-burning mode and then the stone reclaims the heat to the combustion air during the burning mode. The alternating heat transfer sequence serves as a regenerative preheating process. Using the regenerative process is the reason why PFR kilns have the lowest specific energy consumption compared with other types of kiln” (Hai Do et al., 2011). The inversion in the operation modes of the kiln occurs every 8-15 minutes. The standard PFR kiln is designed to accept feed-stones in the range of 25-200 mm. Moreover, a modified design is able to accept a feed-stone in the range 10 to 30 mm. Because the kiln is designed to operate with a high level of excess air, the level of CO₂ in the exhaust gases is low at 20% by volume (dry). PFR kilns can be fired with natural gas, oil, or solid fuels. Especially, when a petcoke is adopted, its specific characteristics must be carefully evaluated (Bes, 2006). Generally, PFR kilns are designed for outputs capacity between 100-600 t/d. Cimprogetti’s PFR kilns are denominated Twin Shaft Regenerative (TSR) kilns (Fig.1.4).

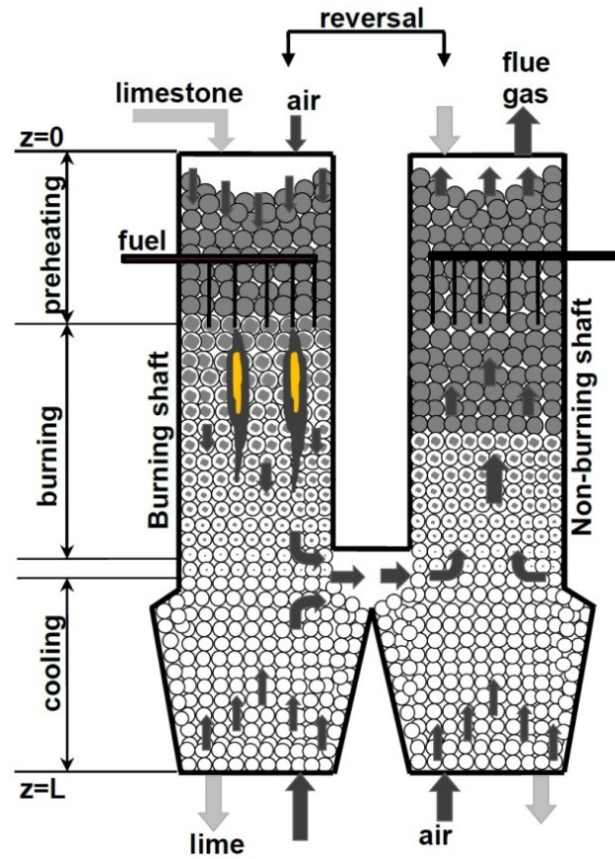


Fig.1.3: Cross section of a parallel-flow regenerative (PFR) kiln. From Hai Do et al. (2011).

Cim-ReVerSy TSR models



Twin-D®
direct cross over channel



Flex ReVerSy®
direct cross over channel



Vanguard®
radial cross over channel

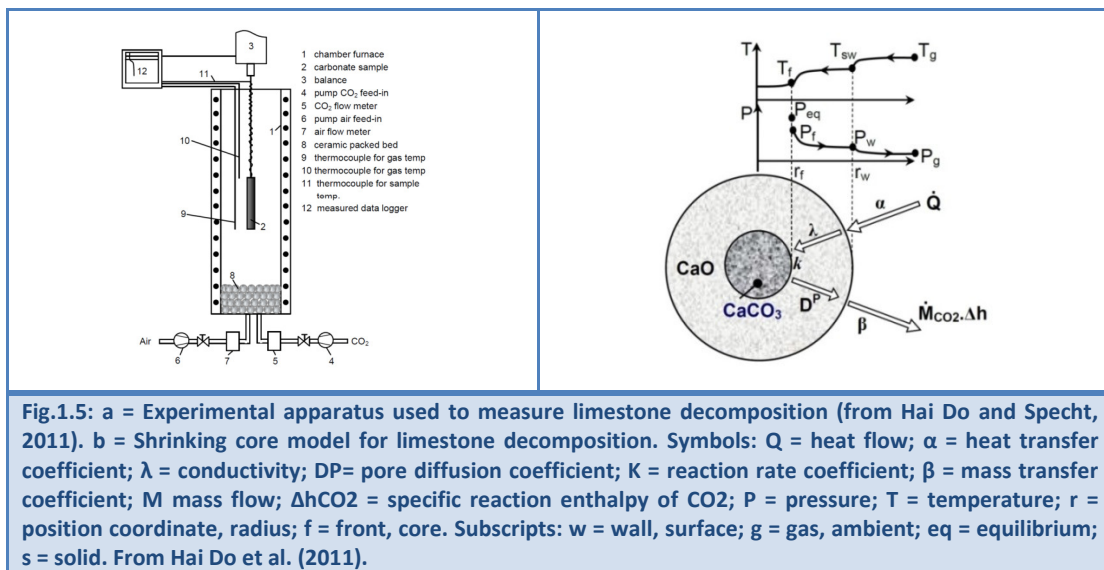
Fig.1.4: Cimprogetti's Twin Shaft Regenerative (TSR) kiln models. From Cimprogetti's web site.

1.2.3. Modelling calcination process in PFR kilns

Over the years many researchers studied the reaction kinetics of limestone decomposition using particle samples in millimeter or micrometer range to exclude the influence of thermal conduction, pore diffusion, heat and mass transfer. In these studies the reaction rate coefficient varies with a factor of 6 (an effective synthesis of the literature is reported in Cheng and Specht, 2006). In the lime industry lumpy pieces with defined

Chapter 1. Introduction

shape, i.e. aggregates with typical grain-size distributions or size-fractions, are used for feeding the PFR kiln. Therefore, Cheng and Specht (2006) described a new method to evaluate the reaction rate coefficients, pore diffusivity and thermal conductivity of the lime layer in the decomposition of limestone, using cm-sized lumps with an experimental thermogravimetric apparatus (Fig.1.5a), considering a shrinking core mathematical model (Fig.1.5b). It's significant to point out that one-dimensional geometry, as a sphere or a cylinder with a length to diameter ratio greater than 6, was suitably selected in order to facilitate determination of the above mentioned parameters. Furthermore, if calcination is performed at constant ambient temperature, conversion degree can be linearized. Experimental coefficients can differ by a factor from 5 to 10 and decomposition temperature difference of up to 80 K between stones of different origin can be observed. The level of the core temperature during the calcination could also provide an idea of the reactivity of the lime. Starting from this experimental method, Hai Do et al. (2011, 2012) developed a steady state one-dimensional mathematical model to describe and simulate the lime calcination process in a PFR kiln.



The proposed model (Hai Do et al., 2011; 2012) comprises conventional differential equation derived from the principle of conservation of mass and energy. The model can be used to predict temperature profiles of the limestone/lime particle in the bed and that of the gas phase along the length of the kiln axis. Moreover other important process parameters of the kiln can be described, such as the pressure drop along the height of the kiln and the heat loss, thus the kiln's heat efficiency (Fig.1.6 and Fig.1.7). The

influences of different operational parameters such as the energy input, the lime throughput and the combustion behavior of the fuel have been investigated with a significant practical relapse in terms of engineering applications. However, this model did consider neither the influence of intrinsic or geological parameters of carbonate raw materials, nor derived parameters of burnt lime products (with the only exception of the conversion rate), and could not provide any realistic model for the prevision of the lime reactivity.

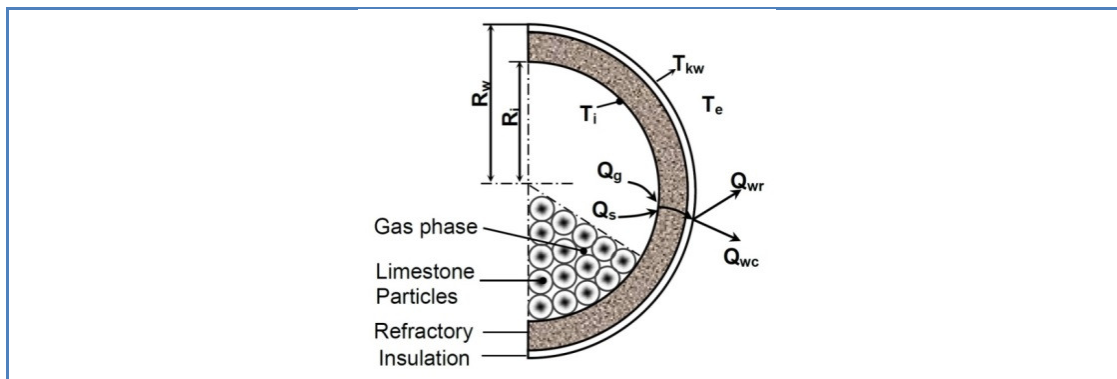


Fig.1.6: Heat transfer at the kiln wall of the PFR shaft kiln. From Hai Do et al. (2011).

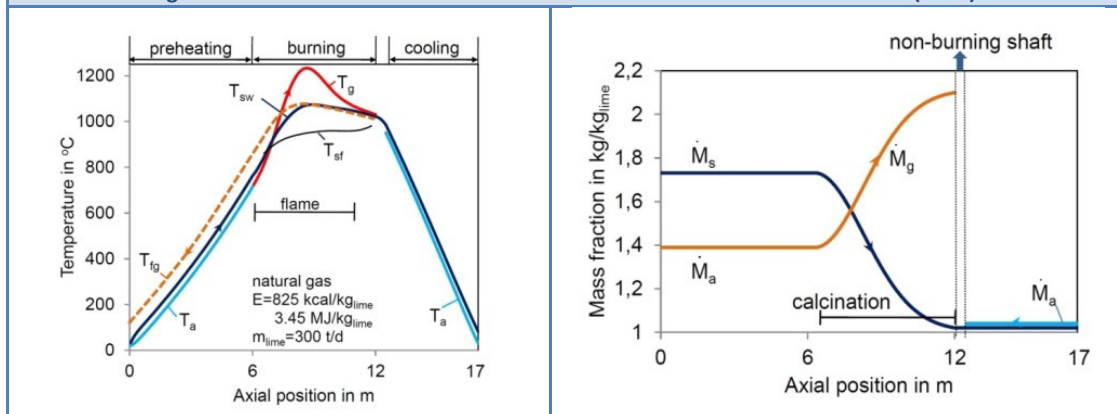


Fig.1.7: a = Principal temperature profile of the PFR lime shaft kiln. b = Principal mass fraction (conversion) profile of the PFR lime shaft kiln. Symbols: M mass flow; T = temperature; Q = heat flow. Subscripts: fg = flue gas; sw = solid wall surface; a = air; ambient; eq = equilibrium; s = solid, f = front, core. From Hai Do et al. (2011).

Silva et al. (2010a, 2010b), Moldenhauer et al. (2016) and Sandaka et al. (2017) tried to bridge the above mentioned gap (not specifically to solve lime reactivity, but mainly to optimize the PFR kiln process) by means of research studies dedicated to the thermophysical properties of limestone as a function of origin: specific heat capacities (part one), calcination enthalpy, and equilibrium temperature (part two), emissivity (part 3), and thermal conductivity (part 4). For the determinations of the specific heat capacity of lime and limestone, the reaction enthalpy at the calcination temperature, and the equilibrium temperature, a Differential Scanning Calorimetry (DSC) was adopted. Disk-shaped

limestone samples of different geological origin, with a diameter of 5 mm, and a thickness of 1-3 mm, were investigated. The following DSC instrumental settings were adopted: heating rate of 20 K/min, from room T up to 1300 °C, under argon atmosphere.

Results from the first part of this research (Silva et al., 2010a), show that the specific heat capacity of limestone increases with temperature and is not influenced by the origin of the stone. Conversely, the specific heat capacity of lime is influenced by the origin of the limestone with fluctuations of $\pm 10\%$, but it is nearly independent of temperature.

In the second part of this research (Silva et al., 2010b) the decomposition enthalpy of limestone is obtained through the integration between 400-1100°C of the specific heat curve determined by DSC for each sample. Higher fluctuations between limestones of different origin, and lower fluctuations between samples of the same origin have been observed (Tab.1.3), mainly due to the presence of impurities. Considering the variation ranges between 1604 up to 1720 J/g, the difference is of 7%. Considering this fluctuation and the typical thermal efficiency of a kiln, the energy consumption can differ by about 5%.

Tab.1.3 – Decomposition enthalpy (J/g_{CaCO_3}) measurements of 3 different samples of each kind of limestone considered in the same study. From Silva et al. (2010b)

Sample	Unit	A	B	C	D
1	J/g_{CaCO_3}	1672	1570	1721	1671
2	J/g_{CaCO_3}	1619	1612	1743	1667
3	J/g_{CaCO_3}	1679	1630	1695	1678
Mean	J/g_{CaCO_3}	1679	1604	1720	1672
Dev. St.	-	60	60	48	11

The decomposition temperature at 1 bar CO_2 of limestone from different origin presented a range between 907-923 °C. Experimental data show that higher temperature is required to decompose crystalline calcium carbonates, i.e. marbles, and dispersion of values reflects the textural anisotropy of the stone. Lower decomposition temperature was observed for argillaceous limestones. Finally, considering decomposition enthalpies of limestone either at normal temperature (from the literature), or at decomposition temperature (from DSC measurements), coupled with the specific heat capacities of CaO, $CaCO_3$, CO_2 , and the corresponding mass fractions, is possible to determinate the energy consumption and the efficiency of the TSR kiln (Bes et al., 2007; Silva et al., 2009).

The third part of this research (Moldenhauer et al., 2016) investigates the emissivity of limestones from different origin in the combustion-temperature range. This parameter determines the temperature homogeneity in the cross-section of the PFR kiln, so its importance in modelling the calcination process. New device for spectral emissivity measurements, based on FT infrared spectrometer with special optical coupling arrangement for external radiation sources, was adopted for experimental tests on limestone blocks (55 mm length – 25 mm width – 3 mm thickness) (see references in Moldenhauer et al., 2016). Emissivity values have been used to calculate the thermal conductivity of limestone bed via radiation for a PFR kiln. Thermal conductivities determined in the temperature range of PFR kilns, which is around 1300 °C, range between 20-40 W/m²K. These values are comparable with those of steels. This illustrates that heat transport by radiation has a significant influence on the homogenization of temperature in the cross-section. The higher the emissivity, the greater the heat flux. The latter may, therefore, differ by a factor of up to 2, depending on the limestone type.

In the fourth part of this research (Sandaka et al., 2017) the thermal conductivity of limestone and lime lumps is analyzed by means of a laser flash apparatus (LFA) up to 1400 °C, and, alternatively, by thermogravimetric electric muffle furnace. In this second configuration a thermocouple was placed at the core of a cylindrical sample previously drilled (diameter: 20-35 mm, length: 5-6 times of the diameter). The thermal conductivity of several limestones was determined. They were plot against with respect to the bulk densities. The higher is the bulk density, the higher the thermal conductivity; the higher is the particle porosity, the lower the conductivity.

1.3. Factors affecting the quicklime reactivity

The state-of-the-art on factors affecting the reactivity of industrial quicklime is subsequently reported. Despite many Authors investigated this topic over the last 80 years, a comprehensive, multidisciplinary and exhausting work is not available in the literature yet. For convenience's sake these factors can be grouped into three main categories:

1. process and kiln parameters;
2. intrinsic or geological parameters of carbonate raw materials;
3. derived parameters of burnt lime products

Parameters pertaining to the first two categories strongly affect the third ones.

1.3.1 Process and kiln parameters

The first category includes temperature raise, i.e. heating rate, heating type, i.e. isothermal or non-isothermal conditions, maximum burning temperature, retention time, static or dynamic atmosphere, combustion atmosphere, CO₂ partial pressure during the experiment, sample weight, i.e. raw materials particle size.

Boynton (1982) reports that a gradual preheating, and a gradual increase in calcination temperature up to the point at which dissociation is complete, rather than a shocking heating rate for a constant time at constant temperature, would guarantee “the greatest influence on lime quality” in terms of shrinkage, porosity and quicklime reactivity. This theory is consistent with the idea that there is “an optimum calcination temperature and rate of heating for every limestone that can only be determined by experimentation”. Actually, even if this approach can be tested by mean of laboratory experiments, it is not representative and reproducible on the industrial scale. In particular, either the retention time, or the burning temperature in a PFR kiln are already fixed, depending on the process technology and the fuel type. This is the reason why industrially-oriented research studies generally test different materials adopting standard protocols, as similar as possible to the process occurring into the industrial lime kiln.

A systematic analysis of fundamental process parameters was performed by Mullins and Hatfield (1970). Authors defined quantitatively the effects of time of calcination, temperature of calcination, and particle size of the limestone upon properties of the calcine, i.e. burnt lime product, for the SO₂ absorption from flue gases. For this

study a pure limestone was adopted to avoid possible complicating effects of impurities and samples were sized by cycles of dry and wet screening with the appropriate mesh openings to obtain uniformity of size and freedom of aggregates. Six size-fractions between 81 and 645 μ m were selected, three calcination times, i.e. 10, 60, 240 seconds, were adopted in a range of temperature between 1000 and 1300°C. Therefore the following analyses were performed on calcined samples: density and pore volume by mercury intrusion porosimetry, crystallite size of calcium oxide by the X-ray line-broadening technique, calcination percentage and absorbed sulfate (SO_3) by thermogravimetric analysis (Fig.1.8).

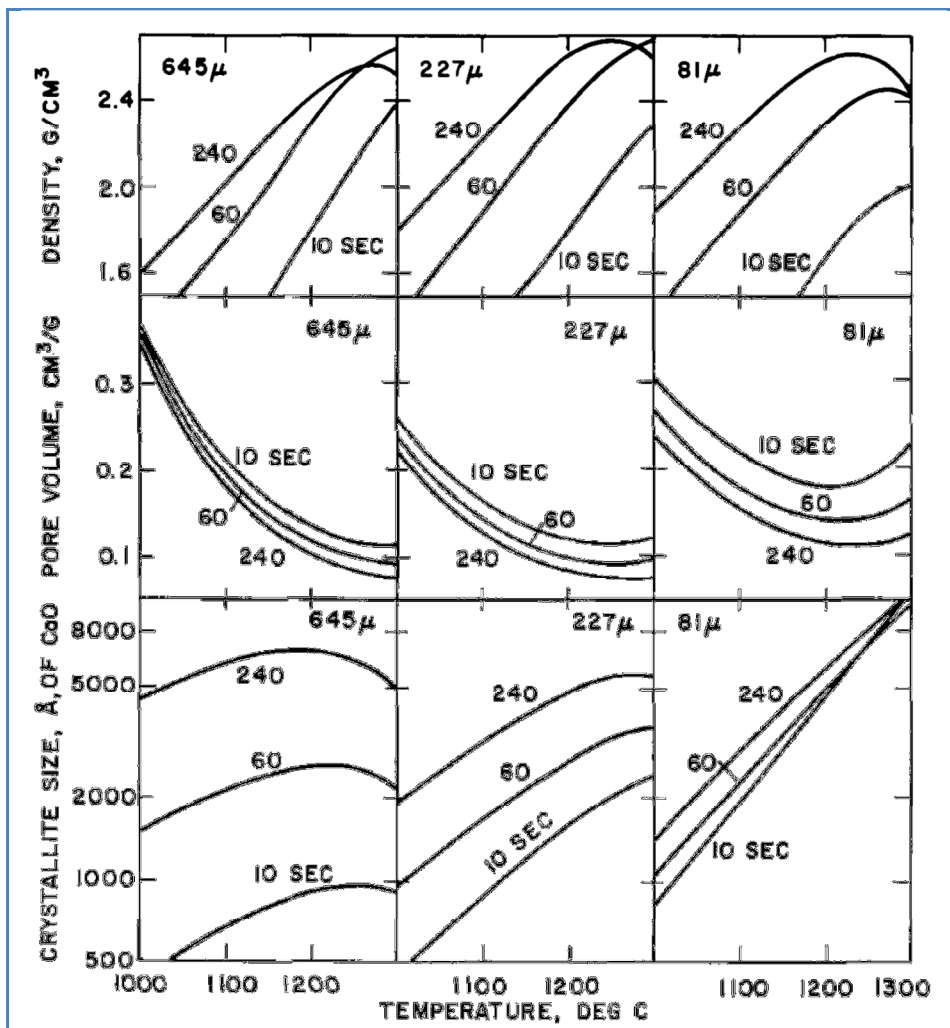


Fig.1.8: Effect of initial particle size and time and temperature of calcination on physical properties of calcines. From Mullins and Hatfield (1970).

Results show that the time of heating affects percent calcination more at low temperatures than at high temperatures. Particle size seems to have little effect on calcination rate. This could be due to the spalling of larger particles subjected to the

thermal shock. Density, pore volume, and crystallite size are strongly interconnected parameters: if density and crystallite size generally increase with temperature, conversely pore volume decreases (Fig.1.8). Moreover unexpected tendency to reach a maximum in density at about 1250°C and in crystallite size at 1200 °C, in particular with coarser 645- μm limestone particles, were observed. Density increases again passed 1300 °C. Finally, results show that the fine grinding of the limestone do not represent a significant advantage for SO_2 absorption, particularly if the calcination temperature is high. In other words the role of the **high calcination temperature is fundamental, more than the time, in sintering the lime by lowering the specific surface area** (Fig.1.9).

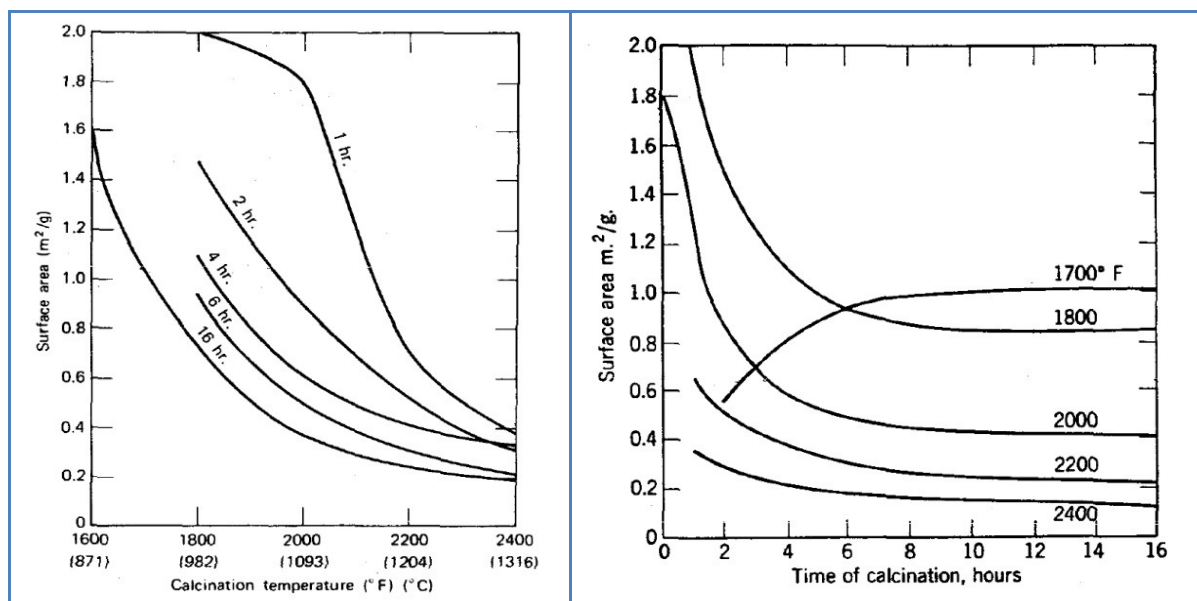
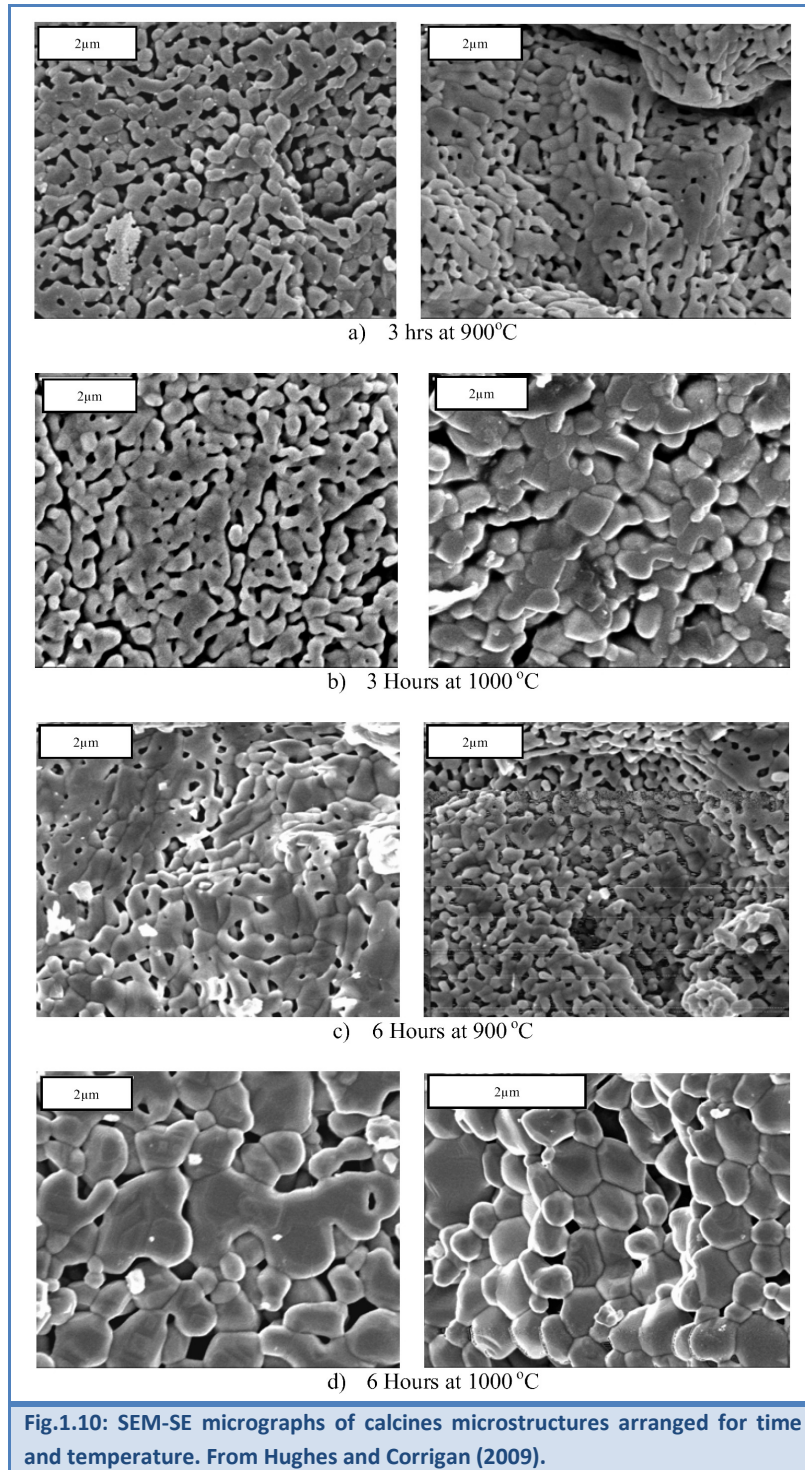


Fig.1.9: a = relation of specific surface area to calcination temperature. b = relation of specific surface area to duration of calcination. From Boynton (1982).

These facts are consistent with the characterization of properties of commercial lime, i.e. soft-burnt and hard-burnt lime, by surface area measurements and SEM analysis performed by Eades and Sandberg (1970). Another pioneering study on the “textural evolution of limestone calcines” after shock burning tests between 750-1300°C was performed by McClellan and Eades (1970) for the flue gas desulfurization.

More recently, Hughes and Corrigan (2009) examined the “microstructure expression of temperature and residence time on laboratory calcined limestone” for building lime-mortars applications. Metamorphic limestone fragments (<3 cm) with approximately the 3% of SiO_2 were burnt in a laboratory furnace up to 1000 °C, at difference times, up to 6 hours. Samples were examined using the Scanning Electron

Microscopy in Secondary Electron mode (SEM-SE) and digital image analysis was performed in order to attempt a semi-quantitative correlation between the conditions of production and the microstructures observed. More details on results from these research studies are reported on the paragraph dedicated to the “derived parameters of burnt lime products” (Fig.1.10).



Akande et al. (2016) reported the application of factorial analysis for quicklime production from a Nigerian limestone, in order to study effects of calcination temperature, calcination time, and limestone particle size. They developed an empirical model based on experimental data. The calcination temperature was tested in the range from 800 to 1000°C, calcination time in the range from 30 to 60 mins and limestone particle in the range from 0.3 to 1.18 mm. The factorial analysis procedure was carried out by means of a mathematical model of the second-order response surface with the best fit. The magnitude of the process parameters, which are independent variables or factors, were estimated using a specific software. The representation of results was performed using factorial plots, i.e. 3-D response surface and 2-D contour graphs. Results confirm that the calcination temperature is considered as the most important parameter in the production of quicklime. Moreover the yield from large particle size is higher than that of lower particle size, and the higher the calcination time, the lower will be the yield of quicklime. Therefore Authors purpose is to optimize the process selecting the best conditions for the yield of quicklime. Considering the purpose of this research activity, this kind of approach can be suitable only by changing the process parameters, which are constants for simulating the lime burning in a TSR kiln (with the only exception of particle size), with intrinsic parameters of carbonate raw materials, and derived parameters of burnt lime products.

1.3.2 Intrinsic parameters of carbonate raw materials

The second category regards intrinsic properties of carbonate rocks. These factors deeply affect the heating behavior or the stone burnability, influencing derived properties of the industrial quicklime. Over the years physicists, chemists and chemical engineers, under the auspices of the National Lime Association, mainly considered physical-chemical properties of the limestone to solve lime reactivity. More recently, i.e. over the last ten years, an increasing number of crystallographic, mineralogical, and petrographic studies were performed, to bridge the geological gap. Because limestone is a naturally occurring material, its composition and physical characteristics do not vary only from different rock formations, but often within the same deposit, and quarry, depending on its age, stratigraphic, paleogeographic, diagenetic and structural settings. Therefore geologists proposed a new approach based on limestone microfacies analysis, resulting from depositional processes, and early to late diagenetic modifications, or metamorphic facies and textures (Soltan, 2011; Soltan et al., 2011; Soltan et al., 2012; Vola and Sarandrea,

2013; Alaabed et al., 2014; Vola and Sarandrea, 2015; Vola et al., 2017; Vola et al., 2018). A similar multidisciplinary approach was adopted to study the heating behavior of limestone in the industrial cement clinker manufacture, as well (Marinoni et al. 2015; Galimberti et al. 2016).

The **chemical purity** of the stone was firstly considered a criterion for the lime quality, before the reactivity was. The quantity (of impurity) is considered more critical than the quality (Boynton, 1982). This is the reason why in Europe and United States lime producers are constantly striving to obtain the purest limestone deposits. Limestone adopted in the production of industrial quicklime must be generally constituted of at least 98% of calcite, meaning that impurities are less than 2% (Schorcht et al., 2013). The typical range of impurities for carbonate rocks adopted in quicklime production is reported in Tab.1.4.

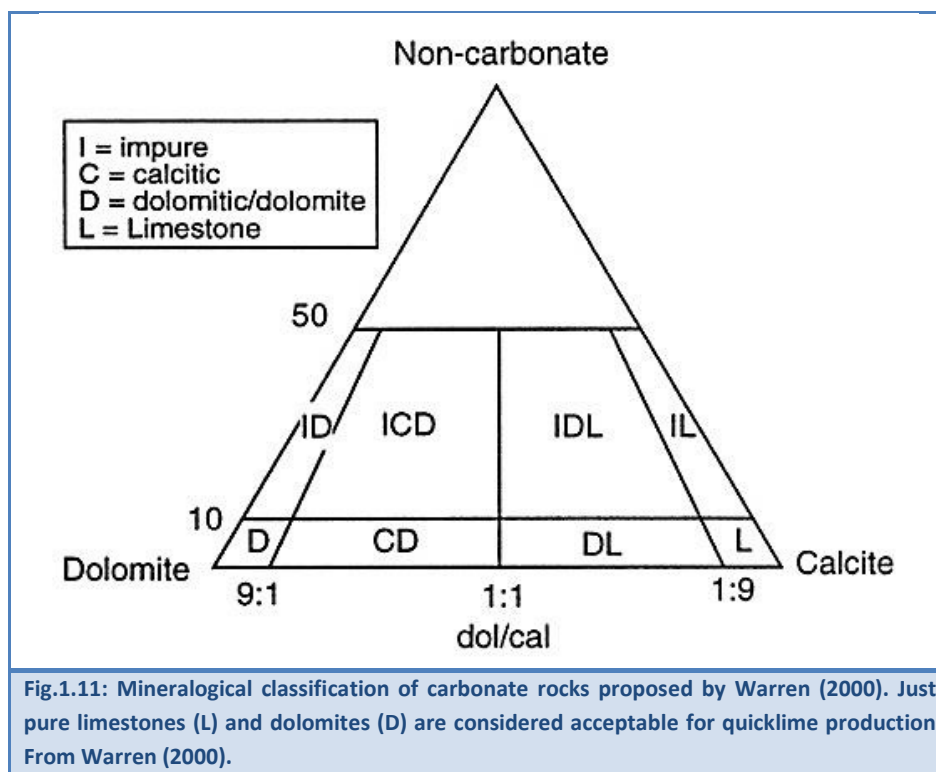
Tab.1.4 – Typical impurities and trace elements in limestone. From Schorcht et al. (2013)

Impurities or metals	Units	Typical range
Silica (SiO ₂)	%	0.1-2.0
Alumina (Al ₂ O ₃)	%	0.04-1.5
Iron (Fe ₂ O ₃)	%	0.02-0.06
Sulfur (S)	%	0.0024-0.118
Carbonaceous matter	%	0.01-0.5
Manganese (Mn ₂ O)	mg/kg	20-1000
Antimony	mg/kg	0.1-3
Arsenic	mg/kg	0.1-15
Boron	mg/kg	1-20
Cadmium	mg/kg	0.1-1.5
Chromium	mg/kg	3-15
Copper	mg/kg	1-30
Lead	mg/kg	0.5-30
Mercury	mg/kg	0.02-0.1
Molybdenum	mg/kg	0.1-4
Nickel	mg/kg	0.5-15
Selenium	mg/kg	0.02-3
Silver	mg/kg	0.2-4
Tin	mg/kg	0.1-15
Vanadium	mg/kg	1-20
Zinc	mg/kg	3-500

The content of **mineralogical impurity** for sedimentary carbonate rocks is mainly represented by subordinated terrigenous, and/or evaporitic minerals (Warren, 2000; Scholle and Ulmer-Scholle, 2003; Flügel, 2010) (Fig.1.11). Typically, the first group includes clays and quartz, more rarely apatite, zircon, titanite, amphiboles, feldspars, plagioclases, amorphous silica and/or other silicates, depending on the orogenetic setting of the carbonate deposit. Carbonates deposited in warm and shallow seawater basins, i.e.

Chapter 1. Introduction

sabkha-like environments, may present sulfates, such as gypsum, or anhydrite, and salts, i.e. halite, and sylvite, while carbonates deposited under anoxic/euxinic conditions may be enriched in organic matter, and pyrite too. Iron oxides, i.e. hematite and magnetite, or hydroxides, i.e. goethite (α -FeOOH) and lepidocrocite (γ -FeOOH), the so-called “limonite” powders, may be present in traces. The impurity content in carbonate rocks can be also ascribed to secondary in-situ precipitation, occurring with early to late diagenesis, or with contact/regional metamorphism, under the synergic action of P-T paths, and secondary fluids circulation. Industrial mineral quality of a limestone deposit can be positively or negatively affected by diagenetic and/or metamorphic events, considering the great variability of possible geological phenomena, ranging from static to dynamic recrystallizations, up to metasomatic processes (e.g. see Kjølle, 2000). Moreover, non-carbonate minerals impurity, e.g. sulfates and chlorides, may arise from the adsorption of fuel volatiles during the burning process into the kiln too (see Boynton, 1982).



Concerning the presence of magnesium in carbonate rocks, a discussion must be performed in a separate section. Marine calcite is generally divided into low-Mg, or high-Mg calcite, based on a boundary of 3–4 mol % MgCO_3 . Magnesium calcite, especially high-Mg calcite with Mg contents higher than 10 mol %, is a biogenic mineral phase, thermodynamically unstable under ambient conditions (Long et al., 2014). Syndepositional

diagenesis generally converts Mg-bearing biogenic calcite into low-Mg calcite, and dolomite. This is the reason why ancient carbonate rocks are mostly composed of calcite and dolomite (Warren, 2000). Dolomite can form as a primary precipitate or, more commonly, by a diagenetic replacement, or as a hydrothermal/metamorphic phase. Sperber et al. (1984) found a bimodal distribution in the percentage of dolomite in carbonate rocks, with modes at 97% (dolomite/dolostone) and at 20% (dolomitic limestones). The same Authors pointed out dolomitic limestones, containing rhombohedral dolomite, are formed during diagenesis in relatively closed systems by the dissolution and the reprecipitation of high Mg-calcite. Conversely, “pure dolomites (dolostones), composed of more nearly stoichiometric dolomite, tend to form in more open systems, characterized by greater volumes of fluids throughput and continuing dissolution-reprecipitation”. Especially the dolomite (mineral) tends toward ideal stoichiometry when formed in evaporite settings, i.e. in hypersaline waters (Warren, 2000).

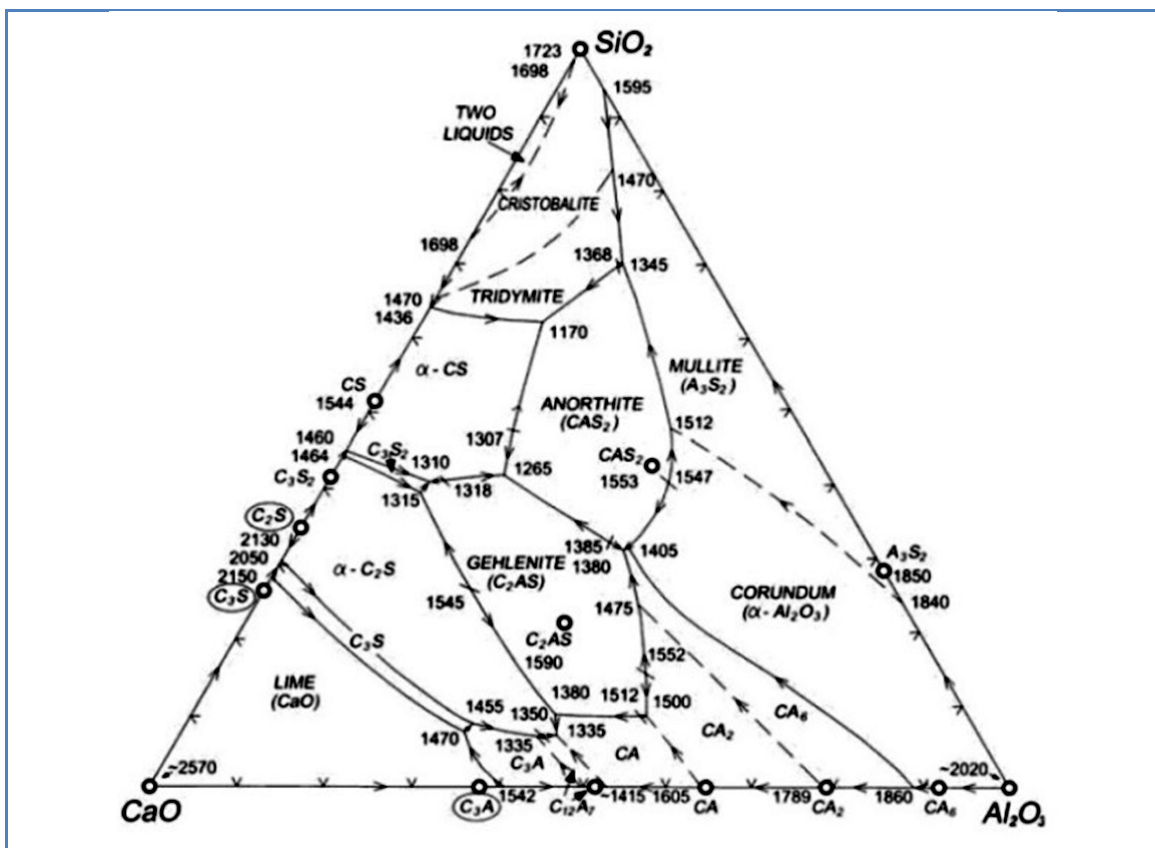
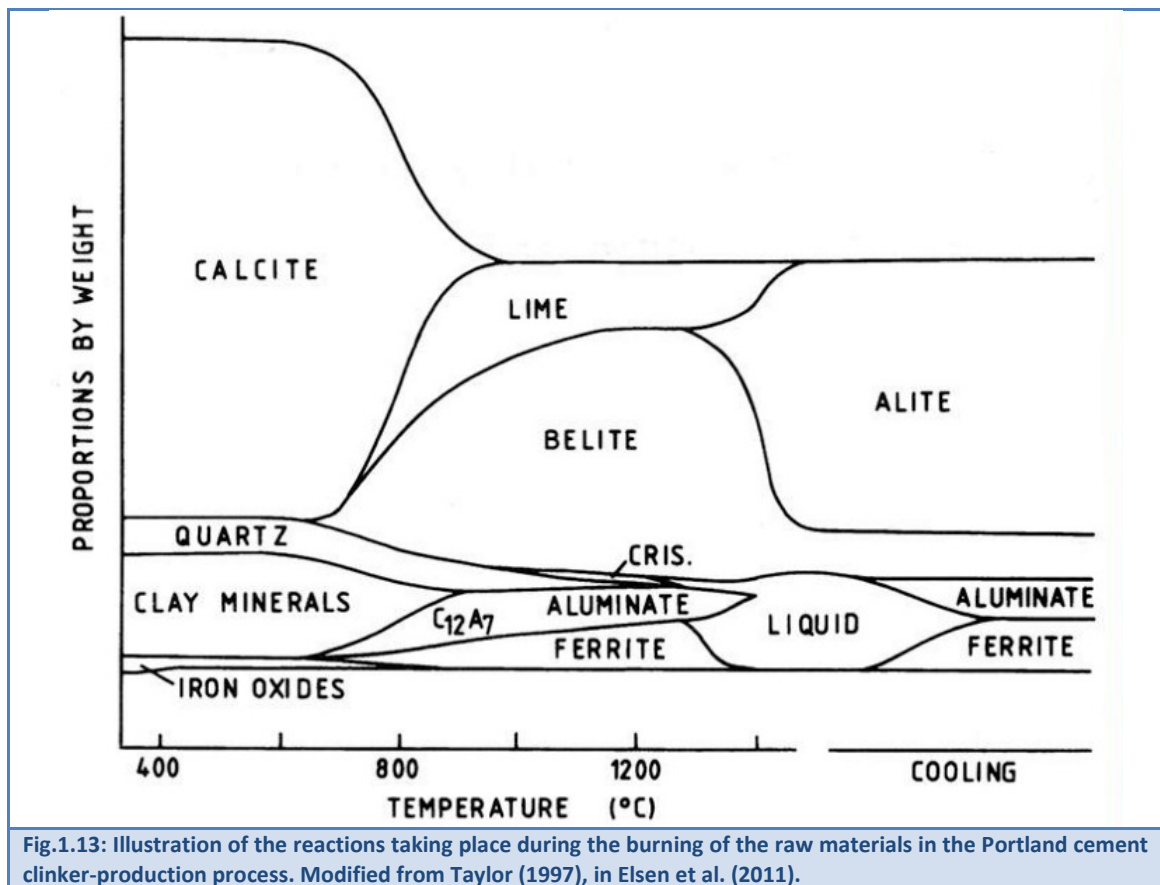


Fig.1.12: Phase diagram of CaO-SiO₂-Al₂O₃ system modified from Taylor (1997) with encircled C₂S, C₃S, and C₃A cement components. From Elsen et al. (2011).



The **impurity content** is critical because lowers the available lime index, and affects the lime reactivity, especially when the calcination is performed at high temperature of 1200 °C. Reactive silica, alumina, and iron from quartz and clay minerals decomposition, react against calcium at low temperatures (900 °C) forming various calcium compounds, such as mono-calcium and di-calcium silicates, i.e. larnite, calcium aluminates, and di-calcium ferrite (Boynton, 1982). At higher temperature ($T > 1250$ °C) tri-calcium silicate, i.e. hatrurite, and calcium aluminate/ferrite minerals may be formed too. However cementitious mineralogical phases are always subordinated, either in high-calcium or in magnesium-rich quicklimes, while they are primary constituents of hydraulic binder limes. An exhausting list is reported in Tab.1.5. For the reactions taking place during the burning of raw meals in the Portland cement clinker-production process see Fig.1.12 and Fig.1.13 from Elsen et al. (2011).

Tab.1.5 – Cement clinker mineral phases. From Elsen et al. (2011)

Cement phase	Abbreviation	Mineral formula	Mineral name
Alite	C3S	Ca ₃ SiO ₅	Hatrurite
Belite	C2S	Ca ₂ SiO ₄	Larnite
Aluminate	C3A	Ca ₃ Al ₂ O ₆	-
Ferrite	C4AF	Ca ₂ (Al,Fe) ₂ O ₆	Brownmillerite
Ghelenite	C2AS	Ca ₂ Al ₂ SiO ₇	Ghelenite

A significant study dedicated to the “effect of impurities on lime reactivity” was performed by Gary Wright (1995). In this study 24 limestones samples were analyzed, using the X-ray Fluorescence spectroscopy (XRF) and thermogravimetric analysis (TG), in order to predict lime quality on the basis of limestone impurities. Linear and multiple regression statistics were used to evaluate experimental results. Two equations describing the correlation between limestone impurities and lime quality were adopted. The first equation [IX] was generated by a statistical software program, while the second [X] derived from the hypothesis that the lime is vitiated about four times the total impurity concentration in the limestone.

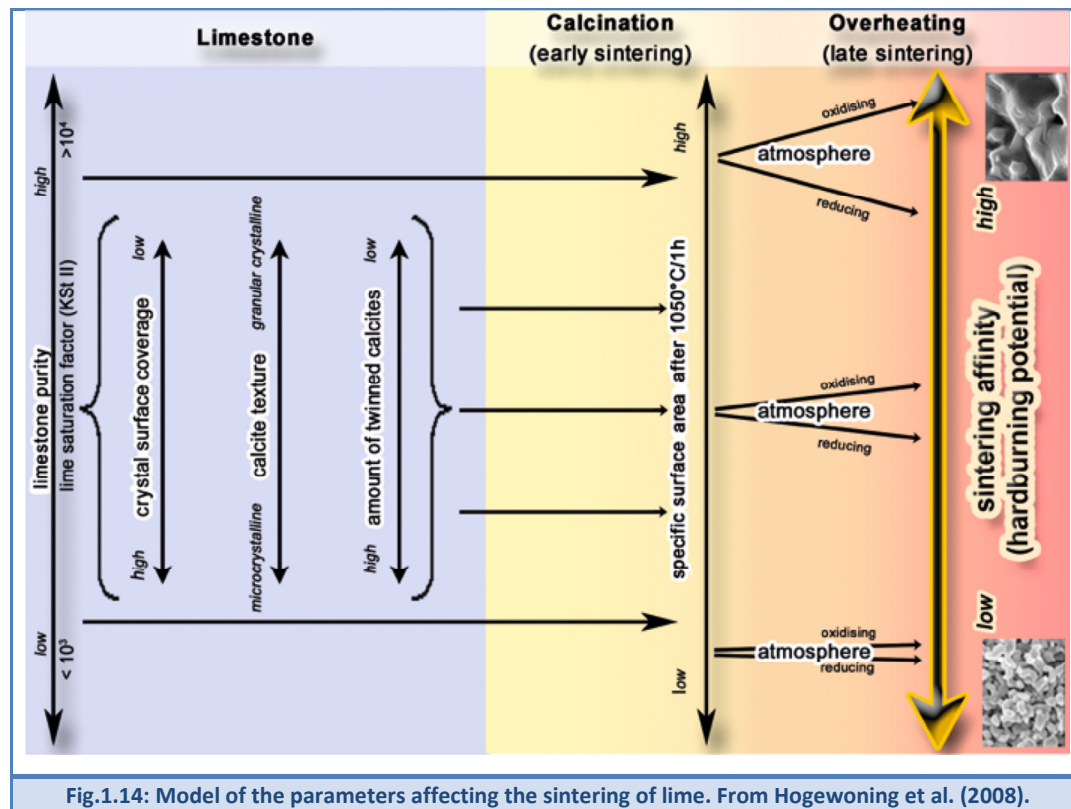
$99.9 - (0.6 \cdot \text{SiO}_2) - (19.2 \cdot \text{Al}_2 \text{O}_3) - (7.0 \cdot \text{Fe}_2 \text{O}_3) +$ $- (2.0 \cdot \text{MgO}) + (2.9 \cdot \text{SO}_3) = \text{Available CaO}$	[IX]
$\text{CaCO}_3 - (\text{MgO} + \text{SO}_3) - [4 \cdot (\text{SiO}_2 + \text{Fe}_2 \text{O}_3 + \text{Al}_2 \text{O}_3)] =$ $= \text{Available CaO}$	[X]

Using the computer generated equation [IX] and limestone impurity concentrations, it is possible to predict resulting available lime with 93.4% of confidence, while using the “4x” equation [X] and limestone impurity concentrations, it is possible to predict resulting available lime with 90.2% of confidence. This study also attests that impurities act as a flux when reacted with calcium, decreasing porosity, affecting heat transfer, the ability of CO₂ to escape from the core of the stone, and ultimately the rate and degree of calcination. Magnesium carbonates, i.e. dolomite and magnesite, dissociate at lower temperatures respect to calcium carbonate does. This difference in the calcination velocity means that the MgO fraction is generally overburnt by the time the CaO fraction is effectively calcined. This is the reason why the presence of magnesium oxide effectively decreases quicklime reactivity, as well (Wright, 1995). By the way, neither crystallographic, nor

textural parameters were considered in this paper, even if these parameters affect calcination rate and heating behavior as well as the impurity content. Moreover, the high available lime index do not always correspond to an high quality lime in terms of quicklime reactivity (e.g. see Vola et al., 2017).

More recently, Hogewoning et al. (2008) understood that natural variability of raw materials has to be accurately investigated, and that a target-oriented production of quicklime requires the knowledge of limestone parameters affecting the properties of the final product. Thus the purpose of this study was to produce a model that was independent of the deposit, to predict the hard burn potential, i.e. the sintering tendency, and quicklime reactivity, from the knowledge of burning conditions. Limestone from 21 deposits were examined petrographically and chemically and submitted to burning trials in a two-zone muffle furnace with difference temperature-time profiles. Burnt products were analyzed for slaking reactivity, apparent density, and microstructure. Results were combined in a model for describing the influence of the limestone property parameters on the hard burn potential of the quicklime produced. First of all burning tests were performed on 2-4 mm size fractions, after comminution of samples in a jaw crusher. Different calcination temperatures (1050 °C, 1100 °C, 1200 °C up to 1300 °C), and times (1 h, 2 h, 4 h, and 8 h) were considered, and the majority of trials were performed under air conditions. Determination of apparent density was performed with a solids pycnometer. Results pointed out that maximum slaking rate and apparent density are directly correlated. As concerns the BET surface area it was only determined on the quicklimes after burning tests at 1050 °C for 1 h, because for higher temperatures “the specific surface area dropped too sharply after the sintering trials and lay within the range of uncertainly”. The apparent densities of quicklimes were compared with the Lime Saturation Factor (LSF) [XI], derived from the cement chemistry, which indicates the ratio of the total CaO content to the amount of CaO that can be combined with SiO₂, Al₂O₃, Fe₂O₃, during the formation of cement clinker phases, as follow:

$\text{LSF} = \frac{\text{CaO}_{\text{total}} \cdot 100}{(2.8 \cdot \text{SiO}_2) + (1.18 \cdot \text{Al}_2\text{O}_3) + (0.65 \cdot \text{Fe}_2\text{O}_3)}$	[XI]
---	-------------



The LSF values were plotted against the apparent densities of quicklimes. This plot allowed grouping samples in three different sets. The first one with a $LSF < 10^3$ includes samples “with minor constituents in a generally very fine-grained limestone microstructure”. This group is characterized by a limited coarsening of crystallites after burning at high temperature, because of shrinkage free-sintering. This may be accompanied by local melt formation, and the generation of melt skin. Minor constituents act as sinter barrier, preventing the diffusion of solids between the CaO clusters, hence any further recrystallization with grain growth. Conversely, the second clearly defined group covers the very pure limes with $LSF > 10^4$ that exhibit a very high hard burn potential. This group is characterized by a significant crystalline coarsening by recrystallization with grain growth on further heating. This is associated with very rapid increase of apparent density and simultaneous reduction of reactivity. These two groups with very distinct characteristics are in contrast to the limes with an intermediate LSF between 10^3 and 10^4 that can have differing sintering characteristics in spite of similar lime saturation factors. For this group the Authors appealed other factors affecting the sintering process. Especially, they considered MgO from dolomite, and K_2O from mica, as good parameters to correlate with apparent densities. These parameters are considered sintering inhibitors, as well as the large calcite crystals with twinning. The first two parameters, referred as

(MgO+K₂O)_{standard}, “reduce the sintering affinity through coating of the interfaces as do a fine-grained microstructure with small calcite clusters and interstitial, diffusion-retarding, minor constituents”. Finally, “twinned individual calcite crystals lower the hard burn potential by destroying the crystalline structure as a result of their anisotropic thermal expansion behavior”. Hogewoning et al. (2008) model of lime sintering affinity or, hard burning potential, is reported in Fig.1.14.

Baziotis et al. (2011) proposed a statistical analysis based on bivariate plots of reactivity against $(\text{CaO}+\text{MgO})_{\text{Lime}}$ and $\text{CaO}_{\text{Rock}}/\text{CaO}_{\text{Lime}}/\text{MgO}_{\text{Rock}}/\text{MgO}_{\text{Lime}} = (\text{CaO}_{\text{Rock}} \cdot \text{MgO}_{\text{Rock}})$ in order to check trends of reactivity with composition of limestone or lime, but this approach did not lead to a significant progress in prediction of quality in high-calcium quicklimes.

The influence of the **organic matter** of carbonate rocks in the reactivity of the produced quicklime was investigated by Kantiranis et al. (2003). A gray and a white crystalline limestone from Greece were considered by the Authors. They presented almost the same mineralogical composition, but very different contents of organic matter, ranging from 0.8% in the gray limestone, up to 0.09% in the white one. The quicklime from gray limestone presents higher porosity value, and is more reactive in comparison with the quicklime from the white crystalline limestone. Differences in reactivity are mainly attributed to differences in the percentage of the organic matter.

Preliminary studies with a multidisciplinary approach, including geological background of the carbonate deposit, coupled with the mineralogical-petrographic analysis, were performed by Triantafyllou et al. (2003), Moropoulou et al. (2001), Kiliç and Mesut (2006). More recently, research activities performed over the last ten years considered the fundamental contribution given by the **microfacies analysis of carbonate rocks** (Soltan, 2009; Soltan and Serry, 2011; Soltan et al., 2011; Soltan et al. 2012; Alaabed et al. 2014; Vola et al., 2017). These studies, based on a solid background of carbonate sedimentology fundamentally consider the carbonate rocks classification proposed by Dunham (1962), and Embry and Klovan (1971), as the starting point for any further characterization (for more references see Flügel, 2010).

In carbonate petrography the fundamental distinguishing feature is between mud-supported and grain-supported primary or depositional textures. Even if mudstones/wackestones from one side, and packstones/grainstones to the other, may present different heating behavior or burnability, and different sintering or overburning tendency (see e.g. Hogewoning et al., 2008), it is hard to identify and quantify textural

parameters to plot against the lime reactivity. In the literature, the point-counting modal analysis has been widely adopted by several Authors for the classification of sedimentary carbonate rocks (Bissell and Chilingar, 1967). For example, Leighton and Pendexter (1962) adopted the “grain/micrite ratio” (GMR) as important factor for textural classification of their limestones. This ratio appears along the vertical axis of their chart, and is the sum of the percentages of grains divided by the percentage of mud-like material (micrite). Essentially, the “grain/micrite ratio” (GMR) is equal to:

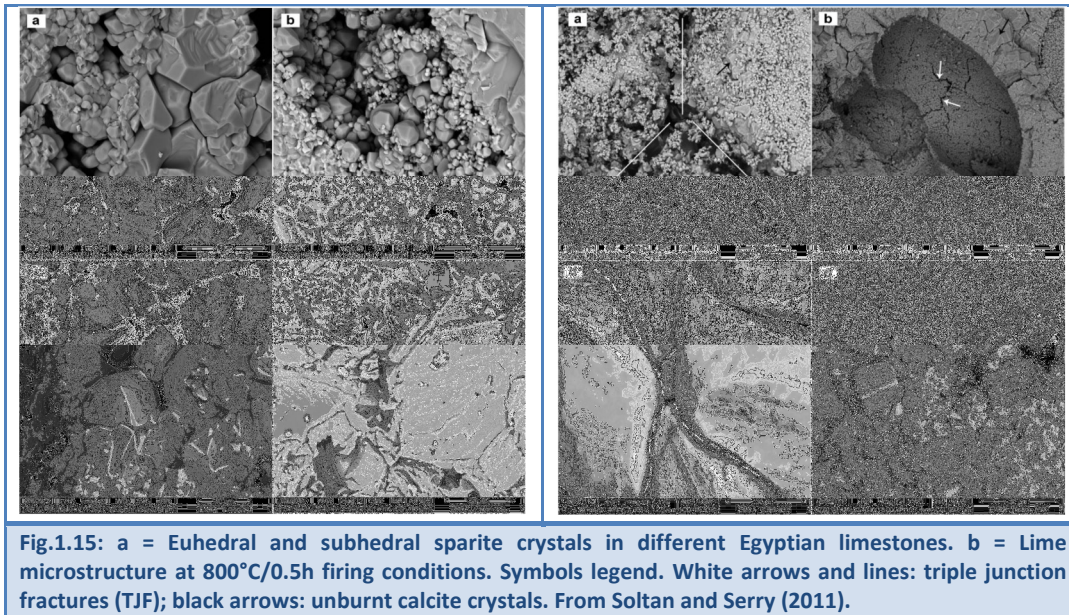
$\text{GRM} = \frac{\%(\text{detrital grains} + \text{skeletal grains} + \text{pellets} + \text{lumps} + \text{coated grains} + \text{mineral grain})}{\% \text{ micrite}}$	[XII]
---	--------------

Vola and Sarandrea (2013) in a paper on “raw materials characterization for industrial lime manufacturing” proposed to consider the “micrite/sparite ratio” (MSR), deriving this textural/microstructural parameter from the petrographic digital image analysis performed on multiple thin sections from the same sample. Unfortunately, this kind of approach presents some limitations, and the quantification of coarse-sized carbonate grains, i.e. allochems, non-carbonate impurities, and/or diagenetic modifications can be critical, as well. The same authors presented another study (Vola and Sarandrea, 2015) dedicated to the quantitative analysis of granoblastic textures in metamorphic carbonates adopted in quicklime manufacture. This paper pointed out the straight correlation between the crystal-size distribution, measured by optical microscopy, and the mechanical degradation/dust formation of derived burnt lime. The relationship between optically-determined crystal-size and lime reactivity was not examined yet.

In the last ten years other fundamental researches were published by Arabian Authors. Soltan (2009) proposed a mathematical model for the optimum petrographic variables that affect quicklime production. This study is based on petrographic semi-quantitative analysis performed on 18 Egyptian limestones. Petrographic data set was statistically analysed by applying the stepwise regression method. 14 petrographic facies have been identified and considered independent variables affecting the rate of lime liberation at each firing conditions, i.e. temperature and soaking or retention time. Although all the components, i.e. allochems and orthochems, are mainly calcitic, their decomposition behaviours affect the lime calcination positively or negatively, depending on the applied burning conditions. Moreover the nature of associated non-carbonate

components play a role in thermal behaviour, as well. For example, the micritic matrix has a retarding role, whereas sparite always increases the lime yield at all applied burning conditions. The role of skeletal grains is contradicting because at 900 °C soaking time the decomposition rate is slower than micrite and sparite, while at 1000 °C is faster, promoting the reaction between neoformed lime with other oxides forming cement phases. The effect of non-skeletal grains is also contradicting, depending on the applied firing conditions. The allochems calcination rate depends on their grain size: fine-grained allochems decompose earlier than coarse-grained ones, at all firing conditions. Finally, the roundness of allochems affects positively calcination rate only for well and very well-rounded grains, at all firing conditions.

Soltan and Serry (2011) investigated the “impact of limestone microstructure on calcination activation energy”. Authors performed the petrographic analysis of 5 different Egyptian limestones in order to evaluate the effect of their microstructure on the calcination activation energy E , calculated from the Arrhenius equation. Egyptian materials considered in this study can be divided into two main groups. The first group is represented by 3 limestones from Eocenic deposits, characterized by large textural anisotropy, including skeletal grains, large nummulites foraminifera, bryozoa, echinoderms, and small planctonic foraminifera (Tab.1.6). Allochems are cemented by sparite groundmass (calcite crystals $>4 \mu\text{m}$) in percentages varying from one sample to another. The second group is represented by an Eocenic and a Cenomanian-Turonian (Upper Cretaceous) limestones presenting isotropic and homogeneous textural features with rare fossil contents and sparite groundmass (Tab.1.6). Selected limestones are very pure, with a CaO content ranging between 54-55 %. Mineralogical impurity is mainly constituted by dolomite crystals and quartz grains, with a concentration ranging between 1.3-0.5 %. Moreover, the petrographic analysis pointed out a significant primary intraparticle, and/or secondary moldic porosity. Thin sections were stained by blu dye for the porosity elaboration, and the SEM analysis was performed too. Authors pointed out how the formation of connected triple junction fractures (CTJF) facilitates the flow of hot gases within the lime particles during the calcination. CTJF is a typical lime microfabric that can be easily formed along the sparite euhedral and subhedral crystal facies in these samples (Fig.1.15).



The intraparticle open porosity, depending on skeletal grains interlocking, contributed in raising the rate of free lime liberation too. The activation energy E of analyzed samples ranges between 37.62 up to 48.37 kcal/mol (corresponding to 157.4 up to 202.4 kJ/mol), and is inversionally proportional to the increase in skeletal grains at the expense of sparite (Tab.1.6 and Tab.1.7).

Tab.1.6 – Main chemical, thermal and physical properties of Egyptian limestone samples. From Soltan and Serry (2011). Symbols legend: LOI = Loss on ignition; TIO = total impurity oxides, E_a activation energy

Sample	LOI	TIO	CaO	MgO	E_a	Bulk Density	Apparent Porosity	Age
	(%)	(%)	(%)	(%)	(kcal/mol)	(g/cm ³)	(%)	-
Sawada	43.04	0.58	55.49	0.50	37.62	2.28	21.65	Early Eocene
Ogra	42.74	0.70	54.81	1.02	41.98	2.35	19.46	Middle Eocene
Libni	43.97	0.51	54.00	0.29	42.21	2.61	10.56	Cenomenian-Turonian
Tebbin	43.05	1.31	54.77	0.41	48.37	2.44	16.96	Middle Eocene

In other words intraparticle open porosity enhances the heat transfer by diffusion of hot gases inside the grains and the fast diffusion of CO₂ as well as the lower E . Conversely, denser and more compact limestone samples, presenting an higher textural homogeneity due to the absence of large skeletal grains, presented a relatively higher E . In conclusion, Soltan and Serry (2011) demonstrated that calcination of studied limestones is a temperature, chemical and microstructural dependent process.

Tab.1.7 – Main petrographic constituents of Egyptian limestone samples (Soltan and Serry, 2011)

Sample	Dunham Classification	Echinos	Bryozoa	Forams Large	Forams Small	Allochems total	Orthochems (Sparite)
		(%)	(%)	(%)	(%)	(%)	(%)
Sawada	grainstone	0	0	70	0	70	30
Ogra	grainstone	15	35	0	10	60	40
Libni	grainstone (?)	5	0	0	0	5	95
Tebbin	grainstone (?)	2	0	1	0	3	97

The “impact of physical properties and chemical composition of limestone on decomposition activation energy” was investigated by Kiliç (2013), as well. This paper doesn’t report any mineralogical-petrographic characterization, but, presents a significant physical characterization, including bulk density, effective porosity, water absorption rate, and P-wave velocities, measured by an ultrasonic non-destructive transmitter and receiver. Results show that samples with higher chemical purity, P-wave velocity, lower bulk density, and porosity show relatively higher activation energy and rate of lime crystalline growth or sintering. This is due to the original grain channel pores and the formation of connected triple junction fractures (CTJF) during calcination, which facilitate transfer of hot gases and diffusivity of evolved CO₂. Therefore, Soltan and Serry (2001), and Kiliç (2013) conclusions agree. Moreover, activation energies found by Kiliç (2013) range between 54.43 up to 55.56 kcal/mol (corresponding to 227.7 up to 232.4 kJ/mol), and are consistent with ones from the litterature. The presence of impurities impact of the activation energy, e.g. aragonite leads to an increase in the energy barrier to calcination, while clay minerals reduce the activation energy (Kiliç, 2013).

In another paper, Soltan et al. (2011) investigated the “thermal microstructural changes of grain-supported Egyptian limestones”, and their quicklime reactivity. This study is based on chemical (XRF) and mineralogical analyses (XRD), coupled with microscopy (OPM and SEM) and X-ray micro-tomography (μ-CT). Results pointed out that sample enriched in large nummulites foraminifera is more reactive than sample dominated by small foraminifera, peloids and miliolids. This fact is mainly attributed to preservation of intraparticle porosity during calcination, and to the development of pinhole and fracture micropores on calcines. Contraction fracture micropores expose a larger surface area of lime to hydration. Moreover, the shape of these pores, and not their amount, is the main controlling variable in quicklime reactivity. Grainstones of compact structure, with very low porosity, have insufficient grain growth for pinhole micropores development. Finally, the lime enriched in perclase (MgO max = 3.9%) shows the lowest

reactivity. Unfortunately, the experimental conditions adopted in this study, i.e. 950°C burning T and 2 hours of retention time, are not representative of a calcination process occurring in an industrial kiln. It would have been interesting to test burning attitude and calcination velocity of these materials at higher burning temperatures and retention times, to verify their overburning or sintering tendency in a PFR kiln.

In another article, Soltan et al. (2012) investigated the “microstructure and reactivity of calcined mud-supported Egyptian limestones” adopting the same analytical techniques and calcination conditions of the previous research paper dedicated to grain-supported limestones. Despite the aforementioned limitations, results from this study clearly attest that mud-supported limestones are unreactive, presenting a low burning attitude or heating behavior, with the only exception of the Chalk sample. Microstructure of lime derived from mud-supported does not preserve any original textural features, so the main controlling variables on the lime reactivity are chemical and mineralogical compositions. These factors affect the crystallinity of lime; especially, the increase of P_2O_5 content increases the degree of crystallinity and decreases the lime reactivity.

Another interesting paper is from Alaabed et al. (2014), dedicated to the “impact of petrography on thermal behavior of United Arab Emirates limestones”. Analytical techniques previously adopted by Soltan et al. (2011; 2012) are here implemented by means of cathodoluminescence microscopy; moreover the burning temperature reached 1100 °C. With the only exception of an impure sample (Ghalilah), presenting a very high silica content ($SiO_2 = 12.85\%$), UAE limestones are suitable for the production of soft-burned, highly reactive quicklime. The optimum calcination conditions are not the same for all samples, depending on significant differences in textural features or depositional microfacies. Especially, results show that an increase in the allochems is always associated with an increase in the bulk density and consequently a decrease in the apparent porosity of the limestone. This fact is consistent with orthosparite fillings within the bryozoan and nummulitic chambers. The highest maximum hydration rate (2.53 °C/s) was found for Late Jurassic Musandam limestone, constituted by medium up to coarse-grained wackestone-packstone, presenting peloids and small neomorphic micro-sparite (allochems 40%, orthochems 60%). This sample also shows an evident sintering or overburning tendency at 1110°C, mainly due to the onset of growth of the lime crystallites. Other two samples, i.e. Shauiba and Muthaymimah limestones, constituted by very coarse-grained packstone-grainstone microfacies, present lower burnability and reactivity, i.e. the hydration rate ranges between 2.49 and 2.18 °C/s. These samples have large skeletal grains with

Chapter 1. Introduction

echinoids, bryozoan, and algal fragments, and approximately the same content of allochems/orthochems. Finally, the lowest burnability and reactivity, i.e. the lowest hydration rate (0.65-0.70 °C/s), was found on two samples, Dammam and Asmari limestones, constituted by grainstone microfacies. They are dominated by gravel-sized (70-80%) well-rounded nummulite bioclasts filled in by subordinated orthosparite (20-30%). The last two samples preserve their “ghost” microfacies and exhibit an incomplete calcination at the applied firing conditions, because their more compact (closely packed), microstructures require longer soaking time to achieve maximum hydration rate. Petrographic data are summarized in Tab.1.8 and Tab.1.9.

Tab.1.8 – Main chemical, thermal and physical properties of UAE limestone samples (from Alaabed et al., 2014).
Symbols legend: LOI = Loss on ignition; TIO = total impurity oxides; E_a = Activation Energy

Sample	LOI	TIO	CaO	MgO	E_a	Bulk Density	Apparent Porosity
	(%)	(%)	(%)	(%)	(kcal/mol)	(g/cm ³)	(%)
Ghalilah	37.65	13.41	48.15	0.13	34.38	2.60	2.2
Musandam	43.62	0.16	55.52	0.11	31.50	2.80	1.6
Shauiba	43.66	0.15	55.53	0.12	28.00	2.84	2.2
Muthaymimah	43.50	0.35	55.42	0.14	16.50	2.60	2.0
Dammam	43.41	0.54	55.25	0.15	14.70	2.90	1.2
Asmari	43.46	0.54	55.32	0.11	26.00	2.85	1.4

Tab.1.9 – Main petrographic constituents of UAE limestone samples (from Alaabed et al., 2014).

Sample	Age	Dunham classification	Allochems Total	Orthochems (sparite)
			(%)	(%)
Ghalilah	Late Triassic	Impure wackestone	20	80
Musandam	Late Jurassic	wackestone/packstone	40	60
Shauiba	late Early Cretaceous	packstone/grainstone	55	45
Muthaymimah	Late Cretaceous early Paleocene	packstone/grainstone	50	50
Dammam	Middle-Late Eocene	grainstone	80	20
Asmari	Early Oligocene	grainstone	70	30

The activation energy E_a required for calcination to commence of UAE limestones ranges between 14.7 and 34.4 kcal/mol (corresponding to 61.5, and 143.8 kJ/mol). The increase in content of allochems correlates either with decrease in the activation energy or in the hydration rates. Conversely, the content of orthochems correlates with increase in the activation energy or in the hydration rates. In other words allochems, i.e. carbonate grains, require lower activation energy for calcination, and present lower reactivity than

orthochems or sparite; moreover allochem-derived lime crystals are larger in size with lower porosity than orthochem-derived lime crystals.

To finalize this paragraph, the study performed by Lech et al. (2009) must be considered too. Authors investigated the “the effect of limestone fabric on the fabric development in burnt lime” performing an in-depth physical characterization of different limestone and derived lime samples. Thermal decomposition of cylindric limestone samples (dimensions: 120 x 1000 mm, weight c. 4000 g) of different origin and age, was performed at 1050 °C in an experimental electric muffle furnace under air conditions. The following porosimetry techniques have been adopted either on both limestone/lime samples: 1) helium pycnometry for skeletal, or real density determination, 2) envelop density analysis, based on the intrusion of a quasi-fluid having a high degree of flow-ability, for bulk or apparent density. The porosity percentage was calculated, as follow:

$$\omega = (\rho_s - \rho_b) / \rho_b \quad \text{[XIII]}$$

Where: ω is the total porosity (%), ρ_s is the skeletal density (g/cm^3) and ρ_b is the bulk density (g/cm^3). In addition the specific surface area by nitrogen absorption with the BET method, the pore size distribution by mercury intrusion porosimetry, the optical and scanning electron microscopy (SEM) of limestone/lime samples were performed, as well. Results pointed out that differences in the starting texture of the limestone impact on differences in the final texture of the lime. The flux of carbon dioxide is transported through the lime during calcination and depends on the typical geometry of the voids. The porosity is formed by micro-, meso-, and macro-pores, plus micro- and macro-cracks. The intensity of occurrence of cracks depends on the size of the calcite/dolomite crystallites. The different contraction of calcite and dolomite during calcination, which depends on their different molar volumes, is the main cause of cracking. The capillary pore model of a porous medium, based on the hydraulic diameter, is not suitable for the description of the carbon dioxide flow through the lime. Conversely, the dusty-gas model is suitable for the description of gas-transport in a porous media, and the Knudsen's diffusion mechanism dominates in the transportation of the CO_2 through the lime layer during calcination. The typical texture of each porous medium is controlled by geometrical coefficients, i.e. porosity-tortuosity and permeability. Therefore the Darcy's equation can be applied in the calculation of the carbon dioxide transportation through the lime layer.

Finally, it's significant to underline that no mineralogical-petrographic researches on reactivity of dolomitic quicklime have been published yet, so this topic is going to be investigated in the present research activity too. For this purpose some different Italian dolostones have been selected and submitted to different burning and technological tests (see Chapters 2-3).

1.3.3 Derived parameters of burnt lime products

The third category consists of physical, chemical, mineralogical and microstructural characteristics of burnt lime products, deriving from the synergic actions of process parameters and intrinsic properties of the parental carbonate stone. Typical properties of Soft-, Medium-, and Hard-Burned quicklimes are reported in Tab.1.10.

A pioneering study, combining the BET method (acronym of Authors Brunauer, Emmett, and Teller: see Brunauer et al., 1938) for the specific surface area and the scanning electron microscopy (SEM) was performed by Eades and Sandberg (1970). The SEM analysis allowed observation of differences in porosity from the same stone calcined at different temperatures and times. In particular calcitic and one dolomitic stones, in the typical commercial size-fractions, were subjected to several different kilns conditions. Partially burned fractured fragments, sampled close to the core of the stone, permitted to observe the initial phases of calcination.

Tab.1.10 – Typical properties of Soft-, Medium-, and Hard-Burned quicklimes. From Oates (1998)

Property		Degree of burning		
Property	Unit	Soft	Medium	Hard
Apparent density	g/mL	1.5-1.8	1.8-2	>2
Porosity	%	55-45	45-39	<39
Reactivity (t_{60})	Min	<3	3-9	>9
Residual CaCO_3	%	4-1	1-0.5	<0.5

Differences in morphology of calcite (CaCO_3) grains and intergranular voids in the original limestones may explain why resulting lime with similar surface areas can differ in reactivity. Limestones used for the production of the commercial limes studied differ greatly in their “physical makeup”, namely depositional microfacies or petrographic primary texture, which may includes shell fragments, pellets, oolites, and “precipitated calcite grains”. Apparently, Authors didn't know the difference between a micritic calcite, and a precipitated sparry-calcite cement, according to classifications of carbonate rocks

based on depositional textures (Dunham, 1962; Embry and Klovan, 1971). They clearly understand that shape and size of the CaO crystallites formed are at least partially influenced by the form and the type of carbonate grains and relative arrangement of grains and voids in the parental carbonate.

Another significant study was published by McClellan and Eades (1970) on the “textural evolution of limestone calcines” burned in the range of 750-1300°C by shock heating. Authors investigated a pure limestone and Iceland spar samples, crushing them between 700-800 micron. A shock calcination was carried out in an environment preheated to a selected temperature in contrast to calcining at rising temperatures. These two materials differ only in their texture, so that the effects of composition can be ignored. Calcines were analyzed by means of SEM and intrusion mercury porosimetry, and the results were used to interpret the textural dependence on calcination temperature. Authors calculated surface areas and equivalent mean spherical pore diameters by the Mayer and Stowe (1964) method, which is considered a technique more applicable to the characterization of solid-fluid reactivities. Main results are that raising the temperature of calcination decreased the total pore volume and shifted the distribution toward larger pores. Although rhombohedral residual morphology is maintained, the number of pores decreases rapidly at the higher temperatures as a sintering effect. The textural feature of the parental carbonate predominates in materials calcined below 1100°C. At higher temperatures the change in physical characteristics of the calcium oxide became dominant, and the lime is more compact as the result of sintering and crystal growth. These changes are characterized by a marked decrease in porosity, because big pores grow at the expense of small ones. Finally, the larger crystallite size of calcines of Iceland spar inhibits the migration of carbon dioxide from the crystal structure, with the possible recarbonation effects.

Borgwardt and Bruce (1986) specifically investigated the “effect of specific surface area on the reactivity of CaO with SO₂” for the flue gas desulfurization in the electric industry, i.e. power plants. Authors studied the calcination kinetics and surface area of small (1-90 μm), well-dispersed limestone particles, to evaluate the sulfur capture capacity for the optimization of limestone injection multistage burner (LIMB) process. Reaction rates were measured in a differential reactor by techniques previously described by the same Author (see references in Borgwardt and Bruce, 1986) to eliminate intraparticle pore diffusion resistances. In absence of these principal variables, the rate of SO₂ capture is controlled by reaction temperature, specific surface area of the CaO, and SO₂ partial

pressure. Main limits, for our purposes, are related to the specific setup of experimental conditions, i.e. fineness of limestone particles, low calcination temperature, and reactivity apparatus type. On the other hand, Authors provide useful insights on the rate-controlling process and the rate-limiting mechanism of reaction, which are mainly derived from the Avrami's type mathematical approach (Avrami, 1940). Many other studies have been published on the calcination kinetics, as already reported on the relative paragraph (for a synthesis see Cheng and Specht, 2006 and Georgieva et al., 2012).

Commandré et al. (2007) studied the reactivity of laboratory and industrial limes, investigating their great difference in hydration activities. Fundamental mechanisms controlling increasing/decreasing effects on specific surface area of quicklime are identified to be the calcination rate, and the sintering of quicklime. In particular, high operating temperatures of industrial kilns, and significant CO₂ accumulation induce quicklime sintering being responsible for the low slaking reactivity. Furthermore, they pointed out that “some correlation between reactivity and specific surface area among classes of quicklimes sintered under a given atmosphere exists, but the knowledge of the specific surface area is not sufficient to predict the reactivity of a quicklime obtained under an unknown atmosphere” (Commandré et al., 2007).

A fundamental recent contribution to the analysis of the reactant/product crystallographic relationship, and textural-mineralogical changes taking place during calcite thermal decomposition in air, was performed by Rodriguez-Navarro et al. (2009). For the first time advanced non-conventional techniques such as Field Emission Scanning Electron Microscopy (FE-SEM), two-dimensional X-ray diffraction (2D-XRD) analysis, and transmission electron microscopy (TEM) coupled with Selected Area Diffraction (SAED) have been adopted on thermal decomposition of Iceland spar single crystals. Results pointed out the calcination reaction [I] is pseudomorphic and topotactic. Especially, the external shape of rhombohedron is preserved during thermal decomposition of calcite crystals. Moreover textural features of nascent CaO aggregates are not dependent on CO₂ partial pressure, even if it influences decomposition temperature and rates, as well as the coarsening of CaO crystals.

1.4. Lime agglomeration, blocks formation and sticking tendency

1.4.1 Introduction to the issue

The block formation and the lime agglomeration into industrial lime kilns are critical events, which should be avoided at all. They can cause unscheduled shutdowns, damages to the refractory lining, and equipment, such as lances, lime extraction and transport systems. Depending on how severe the problem is, maintenance labor, purchase of lime to make up the difference, and the expense of lime mud disposal can bring the cost of a blockage from tens to hundreds of thousands of euros. For this reason, more than twenty years ago Cimprogetti's engineers invented a practical method, the so-called "Overburning Test" (OT) method to predict the lime agglomeration and the sticking tendency (ST) occurring at 1300 °C, which is ideally considered the maximum operative temperature in the lime kiln (Vola and Sarandrea, 2014). This test is currently performed on contractual raw materials for designing and commissioning new kilns. Moreover some important lime producers require performing this test periodically for testing raw materials suitability. Especially, the OT is systematically required for testing different quarries or different layers from the same quarry, according to the normal progression of the mining activity (Manocha and Ponchon, 2018).

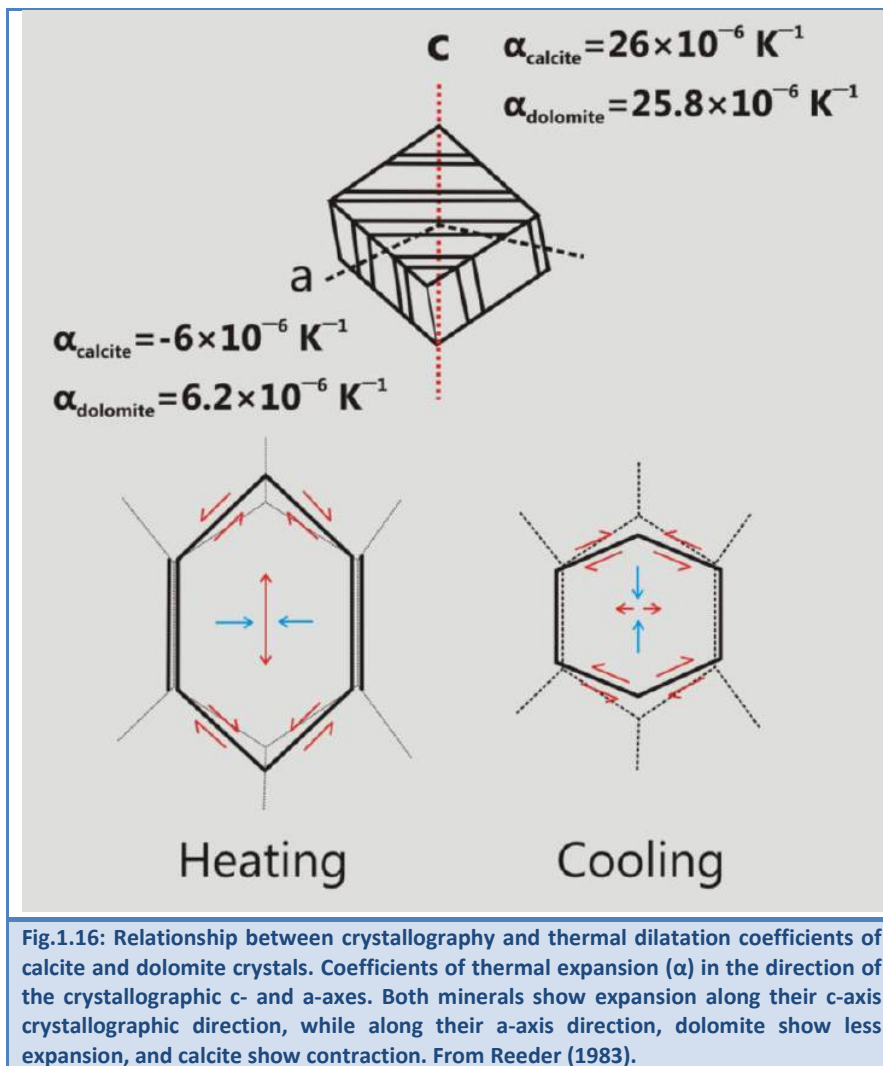
An exhaustive and comprehensive scientific explanation clarifying the sticking tendency and blocking mechanism in vertical lime kilns is not available in the literature yet. Nevertheless, the formation of annular concretions, generally reported as "rings" on the refractory walls of long rotary lime kilns have been thoroughly investigated by chemical engineers since the end of the 80s of the last century (Tran and Barham, 1991; Tran et al., 1993). Ringing also occurs in cement kilns (Taylor, 1997), but there are no evidences that both phenomena are related, considering the wide difference in chemistry and temperature between lime and cement kilns and processes (Tran et al., 1993). Recently, numerical combustion model was elaborated for counteracting ring formation in rotary kilns for cement production (Pisaroni et al. 2012).

Three different lime rings have been identified, e.g. "mud-rings", "mid-kiln rings", "front-end rings", occurring at different temperatures and positions along the kiln's section, and different technical explanations for their formation have been proposed, including recarbonation, sulphation, agglomeration of lime particles in the presence of liquid phase, and possible melting of sodium compounds (Tran, 2006). Obviously, sulphation is more likely to occur in a kiln firing high sulfur content oil (Francey and Tran,

2012). Certainly, this phenomenon can be initially described in terms of “firing” or “sintering”, including both solid-state and liquid-phase sintering processes (De Jonghe and Rahaman, 2003). Moreover, unusual molten of limestone/dolomite occurring in lime kilns, can be investigated starting from a wide geological literature on the petrogenesis and evolution of natural carbonate melts and carbonatite magmas (Le Bas, 1981; Bell, 1989; Jones et al., 2013).

Considering a practical perspective the blocks formation in TSR kilns is generally linked to several factors or combination of factors, and often related to the poor quality, or impurity content, i.e. the insoluble residue, of raw materials feeding to the kiln. As already described in Chapter 1, the impurity content of carbonate rocks is represented by subordinated terrigenous, and/or evaporitic minerals, plus the organic matter, as well (Warren, 2000; Scholle and Ulmer-Scholle, 2003; Flügel, 2010). More rarely, impurity content is also represented by superficial dust, consisting of soil and/or clayey particles lumped on the surface of the aggregate during its storage into the stockpile. The experience indicates that small amount of impurity, e.g. an insoluble residue <1%, could negatively impacts on calcination process, promoting the lime agglomeration, and finally causing serious obstructions or blockages. Moreover, it is well-known that potassium-bearing silicates, such as K-feldspar, illite, and other clay minerals, are commonly used as fluxing agents to form the glassy phase in the ceramic manufacturing and/or in the clinkerization process, by lowering the melting point of the of $\text{CaO-SiO}_2\text{-Al}_2\text{O}_3\text{-Fe}_2\text{O}_3$ system (Baumgart et al., 1984; Taylor, 1997). The liquid-phase formation may starts at temperatures between 1250-1350 °C, or even at ~800-900 °C, depending on the presence of halides or other fluxes (Elsen et al., 2011). However, the topic is still somewhat unclear, and requires more deep insights.

Another critical issue to be considered, which simultaneously acts on blocks formation, is lime dust occurring during the calcination process. The low mechanical behavior of the lime essentially depends on characteristic thermo-mechanical degradation of raw materials feeding to the kiln. Especially, the statistical analysis pointed out that fines are linearly correlated with textural-microstructural properties of parental raw materials, including the crystal-size distribution (CSD), the crystal-shape preferred orientation (SPO), the crystal-lattice preferred orientation (LPO), and the grain-boundary type (GBT) (Vola and Sarandrea, 2015).



Basically, calcite and dolomite have a large anisotropy in their coefficients of thermal expansion, so misfit strains due to differential thermal expansion can lead to large internal stress and final granule disintegration either on heating or on cooling (Fig.1.16) (Reeder, 1983; Siegesmund et al., 2000; Shushakova et al. 2013a, 2013b).

Effectively, coarse- and very coarse-grained marbles (CSD >400 μm) systematically present high mechanical degradation during the calcination process, which is mainly due to a destructive cracking along grain boundaries, especially triple junctions (Vola and Sarandrea, 2015). Conversely, medium- and fine-grained marbles (CSD <250 μm), generally present a lower mechanical degradation, excepting for samples with strong crystal-shape preferred orientation. Furthermore, the tendency to decrepitate, which generally occurs during the lime cooling, could be probably related to phase transitions between different polymorphs of calcium silicates (Taylor, 1997).

1.4.2 Ringing in lime rotary kilns

The formation of annular concretions on the refractory walls of lime rotary kilns is generally reported in the specialized literature as “ringing” (Tran and Barham, 1991). This critical issue occurs when lime mud or product lime particles adhere to the kiln wall and subsequently become hard and resistant to the abrasive action of the sliding/tumbling motion of product lime pellets (Tran et al., 1993). According to recent studies, the formation of liquid phase in the granular material occurs into the maximal radiative heat transfer zone. Indeed, the liquid phase tends to stick to the kiln’s wall to form rings (Pisaroni et al., 2012). Subsequently, the hardening of ring deposits is mainly caused by sintering and/or recarbonation. The last factor occurs when the ring temperature is below the lime mud calcination temperature. Other factors affecting rings hardening are sulphation and maybe phosphation reactions too. Kilns that burn high sulfur containing non-condensable gases (NCG) from recovery processes are often reported to have more ringing problems. From a practical standpoint, rings occur due to a combination of high sodium content in the lime mud, and the instability of kiln operation (Tran et al., 1993).

1.4.3 Factors affecting the lime sintering at high temperature

Calcium and magnesium oxides present very high melting points, ranging from 2571 °C for CaO up to 2823 °C for MgO. The calculated CaO–MgO phase diagram by Wu et al. (1993) presents a eutectic point at 2374 °C. At lower temperatures there is a large miscibility gap (Fig.1.17).

The phase equilibria, thermodynamic properties of solid and liquid phases and structural properties of solid solutions of the CaO–MgO–SiO₂ system have been widely investigated at 1 bar, and also at high pressure, by Jung et al. (2005). Indeed microstructural modifications of particle materials occurring at the highest operative temperature of the lime TSR kiln, about 1300 °C, can be mainly described in terms of “firing” or “sintering”, considering that field of CaO-MgO solid solutions is present just at higher temperatures. Several texts have been published in the recent years providing a detailed treatment of the theory, principles, and practice of sintering of ceramics (see De Jonghe and Rahaman, 2003 for references).

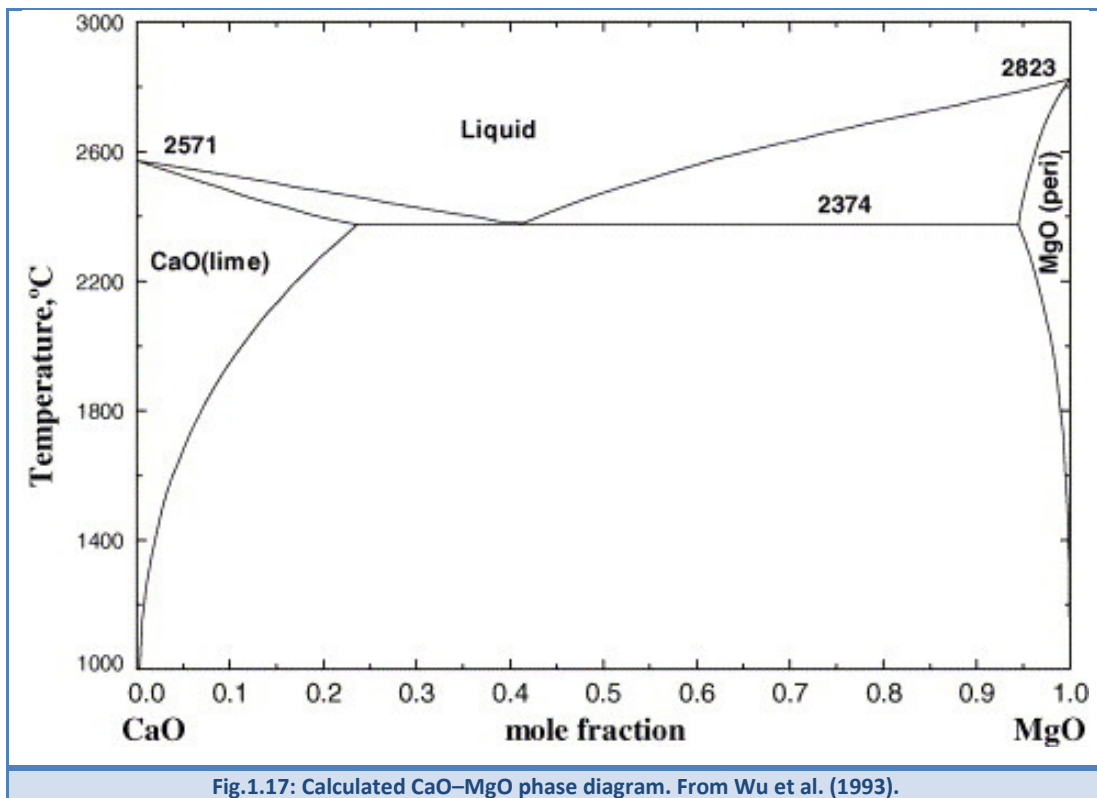
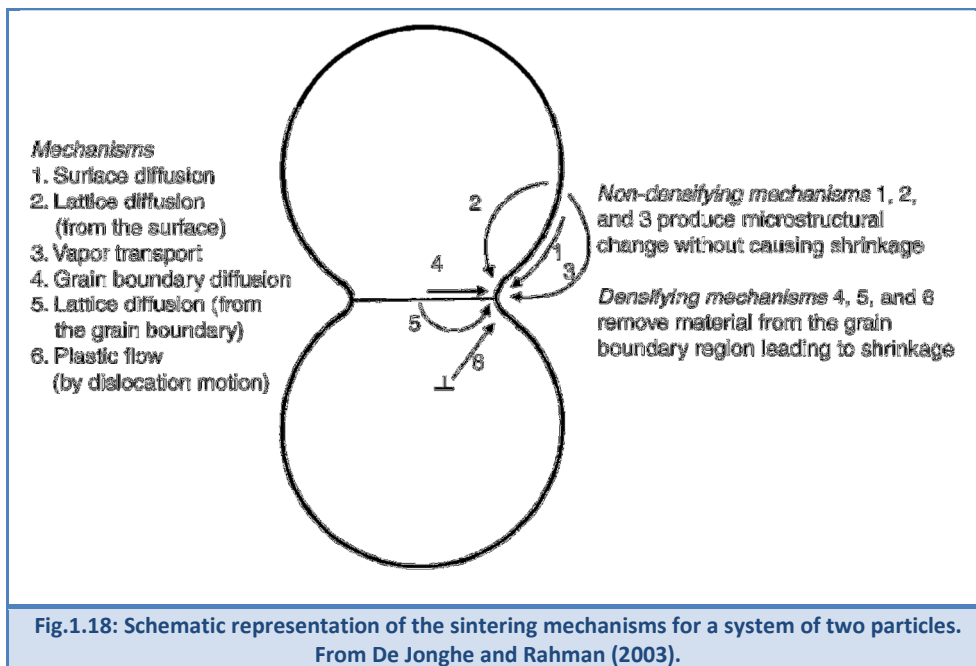


Fig.1.17: Calculated CaO–MgO phase diagram. From Wu et al. (1993).

There are four categories of sintering, depending on the composition of burnt materials, and secondary on phases formed during the heat treatment: 1) **solid-state sintering**, 2) **liquid-phase sintering**, 3) **vitrification**, and 4) **viscous sintering**. Considering that calcium and magnesium oxides are completely crystalline materials, the vitrification and the viscous sintering, regarding heating glasses, are not to be considered. Solid-state sintering regards heating to a temperature that is typically 0.5-0.9 of the melting point. No liquid is present and atomic diffusion in the solid-state produces joining of particles and reduction of porosity, then densification. Liquid-phase sintering process presents a small amount of liquid, typically less than a few volume percent of the original raw materials, depending on presence of impurity content, such as clay minerals, and/or other fluxing agents. The liquid phase, even if insufficient to fill the pore space, enhances the densification at lower temperatures. Both solid-state and liquid-phase sintering processes can be related to blocks formation and lime agglomeration in the lime kilns, depending on presence of fine lime particles, impurities, and soil dust or clayey particles coating the aggregates. Another factor enhancing the densification is the hot isostatic pressure occurring into the TSR kiln, in a particular way, into the burning zone.

1.4.4 Solid-state sintering

Driving forces of the solid-state sintering is the surface free energy reduction due to the elimination of internal surface area associated with pores. The decrease in the surface free energy during sintering is rather small when compared to other process, i.e. chemical reactions, but the distance that matter has to be transported is of the order of the particle size. This energy reaches about 100 J/mol for particles with a diameter of 1 μm . Thermodynamic work required for the reduction of the free surface energy can be expressed in terms of a mechanical stress or sintering stress, Σ , which is “the equivalent to externally applied stress that has the same effects on sintering as the curved surfaces of pores and grain boundaries” (De Jonghe and Rahaman, 1988). The **microstructure evolution** of a powder compound evolves continuously during sintering (please note that raw materials feeding the lime kiln are coarser than ceramics powders, i.e. mm-sized aggregates). The initial stage would begin as soon as some degree of atomic mobility is achieved and sharply concave necks form between individual particles. The initial densification is small, less than 5% of linear shrinkage, and can be lower if coarsening mechanisms are very active. In the intermediate stage the microstructure presents “three-dimensional interpenetrating network of solid particles and continuous, channel-like pores”, and densification starts became important. In the third stage the grain growth or coarsening becomes significant, and channel-like pore break down into isolated, closed, voids, which marks the final stage, consisting in the progressive reducing of the final few percent of porosity (De Jonghe and Rahaman, 2003). There are several mechanisms of sintering, including **vapor transport, surface diffusion, lattice or volume diffusion, grain boundary diffusion, and dislocation motion** (Fig.1.18).



A distinction is commonly made between **densifying** and **non-densifying mechanisms**. The first three mechanisms lead to neck growth and particles coarsening without densification; the last two mechanisms lead to shrinkage and densification, and are common in polycrystalline materials. Complications may arise from the diffusion of different ionic species making up the compound, which can diffuse along different paths with different diffusion-rates. Moreover sintering process involves a **competition between densification and coarsening**. The migration of grain boundaries imply a new equilibrium in pore shape, due to the elimination of surface area and the energy reduction at the junction between grain boundary and pore surface. The pore stability is demonstrated to be function of the pore number coordination, i.e. the number of grains surrounding a pore, and the dihedral angle (ψ). When the dihedral angle (ψ) is concave, i.e. it presents negative curvature, pores shrink. When the dihedral angle (ψ) is convex, i.e. it presents positive curvature, pores will grow or became metastable (Fig.1.19).

Therefore matter transport is driven by chemical potential gradients. Different **mathematical models for sintering** have been developed to express the balance between these forces and analyze the rate of matter transport. Analytical models considering highly idealized geometry for each stage and mechanism of sintering provide equations for sintering kinetics. This approach provides an excellent qualitative understanding of sintering in terms of driving forces and factors affecting the sintering process, including particle size, temperature, applied pressure, heating rate and atmosphere. According to

equation [XIV] for any stage of the sintering process, the **densification rate** (ϵ_ρ) can be expressed in the general form:

$$\epsilon_\rho = \left(\frac{1}{\rho}\right) \cdot \frac{d\rho}{dt} = \frac{H \cdot D \cdot \Omega \cdot \varnothing \cdot \frac{(m+1)}{2}}{G^m \cdot k \cdot T} \cdot (p_a \cdot \Sigma) \quad \text{[XIV]}$$

Where H is a numerical constant that depends on the assumed geometry of the model and on the sintering mechanism, D is the diffusion coefficient, \varnothing is the stress intensification factor, m is the grain size exponent factor, depending on given mechanism, i.e. m=2 lattice diffusion, m=3 grain boundary diffusion, Ω is the atomic volume of the rate controlling species, G is the grain or particle size, k is Boltzmann constant, T is the absolute temperature, p_a is the applied pressure, and, finally, Σ is the sintering stress, previously defined as “the equivalent externally applied stress that has the same effects on sintering as the curved surfaces of pores and grain boundaries”.

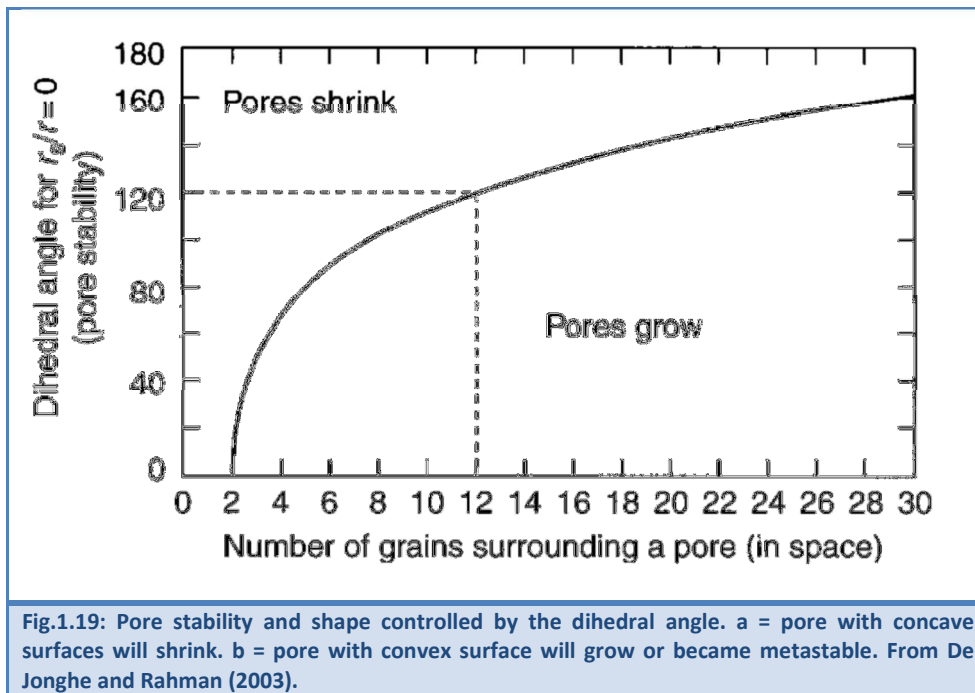


Fig.1.19: Pore stability and shape controlled by the dihedral angle. a = pore with concave surfaces will shrink. b = pore with convex surface will grow or become metastable. From De Jonghe and Rahman (2003).

The **sintering equation** [XIV] has been verified by experiments. Measurements of densification rates are generally lower than predicted values because of inhomogeneity particle packing. In practice, more than one mechanism operates during sintering. Even if the above mentioned mechanisms have been treated by **analytical models**, the problem can be solved by numerical simulations based on more realistic geometries. Especially,

finite-elements modeling was used for different sintering problems, but calculations are quite complex, and for this reason this approach was not so much popular. Moreover sintering maps have been adopted to show dominant mechanisms as a function of temperature and density. This kind of approach was limited too. The formulation of the driving forces for sintering in terms of equivalent external stress provides a conceptual basis for designing experiments to measure the sintering stress. Several papers were dedicated to develop a loading dilatometry experimental technique, considering a small applied uniaxial stress condition equivalent to the hydrostatic pressure (see references in De Jonghe and Rahaman, 2003).

As already mentioned the term **grain growth** is used to describe the increase in the average grain size of polycrystalline materials. The term **coarsening** is frequently used to describe a process in a porous ceramic whereby the increase of the average grain size is accompanied by an **increase of pore size**. Coarsening reduces the driving forces for sintering, thus acts against densification. The same process, generally reported as “**Ostwald Ripening**”, is particularly important in solid-state, as well as, in liquid-phase sintering processes. Two different types of grain growths can be distinguished: 1) normal grain growth, and 2) abnormal or anisotropic grain growth.

The “**Ostwald Ripening**” process, also known as **Lifshitz-Slyozov-Wagner (LSW) theory**, regards solid-solutions or colloidal-solutions, in which small crystals or sol particles dissolve, and redeposit onto larger crystals or sol particles, as firstly described by Wilhelm Ostwald in 1896 (Lifshitz and Slyozov, 1961; Wagner, 1961). This thermodynamically-driven spontaneous process occurs because larger particles are more energetically favored than smaller particles (Ratke and Voorhees, 2002). This stems from the fact that molecules on the surface of a particle are energetically less stable than the ones in the interior. A simple form of the law is given [XV]:

$$(r^*)^m = (r_0^*)^m + Kt \quad [XV]$$

Where K is a temperature-dependent rate constant, t is the time, and m is an exponent that depends on the rate-controlling mechanism: m = 3 for diffusion control, and m = 2 for surface reaction control.

1.4.5 Liquid-phase sintering

From a technological point of view the liquid-phase is required for many sintering processes because enhances the densification rate. Grain growth acceleration and specific grain boundaries can be also obtained, by means of few percent of liquid phase. Sometimes the liquid phase grain boundary represents a nanometer film, which can only be detected by high-resolution Transmission Electron Microscopy (TEM). The so-called “activated sintering” is a process in which a minor amount (less than 1%) of liquid-forming additive is specifically adopted to accelerate densification by enhancing the grain boundary migration. Clearly, activated sintered materials are prone to degrade at high-temperature because of persisting intergranular films of nanometer thickness. The liquid-phase sintering includes the following sequence of stages: 1) melting of liquid-forming additive and liquid redistribution along grain boundaries, 2) rearrangement of solid phases by capillary stress gradients, 3) densification and shape accommodation involving solution-precipitation, and, 4) final densification driven by residual porosity and the liquid phase redistribution.

As regards the first step, one difficulty is modelling liquid redistribution considering differences in local geometry, so quantitative statements can only be made for theoretical (homogeneous) microstructures. Moreover these models assume that liquid phase does not change composition or structure. Several studies reported that composition of grain boundary film changes from that of the liquid phase in the triple junction or even from boundary to boundary. Finally, the liquid phase can also penetrate the grain boundary when the dihedral angle is near zero. The following equation [XVI] points out the relationship between the solid/liquid interfacial energy (γ_{sl}), the dihedral angle (ψ) and the grain boundary energy (γ_{gb}):

$$2\gamma_{sl} \cdot \cos\left(\frac{\psi}{2}\right) = \gamma_{gb} \quad \text{[XVI]}$$

From a technological viewpoint, the liquid-phase redistribution is facilitated with rounded grains and uniform microstructures, or in systems constituted by liquid-phase pre-coated particles, e.g. fluidized bed vapor deposition, and chemical precipitation from aqueous suspensions. Another important deformation affecting systems interested by liquid-phase sintering regards the possible creep occurring due to the gravity effect, which could be particularly critical when the amount of liquid phase is >5%.

Liquid-phase sintering system can be described by means of soil mechanisms too (see references in De Jonghe and Rahaman, 2003), so the equilibrium between particles in the presence of liquid film grain boundary can be described in terms of **effective stress**, given by the equation [XVII]:

$$\sigma_y^{\text{eff}} = \frac{(\sum F_{iy})}{a} \quad \text{[XVII]}$$

Where F is the component of the force in y direction and the i^{th} particle-particle contact, and a is the external cross-section of the sample. In absence of any external applied stress, and pressure gradients the effective stress is the **capillary porosity** (p) in the liquid-phase [XVIII]:

$$\sigma_y^{\text{eff}} = p \cdot (1 - a) \quad \text{[XVIII]}$$

The effective stress is the driven force for solution precipitation mechanisms, together with the “Ostwald ripening” process. The rearrangement of particle network may occur in few minutes, and once a quasi-steady-state grain boundary film is achieved, densification proceeds similar to solid-state sintering. Another key-factor is represented by the wetting angle, which can be distinguished in reactive or non-reactive one. Reactive wetting angle can be taken as referring to the case where the liquid and the solid react to form a new solid phase. Finally, the distribution of the liquid phase depends on the dihedral angle, the relative amount of liquid phase, and the porosity. For contact angles larger than zero, it’s possible to have repulsive forces between particles. In such case further densification can only proceed by grain growth. If the liquid phase is sufficient, initial rearrangement leads to a denser material. When the molten phases are silicates, they remain as glass after cooling. The liquid phase and its composition can be determined, in principle, from phase diagrams, although they are often incomplete or difficult to interpret when more than two components are present. Finally, reaction sintering process regards new phases formation during the firing process. Considering the presence of subordinated constituents in limes burnt at high temperatures, the system is then interested by reaction sintering too.

1.5. Lime Hydration

The reaction of lime hydration is a classical *solid-liquid phase reaction* occurring with varying amounts of water, essentially depending on different applications and final products to be obtained. Formally, the term hydration and slaking are synonymous, but practically they refer to different processes. In particular, hydration (or dry hydration) yields a dry powdered hydrate, whereas slaking (or wet hydration) involves more water, producing wet hydrates, including putty, slurry, milk-of-lime and lime water (Boynton, 1982). Considering the fundamental topic of this dissertation, i.e. the lime reactivity, chemical reactions and factors affecting hydration rates (not previously discussed) will be considered in order to finalize the present “Introduction Chapter”.

1.5.1 Chemical reactions

The hydration of both high calcium and dolomitic quicklime is strong exothermic reaction, even though reversible. In particular, three different reactions can be defined. The first one [XIX] regards the high-calcium hydrate, the second [XX] the so-called “normal” dolomitic hydrate, and the last one [XXI], the highly hydrated dolomitic lime (Boynton, 1982).

$\text{CaO} + \text{H}_2\text{O} \rightleftharpoons \text{Ca(OH)}_2 + \text{heat} \uparrow$	[XIX]
$\begin{array}{cccc} 56 \text{ g} & 18 \text{ g} & 74 \text{ g} & \end{array}$	
$\text{CaO} + \text{MgO} + \text{H}_2\text{O} \rightleftharpoons \text{Ca(OH)}_2 + \text{MgO} + \text{heat} \uparrow$	[XX]
$\begin{array}{cccc} 96.4\text{g} & 18 \text{ g} & 74.1\text{g} & 40.3\text{g} \end{array}$	
$\text{CaO} + \text{MgO} + 2\text{H}_2\text{O} + \text{pressure} \rightleftharpoons \text{Ca(OH)}_2 + \text{Mg(OH)}_2 + \text{heat} \uparrow$	[XXI]
$\begin{array}{cccc} 96.4\text{g} & 18 \text{ g} & 74.1\text{g} & 58.3\text{g} \end{array}$	

These equations demonstrate that high calcium quicklime slakes much more readily than dolomitic. The dolomitic lime, because its hard-burned MgO component, usually requires pressure for complete hydration. Some dead-burned or sintered dolomitic limes require pressure plus temperature and time to be hydrated. However is possible to produce relatively soft-burned dolomitic quicklime from pure dolomite by calcining small-sized stone (c 25 mm) at low calcination temperature under rigid time-temperature conditions (Boynton, 1982).

1.5.2 Hydration kinetics

Generally, highly reactive high-calcium quicklimes slake with water with explosive violence. The more rapid the rate of hydration the greater the turbulence and temperature rise. Conversely, dense, hard-burned high-calcium or dolomitic limes hydrate very slowly (Boynton, 1982). Effectively, soft-burned dolomitic limes present a rapid hydration rate too, but the final temperature rise will be lower than high-calcium ones. This is the reason why the most significant reactivity parameters, according to UNI EN 459-2, are the t_{60} (or ΔT 40 °C) for high-calcium, and the t_{50} (or ΔT 30 °C) for dolomitic quicklimes, respectively. Main factors influencing the rate of reaction were already discussed in Paragraph 1.3. Indeed, some physical factors and technical parameters strictly related to the hydration procedure are discussed yet. They include particle-size, temperature, quantity and quality of water, agitation, and recarbonation. The last factor is mainly related to the storage conditions. For the detailed theoretical examination of physical-chemical phenomena of lime hydration kinetics readers are pleased to refer to Ritchie and Xu (1990), Giles et al. (1993), and Maciel-Camacho et al. (1997).

1.5.3 Effects of particle-size, temperature, and agitation

Effectively, the particle-size of quicklime results to be a fundamental parameter controlling the lime reactivity. Small-sized ground quicklime between 6.35-12.7 mm is appreciably more rapid in slaking than lump or pebble. Still finer, dust-like particles increase the rate even more (Boynton, 1982). Slaking test methods established a quicklime particle-size <0.2 mm according to UNI EN 459-2, or <3.35 mm according to ASTM C110, respectively. This fundamental difference between the above mentioned standards is generally underestimated, but could have large practical repercussions.

The temperature of water accelerates hydration rates too. Many limes reach the peak with steam, thus an explosion is possible when hot water is employed. The UNI EN 459-2 standard fixes the water temperature for the slaking test at 20 °C, whereas the ASTM C110 fixes the same temperature at 25 °C. The quicklime must be at room temperature, as well.

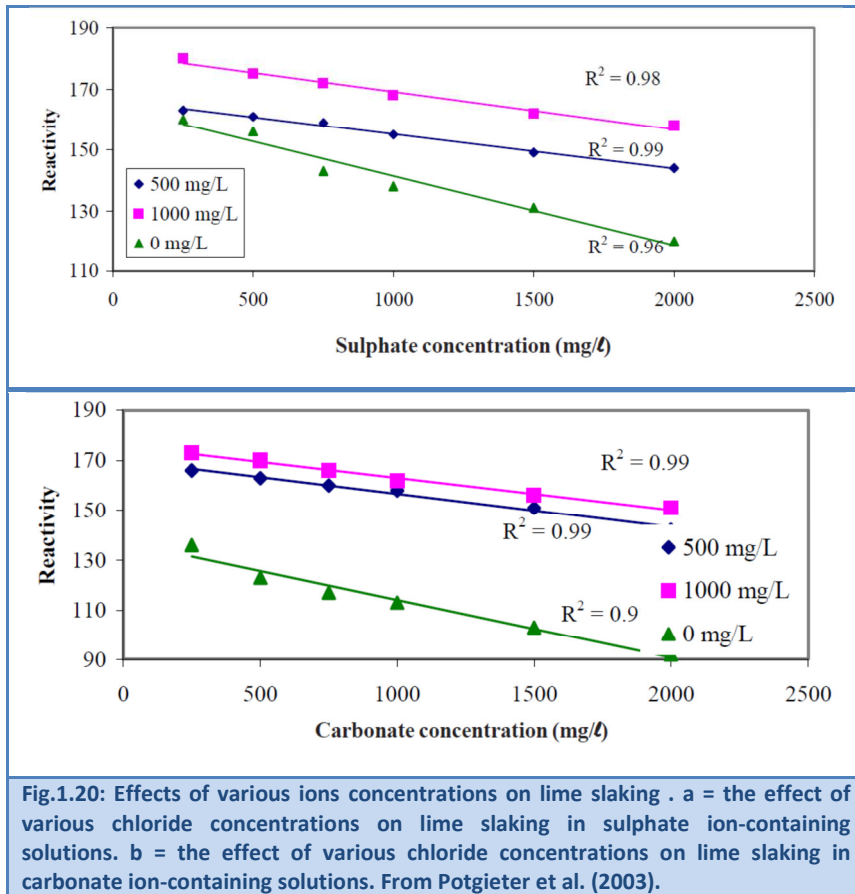
The agitation of the lime and water increases the hydration rate and dispersion of lime particles markedly, thus stirrer and Dewar apparatus, as well as, amounts of quicklime

and water are previously fixed (for more details on slaking tests see ASTM C110, 2016 and UNI EN 459-2, 2010, for more details on the slaking process see Boynton, 1982).

1.5.4 Effects of slaking water composition

The chemical composition of water in terms of ions concentrations, considerably affects the lime slaking reactivity. The presence of some substances can accelerate or decrease the slaking rate of lime in water. In particular, the major effects are caused by phosphorus, sulfides, sulphates and chlorides (Potgieter et al., 2003). Especially, the presence of chloride (CaCl_2) in the slaking water increases the solubility of the lime and the hydration rate, whereas sulphate and magnesium carbonates decrease the slaking rate and delay the process, acting as inhibitors of reaction (Gallala et al., 2008). Experiments performed by Gallala et al. (2008), were carried out on lime samples burnt at 1000°C . Conversely, Gheevahese et al. (2002) pointed out that hydration rates of different limes burnt at 900°C are slightly retarded in the presence of a high concentration of chloride ions, while sulphate ions retarded the lime slaking significantly. The decrease in the slaking rate can be explained by the incapsulation of the lime by the sulfate, which is fairly insoluble compound. This means that water has to diffuse in a skin of calcium sulphate before reaching the contact with the lime to form the $\text{CaSO}_4 \cdot x \text{H}_2\text{O}$. Moreover, Gheevahese et al. (2002) pointed out that the lime reactivity is affected by the geological origin and chemical composition of the calcined limestone. Especially, they report that silica content does not seem to influence the slaking reactivity, while the MgO amount is significant, because hydrates slower than CaO. A more detailed study on effects of magnesium oxide, was performed by Potgieter et al. (2003). The adapted experimental slaking test procedure described in details by Potgieter et al. (2002b) includes grit measurements. The slurry produced during the slaking test was passed through a 0.5 mm sieve, then unreacted residual particles, mostly including impurities, were dried for 3 h at 100°C and weighed to calculate the % grit of the original lime mass. Authors added various amounts of MgO to a calcined limestone for evaluating its hydration behaviour. They observed that MgO initially increases the slaking rate of the lime undergoing hydration, while at higher concentrations lowers the reactivity, as already documented in the literature (Boynton, 1982; Oates, 1998). This apparent initial effect can be explained by the fact that the added MgO was chemically pure, and not hard burnt as it would have been under real operating conditions. Effectively, the magnesium oxide from dolomitic limestone is generally

overburnt because it decomposes at lower temperature than calcium carbonate (see the calcination kinetics paragraph). Apart from decreasing effect on hydration rate, it was observed the increasing amount of grit, incrising the MgO contents. This could have severe consequences on the operation of commercial slakers.



Furthermore, Potgieter et al. (2003) studied effects of chloride, carbonate and sulphate ions on kinetics of lime slaking in water, as well. This study was performed for evaluating positive and negative repercussions on the industrial process. From a theoretical point of view chlorides should accelerate the lime slaking because they are more soluble than calcium hydroxide, then should facilitate the dissolution of lime, facilitating the reaction. At the same time carbonates and sulphates, which form more insoluble calcium compounds than CaO, should retard the slaking process. However, these influences cannot be quantitatively predicted, indeed laboratory tests are required. Experiments pointed out that slaking rate of lime and amounts of grits increase with chloride concentrations. From a practical perspective this indicates that poor slakers performance can possibly be rectified by the addition of common salt to the hydration mixture. This can be particularly useful if

the lime reactivity is particularly low, e.g. see the specific South African case-study (see Vola et al. 2017, and other works in the present dissertation).

Conversely, the slaking rate decreases linearly with increasing concentrations of sulphates and carbonates ions in the slaking water. The effect of carbonates and sulphates can be explained by coating of insoluble layers of either CaCO_3 and CaSO_4 on lime particles. Significantly, the retarding action of carbonates is more severe than that of sulphates at the same ions concentration. Moreover slurries with sulphate anions produce more grit than those containing carbonate anions. This has possible practical implications for hydration process in industrial plants too. It's significant to remark that this work was performed on South African burnt limes, deriving from Neoproterozoic calcined limestones, which are commonly affected by very high sintering or overburning tendency, and consequently low slaking reactivity in comparison with more recent carbonates from other countries (see Vola et al., 2017, and other works in the present dissertation).

1.5.5 Effects of air-slaking and recarbonation

This topic is reported by Potgieter et al. (2002a) with regards to the effect of storage conditions. Effectively, conditions after production can also influence the reactivity and, consequently, the slaking rate of the lime. Due to the strong affinity for moisture, i.e. its hygroscopic nature, lime can be converted in portlandite [$\text{Ca}(\text{OH})_2$] by any humidity present in the atmosphere, or revert to calcite (CaCO_3) due to the laws of thermodynamics, which favor the more stable naturally occurring form (Gheeverhese et al., 2002). Both back conversions can affect the hydration kinetics. Furthermore it is known that recarbonation is influenced by prevailing relative humidity, and that initial hydration precedes and catalyses physical absorption of CO_2 , which is then chemically combined with the lime to form calcite. Obviously, these phenomena can cause considerable operational problems at plant level, especially in tropical and subtropical environments.

1.6. References

- Akande H.F., Abdulkareem A.S., Kovo A.S., Azeez O.S., and Onifade K.R. (2016) – *Application of factorial analysis for quicklime production from limestone*. Nigerian Journal of Technological Research, 11:2, 16-25., <http://dx.doi.org/10.4314/njtr.v11i2.4>
- Alaabed S., Soltan M.A., Abdelghany O., Amin B.E.M., Tokhi M.E., Khaleel A., Musalim A. (2014) – *United Arab Emirates limestones: impact of petrography on thermal behaviour*. Mineral Petrol, <https://doi.org/10.1007/s00710-014-0329-3>
- ASTM C110 (2016) – *Standard Test Methods for Physical Testing of Quicklime, Hydrated Lime, and Limestone*. ASTM Book of Standards, 04.01, 20p.
- Barin I. (1989) – *Thermochemical Data of Pure Substances. Chapter 1. Thermodynamic Functions and Relations*. Weinheim, New York, VCH. <http://dx.doi.org/10.1002/9783527619825>
- Barker R. (1973) – *Reversibility of the reaction CaCO_3 reversible reaction CaO plus CO_2* . J. Appl. Chem. Biotechnol., 23, 733-742.
- Baziotis I., Leontakianakos G., Proyer A., Lee H., and Tsimas S. (2011) – *Physico-chemical Properties of Different Carbonate Rocks: Are They Highly Enough to Control Lime Reactivity?* International Journal of Chemistry, <http://dx.doi.org/10.5539/ijc.v3n2p187>
- Berman R.G. (1988) – *Internally-consistent thermodynamic data from minerals in the system $\text{Na}_2\text{O}-\text{K}_2\text{O}-\text{CaO}-\text{MgO}-\text{FeO}-\text{Fe}_2\text{O}_3-\text{Al}_2\text{O}_3-\text{SiO}_2-\text{TiO}_2-\text{H}_2\text{O}-\text{CO}_2$* . J. Petrol., 29, 445-522, <https://doi.org/10.1093/petrology/29.2.445>
- Beruto T.D., Vecchiattini R., and Giordani M. (2002) – *Solid products and rate-limiting step in the thermal half decomposition of natural dolomite in a CO_2 (g) atmosphere*. Thermochemica Acta, 405, 183–194, [https://doi.org/10.1016/S0040-6031\(03\)00190-4](https://doi.org/10.1016/S0040-6031(03)00190-4)
- Bes A. (2006) – *Dynamic Process simulation of limestone calcination in normal shaft kilns*. Otto Von Guericke University, Magdeburg, Germany, PhD Thesis, 118p.
- Bes A., Specht E., and Kehse G., (2007) – *Influence of the kind of fuel on the energy consumption in the lime burning*. ZKG International, 60:9, 84-93.
- Bell K. (ed.) (1989) – *Carbonatites: Genesis and Evolution*. London: Unwin Hyman.
- Bissell H.J., and Chilingar G.V. (1967) – *Chapter 4. Classification of Sedimentary Carbonate Rocks*. Developments in Sedimentology, 9:A, 87-168. [https://doi.org/10.1016/S0070-4571\(08\)71112-9](https://doi.org/10.1016/S0070-4571(08)71112-9)

Chapter 1. Introduction

- Borgwardt R.H., and Bruce K.R. (1986) – *Effect of Specific Surface Area on the Reactivity of CaO with SO₂*. AIChE Journal, 32:2, 239-246, <https://doi.org/10.1002/aic.690320210>
- Boynton R.S. (1982) – *Chemistry and Technology of Lime and Limestone*. Wiley & Sons, New York, 592 p. ISBN: 978-0-471-02771-3.
- Brunauer S., Emmett P.H., and Teller E. (1938) – *Adsorption of Gases in Multimolecular Layers*. Journal of the American Chemical Society, 60:2, 309–319, <https://doi.org/10.1021/ja01269a023>
- Cheng C., and Specht E. (2006) – *Reaction rate coefficients in decomposition of lumpy limestone of different origin*. Thermochemica Acta, 449, 8–15, <https://doi.org/10.1016/j.tca.2006.06.001>
- Cho S.-H., Joo S.-M., Cho J.-S., Yu Y.-H. et al. (2006) – *Kinetic Analysis of the Decomposition of Calcium Carbonate using Danyang Limestone*. Materials Science Forum, 510-511, 502-505, <https://doi.org/10.4028/www.scientific.net/MSF.510-511.502>
- Chai L., and Navrotsky A. (2009) – *Thermochemistry of carbonate-pyroxene equilibria*. Contr. Mineral. and Petrol., 114:2, 139-147, <https://doi.org/10.1007/BF00307751>
- Commandré J.-M., Salvador S., and Nzihou A. (2007) – *Reactivity of laboratory and industrial limes*. Trans IChemE, 85:A4, 473–480, <https://doi.org/10.1205/cherd06200>
- Dunham R.J. (1962) – *Classification of carbonate rocks according to depositional texture*. In: W.E. Ham (Ed.) “Classification of carbonate rocks, American Association of Petroleum Geologists Memoir”, 1, 108–121.
- Eades J.L., and Sandberg P.A. (1970) – *Characterization of the Properties of Commercial Lime by Surface Area Measurements and Scanning Electron Microscopy*. The Reaction Parameters of Lime, ASTM STP 472, 3-24.
- Elsen J., Mertens G., and Snellings R. (2011) – *Portland cement and other calcareous hydraulic binders: History, production and mineralogy*. In: G.E. Christidis (Ed.) “Advances in the characterization of industrial minerals”, EMU Notes in mineralogy, London, 9:1, 441-479, <https://doi.org/10.1180/EMU-notes.9.11>
- Embry A.F., and Klovan J.S. (1971) – *A Late Devonian reef tract on northeastern Banks Island*. N.W.T. Bulletin of Canadian Petroleum Geology, 4, 730-781.
- European Commission (2014) – *Report on Critical Raw Materials for the EU: Report*

of the Ad Hoc Working Group on Defining Critical Raw Materials, Brussels, Belgium.

- Flügel E. (2010) – *Microfacies of Carbonate Rocks. Analysis, Interpretation and Application*. Springer-Verlag Berlin Heidelberg, 984 p. ISBN: 978-3-642-03795-5, <https://doi.org/10.1007/10.1007/978-3-642-03796-2>
- Flynn J.H., and Wall L.A. (1966) – *General Treatment of the Thermogravimetry of Polymers*. Phys. Chem., 70, 487–523.
- Francey S., and Tran H. (2012) – *Impacts of burning high-sulphur fuels in lime kilns*. Journal of Science & Technology for Forest Products and Processes, 2:3, 32-37.
- Fuoss R.M., Salymer I.O., and Wilson H.S. (1964) – *Evaluation of Rate Constants from Thermogravimetric data*. Journal of Polymer Science, A:2, 3147-3151.
- Jones A.P., Genge M., and Carmody L. (2013) – Carbonate Melts and Carbonatites, Reviews in Mineralogy & Geochemistry, 75, 289-322, <https://doi.org/10.2138/rmg.2013.75.10>
- Jung I.-H., Decterov S.A., and Pelton A.D. (2005) – *Critical thermodynamic evaluation and optimization of the CaO–MgO–SiO₂ system*. J. Eur. Ceram. Soc. 25, 313–333, <https://doi.org/10.1016/j.jeurceramsoc.2004.02.012>
- Galimberti M., Marinoni N., Della Porta G., Marchi M., and Dapiaggi M. (2016) – *Effects of limestone petrography and calcite microstructure on OPC clinker raw meals burnability*. Miner Petrol, <https://doi.org/10.1007/s00710-016-0485-8>
- Gallala W., Gaied M., Tlili A., Montacer M. (2008) – *Factors influencing the reactivity of quicklime*. Proc. Institution of Civil Engineers - Construction Materials, 161:1, February 2008, 25-30, <https://doi.org/10.1680/coma.2008.161.1.25>
- Galwey A.K., and Brown M.E. (2002) – *Application of the Arrhenius equation to solid state kinetics: can this be justified?* Thermochemica Acta, 386, 91-98, [https://doi.org/10.1016/S0040-6031\(01\)00769-9](https://doi.org/10.1016/S0040-6031(01)00769-9)
- García-Labiano F., Abad A., de Diego L.F., Gayán J., and Adánez P. (2002) – *Calcination of calcium-based sorbents at pressure in a broad range of CO₂ concentrations*. Chem. Eng. Sci., 57:13, 2381-2393, [https://doi.org/10.1016/S0009-2509\(02\)00137-9](https://doi.org/10.1016/S0009-2509(02)00137-9)
- Georgieva V., Vlaev L., and Gyurova K. (2012) – *Non-Isothermal Degradation Kinetics of CaCO₃ from Different Origin*. Journal of Chemistry, 2013, ID 872981, 12p., <http://dx.doi.org/10.1155/2013/872981>
- Gheeverhese O., Strydom C., Potgieter J.H. (2002) – The influence of chloride and

- sulphate ions on the slaking rate of lime derived from different limestone deposits in South Africa. *Water SA* 28 (1) 45-48, <http://dx.doi.org/10.4314/wsa.v28i1.4866>
- Giles E.D., Ritchie I.M., Xu B.A. (1993) - *The kinetics of dissolution of slaked lime*. *Hydrometallurgy*, 32, 119-128, [https://doi.org/10.1016/0304-386X\(93\)90061-H](https://doi.org/10.1016/0304-386X(93)90061-H)
 - Green D.W., and Perry R.H. (2007) – *Perry's Chemical Engineers' Handbook*. 8th Ed., ISBN:9780071422949.
 - Gunasekaran S., and Anbalagan G. (2007) – *Thermal decomposition of natural dolomite*. *Bull Mater Sci*, 30, 339–344, <https://www.ias.ac.in/article/fulltext/boms/030/04/0339-0344>
 - Hai Do D., and Specht E. (2011) – *Determination of Reaction Coefficient, Thermal Conductivity and Pore Diffusivity in Decomposition of Limestone of Different Origin*. Proc. WCECS 2011, 2, San Francisco, USA. ISBN 978-988-19251-7-6.
 - Hai Do D., Specht E., Kehse G., Ferri V., Christiansen T.L., and Bresciani P. (2011) – *Simulation of lime calcination in PFR kiln. Influence of energy input and lime throughput*. *ZKG International*, 12, 52-64.
 - Hai Do D., Specht E., Kehse G., Ferri V., Christiansen T.L., and Bresciani P. (2012) – *Simulation of lime calcination in PFR kiln. Influence of origin and size of limestone*. *ZKG International*, 4, 56- 65.
 - Hai Do D. (2012) – *Simulation of Lime Calcination in Normal Shaft and Parallel Flow Regenerative Kilns*. Otto Von Guericke University, Magdeburg, Germany, PhD Thesis, 117 p.
 - Halikia I., Zoumpoulakis L., Christodoulou E., and Prattis D. (2001) – *Kinetic study of the thermal decomposition of calcium carbonate by isothermal methods of analysis*. *The European Journal of Mineral Processing and Environmental Protection*, 1:2, 1303-0868, 89-102.
 - Helgeson H.C., Delany J.M., Nesbitt H.W., and Bird D.K. (1978) – *Summary and critique of the thermodynamic properties of rock-forming minerals*. *Am. J. Sci.*, 278:A, 1-229.
 - Holland B., and Powell R. (1990) – *An enlarged and updated internally consistent thermodynamic dataset with uncertainties and correlations: the system K₂O–Na₂O–CaO–MgO–MnO–FeO–Fe₂O₃–Al₂O₃–TiO₂–SiO₂–C–H₂–O₂*. *J. Metam. Geol.* 8, 89-124. DOI: 10.1111/j.1525-1314.1990.tb00458.x.
 - Hogewoning S., Wolter A., and Schmidt S.-O. (2008) – *Dependence of hard burn*

potential on limestone properties. ZKG International, 61:6, 54-60 (Part 1); 61:7, 84-93 (Part 2).

- Hughes J.H., and Corrigan M. (2009) – *Microstructural expression of temperature and residence time in laboratory calcinated limestone*. Proc. 12th EMABM, Dortmund, 328–334.
- Kantiranis N., Filippidis A., Christaras B., Tsirambides A., and Kassoli-Fournaraki A. (2003) – *The role of organic matter of carbonate rocks in the reactivity of the produced quicklime*. Materials and Structures/Materiaux et Constructions, 36, 135-138.
- Kiliç Ö. (2005) – *Comparison of Calcination Parameters of Classic (Eberhart) and Parallel Flow Regenerative Kiln (Maerz) and Applications on Çukurova Region Limestones*. Department of Mining Engineering, Institute of Natural and Applied Sciences, University of Çukurova, Adana, Turkey, Ph.D. Thesis, 171 p.
- Kiliç Ö., and Mesut A. (2006) – *Effects of limestone characteristic properties and calcination temperature on lime quality*. Asian Journal of Chemistry, 18:1, 655-666.
- Kiliç Ö. (2013) – *Impact of Physical Properties and Chemical Composition of Limestone on Decomposition Activation Energy*. Asian Journal of Chemistry, 25:14, 8116-8120. DOI: <http://dx.doi.org/10.14233/ajchem.2013.15172>.
- Kjølle I. (2000) – *Industrial mineral quality of limestone: the effect of contact metamorphism on textural properties, brightness and geochemistry*. Norges geologiske undersøkelse Bulletin, 436, 85-91.
- König G., Rellermeyer H., and Obst K.H. (1967) – *Processes Taking Place in the Dissolution of Hard and Soft-Burnt Lime in the Slags from the Basic Oxygen Furnaces*. Stahl und Eisen, 87:18, 1071-1077.
- Kumar G.S., Ramakrishnan A., and Hung Y.-T. (2007) – *Lime Calcination*. In: Wang L.K., Hung YT., Shammam N.K. (eds) “Advanced Physicochemical Treatment Technologies”. Handbook of Environmental Engineering, 5, Humana Press, https://doi.org/10.1007/978-1-59745-173-4_14.
- Limes R.W., and Russell R.O. (1970) – *Crucible Test for Lime Reactivity in Slags*. The Reaction Parameters of Lime, ASTM STP 472, 161-172.
- Lech R., Wodnicka K., and Pezdich Z. (2009) – *Effect of the limestone fabric on the fabric development in burnt lime*. ZKG International, 6/7, 62, 94-101 (part 1); 8, 62, 63-72 (part 2).
- Lifshitz I.M., and Slyozov V.V. (1961) – *The Kinetics of Precipitation from*

- Supersaturated Solid Solutions*. Journal of Physics and Chemistry of Solids, 19:1–2, [https://doi.org/10.1016/0022-3697\(61\)90054-3](https://doi.org/10.1016/0022-3697(61)90054-3)
- Long X., Ma Y., and Qi L. (2014) – *Biogenic and synthetic high magnesium calcite – A review*. Journal of Structural Biology, 185, 1–14.
 - Manocha S. and Ponchon F. (2018) – *Management of Lime in Steel*. Metals, 8, 686, 16p., <https://doi.org/10.3390/met8090686>
 - Marinoni N., Allevi S., Marchi M., and Dapiaggi M. (2012) – *A Kinetic Study of Thermal Decomposition of Limestone Using In-Situ High Temperature X-ray Powder Diffraction*. J Am Ceram Soc, 95, 2491-2498, <https://doi.org/10.1111/j.1551-2916.2012.05207.x>
 - Marinoni N., Bernasconi A., Della Porta G., Marchi M., and Pavese A. (2015) – *The role of petrography on the thermal decomposition and burnability of limestones used in industrial cement clinker*. Miner Petrol, 109, 719–731, <https://doi.org/10.1007/s00710-015-0398-y>
 - Mayer R.P., and Stowe R.A. (1964) – *Physical Characterization of Limestone and Lime*, Azbe Award No. 4, National Lime Association, Washington, D.C.
 - McClellan G.H., and Eades J.L. (1970) – *The Textural Evolution of Limestone Calcines*. The Reaction Parameters of Lime, ASTM STP, 472, 209-227.
 - Moldenhauer A., Bauer W., and Specht E. (2016) – *Thermophysical properties of lime as a function of origin (Part 3): Emissivity*. ZKG International, 9, 58-62.
 - Moropoulou A., Bakolas A., and Aggelakopoulou E. (2001) – *The effects of limestone characteristics and calcinations temperature to the reactivity of the quicklime*. Cem Concr Res, 31, 633-639, [https://doi.org/10.1016/S0008-8846\(00\)00490-7](https://doi.org/10.1016/S0008-8846(00)00490-7)
 - Mullins R.C., and Hatfield J.D. (1970) – *Effects of Calcination Conditions on the Properties of Lime*. The Reaction Parameters of Lime, ASTM STP, 472, 117-131.
 - Oates J.A.H. (1998) – *Lime and Limestone: Chemistry and Technology, Production and Uses*. Weinheim, Germany, WILEY-VCH Verlag GmbH. <https://doi.org/10.1002/9783527612024.ch01>
 - Obst K.-H., Stradtman J., Ullrich W., and König G. (1970) – *Present Status and Technical Advances of Steelworks Lime for Basic Oxygen Furnaces in Germany*. The reaction parameters of Lime, ASTM STP, 472, 173-192.
 - Ozawa T. (1965) – *A New Method of Analyzing Thermogravimetric Data*. Bull. Chem. Soc. Jpn., 38, 1881–6.

- Pisaroni M., Sadi R., and Lahaye D. (2012) – Counteracting ring formation in rotary kilns. *Journal of Mathematics in Industry* 2:3, <https://doi.org/10.1186/2190-5983-2-3>
- Potgieter J.H., Potgieter S.S., Moja S.J., and Mulaba-Bafubiandic A. (2002a) – *An empirical study of factors influencing lime slaking. Part I: production and storage conditions.* *Minerals Eng.*, 15:3, 201-203, [https://doi.org/10.1016/S0892-6875\(02\)00008-0](https://doi.org/10.1016/S0892-6875(02)00008-0)
- Potgieter J.H., Potgieter S.S., Moja S.J., and Mulaba-Bafubiandic A. (2002b) – *The standard reactivity test as a measurement of lime's quality.* *Journal of the SA Inst. of Mining and Metallurgy* 102:1, 67-69.
- Potgieter J.H., Potgieter D., De Waal D. (2003) – *An empirical of factors influencing lime slaking. Part II: Lime constituent and water composition.* *Water SA*, 29:2, 157-160, <http://dx.doi.org/10.4314/wsa.v29i2.4850>
- Ratke L., and Voorhees P.W. (2002) – *Growth and Coarsening: Ostwald Ripening in Material Processing.* Springer. pp. 117–118. ISBN 978-3-540-42563-2.
- Reeder R.J. (1983) – *Crystal Chemistry of the Rhombohedral Carbonates.* In: Reeder R.J. (Ed.) “Carbonates: Mineralogy and Chemistry”, *Reviews in Mineralogy*, 11, Mineralogical Society of America, 1-48.
- Ritchie I.M., and Xu B.A. (1990) – *The kinetics of lime slaking.* *Hydrometallurgy*, 2-3, 377-396, [https://doi.org/10.1016/0304-386X\(90\)90018-W](https://doi.org/10.1016/0304-386X(90)90018-W)
- Robie R.A., Hemingway B.S., and Fisher J.R. (1978) – *Thermodynamic properties of minerals and related substances at 298.15 K and 1 bar (105 pascals) pressure and at higher temperatures.* *US Geol. Surv. Bull.*, 1452, 456 p.
- Rodriguez-Navarro C., Ruiz-Agudo E., Luque A., Navarro A.B., and Ortega-Huertas M. (2009) – *Thermal decomposition of calcite: Mechanisms of formation and textural evolution of CaO nanocrystals.* *Am Mineral* 94, 578–593. <https://doi.org/10.2138/am.2009.3021>
- Sandaka G., Al-Karawi J., Speck E., and Silva M. (2017) – *Thermophysical properties of lime as a function of origin (Part 4): Thermal conductivity.* *ZKG International*, 3, 36-41.
- Schiele E., and Berens L.W. (1976) – *La Calce. Calcare – Calce viva – Idrato di calcio.* Hoepli, Milano, 588 p., ISBN: 9786000635251.
- Schlitt W.J., and Healy G.W. (1970) – *Characterization of Lime: A Comparison and Scaling Down of the Coarse Grain Titration Test and the ASTM Slaking Rate Test.* The

Reaction Parameters of Lime, ASTM STP, 472, 143-160.

- Scholle P.A., and Ulmer-Scholle D.S. (2003) – *A Color Guide to the Petrography of Carbonate Rocks: Grains, Textures, Porosity, Diagenesis*, AAPG Memoir 77, 474 p.
- Schorcht F., Kourti I., Scalet B.M., Roudier S., and Sancho L.D. (2013) – *Best Available Techniques (BAT) Reference Document for the Production of Cement, Lime and Magnesium Oxide*. Joint Research Center (JRC), 171-292, http://eippcb.jrc.ec.europa.eu/reference/BREF/CLM_Published_def.pdf
- Schwarzkopf F. (1994) – *Lime Burning Technology – a manual for lime plant operators*. 3rd ed., Svedala Industries Kennedy, Van Saun.
- Schwiete H.E., and Ziegler G. (1956) – *Beitrag zur Thermochemie des Kalkes*. Tonindustrie-Zeitung und Keramische Rundschau, 80.
- Silcox G.D., Kramlich J.C., and Pershing D.W. (1989) – *A mathematical model for the flash calcination of dispersed CaCO₃ and Ca(OH)₂ particles*. Ind. Eng. Chem. Res. 28, 155–160.
- Silva M., Specht E., Schmidt J., and Al-Karawi J.(2009) – *Influence of the origin of limestone on its decomposition temperature and on the specific heat capacity and conductivity of lime*. High Temperatures-High Pressures, 38:4, 361-378.
- Silva M., Specht E., and Schmidt J. (2010a) – *Thermophysical properties of the limestone as a function of origin (Part 1): Specific heat capacities*. ZKG International, 2, 55-62.
- Silva M., Specht E., and Schmidt J. (2010b) – *Thermophysical properties of the limestone as a function of origin (Part 2): Calcination enthalpy and equilibrium temperature*. ZKG International, 6, 51-57.
- Soltan A.M.M. (2009) – *Petrographic modelling of Egyptian limestones for quicklime manufacture*. Arabian Journal of Geosciences, 4, 803–815. <https://doi.org/10.1007/s12517-009-0095-4>
- Soltan A.M.M., and Serry M.A.-K. (2011) – *Impact of limestone microstructure on calcination activation energy*. Advances in Applied Ceramics, 110:7, 409-416, <https://doi.org/10.1179/1743676111Y.0000000042>
- Soltan A.M.M., Kahl W.-A., Hazem M.M., Wendschuh M, and Fischer R.X. (2011) – *Thermal microstructural changes of grain-supported limestones*. Miner Petrol, 103, 9-17, <https://doi.org/10.1007/s00710-011-0151-0>
- Soltan A.M.M., Kahl W.-A., Wendschuh M., and Hazem M.M. (2012) –

Microstructure and reactivity of calcined mud supported limestones. Mineral Processing and Extractive Metallurgy, <https://doi.org/10.1179/1743285511Y.0000000024>

- Specht E. (1993) – *Kinetik der Abbaureaktionen*. Cuvillier Verlag, Göttingen.
- Sperber C.M., Wilkinson B.H., and Peacor D.R. (1984) – *Rock composition, dolomite stoichiometry and rock/water reactions in dolomitic carbonate rocks*. J. Geol. 92, 609–622, <https://doi.org/10.1086/628901>
- Stanmore B.R., and Gilot P. (2005) – *Review—calcination and carbonation of limestone during thermal cycling for CO₂ sequestration*. Fuel Processing Technology, 86, 1707–1743, <https://doi.org/10.1016/j.fuproc.2005.01.023>
- Taylor H.F.W. (1997) – *Cement Chemistry*. Academic Press, London, 2nd Edition, Thomas Telford Publishing, London, 361, <http://dx.doi.org/10.1680/cc.25929>
- Tran H.N. (2006) – *Lime Kiln Chemistry and Effects on Kiln Operations*. 2006 TAPPI Kraft Recovery Short Course, St. Petersburg, FL, USA.
- Tran H.N., and Barham D. (1991) – *An overview of ring formation in lime kilns*. Tappi J, 74:1, 131-136.
- Tran H.N., Mao X., and Barham D. (1993) – *Mechanisms of Ring Formation in Lime Kilns*. Journal of Pulp and Paper Science, 19:4, 167-175.
- Triantafyllou G., Christidis G., and Markopoulos T. (2003) – *Influence of porosity and grain size of carbonate rocks in the reactivity of lime*. In: Demetrios et al. (Eds.) “Proc. 7th Biennial SGA Meeting”, Athens, Greece, 931-934.
- UNI-EN 459-2 (2010) – *Building lime – Part 2: Tests methods*. CEN/TC 51, 116p.
- Valverde J.M., and Medina S. (2015) – *Crystallographic transformation of limestone during calcination under CO₂*. Phys. Chem. Chem. Phys., 17, 21912-21926, <https://doi.org/10.1039/C5CP02715B>
- Valverde J.M., Sanchez-Jimenez P.E., and Perez-Maqueda L.A. (2015) – *Limestone Calcination Nearby Equilibrium: Kinetics, CaO Crystal Structure, Sintering and Reactivity*. J. Phys. Chem. C, 119, 1623–1641, <https://doi.org/10.1021/jp508745u>
- Vola G., and Sarandrea L. (2013) – *Raw materials characterization for industrial lime manufacturing*. ZKG International, 66:5, 62-70.
- Vola G., and Sarandrea L. (2014a) – *Lime reactivity study. Raw material quality, kiln control and influence on lime reactivity in a Twin Shaft Regenerative Kiln (TSR)*. World Cement, 45:6, June 2014, 49-55.

- Vola G., and Sarandrea L. (2014b) – *Investigating and predicting blockages*. World Cement, October 2014, 85-92.
- Vola G., and Sarandrea L. (2015) – *Investigation and prediction of marble mechanical degradation and dust formation during calcination process in Twin Shaft Regenerative (TSR) kilns*. Cement International, 3, 42-47.
- Vola G, Sarandrea L, Della Porta G, Cavallo A, Jadoul F, and Cruciani G. (2017) – *The influence of petrography, mineralogy and chemistry on burnability and reactivity of quicklime produced in Twin Shaft Regenerative (TSR) kilns from Neoproterozoic limestone (Transvaal Supergroup, South Africa)*. Miner Petrol, 2017, <https://doi.org/10.1007/s00710-017-0542-y>
- Vola G., Bresciani P., Rodeghero E., Sarandrea L., and Cruciani G. (2018) – *Impact of rock fabric, thermal behavior, and carbonate decomposition kinetics on quicklime industrial production and slaking reactivity*. Journal of Thermal Analysis and Calorimetry, <https://doi.org/10.1007/s10973-018-7769-7>
- Yan C., Grace J.R., and Lim C.J. (2010) – *Effects of rapid calcination on properties of calcium-based sorbents*. Fuel Process. Technol., 91, 1678-1686, <http://dx.doi.org/10.1016/j.fuproc.2010.07.004>
- Wagner C. (1961) – *Theorie der Alterung von Niederschlägen durch Umlösen (Ostwald-Reifung)*. Zeitschrift für Elektrochemie, 65:7, 581–591.
- Warren J. (2000) – *Dolomite: occurrence, evolution and economically important associations*. Earth-Science Reviews, 52, 1-81, [https://doi.org/10.1016/S0012-8252\(00\)00022-2](https://doi.org/10.1016/S0012-8252(00)00022-2)
- Watkinson A.P., and Brimacombe J.K. (1982) – *Limestone calcination in a rotary kiln*. Metall. Trans. B 13B, 369, <https://doi.org/10.1007/BF02667752>.
- Wright G. (1995) – *Effect of impurities on lime reactivity*. Ash Grove Cement Company, Rivergate Lime Plant, Confidential Internal Report, 41 p.
- Wu P., Eriksson G., and Pelton A.D. (1993) – *Critical evaluation and optimization of the thermodynamic properties and phase diagrams of the calcia-iron(II) oxide, calcia-magnesia, calcia-manganese(II) oxide, iron(II) oxide-magnesia, iron(II) oxide-manganese(II) oxide, and magnesia-manganese(II) oxide systems*. J. Am. Ceram. Soc., 76, 2065–2075, <https://doi.org/10.1111/j.1151-2916.1993.tb08334.x>
- Wuhler J. (1956) – *Report*. Schriftenreihe des Bundesverbandes der Kalkindustries, 2, 101-106.

2 MATERIALS AND EXPERIMENTAL METHODS

2.1 Materials supply

Carbonate rocks selected for this research activity, namely pure limestones and dolomites, have been supplied to Cimprogetti S.r.l. by several customers worldwide to verify their suitability for the industrial production of high-grade quicklime and slaked lime products. Samples have been received in the typical grain-sizes or size-fractions, i.e. 15-30, 30-60 up to 40-80 mm, used to feed industrial lime kilns.

2.1.1 Materials supply for article no.1

The first part of the research activity was carried out on a Neoproterozoic limestone case-study (Vola et al., 2017). Eight main samples (2P1, 2P2, 2P3, 2P4; 4P1, 4P2, 4P3, 4S) from three different benches (2P, 4P and 4S) of the Ouplaas Mine, Daniëlskuil, Griqualand West, South Africa, were considered (Tab.2.1). The preliminary lithofacies inspection was performed on prismatic chunks cut with a diamond wire.

Tab.2.1 – Carbonate rock samples considered in the article no.1 (Vola et al., 2017)

Code	Name	Material	Fraction	Provenance
2P1	IDW	Limestone	prismatic chunks 20x20x20 cm	Ouplass Mine, Daniëlskuil, South Africa
2P2	IDW	Limestone	prismatic chunks 20x20x20 cm	Ouplass Mine, Daniëlskuil, South Africa
2P3	IDW	Limestone	prismatic chunks 20x20x20 cm	Ouplass Mine, Daniëlskuil, South Africa
2P4	IDW	Limestone	prismatic chunks 20x20x20 cm	Ouplass Mine, Daniëlskuil, South Africa
4P1	IDW	Limestone	prismatic chunks 20x20x20 cm	Ouplass Mine, Daniëlskuil, South Africa
4P2	IDW	Limestone	prismatic chunks 20x20x20 cm	Ouplass Mine, Daniëlskuil, South Africa
4P3	IDW	Limestone	prismatic chunks 20x20x20 cm	Ouplass Mine, Daniëlskuil, South Africa
4S	IDW	Limestone	prismatic chunks 20x20x20 cm	Ouplass Mine, Daniëlskuil, South Africa

2.1.2 Materials supply for article no.2

The second part of this study, dedicated to the impact of rock fabric and carbonate decomposition kinetics on slaking reactivity, was carried out on 15 carbonate rocks selected from different customers worldwide. They include 9 pure limestones, 3 pure dolomites, and 3 impure carbonates, i.e. 2 marly limestones and 1 silicate-bearing marble. Some materials are currently used to feed vertical shaft kilns in different countries, some others are going to be adopted in the early future, considering it was recently commissioned the design of new Twin Shaft Regenerative (TSR) kilns. Some historical Italian carbonate stones were considered, as well (Tab.2.2).

Tab.2.2 – Carbonate rock samples considered in the article no. 2 (Vola et al., 2018)

Code	Name	Material	Fractions	Provenance
598	SCH	Marly limestone	40-80 mm	Lienen, Germany
2743	INT	Marly limestone	40-80 mm	Thala, Tunisie
2001	SAC	Limestone	40-80 mm	Siracusa, Italy
2004	CMI	Limestone	40-80 mm	Sohar, Oman
2828	VER	Limestone	15-30 mm	Rosso Verona district, Valpolicella, Verona, Italy
1880	QSC	Limestone	40-80 mm	Rawdat Rasid, Qatar
1990	IDW-1	Limestone	40-80 mm	Ouplass Mine, Daniëlskuil, South Africa
1991	IDW-2	Limestone	40-80 mm	Ouplass Mine, Daniëlskuil, South Africa
1992	SMA	Limestone	40-80 mm	Storugns, Gotland, Sweden
2450	PSP	Limestone	30-60 mm	Rembang, Java, Indonesia
1895	CRM	Impure marble	40-80 mm	Seilles, Belgium
2829	CAR	Calcitic Marble	15-30 mm	Carrara marble district, Carrara, Italy
2830	ZAN	Dolomite	15-30 mm	Grena Valley, Zandobbio, Bergamo, Italy
2782	PED	Dolomite	40-80 mm	Balvano, Potenza, Italy
2112	MME	Dolomite	15-30 mm	Medan Area, North Sumatera, Indonesia

2.1.3 Materials supply for article no. 3

For this research activity, dedicated to sticking tendency and blocks formation by means of the so-called “Overburning Test” method, 46 carbonate rocks with different compositions and textures were selected from several lime producers worldwide. They include mud-supported and grain-supported limestones, diagenetic dolomites, granoblastic marbles, and other impure carbonates (Tab.2.3).

Tab.2.3 – Carbonate rock samples considered in the article no. 3

Codes	Name	Material	Provenance
2001	SAC	Limestone	Siracusa, Italy
2004	CMI	Limestone	Sohar, Oman
2005	CAL-1	Limestone	Monterrey, Mexico
1818	CHO	Calcitic Marble	Guro-gu, South Korea
1854	ISP-1	Limestone	Burnpur, India
1849	HOS-1	Limestone	Mirzaci, Iran
1850	HOS-2	Limestone	Bakiabad, Iran
1851	HOS-3	Limestone	Angoran, Iran
1852	HOS-4	Limestone	Kashigari, Iran
1853	HOS-5	Limestone	Dargaz, Iran
2828	VER	Limestone	Rosso Verona district, Valpolicella, Verona, Italy
2829	CAR	Calcitic Marble	Carrara marble district, Carrara, Italy
1990	IDW-1	Limestone	Ouplass Mine, Daniëlskuil, South Africa
1991	IDW-2	Limestone	Ouplass Mine, Daniëlskuil, South Africa
1880	QSC-1	Limestone	Rawdat Rasid, Qatar
2450	PSP-1	Limestone	Rembang, Java, Indonesia
2451	PSP-2	Limestone	Rembang, Java, Indonesia
2665	CRM-d	Limestone	Seilles, Belgium
2666	CRM-w	Limestone	Seilles, Belgium
2701	PTL-1a/b	Limestone	Laramie, Wyoming, USA
2702	PTL-2	Limestone	Laramie, Wyoming, USA

2887	DOC	Limestone	Rep. Dominicana
2005	CAL-2	Dolomite	Monterrey, Mexico
1856	ISP-2	Dolomite	Burnpur, India
1867	CRM-1	Dolomitic marble	Seilles, Belgium
1873	CRM-2	Dolomitic marble	Seilles, Belgium
2830	ZAN	Dolomite	Grena Valley, Zandobbio, Bergamo, Italy
2025	SRI	Dolomitic marble	Subang Jaya, Malaysia
2112	MME	Dolomite	Medan Area, North Sumatera, Indonesia
1735	INT	Dolomite	Dnepropetrovsk, Ukraine
2019	SAL	Dolomite	Campiglia Marittima, Grosseto, Italy
1881	QSC-2	Dolomite	Qatar
2309	USI	Dolomite	Kuwait
2667	MON	Dolomitic marble	India
2668	ESH	Dolomitic marble	India
2669	JIG	Dolomitic marble	Bhutan
2762	UNI-1	Dolomite	Ponte del Costone quarry, Casnigo, Bergamo, Italy
2777	PED	Dolomite	La Pedicara quarry, Balvano, Potenza, Italy
598	SCH	Marly limestone	Lienen, Germany
2743	INT	Marly limestone	Thala, Tunisie
2904	TAS	Calcitic Marl	Tassullo, Trento, Italy
2217	UNI-2	Dolomitic Marl	Vaiolo quarry, Lecco, Italy
2261	UNI-3	Dolomitic Marl	Vaiolo quarry, Lecco, Italy

2.1.4 Materials supply for article no.4

The third part of this study, dedicated to the slaking reactivity modelling and sintering tendency at high burning temperature, was carried out on 12 carbonate rocks selected from different customers worldwide. They include 8 pure limestones and 4 pure dolomites (Table 2.4). For some of the above mentioned materials, two fractions were analyzed. Some of these materials are currently used to feed vertical shaft kilns, some others are going to be adopted in the early future for new kilns designing and commissioning. Finally, some historical Italian carbonate stones were considered, as well.

Tab.2.4 – Carbonate rock samples considered in the article no. 4

Code	Name	Material	Fractions	Provenance
2450-51	PSP	Limestone	41-75 mm; 25-55 mm	Rembang, Java, Indonesia
2452-53	IDW	Limestone	44-77 mm; 31-53 mm	Daniëlskuil, S. Africa
2454-55	WOP	Limestone	40-65mm; 31-46 mm	Dürnbach, Waldegg, Austria
2462-63	SMA	Limestone	48-68 mm; 34-48 mm	Storugns, Gotland, Sweden
2737-38	EUR	Limestone	Cores (d: 40 mm)	Zhambyl, Kazakhstan
2828	CAR	Calcitic Marble	15-30 mm	Carrara, Italy
2829	VER	Limestone	15-30 mm	Verona, Italy
2943	PRO	Limestone	40-80 mm	Maycopt, Russia
2830	ZAN	Dolomite	15-30 mm	Grena Valley, Zandobbio, Bergamo, Italy
2776-77	PED	Dolomite	40-80 mm; 30-60 mm	La Pedicara, Balvano, Potenza, Italy
2662A-B	UNI	Dolomite	40-80 mm; 30-60 mm	Ponte del Costone, Casnigo, Bergamo, Italy
2112	MME	Dolomite	15-30 mm	North Sumatera, Indonesia

2.2 Tests and experimental methods

2.2.1 Carbonate rocks and burnt limes nomenclature

According to the geological literature, terms of *limestone* and *dolomite* (or *dolostones*) indicate sedimentary carbonate rocks presenting characteristic primary or depositional textures, and secondary or diagenetic modifications. Furthermore the term *marble*, including *calcitic* or *dolomitic* ones, indicates a metamorphic carbonate rock, presenting typically recrystallized granoblastic textures. Finally, impure sedimentary carbonate rocks are defined *marly limestones or dolomites*, while metamorphic impure carbonates are just defined *impure marbles*. For this study it was adopted the chemical classification of carbonate rocks proposed by Frolova (1959), as reported in Chilingar (1960). Moreover, we also defined carbonate rocks on the basis of their impurity content, i.e. the insoluble residue (IR). Therefore the following classification was also adopted: 1) *pure or high-grade carbonates* with IR <1%; 2) *slightly impure carbonates* with IR = 1-5%; 3) *impure carbonates* with IR >5%. Finally, high-calcium, dolomitic and hydraulic limes are defined according to the European standard for building limes (UNI EN 459-1).

2.2.2 Pre-treatments for insoluble residua and clay minerals extraction and purification

The extraction of the insoluble residua of limestones and dolomites are generally performed by “classic” chemical pre-treatments with hydrochloric acid. The use of 1N hydrochloric acid is recommended only for shorts times (max 20 min) to minimize the digestion of impurities such as clay minerals, especially illite/montmorillonite mixed layers (Bonazzi, 1984; Bonazzi et al., 1987; Cook, 1992). We specifically adopted a procedure designed for the extraction of secondary constituents from pure and ultrapure carbonates, containing an insoluble residue generally <2%, but mostly <0.5% (Brignoli, 2017). The following steps were subsequently performed:

1. **Acid attack.** An aliquot of 100 g of sample powder is placed in a beacker with some dozen millilitres of demineralized water and a magnetic still. The beacker is placed on the heating plate at boiling temperature. The HCl 1N is gently poured into the beacker, making attention to avoid the leakage of liquid due to the possible effervescence. It’s important to monitor the acidity of solution, using pH digital meter to avoid low pH (below 5) that could damages clay minerals. The acid attack must allow the complete dissolution of all the carbonates, including dolomite that at

this condition requires heating at 70-80°C. When the pH of the solution is about 5 and stable, all the carbonates are removed. As soon as the solution is cooled, clay minerals will flocculate and precipitate at the bottom of the beaker, leaving the supernatant liquid clear. A part of this liquid can be eliminated. The remaining suspension is then agitated and moved into the centrifuge tube.

2. Centrifugation. The centrifugation was performed for 1 min at 3600 rpm. The insoluble residue is then concentrated at the bottom of the tube: the supernatant liquid has to be eliminated, and demineralized water is added. Using a glass stirring rod the suspension with deposited clays is shaken and washed to remove the acid excess. The tube is tapped and shaken again. Then the tube is placed again within the spin-dryer and the centrifugation is performed again until the supernatant liquid will assume a milky color. At least 4-5 washing cycles are generally required to eliminate the acid excess. The residual deposit is gently de-caked, and removed from the bottom of the tube using a glass stirring rod, and deposited on a glass cup. The insoluble residue is dried at 105°C and weighted, for calculating its concentration with respect to the whole-rock sample.
3. Oriented-samples preparation. A fraction of the insoluble residue is dispersed in demineralized water adding some drops of a deflocculant agent, i.e. sodic pyrophosphate. The suspension has to be vigorously shaken. According to the Stokes's law, after 145 minutes about 1 cm³ of the solution is pipetted from the upper portion of the suspension, avoiding creating turbulence into the sample holder. Some drops of the pipetted suspension are then deposited on a couple of slide glasses. After about 12 hours the solution will evaporate, leaving a thin layer of basal peaks (001) iso-oriented minerals, the so-called “air-dried” (AD) sample. This procedure, generally reported in the literature as “pipette-on-slide method” (Moore and Reynolds, 1997), allows concentrating the clay bearing <2 μm grain-size fraction. The thickness of specimen is maintained as constant as possible, with at least 3 mg of clay per cm² of glass slide (Kisch, 1991).

2.2.3 Wavelength Dispersive X-ray Fluorescence Spectroscopy (XRF-WDS)

The chemical analysis was performed on pressed whole-rock and burnt lime powdered samples, previously pulverized in a stainless steel vessel ring mill. An aliquot of each sample was dried at 105 °C and after roasted at 1050 °C to determine the loss on

Chapter 2. Materials and Methods

ignition (LOI). Powders were mixed with an organic wax (9:1) and pelletized in 40 mm aluminium cups using a manual hydraulic press at 15 tons for 1 minute. Similarly, some milligrams of insoluble residua were previously gently de-agglomerated by manual grinding in an agate mortar then pelletized using boric acid as background. The chemical analysis was carried using a Rigaku Supermini 200 benchtop X-ray fluorescence spectrometer (XRF-WDS) with a Pd-anode operating at 200 W. Calibration was obtained through the analysis of available international standards of carbonate rocks. The calibration curves show good linearity for both major and minor components. Repeatability tests for dolomites and limestones were carried out and the standard deviations for both major and minor components are very small (Rigaku, 2015). The declared detection limit (DDL) expressed in ppm for major and minor elements according to Rigaku’s documentation, is reported in the Fig.2.1.

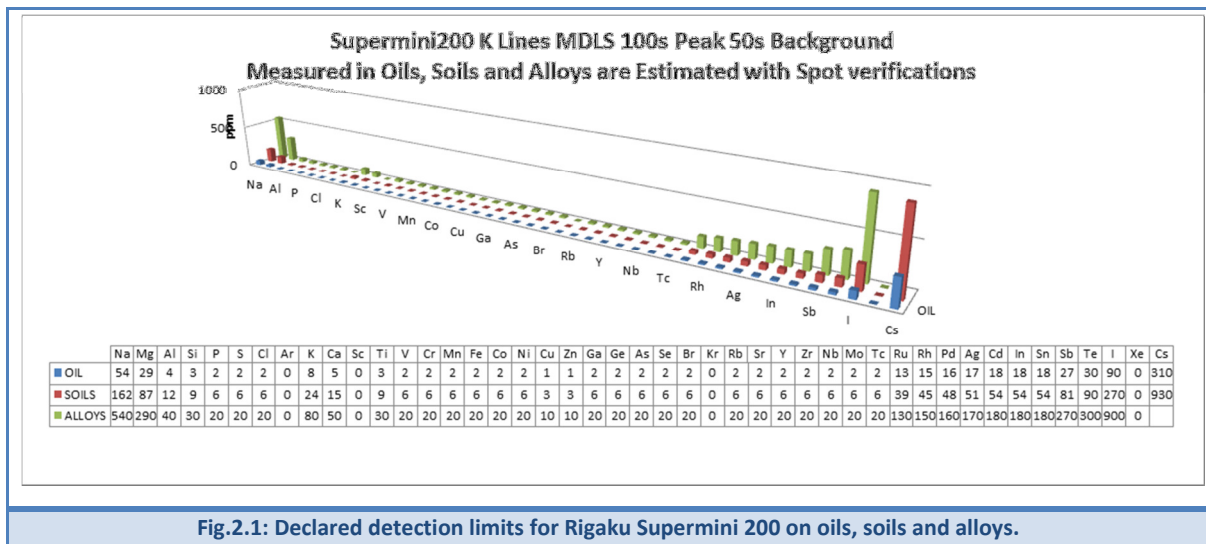


Fig.2.1: Declared detection limits for Rigaku Supermini 200 on oils, soils and alloys.

2.2.4 Inductively coupled plasma mass spectrometry (ICP-MS)

To assess the reliability of the XRF-WDS analyses, investigate ultralight (Li, Be, B, C, N) and trace elements content at very low concentration (< 1ppm), the Inductively Coupled Plasma Mass Spectrometric (ICP-MS) analysis was performed. Sample powders (0.15g) were totally digested with suprapure grade hydrofluoric acid HF and nitric acid HNO₃ (Merck, Darmstadt, Germany) on a hot plate. Dissolved samples were dried out and then re-dissolved in ultrapure water obtained from a Milli-Q purifier system (Millipore Corp., Bedford, MA, USA). The analyses were carried out using an X Series Thermo-Scientific spectrometer at the Department of Physics and Earth Sciences of the University of Ferrara. Specific amounts of Rh, In and Re were added to the analysed solutions as an internal standard, in order to correct for instrument drift. Accuracy and precision, based on replicated analyses of samples and standards, are better than 10 % for all considered elements.

2.2.5 Elemental analysis coupled with isotope ratio mass spectrometry (EA-IRMS)

The elemental carbon and nitrogen content coupled with the carbon isotopic composition have been carried out on a subset of 25 samples (of the total 46 reported in Tab.2.4) by the use of an Elementar Vario (EA) Micro Cube Elemental Analyzer in line with an ISOPRIME 100 Isotopic Ratio Mass Spectrometer (IRMS) operating in continuous-flow mode. The system allows variations of the combustion module temperature up to 1050 °C; this theoretically permits extraction of different components having distinctive destabilization temperatures and to analyze the respective C, N (wt %), and ¹³C/¹²C ratio.

The elemental and isotopic compositions of the Total Carbon (TC, and the associated nitrogen content TN), and Organic Carbon (OC), have been carried out slightly modifying the method described by Natali and Bianchini (2015). According to this analytical protocol: 1) TC (and TN) was carried out by EA-IRMS, combusting at 950 °C the bulk sample; 2) OC was carried out by EA-IRMS, combusting at 500 °C the bulk sample. Powdered samples were introduced in tin capsules that are wrapped and weighed. These capsules, that allow loading up to 40 mg of sample, are subsequently introduced in the Vario Micro Cube autosampler to be analyzed. Flash combustion takes place in a sealed quartz tube filled with copper oxide grains (padded with corundum balls and quartz wool) which acts as catalyst, in excess of high purity (grade 6.0) O₂ gas. Freed gaseous

species are transferred through a reduction quartz tube (at 550 °C) filled with metallic copper wires that reduce the nitrogen oxides (NO_x) to N₂. The formed analyte gases (N₂, H₂O and CO₂), carried by dry He (grade 5.0) gas, pass through a water-trap filled with Sicapent ensuring complete removal of moisture, are sequentially separated by a temperature programmable desorption column and quantitatively determined on a thermal-conductivity detector. Sample N₂ goes directly to the interfaced IRMS for isotopic composition determination, while CO₂ is held by the TPD column, kept at room temperatures 20–25 °C. When N₂ isotopic analysis is over, CO₂ is desorbed from the TPD column raising the temperature to 210 °C, and finally reaches the IRMS compartment for the determination of carbon isotopic ratios. The detection of the distinct isotopic masses of the sample are sandwiched between those of reference N₂ and CO₂ (5 grade purity) gases, which have been calibrated using a series of reference materials, in turn calibrated against IAEA international standards, such as the limestone JLs-1 (Kusaka and Nakano, 2014), the peach leaves NIST SRM1547 (Dutta et al., 2006), the Carrara Marble (calibrated at the Institute of Geoscience and Georesources of the National Council of Researches of Pisa), and the synthetic sulfanilamide provided by Isoprime Ltd. Mass peaks were recalculated as isotopic ratios by the Ion Vantage software package. Reference and carrier gases of certified purity were provided by SIAD Ltd. Precision of elemental concentration measurements were estimated by repeated analyses of the standards, and accuracy estimated by the comparison between reference and measured values, were in the order of 5% of the absolute measured value. Uncertainties, increase for contents approaching the detection limit (0.001 wt %). Carbon isotope ratios are expressed in the standard (δ) notation in per mil (‰) relative to the international Vienna Pee Dee Belemnite (V-PDB) isotope standard (Gonfiantini et al., 1993). The δ¹³C values were characterized by an average standard deviation (1 sigma) of ±0.1 ‰ and ±0.3 ‰, respectively as defined by repeated analyses of the above mentioned standards.

2.2.6 Carbon-Sulphur (C-S) elemental analysis

The analytical determination of total carbon (TC), total organic carbon (TOC), and total sulfur (S) on limestone samples from Ouplaas Mine in Daniëlskuil (Griqualand West, South Africa) (Tab.2.1) were carried out by means of a combustion infrared detection technique using a Leco CS844ES analyzer with declared detection limit of 0.02 %.

2.2.7 BET Specific Surface Area by Nitrogen absorption (BET/N₂ method)

The specific surface area of raw materials and derived burnt lime products was investigated according to the Brunauer-Emmett-Teller (BET) method (ISO 9277, 2010), using a Micromeritics TriStar II Plus automated gas sorptometer, having a stated resolution of $>0.01 \text{ m}^2/\text{g}$. Crushed aggregate samples $<2 \text{ mm}$ and/or their powders were dried at $200 \text{ }^\circ\text{C}$ for 20 min in a nitrogen gas flux, using the SmartPrep device. Subsequently, an aliquot of each sample (about 3.5 g) was loaded on a standard burette. Samples were first outgassed at $30 \text{ }^\circ\text{C}$ for 30 min under vacuum to a final pressure of 100 mmHg (0.338 MPa) and then the isotherm measured over the relative pressure range of (P_s/P_0) from 0.05 to 0.3 and back. The BET specific surface area and the volume of monolayer coverage were determined according to the BET theory. Microporous volume and pore size distribution were calculated using Barnett-Joyner-Halenda (BJH) procedure.

2.2.8 Mercury Intrusion Porosimetry (MIP)

The mercury intrusion porosimetry (MIP) was carried out at the University of Milano-Bicocca using a PASCAL 140-240 Thermo Fisher Scientific Hg porosimeter. Samples were first degassed four 30 minutes and then intruded by Hg with 2 intermediate degassing steps. The pressurization is achieved using the PASCAL (Pressurization with Automatic Speed-up by Continuous Adjustment Logic) method, with pressure from 0.1 kPa to 200 MPa. Open porosity and pore size distribution (pore radius between 0.002 and 100 μm) of each sample are computed with Washburn's equation. This equation assumes cylindrical pores, a contact angle between mercury and sample of 140° , a surface tension of mercury vacuum of 480 mN/m and mercury density equal to $13.54 \text{ g}/\text{cm}^3$. The following fundamental parameters were computed running the SOLID-SOLver Intrusion Data Software: bulk density, apparent density, total cumulative volume, total specific surface area, accessible porosity, and finally, average pore diameter. The bulk density is the density of the sample referred to its external volume. The apparent density is defined as the density of the sample referred to the real sample volume. The apparent density is very close to the real density (or true density) in the following cases: the sample is not compressed and not collapsed by the high pressure; the sample has not pores smaller than the mercury porosimetry lower limits. Total Cumulative Volume is given by the total volume of mercury penetrated into the sample at the end of measurements. Total Specific Surface Area represents the sum of the specific surfaces of the sample pores to hypothesize

cylindrical shape. Accessible porosity is a measure of the void spaces in a material, and is a fraction of the volume of voids over the total volume, between 0 % and 100 %. Average pore diameter was calculated by Washburn's equation. The analysis was corrected by blank measurement, adopting a speed of pressurization similar to the one subsequently adopted for analyzed sample. This procedure minimizes the temperature effect due to the pressurization process. In fact, during the pressurization, mercury undergoes a temperature change, resulting in a density and volume change. Contemporary to the mercury temperature increase, the system (dielectric oil and dilatometer glass) diffuses the heat. The heat transfer process during the pressurization/depressurization steps depends on the mercury and sample quantities in the dilatometer, on the sample nature and, especially, on the pressurization/depressurization speed.

2.2.9 Real Density by gas pycnometry

The analysis of real (absolute or true) density was performed using a Micromeritics AccuPyc II 1340 helium gas pycnometer, equipped with a sample cell volume of 10 cm³. The analysis is based on the following calculations:

$$V_s = V_c - \frac{V_x}{\frac{P_1}{P_2} - 1} \quad \text{[I]}$$

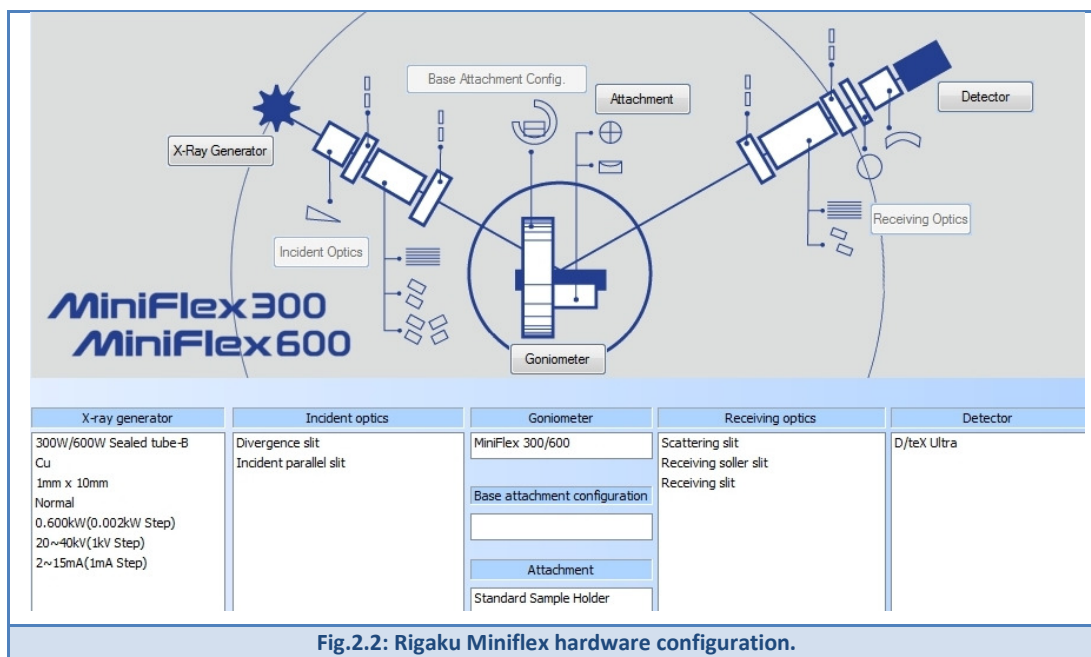
$$\rho_s = \frac{m_s}{V_s} \quad \text{[II]}$$

Where V_c is the sample chamber volume, V_x is the expansion chamber volume, V_s is the sample volume, m_s is the sample mass, ρ_s is the sample density, P_1 is the gauge pressure after fill, and P_2 is the gauge pressure after expansion.

2.2.10 X-Ray powder Diffraction analysis (XRD) and clay mineralogy

The X-ray powder diffraction analysis (XRD) was performed using a Rigaku Miniflex 600 Bragg-Brentano benchtop diffractometer with CuK α radiation (1.5417 Å, 40 kV, and 40 mA), equipped with the D/teX Ultra-high-speed detector (Fig.2.2 and Fig.2.3). Randomly-oriented whole-rock powders, insoluble residua and burnt limes were side-

loaded in a flat sample-holder. Insoluble residua were previously kindly deagglomerated by manual grinding into an agate mortar. Zero background sample holder was alternately used just for small amount of insoluble residue (few milligrams). The analysis was performed between $5\text{--}90^\circ 2\theta$ on rocks, and between $2.5\text{--}120^\circ 2\theta$ on insoluble residua and burnt limes, respectively, with a step of 0.02° and a speed of $4^\circ/\text{min}$. The identification and the quantification of mineral phases were performed running the Rigaku PDXL2 software analysis.



A specific diagnostic procedure for clay minerals identification was performed on oriented slide glasses (see pre-treatments procedure) according to the pipette-on-slide method (Moore and Reynolds, 1997). This procedure is required to solve basal peaks overlapping (Thorez, 1976; Brown and Brindley, 1980; Veniale et al., 1987; Moore and Reynolds, 1997). In particular, the presence of expandable clay minerals, i.e. smectites and smectite-mixed layers, was determined on oriented air-dried (AD) films and by ethylene glycol (EG) saturated samples at room temperature with a new vaporization method (Brignoli, 2017). Heat Treatment of the films at 550°C (HT_{550}) for 1h was applied for kaolinite/chlorite identification: kaolinite lattice collapses around 500°C , instead of chlorite enhances the first reflection at 14 \AA . The XRD analysis on oriented slide glasses was performed between $2.5\text{--}35^\circ 2\theta$ with a step of 0.02° and a speed of $4^\circ/\text{min}$.



Fig.2.3: Rigaku Miniflex 600 Bragg-Brentano benchtop diffractometer equipped with the D/teX Ultra-high-speed detector

2.2.11 Quantitative Phase Analysis (QPA) by the Rietveld method

The collected XRD diffraction patterns were submitted to the structural refinement using the Rietveld method (Bish and Howard 1988; Young 1993) to perform the Quantitative Phase Analysis (QPA). Crystallographic structural models were selected from the literature. Rietveld refinements were performed running the PDXL2 Integrated X-ray powder diffraction software by Rigaku. The reliability of QPA of hydrated limes was checked comparing the chemical analysis of each sample determined by XRF-WDS with that calculated by theoretical chemical composition from the literature and the QPA determinations. Differences of these complementary chemical compositions are close among them, attesting the good accuracy of the QPA by XRD.

2.2.12 Crystallite-size analysis by Fundamental Parameters method

The Fundamental Parameters (FP) powder profile fitting method was used for analyzing diffraction line broadening and extrapolating the crystallite-size of lime samples burnt at different temperature (Cheary and Coelho, 1992; Cheary et al., 2004). The XRD peak shape changes depending on measurements conditions as well as crystallite-size and size distribution (size variation) of the samples. If these characteristics are correctly

utilized, the crystallite-size and size distribution can be determined by analyzing the peak shape. The Rigaku PDXL2 integrated software package was adopted for this scope. Please refer to the Rigaku PDXL2 Comprehensive Analysis User Manual for mathematical explanations. The following refinement strategy was adopted. Initially it was set the criteria to execute all the pattern analyses using the FP method from the “set model function” menu. Values for the data, like wavelength, optics, scan mode, slit width and opening angle of parallel slit, which were used in measurements and stored in the RAS format were correctly configured. The following step consisted in selecting crystallite shape from the “Edit parameters” menu. Two possibilities are available: spherical or ellipsoidal shape. From the same menu it was selected the Lognormal distribution in the cell “Distribution type”. Another possibility was to select Gamma distribution (for details on this choice see Bromideh and Valizadeh, 2014 and Limpert et al., 2001). Right click on the cell Distribution RSD (relative standard deviation) was done and Refine from the context menu was displayed. The starting RSD value was set at 1.6, instead of the 0.7 prefixed value. This factor derived from the refinement performed by the FP method on the Standard Reference Material NIST 640, which was adopted for the crystallite-size calibration. This certified material (Silicon Powder) presents a mean volume-weighted domain size of approximately 0.4 μm . Finally, the Ok button was used to close the Edit Parameter box, and Refine button was clicked on the analysis bar. Results were reported in Analysis Results View menu. Especially “crystallite size” and “microstrain” values are reported in Ang. (Angstrom) and % (percentage), respectively.

2.2.13 Synchrotron X-ray powder diffraction at high-temperature (HT-XRD)

High-temperature data collections on a subset of 5 samples (PSP, IDW-2, WOP, SMA, ZAN) were carried out in situ at the ID22 high-resolution powder diffraction beamline (European Synchrotron Radiation Facility, Grenoble, France) (Fig.2.4a-b). Each sample was loaded into a quartz glass capillary (diameter of 0.5 mm), and subsequently mounted on a spinner which rotated along the axis of the diffractometer. Once diffracted, the highly energetic incident X-ray beam ($\lambda = 0.400080$ (6) \AA) was directed through a multianalyzer made of nine Si 111 crystals mounted on single rotation device. Scanned in a continuous mode, nine high-resolution diffraction patterns were collected in parallel by means of nine scintillation detectors. Through this experimental setup the diffracted peaks are very narrow, with an instrumental contribution to the FWHM of around 0.003 $^{\circ}2\theta$.

Those registered patterns were normalized and combined in a subsequent data-reduction step to produce the equivalent step scan. X-ray diffraction patterns were collected according to the following temperature schedule: (i) at room temperature, (ii) in ramp from 700 °C to a maximum temperature of 1000 °C every 50 °C; (iii) in isotherm at 1000 °C every 60 s; and (iv) at room temperature after the thermal treatment at 1000 °C. After each stage but the last one, a new capillary loaded with an untreated sample was mounted in the diffractometer. The high temperature was generated by means of a hot-air blower: a hot air generator controlled by a Eurotherm regulator and a gas flow controller which ensures a precision of about ± 2 °C.



Fig.2.4: Details of the ID22 high-resolution XRD beamline at the ESRF, Grenoble, France

2.2.14 Optical Polarized Microscopy (OPM) and Cathodoluminescence (CL)

The petrographic analysis was performed on several thin section adopting Optical Polarized microscopy (OPM) equipped with high-resolution digital camera. Carbonate depositional textures were described according to the classification of carbonate rocks proposed by Dunham (1962), Friedman (1965), Embry and Klovan (1971), Sibley and Gregg (1987). Micrite refers to microcrystalline calcite crystals with size <4 μm ; microsparite indicates calcite crystals between 10-50 μm ; sparite indicates clear calcite crystals theoretically between 5-62 μm , but mostly larger than 62 μm (Tucker and Wright 1990; Flügel 2010). Thin sections have also been examined under a cold cathodoluminescence microscope (CL) performed with a Nuclide Luminoscope ELM 2B,

operating at 10 kV with a beam current between 4-6 mA and vacuum gauge 60–80 mTorr, at the Earth Sciences Department of the University of Milan.

2.2.15 Quantitative petrography by the Micrite-to-Sparite ratio (MSR)

Quantitative interpretation on representative number of micrographs (at least 10) taken at 4x under plane polarized light (PPL) from a representative number of thin sections, was achieved by a set of computational tools that includes simple image statistical thresholding and binarization. Black digital color counts micrite, microsparite and non-carbonate microcrystalline impurity, including the organic matter, scattered within the carbonate matrix. Conversely, white digital color represents medium- up to coarse crystals, including equant and poikilotopic calcite cement, hypidiotopic to hydiotopic diagenetic dolomite, and hypidiomorphic to idiomorphic calcite in metamorphic marbles. The porosity appears to be white under PPL, thus counted as sparite. This approximation can be considered acceptable, and it's partially balanced by the presence of non-carbonate impurity scattered into the microcrystalline matrix that appears to be black, and thus counted as micrite (Vola et al., 2018). Indeed the so-called “micrite-to-sparite ratio” (MSR) represents a synthetic textural-microstructural and mineralogical tool, useful to perform linear regression analysis with other compositional, kinetic or technical parameters.

2.2.16 Thermogravimetric analysis (TG-DTG) and calcination kinetics

Thermogravimetric and Differential Thermogravimetric analysis (TG-DTG) was performed at Cimprogetti on crushed carbonate rock samples <3.35 mm (about 80-120 g) using a Nabertherm electric muffle furnace under static air. The following experimental heating conditions were adopted: 2 hours of preheating, followed by 3 hours burning at 1200 °C, meaning a heating rate of about 10°C/min. The differential thermogravimetric analysis (DTG) was graphically displayed to evaluate peaks occurring during the decomposition of carbonate minerals between 600-1200°C, but mostly at temperature >700 °C (Emmerich, 2011). Calcination parameters, i.e. starting and ending time, maximum peak and delta reaction time (t_1 , t_2 , t_{max} , Δt), starting and ending temperature, maximum peak and delta reaction temperature (T_1 , T_2 , T_{max} , ΔT), were extrapolated from the thermogravimetric analysis, as well. Finally, the (apparent) activation energy (E [kJ/mol])

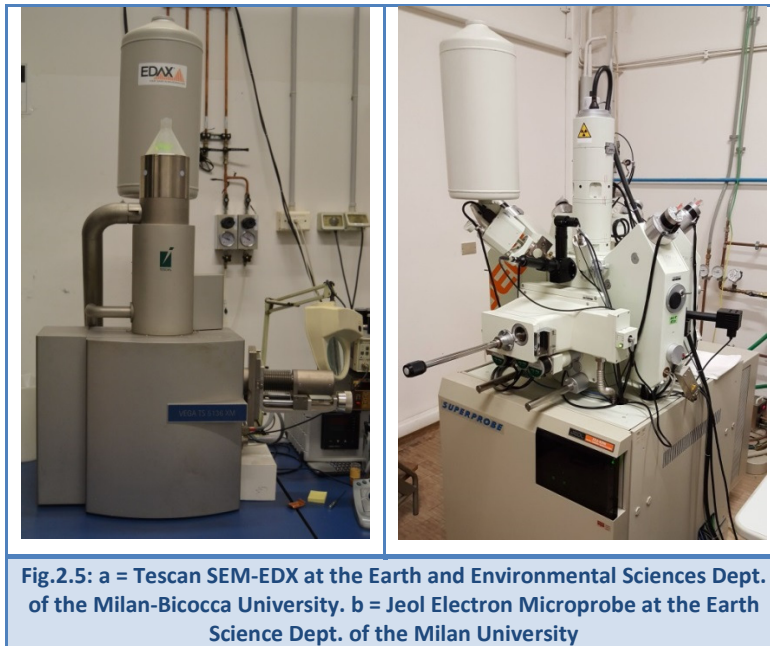
and the time factor (A [1/s]) from thermogravimetric (TG) analyses were calculated according to Fuoss-Salymer-Wilson (FSW) method (Fuoss et al., 1964).

2.2.17 Thermal analyses (TG-DTA)

To assess the reliability of the method, Thermogravimetric analysis (TG) and Differential Thermal Analysis (DTA) measurements were repeated at the University of Ferrara, using a Netzsch STA 409 PC LUXX® simultaneous TG/DTA thermogravimetric analyzer. Thermal analyses were performed on whole-rock powders (about 90 mg per each sample) using a heating rate of 10 °C/min, from room temperature (25 °C) up to 1400 °C, under constant flux of dry air. Mass losses at different temperatures were determined, i.e. 25-200, 200-500, 500 °C up to the on-set calcination temperature, in order to evaluate the presence of subordinated mineral phases associated to the main carbonate constituents. Moreover the decomposition enthalpy (ΔH [μ Vs] and [μ Vs/mg]) and the heat capacity (C_p [mVs/K] and [mVs/K]) were extrapolated from DTA analyses.

2.2.18 Scanning Electron Microscopy (SEM-EDS)

The microstructural analysis combined with the elemental analysis on limestone and burnt lime samples was performed at the Earth and Environmental Science Department of the Milan-Bicocca University, using a Scanning Electron Microscope (SEM) Vega TS Tescan Univac 5163 XM, equipped with an Energy Dispersive X-ray Spectrometer (EDS) EDAX Genesis 4000 XMS Imaging 60 for microanalysis (Fig.2.5a). Samples in the form of centimeter-sized prismatic chunks have been carbon coated by sputtering under vacuum conditions. The analysis was performed running high-vacuum mode for high-resolution Back-Scattered Electrons (BSE) imaging, for describing the microstructure. In addition Secondary Electrons (SE) imaging was adopted too.



2.2.19 Electron Microprobe Analysis (EMPA)

The quantitative mineral chemistry of selected limestone samples, i.e. pure and impure carbonates, was performed by an Electron Microprobe Analyzer (EMPA) JEOL JXA-8200 Superprobe at the Earth Sciences Department of the University of Milan (Fig.2.5b). This device is equipped with scanning electron imaging with back-scattered electron (BSE), secondary electron (SE), X-ray using WDS or EDS (elemental mapping), and cathodoluminescence (CL) (Chatterjee, 2012). For this specific case, different polished thin sections of limestone were previously carbon coated by sputtering under vacuum conditions. The microanalysis was performed running a Wavelength Dispersive X-ray Spectrometry (WDS) system, working at the following operative conditions: electron beam of 1 μm diameter, current intensity of 5 nA, and potential of 15 keV. Acquisition time: 30 seconds counting for the peak, 10 seconds counting for the background.

2.2.20 Burning tests on limestone/dolomite lumps at 1050-1150-1250 °C

Standard burning tests, according to Cimprogetti's internal method no. 39, were carried out on carbonate rock samples as received, i.e. in the typical size-fractions, using a muffle furnace under air conditions. Trials at different burning temperatures were performed in order to simulate industrial calcination process with different fuels. Especially, the following theoretical assumption was adopted: 1) soft-burning conditions occurring in a PFR kiln firing diesel oil fuel are simulated in laboratory at 1050 °C; 2)

medium-burning conditions occurring in a PFR kiln firing solid fuels, i.e. coal, lignite, anthracite, saw dust, and petcoke, are simulated at 1150 °C; 3) over-burning or dead-burning conditions occurring in a PFR kiln firing a fuel excess, are simulated in laboratory at 1250 °C. The following heating rate was adopted: 3 hours of pre-heating time, followed by 3 hours at the maximum burning temperature, as reported in Tab.2.5.

Tab.2.5 – Standard burning tests heating conditions. Legend symbols: HR = heating rate

Standard Burning Test at 1050°C			Standard Burning Test at 1150°C			Standard Burning Test at 1250°C		
T (°C)	Time (min)	HR (°C/min)	T (°C)	Time (min)	HR (°C/min)	T (°C)	Time (min)	HR (°C/min)
20	0		20	0		20	0	
850	60	14.17	850	60	14.17	850	60	14.17
950	60	1.67	950	60	1.67	950	60	1.67
1050	60	1.67	1150	60	3.33	1250	60	5.00
1050	360		1150	360		1250	360	

2.2.21 High temperature or “Overburning Test” (OT) method

This test, currently defined “internal test method no. 31” (TM-31), was invented by Cimprogetti to simulate the lime agglomeration, blocks formation, and ST at the maximum theoretical temperature of the Twin Shaft Kiln (TSR), i.e. 1300 °C. A preliminary description of this method is reported in Vola and Sarandrea (2014). It consists in burning a massive granulated sample of 75 g, under isothermal conditions for 3 h, using a specific quartz crucible (see dimensions in Fig. 2.6a). The sample has to be prepared by putting in contact a specific grain-size distribution, designed by sieving and mixing 3 gravel-sized fractions, with the powder from the same sample. Lime blocks formed into the muffle furnace are then cooled and weighted, and finally weighted and classified according to the ST classification (Tab.2.6 and Fig. 2.6 and Fig. 2.7). The following fundamental steps are described in details:

Tab.2.6 – Sticking Tendency (ST) classification

Block mass (g)	ST (%)	ST class	ST group
≈42	Max	Melted (A)	A
>20	>47.6	very high (B1)	B
18-20	42.9 – 47.6	high (B2)	
16-18	38.1 – 42.9	medium-high (B3)	
14-16	33.3 – 38.1	medium (C1)	C
12-14	28.6 – 33.3	medium-low (C2)	
10-12	23.8 – 28.6	low (D1)	D
<10	<23.8	no ST (D2)	

- 1) Rock crushing/milling. Bulk-rocks are crushed into a jaw crusher. Three different fractions are separated by sieving: 1) 6.3-5.0 mm, 2) 5.0-4.0 mm and 3) 4.0-3.35 mm. The following aliquots are weighted and mixed together to reproduce a gravel-like matrix with a specific particle-size distribution: fraction between 6.3-5.0 mm (18 g), fraction between 5.0-4.0 mm (25 g), and fraction between 4.0-3.35 mm (22 g). The obtained gravel's mass is then 65.0 g. The remaining granulated material <3.35 mm is then powdered for 30 s into a stainless steel vessel mill ring. An aliquot of 10 g of the obtained powder is put in contact with the gravel.
- 2) Sample preparation. 50 g of the gravel obtained according to point 1 are placed into a quartz crucible to form a bottom layer (Fig. 2.6a). A depression at the core of the gravel is created by a light pressure of fingers, using specific polyethylene gloves (Fig. 2.6b). 10 g of the fine powder are then placed at the core of the depression and gently pressed with fingers too (Fig. 2.6c-d). Finally, 15g of the gravel are placed as the top layer to cover all the powder (Fig. 2.6e). The quartz crucible is then placed into the warmed muffle furnace at $1300\text{ }^{\circ}\text{C} \pm 5\text{ }^{\circ}\text{C}$ for 3 h (Fig. 2.6f).
- 3) Sample extraction and block weighting. After burning 3 h at 1300°C , the crucible is extracted from the muffle furnace and quickly cooled. The preliminary visual inspection permits to evaluate if sample is partially melted or not (Fig. 2.7c). Therefore the core block is carefully removed using two small shovels, taking away lime grains on the top of the block, and the block is weighted on a digital balance (Fig. 2.7d). The cleaning operation must be done as quickly as possible, because blocks upon cooling could have the tendency to disintegrate.

Finally, the mass percentage of the lime block can be calculated [III] and the ST evaluated according to the classification proposed in Tab.2.6.

$\text{Sticking Tendency (\%)} = \frac{\text{block weight (g)}}{42} \cdot 100$	[III]
--	-------

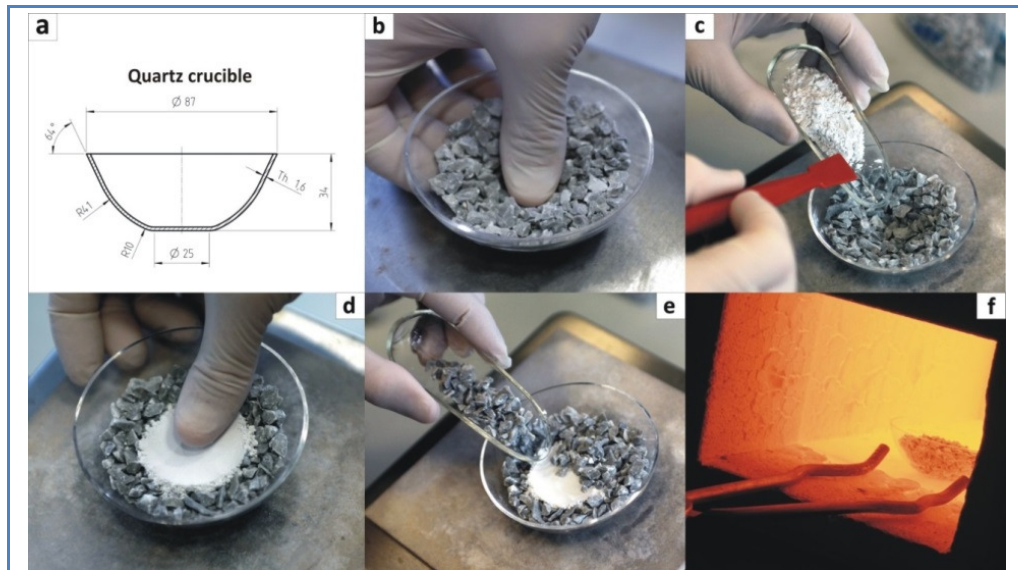


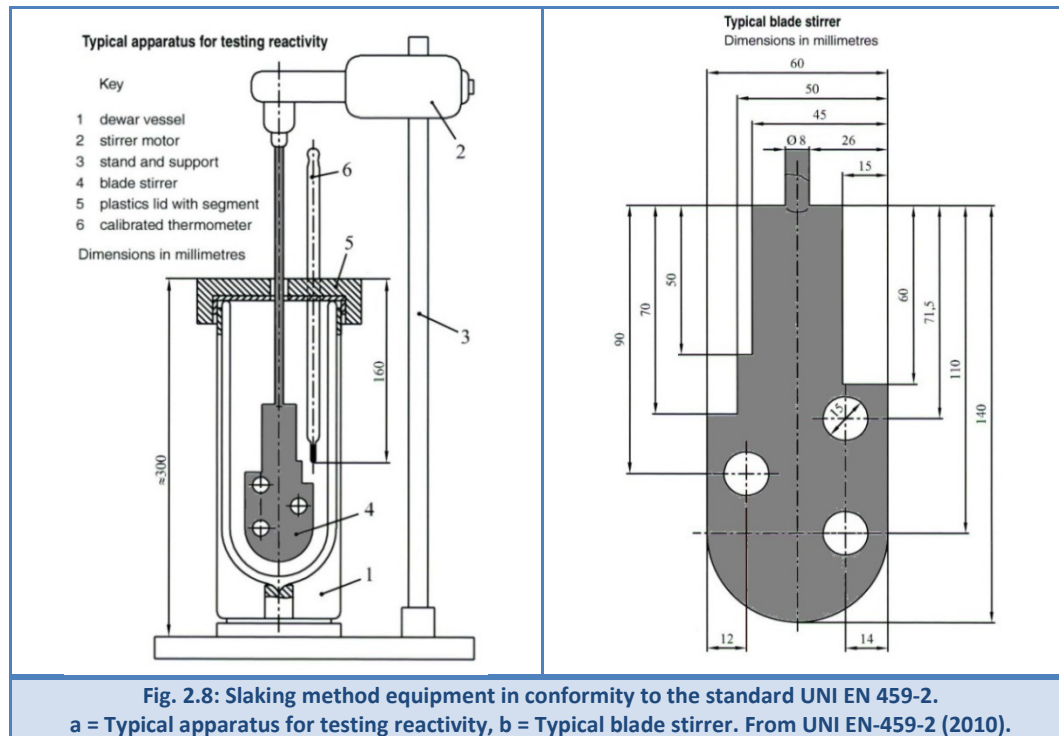
Fig. 2.6: Overburning Test (OT) method preparation procedures. a =quartz crucible dimensions; b-c = the depression at the core of gravel-sized aggregate (50 g) is filled in with the powder from the same sample (10 g). d = the powder is gently pressed by a light pressure of fingers, using polyethylene gloves. e = gravel-size aggregate (50 g) and pressed powder (10 g) are covered by a top layer of gravel-size aggregate (15 g). f =sample insertion into the muffle furnace at 1300 °C.



Fig. 2.7: Overburning Test (OT) method. Extraction and evaluation procedures. a = sample extraction after 3 h burning at 1300 °C. b = fast cooling. c = block extraction. d = visual evaluation and block weighing. e = example of a fused sample (CRM-3).

2.2.22 Slaking reactivity test and Available Lime Index (ALI)

The lime slaking reactivity is evaluated according to the European UNI EN 459-2 (2010) standard test method for building limes. The typical apparatus required is reported in the Fig. 2.8. The Dewar flask is filled with 600 ± 1 g of demineralized water at a temperature of 20 ± 2 °C. The thermocouple is put in position of 160 mm below the cover of the Dewar flask. The stirrer is put in a position corresponding to a distance between the stirrer and the bottom of the Dewar flask of 5 mm (see Fig. 2.8a-b)



The stirrer is kept moving at 400 ± 50 rpm. The test starts at time zero, when the whole sample of 150 ± 0.5 g of powdered quicklime at 20 °C is put down into the Dewar with water. The temperature is recorded from time zero every 30 seconds, until the maximum temperature is reached, and the slaking test is then completed. The temperature rise (ΔT 40 °C or t_{60}), the maximum slaking temperature (T_{\max}), the Maximum Heating Rate (MHR) [°C/min], and the Total Active Slaking Time (TAST) are determined. According to the European practice used throughout the lime producers, when $t_{60} < 3$ min the reactivity is high ($t_{60} < 1$ min very high), when t_{60} is between 3-6 min the reactivity is medium, and when $t_{60} > 6$ min the reactivity is low.

A mathematical approach based on Shrinking Core Model (SCM), mainly controlled by chemical reaction, was adopted for quantifying the hydration rates

(Levenspiel, 1999; Gbor and Jia, 2004; Liddel 2005; Blamey et al., 2016). Experimental data and results discussion are reported in the article no. 4.

Finally, the available lime index (ALI) was determined according to the sugar method (ASTM C25, 2017), where a definite portion of powdered quicklime is dissolved in a sugar solution and titrated against standardized hydrochloric acid solution.

2.2.23 Mechanical Degradation (MD) and Drop Tests (DT)

Test of quicklime mechanical degradation (MD) allows simulating the lime decrepitation occurring during the calcination process, and predicting the formation of fines inside the TSR kiln (Gallala et al., 2008; Vola and Sarandrea, 2013; 2015). The amount of fines, passing the sieve at 10 mm, is an important value to plot in the mathematical model for calculation of kiln production. The difference between values at 10 mm and 19 mm gives an indication of the tendency of the lime to split in smaller pieces during the calcination. A high splitting tendency will reduce significantly the kiln production. Finally, the so-called “drop test” (DT) is used to predict the tendency of the quicklime to break into fine particles at the discharging drawers of the TSR kiln. The procedure consists in selecting at least 5 lime pebbles with a grain-size between 37.5-45 mm. This test has to be performed just on hot lumps, after a standard burning test at 1050 °C. The sample is automatically sieved for 10 minutes, then the material passing through the sieve at 10 mm (<10 mm) and remaining material (>10 mm) are weighted, and the mechanical degradation is calculated, according to [IV].

MD (%) at 10 mm = $\frac{\text{sample weight (g) < 10 mm}}{\text{sample weight before sieving}} \cdot 100$	IV
MD (%) at 19 mm = $\frac{\text{sample weight (g) < 19 mm}}{\text{sample weight before sieving}} \cdot 100$	V
DT (%) = $\frac{\text{sample weight (g) < 19 mm}}{\text{sample weight before drop test}} \cdot 100$	VI

Moreover lime lumps remaining on 10 mm sieve (>10 mm) are also manually screened on 19 mm sieve (>19 mm) and weighted, so the mechanical degradation (%) of quicklime between 10-19 mm is calculated, according to [V]. The procedure for the DT consists in taking all lime lumps manually screened remaining at sieve of 19 mm (>19 mm) and putting them in a hermetically closed plastic bag. This bag is then dropped 5

times from the height of 2 m, after that the sample is sieved again on 19 mm sieve. Remaining lime lumps at sieve of 19 mm (>19 mm) are weighted, and the drop test degradation (%) is calculated, according to [VI].

2.3 References

- ASTM C25 (2017) – *Standard test methods for chemical analysis of limestone, quicklime, and hydrated lime*. ASTM Book Stand 04.01, 28–30.
- Bish D.L., and Howard S.A. (1988) – *Quantitative phase analysis using the Rietveld method*. J. Appl. Cryst. 21, 86–91, <https://doi.org/10.1107/S0021889887009415>
- Blamey J., Zhao M., Manovic V. et al. (2016) – *A shrinking core model for steam hydration of CaO-based sorbents cycled for CO₂ capture*. Chemical Engineering Journal, 291, 298–305, <https://doi.org/10.1016/j.cej.2016.01.086>
- Bonazzi A., Salvioli Mariani E., and Vernia L. (1984). *Tecniche di determinazione dell'indice di cristallinità dell'illite in campioni di argilla*. Mineralogica et Petrographica Acta, 28, 89-99.
- Bonazzi A. (1987) – *Procedure di determinazione e attendibilità dell'indice di cristallinità dell'illite*. In: Ferretti O., and Maffei P. (Eds.) “Procedure di analisi dei materiali argillosi”, Proc. ENEA workshop, 1-2 giugno 1987, S. Teresa, 245-261.
- Brignoli G. (2017) – *Procedura di preparazione di provini per l'analisi diffrattometrica di materiali argillosi*. Confidential Report for Cimprogetti S.r.l., 6 p.
- Bromideh A-A., and Valizadeh R. (2013) – *Discrimination between Gamma and Log-Normal Distributions by Ratio of Minimized Kullback-Leibler Divergence*. Pak. j. stat. oper. res., IX:4, 441-451.
- Brown G, and Brindley GW (1980) – *X-ray diffraction procedures for clay mineral identification*. In: Brindley G.W. and Brown G. (Eds.) “Crystal Structures of Clay Minerals and Their X-ray Identification”, Monograph 5, Mineralogical Society, London, 305-360.
- Chatterjee N. (2012) – *Electron Microprobe Analysis. Course 12.141. Notes*. MIT, Cambridge, MA, USA, 43 p.
- Cheary R.W., and Coelho A.A. (1992) – *A fundamental parameters approach to X-ray line-profile fitting*. Journal Appl Cryst, 25, 109-121, <https://doi.org/10.1107/S0021889891010804>
- Cheary R.W., Coelho A.A., and Cline J.P. (2004) – *Fundamental Parameters Line Profile Fitting in Laboratory Diffractometers*. J. Res. Natl. Inst. Stand. Technol., 109, 1-25, <https://nvlpubs.nist.gov/nistpubs/jres/109/1/j91che.pdf>
- Chilingar G.V. (1960) – *Notes on classification of carbonate rocks on basis of chemical composition*. J. Sediment. Res., 30,157–158.

- Cook R.J. (1992) – *A comparison of methods for the extraction of smectites from calcareous rocks by acid dissolution techniques*. Clay Minerals, 27, 73-80.
- Dunham R.J. (1962) – *Classification of carbonate rocks according to depositional texture*. In: Ham W.E. (Ed.) “Classification of carbonate rocks”, American Association of Petroleum Geologists Memoir, 1, 108–121.
- Dutta K., Schuur E.A.G., Neff J.C., and Zimov S.A. (2006) – *Potential carbon release from permafrost soils of Northeastern Siberia*. Glob. Change Biol., 12, 1–16, <https://doi.org/10.1111/j.1365-2486.2006.01259.x>
- Embry A.F., and Klovan J.S. (1971) – *A Late Devonian reef tract on northeastern Banks Island*. N.W.T. Bulletin of Canadian Petroleum Geology, 4, 730-781.
- Emmerich K. (2011) – *Thermal analysis in the characterization and processing of industrial minerals*. In: Christidis G.E. (Ed.), “Advances in the characterization of industrial minerals”, EMU Notes in mineralogy, London, 9:1, 129–170, <https://doi.org/10.1180/EMU-notes.9.5>
- Flügel E. (2010) – *Microfacies of Carbonate Rocks. Analysis, Interpretation and Application*. Springer-Verlag Berlin Heidelberg, 984 p. ISBN: 978-3-642-03795-5, <https://doi.org/10.1007/10.1007/978-3-642-03796-2>
- Friedman G.M. (1965) – *Terminology of recrystallization textures and fabrics in sedimentary rocks*. Journal of Sedimentary Petrology, 35, 643–655.
- Frolova E.K. (1959) – *On classification of carbonate rocks of limestone-dolomite-magnesite series*. Novosti Neft Tekhn, Geol, 3, 34–35.
- Fuoss R.M., Salymer I.O., and Wilson H.S. (1964) – *Evaluation of Rate Constants from Thermogravimetric data*. Journal of Polymer Science, A:2, 3147-3151.
- Gallala W., Gaied M., Tlili A., Montacer M. (2008) – *Factors influencing the reactivity of quicklime*. Proc. Institution of Civil Engineers - Construction Materials, 161:1, February 2008, 25-30, <https://doi.org/10.1680/coma.2008.161.1.25>
- Gbor P. K., and Jia C.Q. (2004) – *Critical evaluation of coupling particle size distribution with the shrinking core model*. Chemical Engineering Science 59, 1979 – 1987, <https://doi.org/10.1016/j.ces.2004.01.047>
- Gonfiantini R, Stichler W, Rozanski K (1993) – *Standards and intercomparison materials distributed by the International Atomic Energy Agency for stable isotope measurements*. In: Stichler W. (Ed.) “Reference and Intercomparison Materials for Stable Isotopes of Light Elements”, IAEA, Vienna, 1993, pp. 13-29.

- Kisch H.J. (1991) – *Illite crystallinity: recommendations on sample preparation, X-ray diffraction settings, and interlaboratory samples*. Journal of Metamorphic Geology, 9, 665-670.
- Kusaka S., and Nakano T. (2014) – *Carbon and oxygen isotope ratios and their temperature dependence in carbonate and tooth enamel using GasBench II preparation device*. Rapid Commun. Mass. Sp., 28, 563–567.
- ISO 9277 (2010) – *Determination of the specific surface area of solids by gas adsorption - BET method*. <https://www.iso.org/standard/44941.html>.
- Levenspiel O. (1999) – *Chemical reaction engineering*, third ed., John Wiley & Sons Inc., New York.
- Liddell K. C. (2005) – *Shrinking core models in hydrometallurgy: What students are not being told about the pseudo-steady approximation*. Hydrometallurgy, 79:1-2, 62-68, <https://doi.org/10.1016/j.hydromet.2003.07.011>
- Limpert E., Stahel W.A., and Abbt M. (2001) – *Log-normal Distributions across the Sciences: Keys and Clues*. BioScience, 51:5, 341-352, [https://doi.org/10.1641/0006-3568\(2001\)051\[0341:LNDATS\]2.0.CO;2](https://doi.org/10.1641/0006-3568(2001)051[0341:LNDATS]2.0.CO;2)
- Moore D.M., and Reynolds R.C. Jr. (1997) – *X-ray Diffraction and the Identification and Analysis of Clay Minerals*. Oxford University Press, Oxford, UK, and New York, 2nd edition.
- Natali C., and Bianchini G. (2015) – *Thermally based isotopic speciation of carbon in complex matrices: a tool for environmental investigation*. Environ. Sci. Pollut. Res., 22, 12162–12173, <https://doi.org/10.1007/s11356-015-4503-x>
- Rigaku (2015) – *Quantitative analysis of dolomite and limestone by pressed powder method with Supermini 200*. Application note XRF 1058, 4p.
- Sibley D.F., and Gregg J.M. (1987) – *Classification of dolomite rock textures*. J Sed. Res., 57:6, 967–975.
- Thorez J. (1976) – *Practical identification of clay minerals*. G. Lelotte Ed., 90 pp.
- Tucker M., and Wright V.P. (1990) – *Carbonate sedimentology*. Blackwell Science, 496 p. ISBN: 978-0-632-01472-9.
- Veniale F., Setti M., and Tortelli M. (1987) – *Influenza delle procedure sui preparati di “polveri” per analisi diffrattometrica RX*. Atti Workshop Procedure di analisi di materiali argillosi, ENEA, S. Teresa, 1-2 giugno, 135-179.
- Vola G. and Sarandrea L. (2013) – *Raw materials characterization for industrial lime*

manufacturing. ZKG International - Cement Lime Gypsum, 66:5, 62-70.

- Vola G., and Sarandrea L. (2014) – *Investigating and predicting blockages*. World Cement, October 2014, 85-92.
- Vola G., and Sarandrea L. (2015) – *Investigation and prediction of marble mechanical degradation and dust formation during calcination process in Twin Shaft Regenerative (TSR) kilns*. Cement International, 3:13, 42-47.
- Vola G, Sarandrea L, Della Porta G, Cavallo A, Jadoul F, and Cruciani G. (2017) – *The influence of petrography, mineralogy and chemistry on burnability and reactivity of quicklime produced in Twin Shaft Regenerative (TSR) kilns from Neoarchean limestone (Transvaal Supergroup, South Africa)*. Miner Petrol., <https://doi.org/10.1007/s00710-017-0542-y>
- Vola G., Bresciani P., Rodeghero E., Sarandrea L., and Cruciani G. (2018) – *Impact of rock fabric, thermal behavior, and carbonate decomposition kinetics on quicklime industrial production and slaking reactivity*. Journal of Thermal Analysis and Calorimetry, <https://doi.org/10.1007/s10973-018-7769-7>
- UNI EN 459-1 (2010) - *Building lime – Part 1: Definitions, specifications and conformity criteria*. CEN/TC 51, 86p.
- UNI EN 459-2 (2010) – *Building lime – Part 2: Tests methods*. CEN/TC 51, 116p.
- Young R.A. (ed.) (1993) – *The Rietveld method*. IUCr, Monograph on Crystallography, No. 5, Oxford University Press, 298 p. ISBN 0–19–855577–6.

3 RESULTS AND DISCUSSION

3.1 Premise

The present chapter, excluding the present paragraph, reports 4 scientific articles. The first two were recently published; the third one was recently submitted on a peer-reviewed international scientific journal. Finally, the last one is going to be finalized for publication in the early future (see Tab.3.1). The title of each paragraph reflects the corresponding study as published or as communicated to the journal during submission process. Part of these studies could result rearranged in the text order and form, or implemented with further data for more exhaustive description. On the other hand, the scientific meaning of the content will be maintained and no data variation will be applied. In order to avoid redundant part (e.g. in some cases the experimental methodologies could be very similar), test and methods paragraphs were condensed in a general one (see the Chapter 2), specifying any difference case after case. Further indications, when necessary, will be given.

Tab.3.1 – Reference to articles presented in this chapter

Article	Journal	State-of-the-Art
no.1	published on: Mineralogy and Petrology	https://doi.org/10.1007/s00710-017-0542-y
no.2	published on: Journal of Thermal Analysis and Calorimetry	https://doi.org/10.1007/s10973-018-7769-7
no.3	recently submitted to: Construction & Building Materials	under revision
no.4	paper has not been submitted yet	to be finalized for submission

3.2 Article no. 1. The influence of petrography, mineralogy and chemistry on burnability and reactivity of quicklime produced in Twin Shaft Regenerative (TSR) kilns from Neoproterozoic limestone (Transvaal Supergroup, South Africa)

This work was written in 2017 by G. Vola, L. Sarandrea, G. Della Porta, A. Cavallo, F. Jadoul, and G. Cruciani. The paper is reported with the addition of a paragraph dedicated to the Economic Significance, which allows contextualizing this specific case-study. Some unpublished micrographs and relative petrographic analyses are reported too (see Fig.3.4 and Fig.3.5).

3.2.9 Abstract

This study evaluates the influence of chemical, mineralogical and petrographic features of the Neoproterozoic limestone from the Ouplaas Mine (Griqualand West, South Africa) on its burnability and quicklime reactivity, considering the main use as raw material for high-grade lime production in twin shaft regenerative (TSR) kilns. This limestone consists of laminated clotted peloidal micrite and fenestrate microbial boundstone with herringbone calcite and organic carbon (kerogen) within stylolites. Diagenetic modifications include hypidiotopic dolomite, micrite to microsparite recrystallization, stylolites, poikilotopic calcite, chert and saddle dolomite replacements. Burning and technical tests widely attest that the Neoproterozoic limestone is sensitive to high temperature, showing an unusual and drastically pronounced sintering or overburning tendency. The slaking reactivity, according to EN 459-2 (2010) is high for lime burnt at 1050 °C, but rapidly decreases for lime burnt at 1150 °C. The predominant micritic microbial textures, coupled with the organic carbon, are key-factors influencing the low burnability and the high sintering tendency. The presence of burial cementation, especially poikilotopic calcite, seems to promote higher burnability, either in terms of starting calcination temperature, or in terms of higher carbonate dissociation rate. In fact, the highest calcination velocity determined by thermal analysis is consistent with the highest slaking reactivity of the lower stratum of the quarry, enriched in poikilotopic calcite. Secondly, locally concentrated dolomitic marly limestones, and sporadic black shales negatively affect the quicklime reactivity, as well. This study confirms that a multidisciplinary analytical approach is essential for selecting the best raw mix for achieving the highest lime reactivity in TSR kilns.

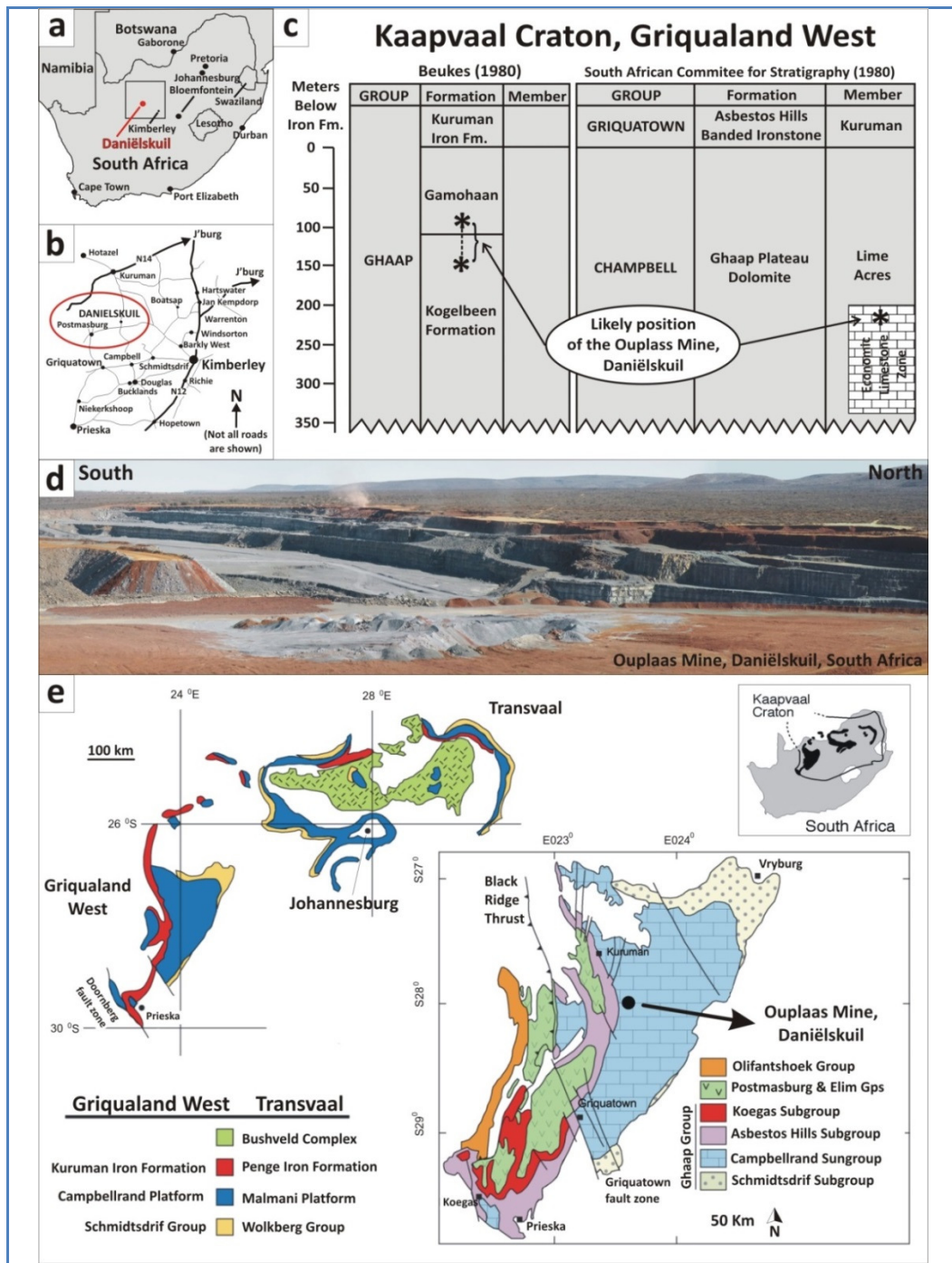


Fig.3.1 a-b = Location of the investigated Ouplaas Mine. c = Simplified stratigraphic columns for a portion of the Transvaal Supergroup of the Kaapvaal Craton in the Griqualand West Basin, according to Beukes (1980) and SACS (1980) (modified after Altermann and Schopf, 1995). d = Landscape photograph of bench 4P and 4S of the Ouplaas Mine. e Simplified geological map of the Kaapvaal Craton, showing the Late Archean Transvaal Supergroup, broadly divided into two structural sub-basins. The inset contains a detailed close-up map of the stratigraphic units in Griqualand West, South Africa. Modified after Paris et al. (2014) in Vola et al. (2017).

3.2.10 Introduction

This research investigates the influence of texture, microstructure, mineralogy, and bulk rock chemistry of Neoproterozoic limestone (Transvaal Supergroup, South Africa) on its thermal behavior and burnability for the production of industrial high reactive quicklime. The traditional calcination models for rotary and vertical shaft kilns (Boynton, 1982; Cheng and Specht, 2006) have recently been revisited. These revised calcination processes take into account not only the carbonate chemistry and mineralogy (Marinoni et al., 2012), but also the effect of the limestone microfacies and microstructure, resulting from depositional processes and early to late diagenetic modifications (Moropoulou et al., 2001; Kiliç and Mesut, 2006; Hughes and Corrigan, 2009; Vola and Sarandrea, 2013; Marinoni et al., 2015). Studies on mud-supported and grain-supported limestones from Egypt (Soltan, 2009; Soltan et al., 2011, 2012) and the United Arab Emirates (Alaabed et al., 2014) demonstrated the impact of different microfacies types and their related open porosity, on the quality of the high-calcium lime, as well as, other compositional and process parameters. The limestone microstructure plays a key role in controlling the calcination activation energy (Soltan and Serry, 2011; Marinoni et al., 2015). Other recent and important studies treat the influence of mineralogy, petrography and microstructure on the thermal decomposition of limestone used for the Portland cement clinker production (Marinoni et al., 2015; Galimberti et al., 2016).

The main goal of this study is to present an industrial case study, by investigating issues related to reaching the target quality of the lime product in Twin Shaft Regenerative (TSR) kilns. Furthermore, this study also attempts to improve the knowledge on burnability and lime reactivity of an ancient microbial limestone, affected by exceptionally long and pervasive diagenesis, and showing an unusual heating behavior with a low burnability associated with an evident sintering tendency at 1150°C.

The Lime Operation at Ouplaas Mine, near Daniëlskuil in the Northern Cape Province, South Africa (Fig.3.1), entails the mining of high-grade calcium carbonate of Neoproterozoic age, crushing, screening, burning, and milling in the production of limestone aggregate, filler, and burnt lime, as well as a hydration facility for the production of slaked lime. Idwala Lime commissioned in 2011 two modern energy efficient Cimprogetti's double TSR kilns with a capacity of 550 tons per day (TPD). The first kiln (K9) was erected in September 2013, and the second (K10) in February 2014. Significant issues were identified during the kiln start-up in the early stage of production and regarded either the low reactivity, or the high residual CO₂ content of the lime. Moreover, lumps of burnt lime observed at the discharging drawers of the kiln presented an evident variability of color, ranging from light

Chapter 3. Results and Discussion

brown (5YR 6/4) to pale brown (5YR 5/2), and medium dark gray (N4), according to the Geological Munsell Rock-color chart (Tab.3.2). Primarily, the color inhomogeneity was explained as due to different oxidation states, namely significant inhomogeneous distribution of the heat flow within the kiln section, because of the different residual CO₂ content. Secondary, the visual inspection of limestone aggregates transported over the conveyor belt to the stockpile allowed identifying at least two or three main different lithofacies types, which could affect the final quality of the lime. During the six-month period of the commissioning phase, different process parameters were controlled, and the production of both kilns was stabilized. The target of a low residual CO₂ content (<2%) was easily matched; on the contrary the slaking reactivity did not reach the expected ($t_{60} < 2$ min), according to the EN 459-2 standard test method (Tab.3.2).

Tab.3.2 – Results of preliminary tests performed on burnt lime samples from the industrial plant (after Vola and Sarandrea 2014). Symbols legend: NR = t_{60} not reached

Burnt state	Unit	Soft	Medium	Hard
Munsell Rock-color		Light brown	Pale brown	Medium dark gray
Residual CO ₂	wt%	2.8	1.7	1.3
Reactivity (t_{60})	min.	1.01	11.43	NR
Reactivity (T_{max})	°C	70.00	61.6	41.7
Available Lime index	wt%	94.5	92.9	89.7
BET Specific Surface Area	m ² /g	4.0	1.4	0.35
Mercury Intrusion Porosity	wt%	47.62	41.89	32.18
Average pore radius	µm	0.31	0.52	1.33

Hence, limestone samples from two different benches of the mine, namely 2P, 4P and 4S, were sampled by the client and sent to Cimprogetti laboratory, to evaluate their compositional, i.e. chemical and mineralogical, microstructural and petrographic features, the thermal behavior, and the burnability at different temperatures, to simulate different combustion conditions in TSR kilns. Data collection described the unusual burnability of the Neoproterozoic limestone, and allowed identifying its sintering or overburning tendency, which seems to be controlled by the pervasive micrite/microsparite distribution within the primary microbial carbonate texture combined with the presence of abundant organic carbon (kerogen), which also burns during the calcination process.

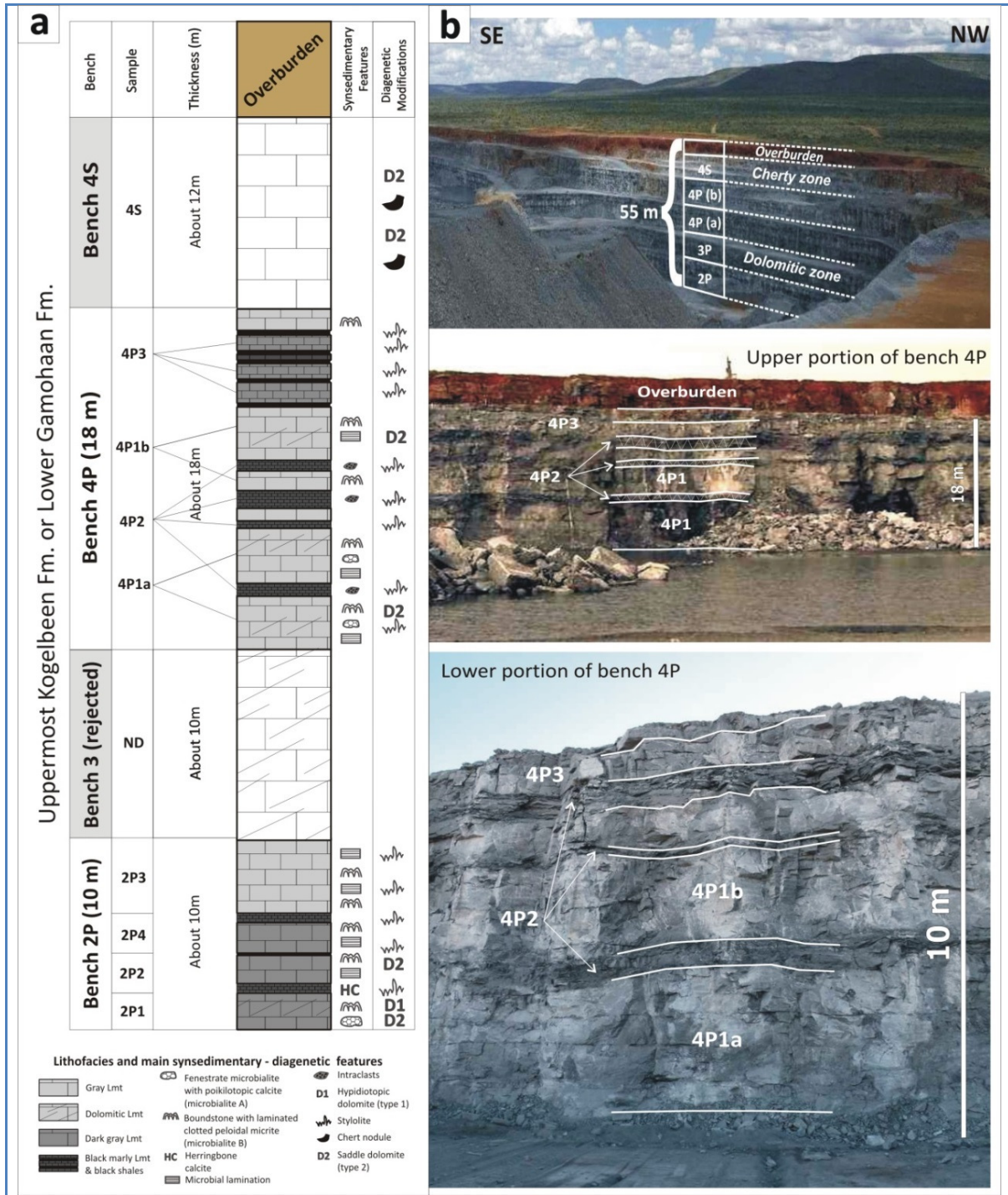


Fig.3.2: a = Stratigraphic log of the Ouplass Mine, Daniëlskuil, Griqualand West, South Africa with location of the analyzed samples. b = Different landscapes of the mine with line drawing of stratigraphy. Five vertically superimposed benches are recognized, namely 2P, 3P, 4Pa, 4Pb, and 4S. Only benches 2P and 4P feed to stockpiles for the production of lime. Bench 3P is mined but rejected, probably because mainly dolomitic in composition. The top bench 4S is strongly silicified and belongs to the “cherty zone”, which goes to optical sorting plant and is partially recovered for feeding to the stockpile. The overburden of this deposit is brownish colored. . From Vola et al. (2017)

Moreover, the uneven distribution of non-carbonate impurity, essentially clay minerals and pyrite, negatively affects the reactivity and the available lime index.

Taking into account the mine stratigraphy (Fig.3.2) and the lime reactivity of different strata, it was possible to calculate the average weighted reactivity of each bench and, subsequently, the expected reactivity of different raw mixes feeding to the kilns. This multidisciplinary research demonstrates that the judicious selection of raw materials from the mine significantly improves the quality control of the quicklime production and that it is good practice selecting the best raw mix to feed to stockpiles and kilns. This step must be considered of primary importance, as well as the fine tuning of different process parameters (see Vola and Sarandrea, 2014).

3.2.11 Geological Setting

The limestone quarried at the Ouplaas Mine in Daniëlsskuil, Griqualand West, northern Cape Province, South Africa, belongs to the “Economic Limestone Zone” of the Lime Acres Member of the Ghaap Plateau Dolomite Fm. according to SACS (1980), whereas according to Beukes (1980) this limestone represents the uppermost part of the Kogelbeen Fm. / the lower part of the Gamohaam Fm. The Ouplaas Mine limestone is part of the Neoproterozoic Campbellrand-Malmani platform, which represents one of the oldest carbonate shelves (2521 ± 3 Ma according to Sumner and Bowring 1996) with microbialites and stromatolites preserved worldwide (Grotzinger, 1989; Grotzinger and James, 2000). The Campbell Group carbonates are host to many economically important mineral deposits in the Northern Cape Province (Altermann and Wotherspoon, 1995). The eastern part of the platform is traditionally called Transvaal Basin, whereas the western part is called Griqualand West Basin (Fig.3.1).

From a structural point of view, the Campbellrand-Malmani carbonate platform (Fig. 3.1e) is extremely well preserved. Undated tectonic events are limited to gentle warping over most of the craton with locally steeper dips around the Bushveld Complex in the North and to intense folding and faulting in the Kheis Belt and Doringberg Fault Zone, which is coincident with the western boundary of the Kaapvaal craton (Walraven et al., 1990; Sumner, 1995) (Fig.3.1).

Metamorphic overprint did not reach temperatures above 200 °C (Button 1973, Miyano and Beukes, 1984). Most outcrops present sub-greenschist facies metamorphism, but amphibole is locally present due to Bushveld contact in the Malmani Subgroup, and

supergene alteration during late fluid flow produced local Pb-Zn, fluorite, and gold deposits in both the Malmani and Cambellrand subgroups (Sumner and Beukes, 2006).

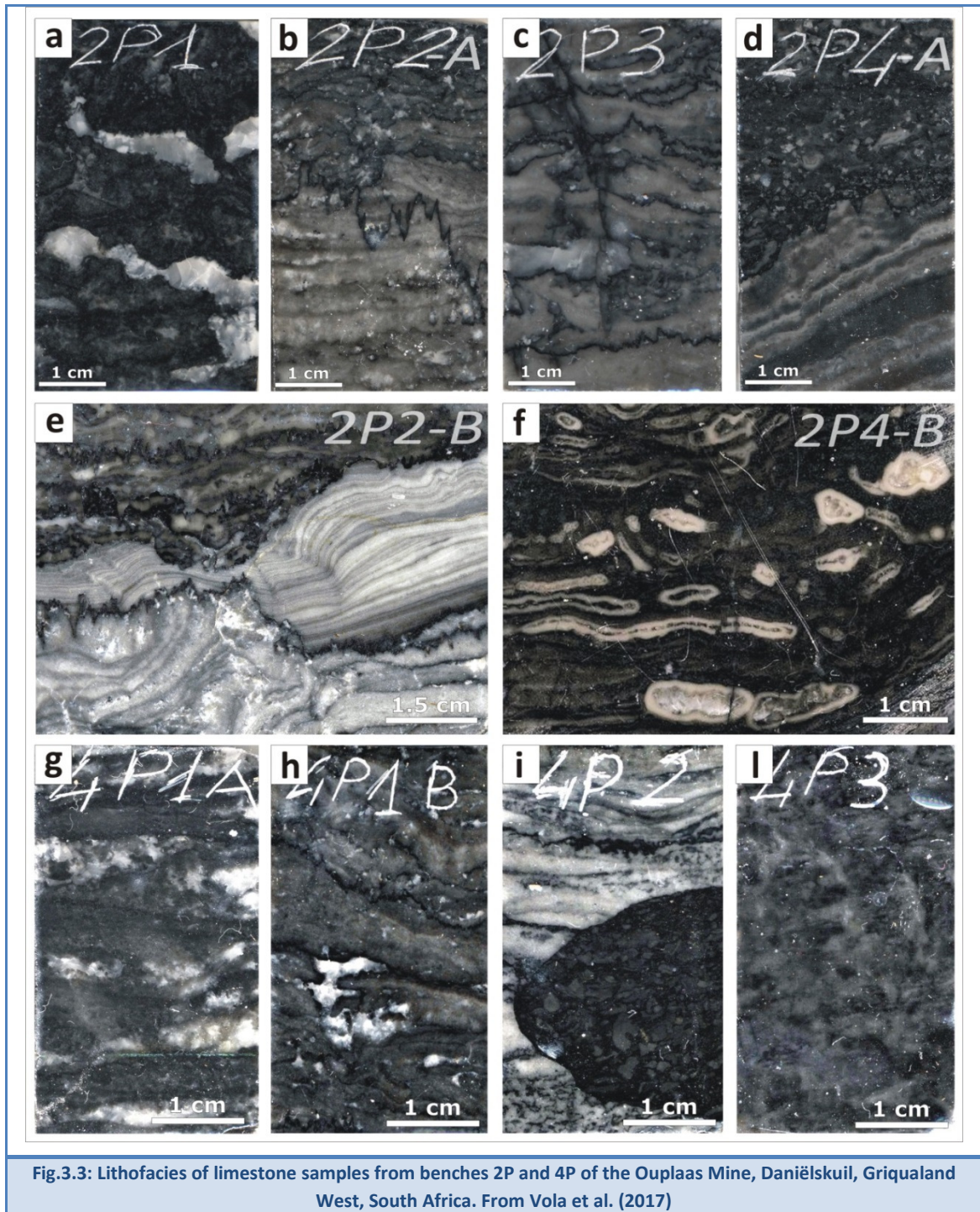
The thickness of the Campbellrand Subgroup carbonates is about 1.5-2 km, with predominantly shallow-water subtidal to peritidal facies in the north and east. Platform slope and basinal deposits are preserved in the south and west (Fig.3.1) and are about 500 m thick (Beukes, 1980, 1987; Sumner 1997a, 1997b). Shallow-water lithofacies include fenestrate microbialites, laminated planar, domal and columnar stromatolites, peloidal packstone to grainstone, and primary radial-fibrous precipitate, i.e. the so-called herringbone calcite (Sumner and Grotzinger, 1996, 2000, 2004). Altermann and Schopf (1995) reported also about filamentous and colonial coccoid microbial fossil assemblage from drill core samples of stromatolite cherty limestones obtained at the Lime Acres.

3.2.12 Economic Significance

The Campbell Group carbonates are host to many economically important mineral deposits in the Northern Cape Province (Altermann and Wotherspoon, 1995). Limestone and dolomite resources of South Africa mainly concentrate in Transvaal and Griqualand West Sequences (Martini, 1987). Mn and Fe mineralization of collapsed karst structures in the Ghaap Group dolomites led to some of the largest mineral deposits of iron and manganese in the world (references in Altermann and Wotherspoon, 1995; see also Gutzmer and Beukes, 1997). The industrial use of limestone and the total production figures for South Africa were described by Badenhorst (1988). The deposits of Chuniespoort Group and of the Ghaap Plateau contribute the largest part of to the 20 MT of annual production. By far the largest consumer of the limestone is the cement industry (Badenhorst, 1988). On the contrary, the Ouplass Mine, located on the Ghaap Plateau in Daniëlsskuil, some 150 km west of Kimberley, is only employed in the manufacture of calcium oxide (CaO) or quicklime. The production of high-grade lime suitable for metallurgic and desulphurization purposes needs a high grade limestone of a much higher quality than for cement manufacture. The lime production of Cimprogetti's TSR kilns is about 360,000 TPD, corresponding to a demand of about 626,000 TPD of limestone. However, the entire demand of limestone from the Union Lime company, which provides virtually all the high grade limestone in South Africa, is about twelve million tons of rock per year (Altermann and Wotherspoon, 1995). The main customers are the gold and uranium mines, the steel industry, and, secondary, the chemical industry.

3.2.13 Materials and Methods

For the experimental details, including sampling, chemical (XRF-WDS, C-S), mineralogical (XRD-QPA), microscopic (OPM, CL, SEM-EDS), and thermal analyses (TG-DTG), plus burning and technical tests, readers are requested to refer to Chapter 2 of the present dissertation.



3.2.14 Results

- *Limestone characterization*

Five main carbonate lithofacies have been distinguished and summarized in Tab.3.4:

- 1) dark gray fenestrate microbial boundstone, slightly dolomitic with fibrous herringbone calcite (microbialite A, sample 2P1; Fig.3.4a-b),
- 2) gray microbial boundstone, slightly dolomitic (samples 2P2, 2P4, and 4P1), with laminated clotted peloidal micrite (microbialite B), sometimes associated with tubular cavity framework (2P4) and subordinated fenestrate microbialite A (Fig.3.4c-d-e-g; Fig.3.5a-b),
- 3) gray marly limestone associated with sporadic black shales made of dolomitic microbial boundstone (microbialite B) with coated grains and characterized by abundant stylolites and solution seams with kerogen and pyrite (samples 2P3 and 4P2; Fig.3.4f; Fig.3.5c-d-e-f),
- 4) dark gray pure limestone (sample 4P3; Fig.3.5g) with centimeter-sized beds of intraclastic packstone to grainstone, peloidal mudstone-wackestone, locally passing into boundstone with laminated clotted peloidal micrite (microbialite B).
- 5) dark gray cherty limestone (sample 4S; Fig.3.5h) with black nodules of replacive chert on coarse neomorphic sparite. This last lithofacies goes to the optical sorting plant and is partially recovered for feeding to the stockpile.

Tab.3.3 – Results of X-Ray Diffraction Quantitative Phase Analysis (XRD-QPA) of limestone samples

Code	Calcite	Dolomite	Quartz	Illite	Chlorite	Pyrite	Plagioclase
2P1	92.8	6.6	0.6	-	-	-	-
2P2	95.8	4.0	0.2	-	-	-	-
2P3	97.9	1.8	0.3	-	-	-	-
2P4a	99.8	0.2	-	-	-	-	-
2P4b	98.4	1.2	0.4	-	-	-	-
2P4c	93.1	5.1	1.7	-	-	-	-
2P4d	94.6	4.6	0.8	-	-	-	-
4P1a	99.1	0.9	-	-	-	-	-
4P1b	99.1	0.9	-	-	-	-	Tr
4P2a	95.2	1.3	1.2	1.6		0.7	-
4P2bs	37.1	2.0	4.8	48.5	3.2	1.8	2.4
4P3	99.7	0.3	-	-	-	-	-

Tab.3.4 – Results of petrographic analysis of limestone samples from bench 2P, 4P and 4S.

Sample	Lithofacies	Components	Diagenetic features	Cathodoluminescence (CL)
2P1	Dark gray, slightly dolomitic fenestrate microbial boundstone (Fig.3.3a) made of clotted peloidal micrite and microsparite crusts supporting fenestrate porosity filled by calcite (microbialite A).	Cm-sized sub-rounded fenestral voids filled by herringbone calcite and equant to poikilotopic calcite cement (Fig.3.4a-b). Dark kerogen soaks microsparite rims.	Herringbone calcite: cloudy radial fibrous banded calcite fans represent the primary marine cement associated with dark microbial laminae. Fenestrate porosity, locally enlarged by dissolution, is filled by equant drusy mosaic and cm-size poikilotopic calcite cement (burial diagenesis). Dolomite (Fig.3.4a) up to 6.5%. Dolomite type 1: hypidiotopic mosaic of subhedral dolomite crystals (100 µm) mimetic to replacive on clotted peloidal micrite (early diagenetic). Dolomite type 2: cloudy rhombohedral crystals (200-500 µm) of saddle dolomite with undulose extinction and etched crystal rims replacive on poikilotopic calcite (burial diagenesis). Stylolites and solution seams due to pressure solution.	The clotted peloidal micrite/microsparite crusts locally present primary non luminescent microbial microstructures (dark peloids and filaments). The equant and the poikilotopic calcites are orange dull, rarely zoned and contain small, non-luminescent crystals of dolomite. The first generation of kerogen soaking the fenestral porosity is opaque under CL, while subsequent generations are orange bright in the CL observation same conditions.
2P2	Gray, slightly dolomitic microbial boundstone (Fig.3.3b) with mm-thick clotted peloidal micrite/microsparite laminae (microbialite B) and herringbone calcite passing into clotted peloidal packstone/grainstone with subordinate fenestrate microbialite A.	Alternation of dark gray micrite/microsparite laminae and light fibrous radial calcite laminae (herringbone calcite) and inferred originally aragonitic botryoidal fans. Matrix of micrite to microsparite with peloidal remnants. Microsparite and sparite range in size from 20 microns to 200 µm but mean size is 60-100 µm. Fenestrae with equant or poikilotopic calcite and impregnated by different films of opaque organic carbon (Fig.3.4c)	Neomorphic microsparite and sparite due to recrystallization of micrite. Fabric-replacive hypidiotopic dolomite (type 1). Submm-sized rhombohedral dolomite crystals (type 2) postdate the mm-size poikilotopic calcite cement in horizontal voids. Stylolites with organic carbon (kerogen) are often associated with partial dolomitization and recrystallization. Few scattered low to high amplitude black stylolites associated with brownish type 2 saddle dolomite.	Equant and poikilotopic calcite are orange with a few dull/bright zonation and a late, thin yellow growth phase. Non luminescent dolomite crystals are locally crossed by black stylolites. The first thin film of kerogen is generally non luminescent conversely, subsequent layers are orange bright luminescent under the same optical conditions.
2P3	Gray laminated microbial boundstone (microbialite B; Fig.3.3c) with subordinate fenestrate microbialite A, associated with marls and black shales. Locally coated grain and peloidal packstone/grainstone.	Micrite and neomorphic microsparite (30-50 µm) form the clotted peloidal micrite. Cloudy radial fibrous banded calcite fans (herringbone calcite). Cavities filled by equant and poikilotopic calcite (100-200 µm) (Fig.3.4f).	Neomorphic microsparite and sparite due to recrystallization of micrite. A few tensional fractures with equant and poikilotopic calcite are cut by late stylolites.	Clotted pelodal micrite to microsparite microbial laminae present well recognizable, non-luminescent small peloids. Equant calcite in small cavities is orange and poorly zoned.
2P4	Gray microbial boundstone (microbialite B) with tubular cavity framework with subordinate fenestrate microbialite A and peloidal intraclastic packstone/grainstone (Fig.3.3d-f).	Tubular structures (possible microfossils; Fig. 4g). Cavity filling is represented by a thin dark micrite rim, not recrystallized, and then by two calcite cements: the first fibrous radial, the second equant calcite, often postdated by poikilotopic calcite.	Recrystallization of the microbial micrite into microsparite to sparite. Cavities are filled by kerogen, which soaked along stylolites after the pressure solution. Different cement generations, possibly related to late diagenetic fluids. Frequent fluid inclusions (along twinning) in the poikilotopic calcite.	In the clotted peloidal microsparite peloids are recognizable because non luminescent. A few poikilotopic calcite crystals present preserved microbial microstructures.

Table 3.4 (continue) – Results of petrographic analysis of limestone samples from bench 4P and 4S.

Sample	Lithofacies	Components	Diagenetic features	Cathodoluminescence (CL)
4P1	Gray laminated microbial boundstone (microbialite B; Fig.3.3g-h) passing into peloidal packstone/grainstone with subordinate fenestrate microbialite A.	Clotted peloidal micrite laminae and fenestral voids filled by cement.	Neomorphic microsparite over clotted peloidal micrite. Large fenestrae filled by equant and poikilotopic calcite. Frequent late diagenetic stylolites cut all the other diagenetic features.	The equant and poikilotopic calcites are orange dull, rarely zoned and contain small, non-luminescent crystals of dolomite. Clotted peloidal microsparite presents well-preserved, non-luminescent small peloids.
4P2	Gray dolomitic marly microbial boundstone (microbialite B) forming spheroidal or domal stromatolites with dark lamination, white bands (herringbone calcite), and cm-size intraclasts of peloidal grainstone (Fig.3.3i), associated with black shales (Fig.3.5c-d).	Cm-sized nodules composed of sub-spherical grains of recrystallized dark gray peloidal and microbial micrite. Cloudy radial fibrous banded calcite fans (herringbone calcite)	Radial fibrous herringbone calcite and the recrystallized neomorphic coarse sparite. Coarse sparite postdates stylolites. Abundant low to medium amplitude black kerogen and pyrite-enriched stylolites and solution seams in shales.	Patches of well-preserved peloidal clotted micrite associated with equant and poikilotopic calcite. Many stylolites with black non-luminescent opaque minerals and kerogen (orange luminescent) (Fig.3.5c-d).
4P3	Dark gray to black laminated mudstone-wackestone to packstone/grainstone with peloids, intraclasts and areas of microbial boundstone (microbialite B; Fig.3.3l).	Lack of poikilotopic calcite. Peloidal packstone/grainstone associated with neomorphic sparite.	Clotted peloidal micrite and microsparite (Fig.3.5g) with intergranular cementation, small primary fenestral cavities. No solution seams and stylolites.	More homogenous clotted peloidal orange luminescent microsparite with preserved non-luminescent peloids. Small primary intergranular cavities filled by orange, poorly zoned equant calcite.
4S	Cherty limestone (Fig.3.5h) made of coarse sparite with microcrystalline quartz and superimposed rhombohedral dolomite.	Chert and neomorphic sparite over probably clotted peloidal micrite and microsparite.	Chert replacement on coarse neomorphic sparite. Dolomite (type 2, saddle dolomite during burial diagenesis) postdates silicification.	

High-grade burnt lime products: impact of calcination kinetics on slaking reactivity; sticking tendency and blocks formation at HT (1300°C)

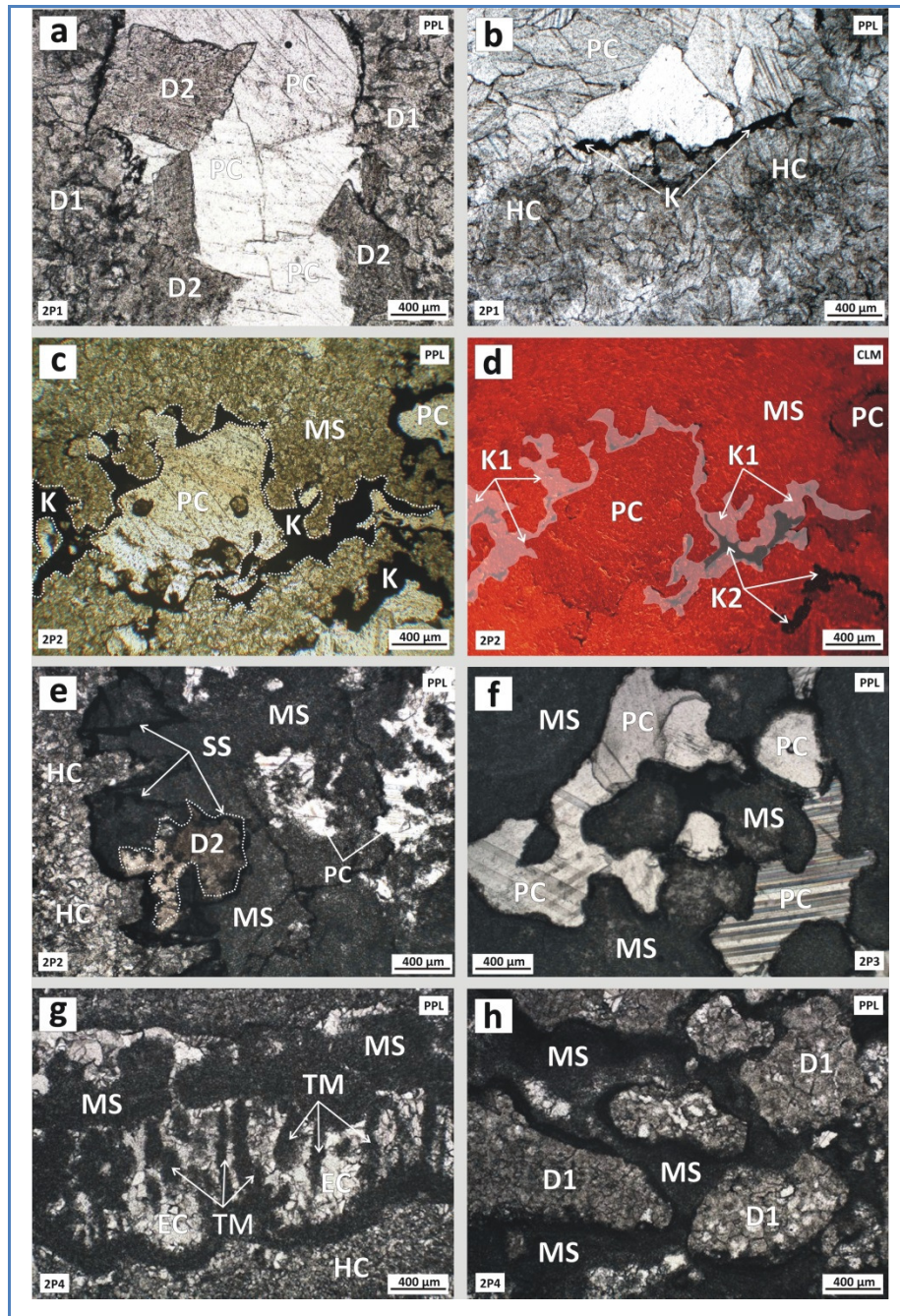


Fig.3.4: Petrographic and cathodoluminescence analysis of limestone samples from bench 2P of the Ouplaas Mine. a = Fenestrate microbialite (microbialite A) with centimeter size fenestrate voids filled by clear and twinned poikilotopic calcite associated with hypidiotopic dolomite (type 1) and late burial brownish saddle dolomite (type 2) and (2P1). b = Cloudy radial fibrous marine precipitate, i.e. herringbone calcite (2P1). c-d = Laminated clotted peloidal micrite (microbialite B) cut by stylolites enriched by two kerogen generations (2P2). e = Laminated clotted peloidal micrite and dark gray radial fibrous calcitic laminae of herringbone calcite cut by stylolites associated with late diagenetic brownish saddle dolomite (type 2) (2P2). f = Fenestrate microbialite with poikilotopic calcite and clotted peloidal micrite (2P3). g = Tubular framework structures (2P4). h = Dolomitized peloidal coated grains coated by dark microbial laminations (2P4). Symbols legend: PPL = plane polarized light; XPL = crossed polarized light; CL = cathodoluminescence microscopy. TM = tubular microbial framework. Main diagenetic features: EQ = equant calcite, HC = herringbone calcite. D1 = hypidiotopic mimetic or fabric-replacive dolomite (type 1), SS = stylolites and solution seams, K = carbon black (kerogen) segregation, K1 = kerogen bright luminescent under CL, K2 = kerogen non-luminescent under CL, MS = microsparite, PC = poikilotopic calcite, D2 = saddle brownish dolomite replacement (type 2).

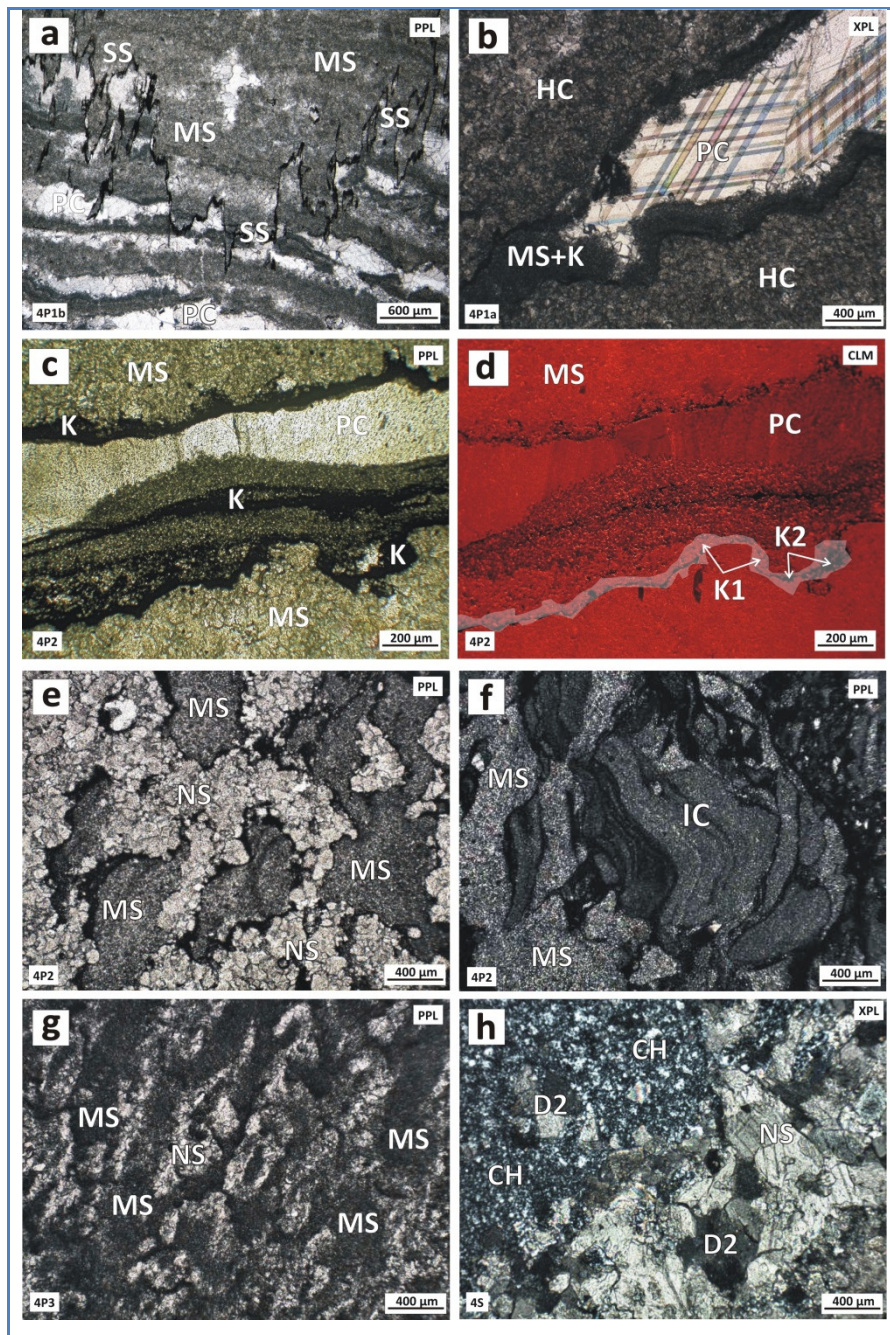


Fig.3.5: Petrographic and cathodoluminescence analysis of limestone samples from bench 4P of the Ouplaas Mine. a-b = Laminated peloidal micrite/microsparite associated with syndepositional voids filled by clear and twinned poikilotopic calcite (4P1a, 4P1b). c-d = Enlarged cavity with different layers of microsparite, thin layers of kerogen associated with stylolites, and poikilotopic calcite (4P2). Kerogen segregation on the rims (4P2). e = Clotted peloidal micrite/microsparite associated with kerogen-bearing black stylolites and plaques of recrystallized neomorphic coarse sparite. This neomorphic sparite probably represents the final late diagenetic event after compaction and kerogen migration-segregation (4P2). f = Dark gray to black intraclastic nodule composed of peloidal micrite/microsparite and microbial coated grains with dark kerogen-bearing rims (4P2). g = Laminated clotted peloidal micrite and microsparite (4P3). h = Chert replacement on coarse sparite is superimposed by burial saddle dolomite (4S). IC = intraclastic nodule. Main diagenetic features: EQ = equant calcite, HC = herringbone calcite, SS = stylolites and solution seams, K = kerogen segregation, K1 = kerogen bright luminescent under CL, K2 = kerogen non-luminescent under CL, MS = microsparite, PC = poikilotopic calcite, NS: neomorphic sparite, CH = chert replacement, D2 = saddle dolomite replacement (type 2).

Tab.3.5 – Results of chemical analysis (XRF and elemental analysis) of limestone samples from the quarry. The carbonate classification is based on Frolova (1959) that considers the CaO/MgO ratio criterion. Symbols legend: SDL = slightly dolomitic limestone; L = pure limestone; SDML = slightly dolomitic marly limestone; ML = marly limestone; BS = black shale; TOT/C = total carbon; TOT/S = total sulfur; C/ORG = organic carbon; HI = hydraulic index according to Elsen et al. (2011)

Code	LLD	2P1	2P2	2P3	2P4a	2P4b	2P4c	2P4d	4P1a	4P1b	4P2a	4P2bs	4P3
Class		SDL	L	L	L	L	SDML	SDL	L	L	ML	BS	L
LOI	0.01	43.48	43.7	43.55	43.58	43.32	42.98	43.32	43.67	43.66	42.39	26.46	43.56
SiO ₂	0.01	0.91	0.15	0.43	0.18	0.63	2.04	1.04	0.05	0.09	1.99	29.64	0.02
Al ₂ O ₃	0.01	0.06	0.02	0.11	<0.01	0.06	0.09	0.07	<0.01	<0.01	0.59	11.51	<0.01
Fe ₂ O ₃	0.01	0.16	0.11	0.1	0.07	0.08	0.15	0.14	0.1	0.09	0.29	2.31	0.07
CaO	0.01	53.09	54.53	54.94	55.33	54.85	53.1	54.43	54.87	54.84	53.58	20.28	55.54
MgO	0.01	1.59	0.92	0.44	0.19	0.34	1.23	1.13	0.33	0.38	0.4	1.99	0.17
Na ₂ O	0.01	<0.01	<0.01	<0.01	<0.01	<0.01	<0.01	<0.01	<0.01	<0.01	<0.01	0.08	<0.01
K ₂ O	0.01	<0.01	<0.01	0.02	<0.01	0.01	0.01	<0.01	<0.01	<0.01	0.17	4.02	<0.01
MnO	0.01	0.62	0.67	0.79	0.63	0.62	0.6	0.66	0.71	0.66	0.62	0.14	0.5
SO ₃	0.002	0.057	0.004	0.044	0.006	0.008	0.029	0.019	0.009	0.012	0.368	2.892	0.019
TiO ₂	0.01	0.01	<0.01	0.01	<0.01	0.01	<0.01	0.02	<0.01	0.01	0.03	0.55	<0.01
P ₂ O ₅	0.01	<0.01	<0.01	<0.01	<0.01	<0.01	<0.01	<0.01	<0.01	<0.01	<0.01	0.05	<0.01
Cr ₂ O ₃	0.01	<0.01	<0.01	<0.01	<0.01	<0.01	<0.01	<0.01	<0.01	<0.01	<0.01	0.02	<0.01
Ba	0.01	<0.01	<0.01	<0.01	<0.01	<0.01	<0.01	<0.01	<0.01	<0.01	<0.01	<0.01	<0.01
Cu	0.001	<0.001	<0.001	<0.001	<0.001	<0.001	<0.001	0.002	<0.001	<0.001	0.002	0.005	<0.001
Ni	0.001	<0.001	0.002	<0.001	<0.001	<0.001	<0.001	<0.001	<0.001	<0.001	<0.001	0.006	<0.001
Pb	0.001	0.003	0.002	<0.001	0.004	<0.001	0.002	0.002	0.002	0.002	0.002	0.004	0.002
Sr	0.002	<0.002	0.003	0.002	<0.002	0.002	0.003	0.003	0.003	0.003	0.003	0.002	<0.002
V ₂ O ₅	0.002	<0.002	0.003	0.002	<0.002	<0.002	0.003	<0.002	<0.002	<0.002	<0.002	0.016	<0.002
Zn	0.001	<0.001	<0.001	<0.001	<0.001	<0.001	<0.001	<0.001	<0.001	<0.001	<0.001	0.001	<0.001
Zr	0.002	<0.002	<0.002	<0.002	<0.002	<0.002	<0.002	<0.002	<0.002	<0.002	<0.002	0.008	<0.002
SUM	-	100.0	100.1	100.4	100.0	99.9	100.2	100.8	99.7	99.7	100.4	99.9	99.9
TOT/C	0.02	12.51	12.43	12.41	12.33	12.75	12.28	12.48	12.81	12.46	12.54	14.26	12.64
TOT/S	0.02	0.03	<0.02	<0.02	<0.02	<0.02	<0.02	<0.02	<0.02	<0.02	0.2	1.68	<0.02
C/ORG	0.02	0.59	0.75	0.75	0.64	1.27	1.26	1.0	1.17	1.02	1.33	1.13	0.89
CaO/MgO	-	33.4	59.3	124.9	291.2	161.3	43.2	48.2	166.3	144.3	134.0	10.19	326.7
HI	-	1.6	0.9	0.5	0.2	0.4	1.3	1.2	0.3	0.4	0.5	-	0.2

Tab.3.6 – Results of chemical analysis (XRF and elemental analysis) on burnt lime samples at 1050 °C (normalized). Symbols legend: TOT/C = total carbon; TOT/S = total sulfur.

Code	LLD	2P1	2P2	2P3	2P4	4P1b	4P2a	4P2b	4P3
SiO ₂	0.01	1.22	0.25	2.4	1.4	0.17	1.69	2.21	0.07
Al ₂ O ₃	0.01	0.10	0.03	0.8	<0.01	0.03	0.43	0.66	0.03
Fe ₂ O ₃	0.01	0.40	0.19	0.3	0.2	0.15	1.17	1.89	0.14
CaO	0.01	93.11	96.88	93.6	96.0	98.35	89.36	81.91	99.75
MgO	0.01	4.43	1.43	1.1	1.2	0.61	6.02	11.46	0.29
Na ₂ O	0.01	<0.01	0.01	<0.01	<0.01	<0.01	<0.01	<0.01	<0.01
K ₂ O	0.01	0.01	<0.01	0.2	<0.01	<0.01	0.08	0.15	<0.01
MnO	0.01	1.16	1.17	1.4	1.1	1.19	1.36	1.54	1.08
TiO ₂	0.01	0.01	0.02	<0.01	<0.01	0.01	0.03	0.04	0.01
SO ₃	0.002	0.10	0.02	0.3	0.1	0.16	0.44	0.33	0.01
Sr	0.002	<0.01	0.01	<0.01	<0.01	0.01	0.01	<0.01	<0.01
SUM	-	100.5	100.0	100.2	100.0	100.7	100.6	100.2	101.4
TOT/C	0.02	0.19	0.21	0.15	0.26	0.19	0.2	0.14	0.21
TOT/S	0.02	0.07	0.03	0.12	0.03	0.02	0.11	0.1	0.02

Tab.3.7 – Results of chemical analysis (XRF and elemental analysis) on burnt lime samples at 1150 °C (normalized). Symbols legend: TOT/C = total carbon; TOT/S = total sulfur.

Code	LLD	2P1a	2P1b	2P2	2P3	2P4	4P1b	4P2a	4P2b	4P3a	4P3b
SiO ₂	0.01	0.61	1.39	0.17	2.06	1.18	0.04	1.51	2.21	0.07	0.10
Al ₂ O ₃	0.01	0.06	0.07	0.02	0.65	0.02	<0.01	0.43	0.90	0.04	0.05
Fe ₂ O ₃	0.01	0.24	0.34	0.13	0.30	0.13	0.18	0.72	1.66	0.17	0.17
CaO	0.01	95.9	94.7	98.3	94.5	97.6	98.1	92.7	82.7	98.0	98.5
MgO	0.01	2.52	2.84	0.79	1.08	0.40	0.54	3.19	10.52	0.36	0.32
Na ₂ O	0.01	<0.01	<0.01	<0.01	0.01	<0.01	<0.01	0.07	<0.01	<0.01	<0.01
K ₂ O	0.01	<0.01	<0.01	<0.01	0.14	<0.01	<0.01	0.08	0.20	<0.01	<0.01
MnO	0.01	1.09	1.09	1.17	1.42	1.13	1.18	1.26	1.41	1.02	0.92
TiO ₂	0.01	0.01	0.02	<0.01	0.03	0.02	0.02	0.02	0.06	<0.01	0.03
SO ₃	0.002	0.04	0.14	<0.01	0.08	0.01	0.09	0.29	0.41	0.08	0.07
Sr	0.002	<0.01	<0.01	<0.01	<0.01	<0.01	<0.01	<0.01	<0.01	<0.01	<0.01
SUM	-	100.5	100.6	100.5	100.3	100.5	100.2	100.3	100.1	99.7	100.2
TOT/C	0.02	0.19	0.16	0.12	0.12	0.13	0.1	0.14	0.1	0.1	0.12
TOT/S	0.02	0.03	0.04	<0.02	0.03	<0.02	<0.02	0.09	0.14	0.04	0.03

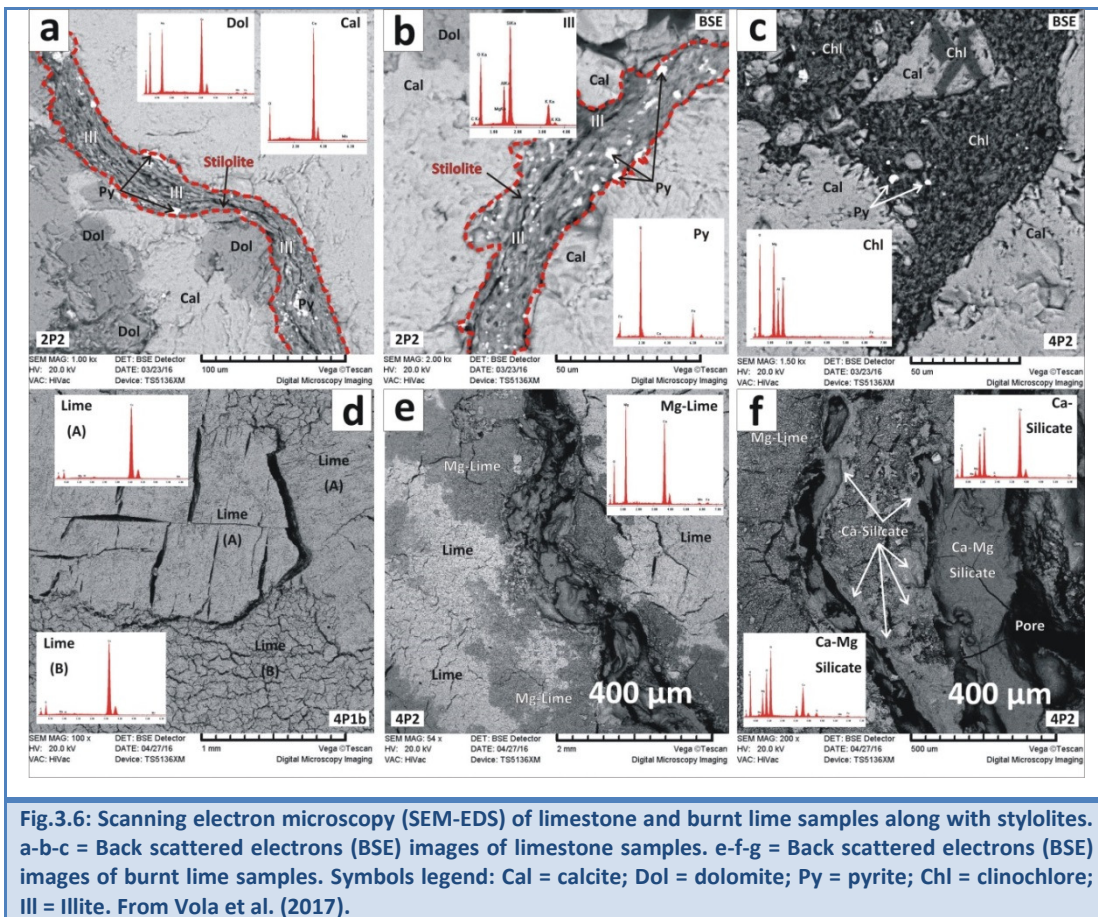
Tab.3.8 – Results of X-Ray Diffraction Quantitative Phase Analysis (XRD-QPA) of limestone samples.

Symbols legend: fundamental mineral phases, Cal = Calcite; Dol = Dolomite; Qtz = Quartz; subordinated mineral phases: Ill = Illite; Chl = Cinchlore; Py = Pyrite; Pl = plagioclase.

Code	2P1	2P2	2P3	2P4a	2P4b	2P4c	2P4d	4P1a	4P1b	4P2a	4P2bs	4P3
Cal	92.8	95.8	97.9	99.8	98.4	93.1	94.6	99.1	99.1	95.2	37.1	99.7
Dol	6.6	4.0	1.8	0.2	1.2	5.1	4.6	0.9	0.9	1.3	2.0	0.3
Qtz	0.6	0.2	0.3	0.0	0.4	1.7	0.8	0.0	0.0	1.2	4.8	-
Ill	-	-	-	-	-	-	-	-	-	1.6	48.5	-
Chl	-	-	-	-	-	-	-	-	-	-	3.2	-
Py	-	-	-	-	-	-	-	-	-	0.7	1.8	-
Pl	-	-	-	-	-	-	-	-	Tr	-	2.4	-

These microfacies include various diagenetic features such as: radial fibrous banded cement, i.e. the herringbone calcite (cf. Sumner and Grotzinger, 1996, 2004), neomorphic microsparite after recrystallization of micrite, equant drusy and poikilotopic sparite cements, mimetic or fabric-replacive hypidiotopic dolomite (type 1), stylolites and solution seams, organic carbon (kerogen) segregation and impregnation, chert, and saddle dolomite (type 2) (see Fig.3.4 and Fig.3.5). Chemical (XRF-WDS, C-S elemental analysis), and mineralogical (XRD-QPA) analyses attest the presence of subordinated non-carbonate impurity, which is mainly ascribed to clay and opaque minerals. The silica content generally ranges between 0.02 up to 2.04%, but can reach the 30% in sporadic black shales associated with gray dolomitic limestones (cf. sample 4P2bs). The calcite content generally varies between 92% up to 99% on the whole rock, but locally it can be lower, especially within the black shales where calcite is just the 37%. Sample 4P2 present the lowest content of carbonates and the highest content of impurity. Impurities are mainly represented by dolomite (2P1, 2P4), quartz (4P2, 2P3), clay minerals (4P2, 2P3) and pyrite (4P2, 2P4, 4P3), coupled with organic carbon (kerogen). Gray marly limestone samples, namely 2P3 and 4P2, locally present microcrystalline quartz and clay minerals, i.e. illite and chlorite, associated with pyrite and abundant organic carbon. These impurities are particularly concentrated along stylolites.

The SEM-EDS microanalysis confirms the chemical composition of clay minerals (Fig.3.6). Moreover some chemical maps on different limestone samples pointed out the ubiquitous distribution of the manganese oxide, which is probably diffused as microcrystalline braunite within the fine matrix of the whole-rock, reaching the average content of 0.65%.



The thermal analysis (TG-DTG) points out some significant burnability differences between samples from different strata (Tab.3.9; Fig.3.7). The plot A, showing the ignition loss (%) vs. time (s) (Fig.3.7a), permits to extrapolate the calcination velocity (g/s), pointing out the highest velocity for sample 2P1, followed by sample 4P2. Plot B, showing the DTG normalized curve (Fig.3.7b), points out the mass flow ((g/s)/g_{initial}%) as a function of burning temperature (°C). All samples present a single peak of dissociation because they are mainly calcitic in composition. The only exception is sample 4P2, which presents double peaks of dissociation, indicating the presence of a double carbonate, most likely dolomite (Gunasekaran and Anbalagan, 2007). The first peak at lower temperature is due to the dissociation of the magnesium molecule (MgCO₃), with the formation of periclase and calcite, while the second peak at the highest temperature is due to the dissociation of the calcitic molecule (CaCO₃), according to the literature (Boynton, 1982; Emmerich, 2011). The height of the peaks is proportional to the total CO₂ emission. The weight loss (LOI) between 200-600 °C is due to the content of bound water of clay minerals and to the organic carbon (kerogen).

Tab.3.9 – Numerical parameters from thermal analysis (TG-DTG). Symbols legend: t = time; T = temperature

Code	Unit	2P1	2P2	2P3	2P4	4P1a	4P1b	4P2
Starting time (t_1)	min.	58.0	70.6	74.1	70.5	68.3	70.4	55.9
Ending time (t_2)	min.	133.0	149.1	149.6	150.0	138.8	148.4	150.9
Max time (t_{max})	min.	97.0	105.6	112.6	106.5	105.3	108.4	100.4
Δt ($t_2 - t_1$)	min.	75.0	78.5	75.5	79.5	70.5	78.0	95.0
Starting T (T_1)	°C	682.0	752.0	744.0	755.0	728.0	746.0	606.0
Ending T (T_2)	°C	1188.0	1195.5	1194.5	1197.0	1187.0	1194.0	1197.0
Max T (T_{max})	°C	1010.0	1020.0	1038.5	1032.0	1021.0	1026.0	993.0
ΔT ($T_2 - T_1$)	°C	506.0	443.5	450.5	442.0	459.0	448.0	591.0

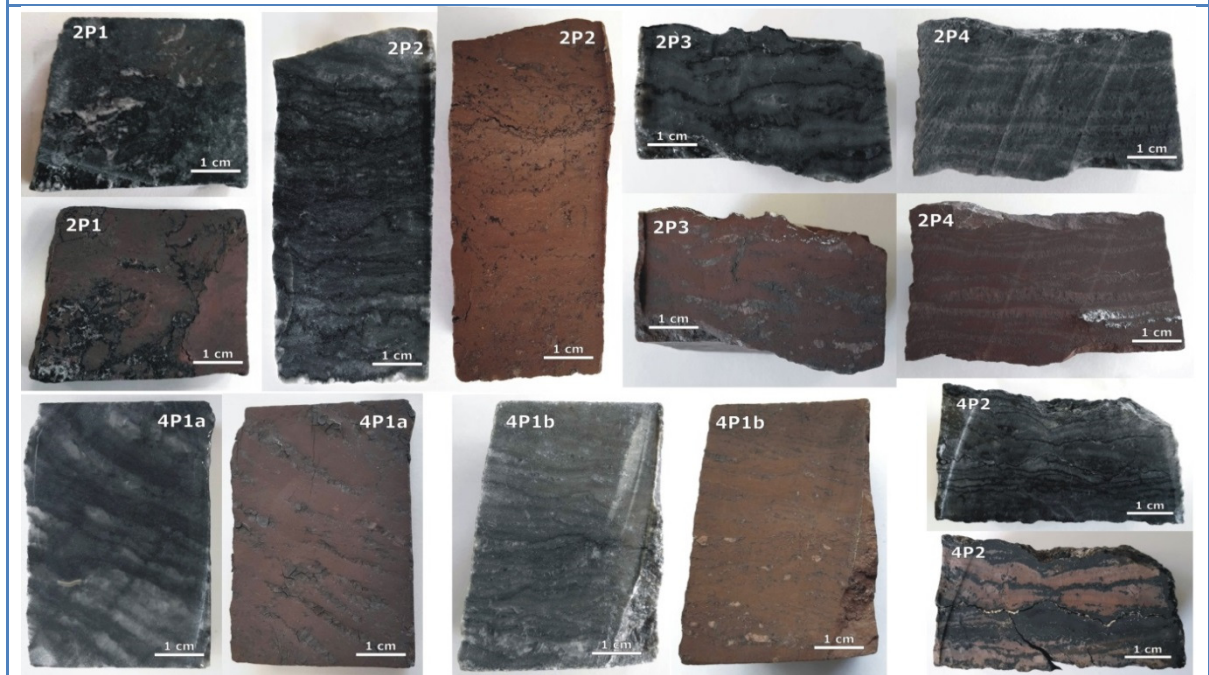
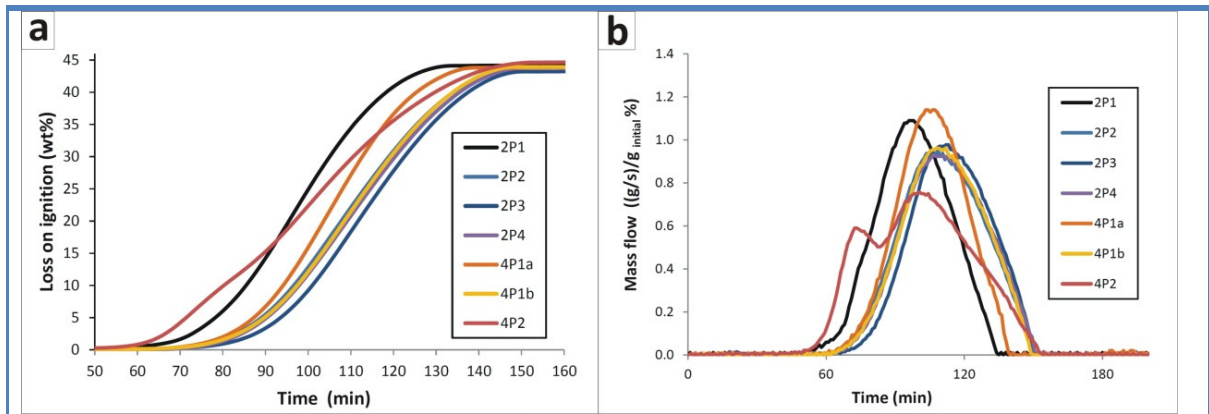


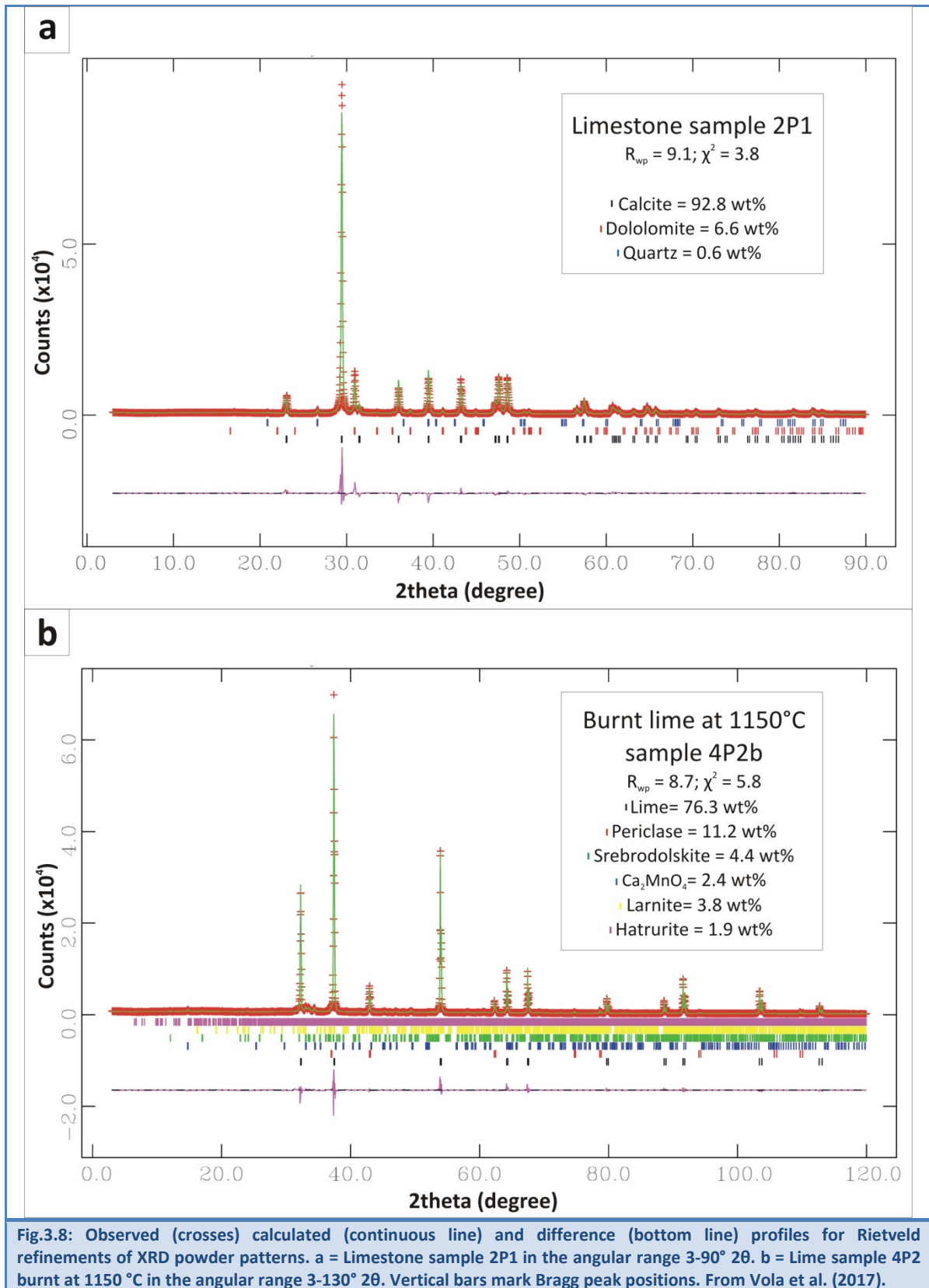
Fig.3.7: Thermal analysis (TG-DTG) of samples from Ouplass Mine by Nabertherm furnace. Plots allow distinguishing calcination duration times. Especially, the sample 4P2 (red line) presents double reaction peaks, pointing out its dolomitic composition, while sample 2P1 (black line) presents the fastest kinetic decomposition. a = Thermogravimetric analysis (TG). b = Differential Thermogravimetric analysis (DTG); c = Macroscopic visual inspection of samples before and after calcination at 1200 °C. Modified from Vola et al. (2017).

Tab.3.10 – Results of X-Ray Diffraction Quantitative Phase Analysis (XRD-QPA) of burnt lime samples at 1050°C. Symbols legend: Per = periclase; Qtz = Quartz; Lar = Larnite (Ca₂SiO₄); Hat = Hatrurite (Ca₃SiO₅); Mer = Merwinite (Ca₃Mg(SiO₄)₂); Al = Tricalcium Aluminate (Ca₃Al₂O₆); Geh = Gehlenite (Ca₂Al(Al,Si)O₇); Sr = Srebrodolskite (Ca₂Fe₃O₅); Man = Dicalcium Manganate (Ca₂MnO₄); Fer = Fersilicide (FeSi); Anh = Anhydrite (CaSO₄); Tr = traces (<0.5%).

Code	T	Lime	Per	Qtz	Lar	Hat	Mer	Al	Geh	Sr	Man	Fer	Anh
	(°C)	(wt.%)	(wt.%)	(wt.%)	(wt.%)	(wt.%)	(wt.%)	(wt.%)	(wt.%)	(wt.%)	(wt.%)	(wt.%)	(wt.%)
2P1	1050	88.5	4.8	1						Tr	6	Tr	Tr
2P2	1050	91.9	1.3				2	0.9		Tr	3.9		Tr
2P3	1050	88.6	0.6		4.1		2.5	Tr			4.2		Tr
2P4	1050	92.6	1.3	0.7	0.9		1				3.5		
4P1b	1050	94.8	0.3								4.9		
4P2a	1050	83.0	6.3	0.7	1.5		2.9		Tr	1.3	4.1		Tr
4P2b	1050	74.6	11.6	Tr	0.9		5.8		Tr	2.9	4		Tr

Tab.3.11 – Results of X-Ray Diffraction Quantitative Phase Analysis (XRD-QPA) of burnt lime samples at 1150°C. Symbols legend: Per = periclase; Qtz = Quartz; Lar = Larnite (Ca₂SiO₄); Hat = Hatrurite (Ca₃SiO₅); Mer = Merwinite (Ca₃Mg(SiO₄)₂); Al = Tricalcium Aluminate (Ca₃Al₂O₆); Geh = Gehlenite (Ca₂Al(Al,Si)O₇); Sr = Srebrodolskite (Ca₂Fe₃O₅); Man = Dicalcium Manganate (Ca₂MnO₄); Fer = Fersilicide (FeSi); Anh = Anhydrite (CaSO₄); Tr = traces (<0.5%).

Code	T	Lime	Per	Qtz	Lar	Hat	Mer	Al	Geh	Sr	Man	Fer	Anh
	(°C)	(wt.%)	(wt.%)	(wt.%)	(wt.%)	(wt.%)	(wt.%)	(wt.%)	(wt.%)	(wt.%)	(wt.%)	(wt.%)	(wt.%)
4P3	1050	94.8	0.6		0.5						4		
2P1a	1150	92.5	2.5					0.7			4.4	Tr	Tr
2P1b	1150	88.8	2.7	Tr	0.5	0.8	3.3				3.5	Tr	
2P2	1150	95.0	0.3					0.5			4	Tr	Tr
2P3	1150	89.7	Tr		2.2		Tr	1.6	1.7		4.4		
2P4	1150	92.2	Tr		3.7						4.1		
4P1	1150	95.4	Tr					Tr			3.8		1.1
4P2a	1150	88.2	3		3.2		0.7	Tr		2.3	2.4	Tr	
4P2b	1150	76.3	11.2		3.8	1.9	Tr	Tr	Tr	4.4	2.5	Tr	Tr
4P3a	1150	95.5	0.6		Tr						3.6	Tr	
4P3b	1150	94.9			Tr		2.6				2.4	Tr	



- *Burnt lime characterization*

Burnt lime presents a typical brownish color, which is light brown at 1050 °C, pale brown at 1150 °C, and medium brown to dark gray at 1200 °C. The only exception is represented by very thin layers of siliciclastic impurity along stylolites, which are generally whitish after the thermal shock. Chemical (XRF-WDS, C-S elemental analysis) and mineralogical (XRD-QPA) analysis of burnt limes (Fig.3.8b) shows that lime (CaO) ranges from 75% up to 95%. The following subordinated mineral phases were identified: periclase (MgO – max 12%), dicalcium manganate ($\text{Ca}_2(\text{MnO}_4)$ – max 6%), larnite (Ca_2SiO_4 – max 4%), hatrurite (Ca_3SiO_5 – max 2%), quartz (SiO_2 – max 1%); merwinite ($\text{Ca}_3\text{Mg}(\text{SiO}_4)_2$ – max 6%); tricalcium aluminate ($\text{Ca}_3\text{Al}_2\text{O}_6$ – max 2%) and srebrodolskite ($\text{Ca}_2\text{Fe}_3+2\text{O}_5$ – max 4%). Finally, some accessory minerals (<0.5%), were also determined: gehlenite ($\text{Ca}_2\text{Al}(\text{AlSi})\text{O}_7$); fersilicide (FeSi) and anhydrite (CaSO_4).

The SEM-EDS analysis, performed on burnt chunk samples, confirms the composition of accessory mineral phases already detected by means of XRD analysis. It points out different calcium and magnesium silicate burnt products, mostly concentrated along stylolites. They appear with apparently fluidal textures, probably indicating a partially and very localized melting (Fig.3.6f).

Tab.3.12 – Results of technical tests on burnt lime samples at 1050°C

Code	Unit	2P1	2P2	2P3	2P4	Weighted Average 2P	4P1	4P2	4P3	Weighted Average 4P
m-thick	m	2.0	2.1	3.9	2.1	-	14.9	2.7	0.4	-
Residual CO ₂	wt%	0.46	0.41	0.40	0.06	-	0.17	0.5	0.5	-
CaCO ₃ (calculated)	wt%	1.05	0.93	0.91	0.14	-	0.39	1.1	1.1	-
Total CaO (XRF-normalized)	wt%	93.1	98.3	93.6	96.0	95.0	98.3	89.4	99.7	97.0
Available Lime Index (ALI)	wt%	91.8	96.5	92.3	97.8	94.2	98.4	92.7	96.1	97.5
t ₆₀ (1050°C)	min.	0.81	1.37	1.74	0.82	1.3	1.24	4.00	0.97	1.6
T _{max} (1050°C)	°C	73.0	66.9	65.4	71.8	68.5	73.6	62.8	77.0	72.1
T.A.S.T.	min.	5.5	5.0	4.5	4.0	4.7	3.5	6.0	6.0	3.9

Tab.3.13 – Results of technical tests on burnt lime samples at 1150°C

Code	Unit	2P1	2P2	2P3	2P4	Weighted Average 2P	4P1	4P2	4P3	Weighted Average 4P
m-thick	m	2.0	2.1	3.9	2.1		14.9	2.7	0.4	
Residual CO ₂	wt%	0.2	0.4	0.0	ND		0.5	0.4	0.7	
CaCO ₃ (calculated)	wt%	0.5	0.8	0.0	ND		1.2	0.8	1.6	
Total CaO (XRF-normalized)	wt%	95.3	98.3	94.5	97.6	96.1	98.1	92.7	95.5	97.2
Available Lime Index (ALI)	wt%	95.2	98.8	98.0	98.6	97.7	98.5	92.7	95.8	97.6
t ₆₀ (1150°C)	min.	1.8	6.8	17.5	9.4	10.5	11.3	6.1	7.3	10.4
T _{max} (1150°C)	°C	70.3	67.3	62.0	64.5	65.3	65.2	63.9	70.4	65.1
T.A.S.T.	min.	6.0	10.5	11.5	11.0	10.1	16.5	8.5	12.5	15.2

According to the slaking test method (EN 459-2, 2010), the reactivity of lime burnt at 1050 °C is very high ($t_{60} < 1$ min) for samples 2P1, 2P4 and 4P3, high ($t_{60} < 2$ min) for samples 2P2, 2P3, 4P1 and medium ($t_{60} = 4$ min) for sample 4P2. In any case, the average reactivity at 1050 °C is high ($t_{60} = 1.3$ min, $T_{max} = 72.3$ °C) (Tab.3.12, Fig.3.9a). Conversely, burnt lime at 1150 °C generally presents a low reactivity. Especially, samples 2P2, 4P2 and 4P3 are medium reactive ($t_{60} = 5-6$ min), while samples 2P3, 2P4 and 4P1 are slowly reactive ($t_{60} > 9$ min). A significant exception is represented by sample 2P1, which maintains a high reactivity ($t_{60} < 2$ min) at 1150 °C. In any case, the average reactivity at 1150 °C is low ($t_{60} = 7.4$ min, $T_{max} = 67.7$ °C) (Tab.3.13 Tab.3.12, Fig.3.9b). Either lime burnt at 1050 °C or at 1150 °C maintains a high available lime index (ALI ranges between 91.8% and 98.4% at 1050 °C; ALI ranges between 95.2% and 98.8% at 1150 °C (see Tab.3.12 and Tab.3.13).

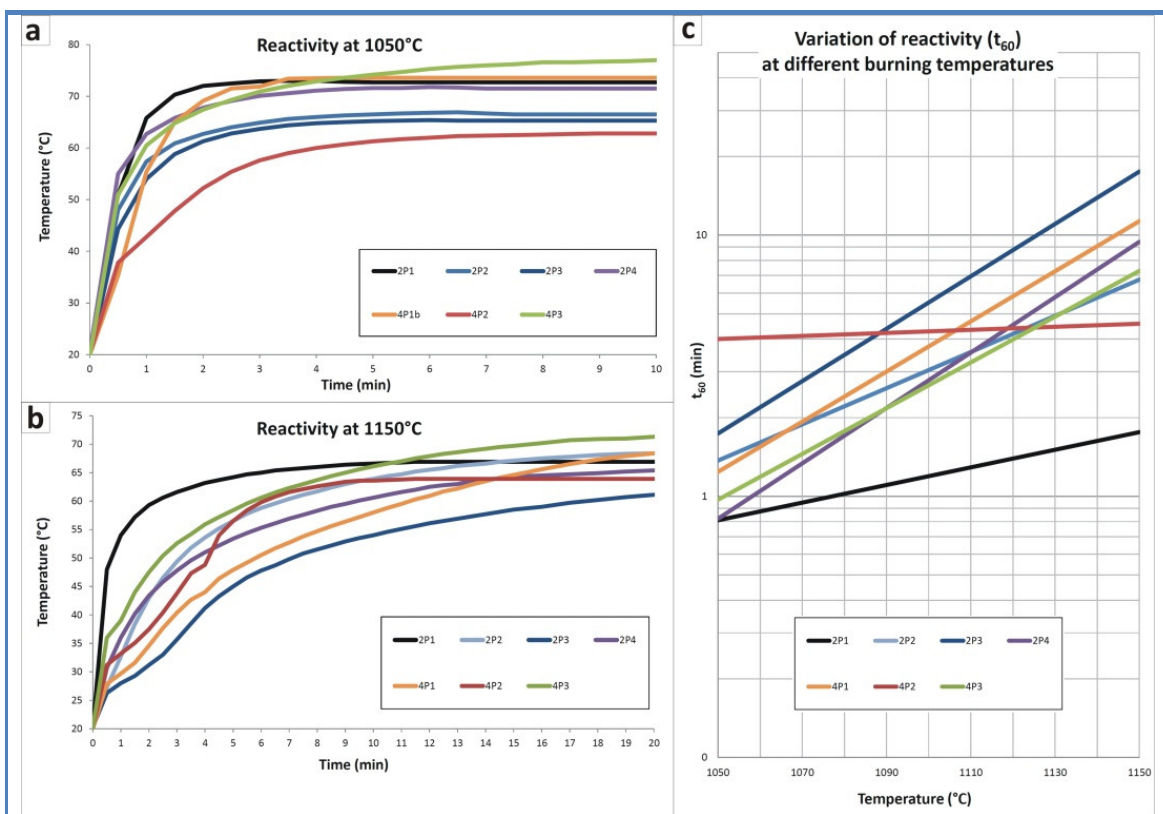


Fig.3.9: Reactivity tests according to EN 459-2. a = Slaking curves of limes burnt at 1050 °C. b = Slaking curves of limes burnt at 1150 °C. c = Variations of reactivity (t_{60}) at different T (1050-1150 °C) help in understanding the sensitivity to high temperature, and the sintering or overburning tendency of burnt limes in the restricted range of temperatures, with exceptions of sample 2P1 and 4P2. From Vola et al. (2017).

Variations of reactivity, plotted against the burning temperature, point out to an unusual and drastically pronounced sintering, or overburning tendency of the Neoproterozoic limestone (Fig.3.9c), with the exception of samples 2P1 and 4P2, which present a similar reactivity either at 1050 °C or at 1150 °C.

The weight average of different technical parameters, including the reactivity (t_{60} and T_{max}) and the available lime index (ALI) of each bench, has been calculated considering the thickness of each stratum. The average of technical tests performed at 1050 °C and 1150 °C is reported in Tab.3.14. These data have been used to calculate the influence of different raw mixes feeding to kilns (see Tab.3.15).

Tab.3.14 – Results of technical tests on burnt limes (average of limes burnt at 1050-1150 °C)

Det.	Unit	Weighted Average 2P	Weighted Average 4P
Total CaO (XRF-normalized)	wt%	95.5	97.1
Available Lime Index (ALI)	wt%	96.0	97.5
Reactivity t_{60}	min.	5.9	6.0
Reactivity T_{max}	°C	66.9	68.6
Reactivity T.A.S.T.	min.	7.4	9.6

Tab.3.15 – Different scenarios showing the influence of raw mixes on reactivity (t_{60} and T_{max}), and available lime index (ALI). Data are from the average of technical tests performed on burnt limes at 1050 °C and 1150 °C

Scenario	Raw mix	t_{60} (min.)	T_{max} (°C)	ALI	Notes
1	2P (100%)	5.9	66.9	96.0	The best raw mix for t_{60}
2	4P (100%)	6.0	68.6	97.5	The best raw mix for ALI and T_{max} (used from September to December 2013)
3	2P(65%)+ 4P(35%)	5.9	67.5	96.5	Raw mix used from February to March 2014
4	2P(35%)+ 4P(65%)	6.0	67.5	97.0	Natural quarry balance

3.2.15 Discussion

- *Depositional facies and diagenetic features*

The Neoproterozoic limestone succession from the Ouplaas Mine is characterized by fenestrate and laminated microbial boundstone, associated with peloidal-intraclastic wackestone to packstone, and grainstone, deposited in a shallow subtidal to intertidal environment. Early marine carbonate cements consist of radial fibrous fans and herringbone calcite (Beukes 1980, 1987; Altermann and Schopf, 1995; Sumner, 1995, 1997a, 1997b; Sumner and Beukes, 2006). Depositional textures are strongly affected by

pervasive diagenetic recrystallization, which converted the micrite into microsparite, and equant and poikilotopic coarse sparite cements. The pervasive recrystallization is probably connected to the circulation of anchimetamorphic or hydrothermal fluids, often in contact with diabase intrusions, even if not directly observed in the mine. This fact is consistent with the Paleoproterozoic magmatism documented by Heaman (1997). Paragenetic pathways of carbonate minerals are broadly similar in all lithofacies with kerogen intimately associated with them. Organic carbon occurs as pigmentation in carbonate crystals, and as segregations of kerogen pigmentation around late diagenetic carbonate crystals and cavities (see Beukes et al., 1990). In marly limestones (samples 4P3 and 4P2, see Tab.3.4, Fig.3.3c-i, and Fig.3.4d-f), clasts are generally composed of kerogen pigmented laminated microsparite, which either floats in a matrix of fine-grained carbonate mud or is cemented by coarse sparite (Klein and Beukes, 1989). According to Beukes et al. (1990), kerogen occurs in four major relationships with the carbonate minerals: 1) kerogen as pigmentation in microsparite, 2) kerogen and carbonate as reworked detritus, 3) kerogen as pigment segregated from calcite spar, and 4) kerogen displaced by carbonate. Some of the kerogen might be related to primary benthic microbial mats and appears to be a light brown pigment in the microsparite. Most of the kerogen observed in the studied samples seems to be strictly connected with the formation of stylolites and represents a thermally-mature late diagenetic graphitic carbon, which probably migrated into the carbonate deposit from another stratigraphically contiguous (or not-contiguous) source rock.

- *Limestone burnability and quicklime reactivity*

Limestone microstructure and composition, depending from primary depositional features and diagenetic modifications, associated with the ancient geologic age of the rock, play a key role in controlling the kinetics of thermal decomposition, including the transfer of hot gases, and the escape of the CO₂ during the calcination process. These factors, as well as the burning temperature, control the microstructure of the neo-formed lime crystals in terms of grain growth, and BET specific surface area, and thereby the hydration rate of the slaking reactivity (t_{60} , T_{max}) (Eades and Sandberg, 1970; Moropoulou et al., 2001; Kiliç and Mesut, 2006; Hughes and Corrigan, 2009; Soltan 2009; Soltan et al., 2011, 2012; Alaabed et al., 2014). In particular, previous studies have demonstrated that limestones with the lowest micrite to sparite ratio exhibit the lowest apparent activation energy value, the highest rate of calcination, and the highest lime reactivity (Vola and Sarandrea, 2013;

Marinoni et al., 2015). Effectively, the presence of euhedral-subhedral sparite crystals in the investigated Egyptian limestone enhances the formation of triple junction fractures, which also contribute to lowering the activation energy with accelerating lime liberation (Soltan and Serry, 2011).

In the analyzed Neoproterozoic carbonates, the dominant micritic texture of the microbialite precipitates, even if interested by pervasive recrystallization, coupled with the presence of abundant organic carbon (kerogen), are key factors influencing the abnormally low burnability. Especially, the low burnability is strictly related to the high sintering or overburning tendency and the low reactivity of the lime. Conversely, the presence of early marine herringbone calcite and late diagenetic burial cementation, i.e. the centimeter-size poikilotopic calcite as in sample 2P1 (Fig.3.3a, Fig.3.4a-b), promotes a locally higher burnability and quicklime reactivity. In fact, sample 2P1 presents an earlier starting calcination temperature (t_1), a faster carbonate dissociation rate or calcination velocity (Δt) and a lower sintering tendency (see Tab.3.9 and Fig.3.7a-b). The evident sintering or overburning tendency of the studied Neoproterozoic limestone is well documented by the progressive darkening of the burnt lime at increasing burning temperature (Fig.3.7c). This fact is combined with the progressive decay of the lime reactivity, while it doesn't affect the available lime index, which still remains high (Tab.3.14 and Tab.3.15, Fig.3.9). The typical brownish color of the lime is probably linked to the ubiquitous content of manganese-bearing minerals, probably microcrystalline braunite within the parental limestone, as shown in the back scattered electron maps obtained by means of the SEM-EDS analysis. Considering the temperature rise from the slaking tests (t_{60}) at 1050 °C and 1150°C, it is possible to classify each sample of the Ouplaas Mine on the basis of its sensibility to the high temperature (Carneuse, 2014). A first group of samples, including 2P2, 2P3, 4P1 and 4P3, was identified which is very much sensitive to high temperature; conversely, a second group, including 2P1 and 4P2 samples, is not so much sensitive to high temperature (Fig.3.10c).

In particular, sample 2P1 shows the highest reactivity either at 1050 °C or at 1150 °C (Tab.3.14 and Tab.3.15; Fig.3.10a-b). This result can be explained considering its different microfacies, presenting predominant fenestrate microbial boundstone (microbialite A), characterized by centimeter-sized cavities filled in by poikilotopic calcite (Fig.3.3a, Fig.3.4a-b). The highest reactivity of sample 2P1 is consistent with results from the thermal analysis, pointing out its highest velocity in thermal decomposition or calcination

velocity (Δt), with respect to other samples, lacking the poikilotopic calcite (Tab.3.13; Fig.3.9b).

Sample 4P2, which shows a medium reactivity either at 1050 °C or at 1150 °C, is not so much sensitive to high temperature as well as sample 2P1, but in this case, the impurity content, mostly represented by dolomite replacements, combined with the highest concentration of clay minerals, affects its reactivity (Tab.3.11, Tab.3.12, and Tab.3.13.). Another factor affecting the limestone burnability could be the organic carbon (kerogen), which also burns during the calcination process.

In any case, considering that it is almost difficult, if not impossible, from the mining point of view, separating materials and strata with a lower technical quality belonging to the same bench, we just calculated the average weighted reactivity of benches 2P and 4P, on the basis of the thickness of each lithofacies assemblage (Fig.3.2 and Fig.3.3). Therefore it was possible estimating the impact of different lithofacies assemblage from each bench on burnt lime technical parameters (Tab.3.12, Tab.3.13, and Tab.3.14). Especially, we calculated four different scenarios, showing the impact of different quarry raw mixes on lime reactivity and available lime index (ALI) (Tab.3.15). Results show different raw mixes have a limited influence (ca. 0.1%) either on the ALI, or on the quicklime reactivity (t_{60} , T_{max}). In a particular way the highest reactivity of sample 2P1 has a limited effect because the thickness of the bottom stratum of the mine is limited, as well. For this reason it could be useful to evaluate a more consistent extraction of this stratum in the early future, by means of an in situ log survey, finalized to evaluate its real thickness below current quarrying level. More in general a deep geological survey of the mine, facilitate the determination of the real thickness and areal distribution of impure lithofacies, i.e. marly limestones and black shales, and to identify any dolomitization fronts. Geological and stratigraphic analysis, coupled with laboratory tests on raw materials from each stratum and bench of the mine, represent an essential approach to optimize the quality of the burnt lime product.

3.2.16 Conclusions

Considering the multidisciplinary analytical approach of this study, we traced the following conclusions:

- 1) The Neoproterozoic limestone from the Ouplaas Mine is very much sensitive to high burning temperatures showing an unusual and drastically pronounced sintering or

overburning tendency. Especially, burnt lime presents a high reactivity at 1050 °C ($t_{60}= 1.5$ min, $T_{\max}=70$ °C), but it rapidly decreases at 1150 °C ($t_{60}=9$ min, $T_{\max}=65$ °C). This fact can be better displayed plotting the reactivity against the burning temperature (see Fig.3.10c).

- 2) The unusual very low thermal behavior or burnability is strongly influenced by depositional textures, diagenetic history and secondly by presence of non-limestone impurities. Especially, the high sintering or overburning tendency and the low quicklime reactivity are related more to the micritic texture of the microbial boundstone, even if affected by diagenetic recrystallization into microsparite, rather than to the restricted presence of non-carbonate mineral contaminations.
- 3) The sample 2P1 represents the most significant exception. It shows characteristic marine herringbone calcite associated with late diagenetic burial cementation, i.e. the centimeter-size poikilotopic calcite. This sample presents the highest carbonate dissociation rate or calcination velocity and the least sensitivity to the high temperature, and thus the highest quicklime reactivity either at 1050°C ($t_{60}=0.8$ min, $T_{\max}=73$ °C) or at 1150°C ($t_{60}=1.8$ min, $T_{\max}=70.3$ °C).
- 4) The sample 4P2 is also not so much sensitive to high temperature, but its quicklime reactivity is medium either at 1050 °C ($t_{60}=4$ min, $T_{\max}=62.8$ °C) or at 1150 °C ($t_{60}=6$ min, $T_{\max}=63.9$ °C), because strongly affected by its impure composition, i.e. diagenetic replacive dolomite and clay minerals.
- 5) The presence of locally concentrated dolomitic marly limestones, back shales, an organic carbon (kerogen), negatively affects the quicklime reactivity because significantly lowers the available lime index, moreover kerogen burns during the heating process, facilitating the sintering or overburning tendency.

According to these observations, we also proposed to the customer perform the following useful actions:

- 1) To perform a deep geological survey of the mine stratigraphy, finalized to the correct determination of the real thickness of the impure strata, to identify dolomitization fronts and impurity distribution to optimize the quality of the extracted stone.
- 2) To perform an in situ log survey, finalized to evaluate the real thickness of the bottom stratum of the mine (2P1) below the current quarrying level, to evaluate the feasibility of its more consistent extraction in the early future.

Chapter 3. Results and Discussion

The detailed knowledge of the mine stratigraphy, combined with the technical characterization of each stratum, allows calculating the real average weighted reactivity of each bench, and subsequently, the expected reactivity of different raw mixes feeding to the TSR kilns. This multidisciplinary approach must be repeated on more representative volumes of material extracted over the months and the years to validate the above results. If the higher reactivity of bench 2P will be validated by a massive campaign of tests, it could be successfully adopted to improve the raw mix feeding to the kilns, depending on the target parameter required by the customer. The judicious selection of raw material from different benches of mines could also reduce the negative influence of strata with a higher overburning tendency, and/or with a lesser compositional quality.



Fig.3.10: Panoramic view of TSR Kilns 9 and 10 installed at Idwala Plant by Cimprogetti in 2013-2014.

3.3 Article no. 2. The Impact of rock fabric, thermal behavior, and carbonate decomposition kinetics on quicklime industrial production and slaking reactivity

This work was written on spring 2018 by G. Vola, P. Bresciani, E. Rodeghero, L. Sarandrea, and G. Cruciani. The paper is reported as submitted to the Journal of Thermal Analysis and Calorimetry, with the only addition of a final paragraph titled “Final remarks” reporting on validation of statistical analyses by means of the Student's t-test.

3.3.9 Abstract

This paper deals with thermal analyses, burning trials and reactivity tests on 15 carbonate rocks, i.e. pure and impure carbonates, mud-supported and grain-supported limestones, crystalline marbles and dolomites, used for the production of different lime products in industrial vertical shaft kilns worldwide. Especially, thermogravimetric and differential thermogravimetric analysis (TG-DTG) on massive (80-120 g) fine-grained (<3.35 mm) samples, allowed the extrapolation of the Arrhenius kinetic parameters, i.e. the (apparent) activation energy (E_a) and the pre-exponential or frequency factor (A). Other calcination parameters, i.e. the duration time, starting and ending calcination times and temperatures, and peaks of maximum calcination rate were also extrapolated in order to enhance their relationships with quicklime reactivity. Moreover thermal analyses (TG-DTA) were repeated on powders (90 mg) using a more accurate analyzer to compare results. The study is completed by a thoroughly chemical-physical and mineralogical-petrographic characterization of carbonate rocks and derived burnt products. Results pointed out that medium- up to coarse crystalline materials, i.e. grain-supported limestones, diagenetic dolomites, and granoblastic marbles presented the highest activation energy, burnability and slaking reactivity. Conversely, microcrystalline carbonates with the highest micrite to sparite ratio, i.e. mud-supported limestones, and impure carbonates, enriched in quartz, clay minerals, and other subordinated non-carbonate impurities, presented the lowest activation energy, burnability, and slaking reactivity. This study also investigated the effect of BET specific surface area and real density, depending on specific sintering tendency, on quicklime reactivity. Results from this multidisciplinary research activity put further constraints on carbonate rocks calcination kinetics and their suitability in the lime industry.

3.3.10 Introduction

Depending on intrinsic or geological features of carbonate materials, applied calcination conditions, and kiln technologies, burnt lime products with different properties and reactivities can be obtained, to satisfy different segments of the market. Since the 60s of the last century, with the introduction of the basic oxygen converter steel furnaces, high-calcium and magnesium-rich quicklimes were used as slagging agents in metallurgy instead of the limestone (König et al., 1967; Obst et al. 1970). This technology created parallel revolution within the lime industry (Limes and Russell, 1970). The lime reactivity became a topic of great interest not only for steel making, but for several other industrial processes, including chemical, pharmaceutical, mining, agricultural, water treatment, food & beverage and environmental purposes, i.e. acids neutralization, pH stabilization and flue gas desulfurization (Boynton, 1982). Dolomitic limes are suitable for glass production, while dead-burnt or double-burnt dolomites are used in production of magnesium refractories too (Boynton, 1982). Conversely, hydraulic lime products are essentially required by the construction sector, having large applications in masonry, plastering, sustainable buildings, and restoration purposes (Elsen et al., 2011).

The thermal decomposition of a pure limestone, the so-called calcination reaction, [I] is apparently very simple. Complications may arise from the contemporary presence of dolomite, and/or other subordinated mineralogical impurities. Dolomite decomposition is more complex because generally consists of a double step reaction [II] and [III]. Sometimes dolomite also decomposes via a single stage [IV] or in an intermediate manner (Oates, 1998).

$\text{CaCO}_3 + \text{Heat} \rightleftharpoons \text{CaO} + \text{CO}_2 \uparrow$	[I]
$\begin{array}{ccc} 100 \text{ g} & 56 \text{ g} & 44 \text{ g} \end{array}$	
$\text{CaCO}_3 \cdot \text{MgCO}_3 + \text{Heat}_{(1)} \rightleftharpoons \text{CaCO}_3 \cdot \text{MgO} + \text{CO}_2 \uparrow$	[II]
$\begin{array}{ccc} 184 \text{ g} & 140 \text{ g} & 44 \text{ g} \end{array}$	
$\text{CaCO}_3 \cdot \text{MgO} + \text{Heat}_{(2)} \rightleftharpoons \text{CaO} \cdot \text{MgO} + \text{CO}_2 \uparrow$	[III]
$\begin{array}{ccc} 140 \text{ g} & 96 \text{ g} & 44 \text{ g} \end{array}$	
$\text{CaCO}_3 \cdot \text{MgCO}_3 + \text{Heat}_{(1+2)} \rightleftharpoons \text{CaO} \cdot \text{MgO} + 2\text{CO}_2 \uparrow$	[IV]
$\begin{array}{ccc} 184 \text{ g} & 96 \text{ g} & 88 \text{ g} \end{array}$	

According to results obtained from different Authors, the apparent magnitude of calcination kinetic parameters ranges from 110 to 3800 kJmol⁻¹ for the activation energy

(E_a), and from 102 to 10157 s⁻¹ for the pre-exponential or frequency factor (A) of the Arrhenius equation (Georgieva et al., 2013). Reasons for widely varying values are different. The first reason is related to intrinsic or geological differences between carbonate samples, including crystallographic, mineralogical and petrographic features of the limestone. On the other hand, kinetic parameters are strongly affected by the sample mass, and the particle-size distribution. Furthermore, process parameters also impact, such as isothermal, or non-isothermal heating conditions, heating rate, CO₂ partial pressure, static or dynamic atmosphere around sample, and atmosphere in the furnace (Tian et al., 2017). Finally, the calculation procedure affects kinetic parameters too (Georgieva et al., 2013). Over the years several studies on kinetics of limestone decomposition were performed using pulverized limestone particles, to exclude the influence of thermal conduction, pore diffusion, heat and mass transfer (Cheng and Specht, 2006). Lumpy pieces or aggregates with defined shape and size, i.e. typical fractions ranging between 20-40 mm (fine fractions) up to 50-100 mm (coarse fractions), are used for feeding industrial kilns. Undoubtedly, decomposition kinetics of limestone aggregates is more complex, also because the contribution of petrographic features is not negligible as well as in a pulverized sample. Furthermore, calcination rates could affect the quicklime reactivity, as well. Previous Authors investigated physical-chemical properties of the limestone to predict the quicklime reactivity. Early studies were performed under the auspices of the American National Lime Association. The characterization of commercial limes, i.e. soft-burnt and hard-burnt products, was initially performed by means of BET surface area measurements and SEM analysis (Eades and Sandberg, 1970). Another pioneering study on the textural evolution of limestone calcines after shock burning tests between 750-1300°C was performed by McClellan and Eades (1970). During the 80s and the 90s of the last century much work was done to evaluate the effect of particle size distribution, calcination rates, specific surface areas and impurity content (Oates, 1998; Borgwardt, 1985; Borgwardt and Bruce, 1986). Different Authors adopted linear and multiple regression statistics or factorial analysis to evaluate experimental results (Wright, 1985; Baziotis et al., 2011; Akande et al., 2016). More recently, i.e. over the last ten years, an increasing number of mineralogical, crystallographic and, finally, petrographic studies were performed, to bridge the geological gap. Because limestone and dolomite are naturally occurring materials, their composition and physical properties change between different rock formations, but often within the same deposit, and quarry, depending on age, stratigraphic, paleogeographic and structural settings. These factors, operating at the macroscopic (regional) and mesoscopic

(outcrop) scales, deeply affect primary (depositional) textures and secondary (diagenetic/metamorphic) modifications at the microscopic scale. Therefore geoscientists proposed studies based on the microfacies analysis, and the petro-physical and crystallographic characterization of carbonate rocks (Hogewoning, et al., 2008; Lech et al., 2009; Rodriguez-Navarro et al., 2009; Soltan, 2009; Soltan and Serry, 2011; Soltan et al., 2011a, 2011b; Soltan et al., 2012; Vola and Sarandrea, 2013; Alaabed et al., 2014; Vola et al., 2017). A mineralogical-petrographic approach was recently adopted to evaluate the thermal decomposition and the heating behavior of limestone in the industrial cement clinker manufacture too (Marinoni et al., 2015; Galimberti et al., 2016).

In this study 15 different carbonate rock samples were selected worldwide. Some are currently used to feed vertical shaft kilns in different countries, others were considered because their possible use in the early future, considering it was recently commissioned the design of new Twin Shaft Regenerative (TSR) kilns. Finally, three historical Italian carbonate stones were also analyzed, i.e. the Carrara marble, the Rosso Verona limestone and the Zandobbio Dolomite. Therefore a multidisciplinary research activity was carried out on raw materials and derived burnt products to investigate their specific burnability, for solving the critical issue of early sintering, or overburning tendency, at high calcination temperature of 1200 °C. Especially, kinetic parameters, including calcination duration time, starting calcination temperature, the (apparent) activation energy and the pre-exponential factor of the Arrhenius equation were extrapolated from thermogravimetric analysis (TG) according to the Fuoss-Salymer-Wilson (FSW) method (Fuoss et al., 1964). These data are fully consistent with values reported in the literature for massive samples (Oates, 1998; Soltan & Serry, 2011; Kiliç, 2013; Alaabed et al., 2014). Moreover, the linear regression analysis pointed out the relationship between the activation energy, the slaking reactivity and the so-called “micrite-to-sparite ratio” (MSR). This factor allowed classifying carbonate rocks burnability in terms of mineralogical-petrographic features. Finally, this study investigated effects of derived parameters of burnt limes, i.e. the BET specific surface area and the real density, on the slaking reactivity, as well.

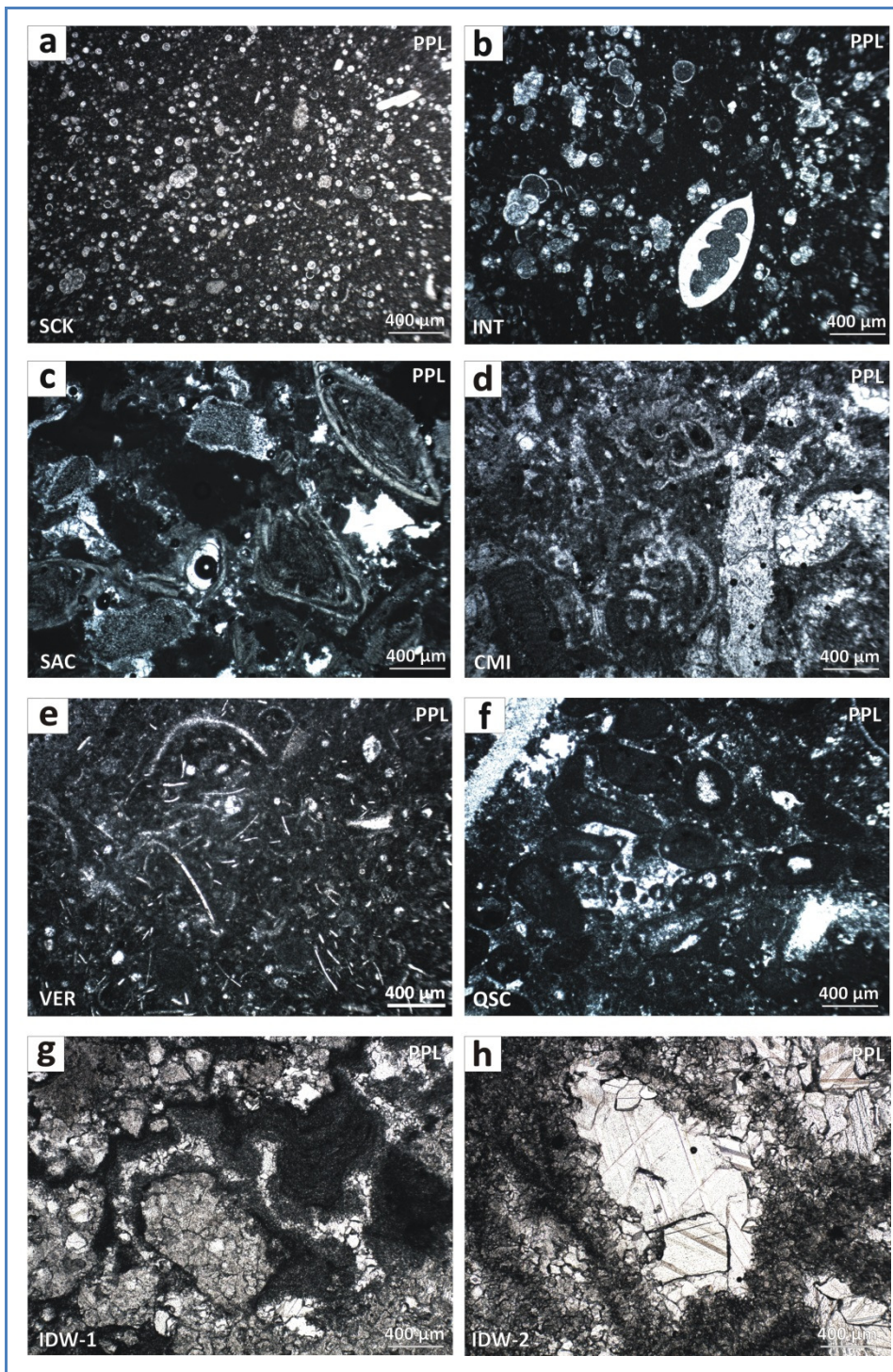


Fig.3.11: Petrographic analysis of mud-supported and marly limestones. a-b = pelagic marly limestones with planktonic foraminifera (SCK and INT). c = intra-platform packstone/wackestones presenting large benthonic foraminifera (nummulites) and echinoderm plates embedded in a dark micritic matrix (SAC). d = intra-platform packstone/grainstones with benthonic foraminifera (milioids), bivalves and echinoids, presenting diagenetic neomorphic sparite (CMI). e = nodular ammonite-bearing pelagic wackestone with thin-shelled bivalves, ostracods, pelagic foraminifera (protoglobigerins) and radiolarians (VER). f = intra-platform peloidal wackestone/packstones associated with coated grains, benthonic foraminifera (milioids), echinoids and rare bivalves. Intraclastic porosity is filled in by equant calcite cement (QSC). g-h = microbial boundstones with clotted peloidal micrite-microsparite associated with large mm-sized equant and poikilotopic calcite (IDW1 and IDW2). PPL = plane polarized light. From Vola et al. (2018).

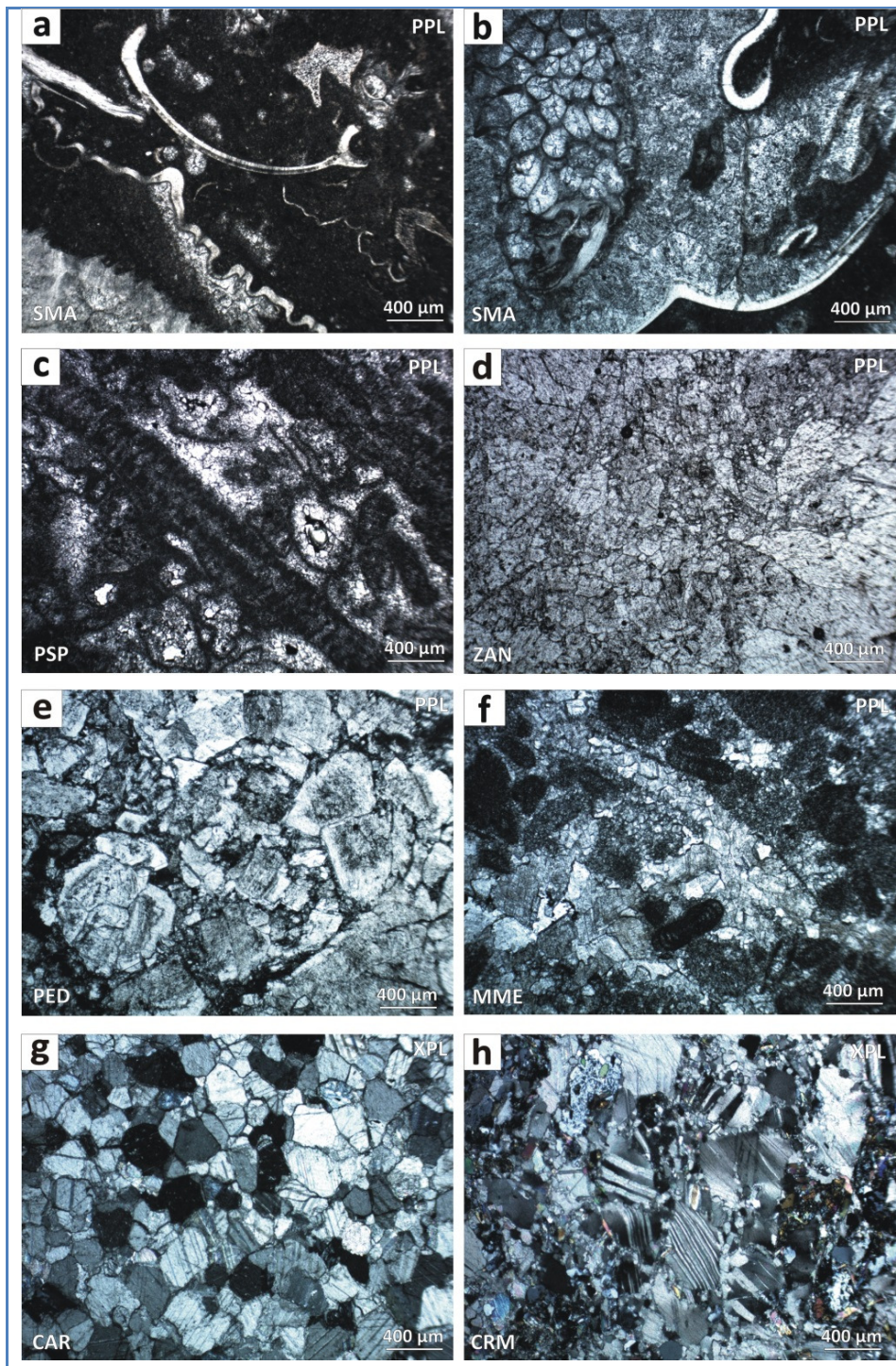


Fig.3.12: Petrographic analysis of grain-supported limestones, hypidiotopic dolomites and hydiorphic marbles. a-b = massive limestone with large mm-sized faunas, i.e. conodont, rugose corals, brachiopods and bivalves from stromatoporoidal reef (SMA). c = coralline-encrusting framestone/rudstones characterized by bryozoan-foraminifera-algae association. d = hypidiotopic diagenetic dolomite (ZAN). e = breccia-like diagenetic dolomite (PED). f = dolomitized packstone-grainstones with benthonic foraminifera (MME). g = idiomorphic calcite granoblastic marble (CAR). h = plastically deformed, idiomorphic, twinned calcite in silicate-bearing granoblastic marble (CRM). Legend symbols: PPL = plane polarized light. XPL = crossed polarizing light. From Vola et al. (2018).

3.3.11 Test Methods

For the experimental details, including sample provenance, physical (BET, MIP, pycnometry), chemical (XRF-WDS), mineralogical (XRD-QPA), microscopic (OPM, SEM-EDS), and thermal analyses (TG-DTG-DTA), plus technical tests, i.e. slaking reactivity and Available Lime Index (ALI), readers are requested to refer to Chapter 2 of the present dissertation.

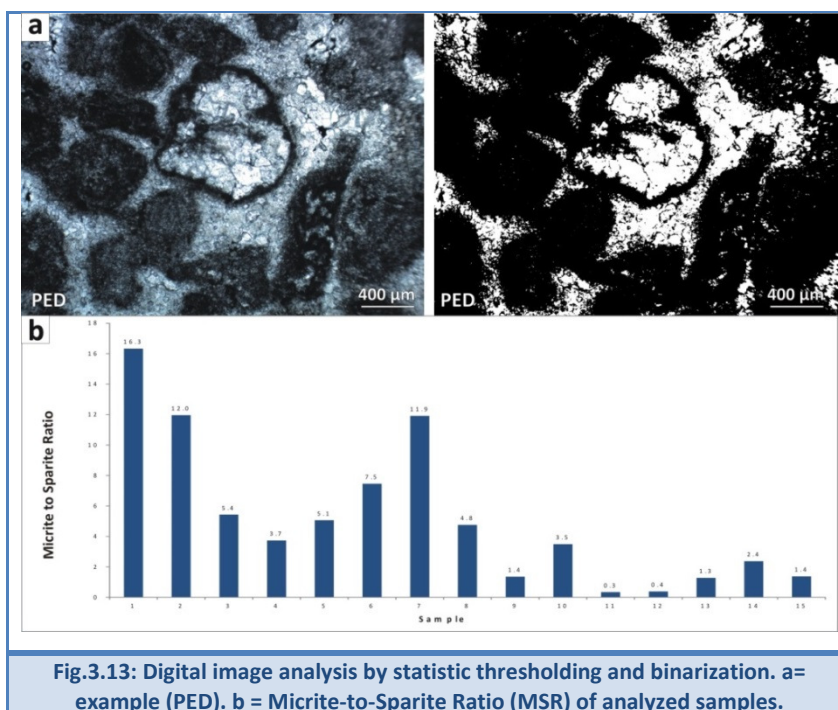
3.3.12 Results

- *Carbonate rocks characterization*

Preliminary geological information on samples provenance, stratigraphic position, textural and microstructural features are reported in Tab.3.16. Unfortunately, information about source deposits and rock units were not always available. Physical, chemical and mineralogical analyses are reported in Tab.3.17, Tab.3.18, and Tab.3.19. A detailed petrographic analysis, including description of depositional textures, diagenetic or metamorphic modifications and the micrite-to-sparite ratio (MSR), is reported in Tab.3.20. The MSR represents a mineralogical-petrographic factor suitable to plot linear regression analysis with kinetic parameters, i.e. the activation energy and the calcination duration time. Moreover it allows investigating relationships between physical and technical parameters of derived burnt limes, including the slaking reactivity. Results demonstrated that mud-supported and marly limestones always present higher values of MSR than grain-supported limestones, hypidiotopic dolomites and hydiomorphic marbles. Polarized micrographs of the most significant petrographic fabrics and microstructures are shown in Fig.3.12 and Fig.3.13. An example of digital image analysis with statistical thresholding and binarization is reported in Fig.3.13a. MSR values of analyzed samples are visualized in Fig.3.13b.

Tab.3.16 – Geological setting of carbonate rocks samples. Symbols legend: p.i. = proprietary information

Sample	Name	Code	Lithofacies	Texture/Microstructure	Stratigraphic position	Geological Unit	Provenance
1	SCH	598	Mud-supported Marly limestone	Wackestones with planktonic faunas	Cenomanian-Turonian	Planerkalk Group Munsterland Cretaceous Basin	Lienen, Germany
2	INT	2743	Mud-supported Marly limestone	Wackestones with planktonic faunas	Paleocene	El Haria Fm.	Thala, Tunisie
3	SAC	2001	Mud-supported limestone	Wackestone/packstones with benthonic faunas (Nummulites)	Paleocene-Eocene	Monti Climiti Fm. Priolo Fm.(?)	Siracusa, Italy
4	CMI	2004	Grain-supported limestone	Packstone/grainstones with benthonic faunas (Miliolids) and neomorphic sparite	Early Eocene	Seeb Fm.	Sohar, Oman
5	VER	2828	Mud-supported limestone	Wackestone/packstones with planktonic faunas (Protoglobigerins, radiolarians)	Middle Jurassic	Rosso Ammonitico Veronese Fm.	Verona, Italy
6	QSC	1880	Mud-supported limestone	Peloidal packstone/wackestones with benthonic faunas (Milioids, echinoids)	Middle Eocene	Dammam Fm.	Rawdat Rasid, Qatar
7	IDW1	1990	Microbial limestone	Microbial boundstone with microsparite	Neoproterozoic	Uppermost Kogelbeen Fm. or Lower Gamohaan Fm.	Daniëlskuil, S.Africa
8	IDW2	1991	Microbial limestone	Microbial boundstone with poikilotopic calcite	Neoproterozoic	Uppermost Kogelbeen Fm. or Lower Gamohaan Fm.	Daniëlskuil, S.Africa
9	SMA	1992	Massive limestone	Reefoidal facies and mosaic calcite cement	Silurian	Lower Wenlock Hangvar Fm.	Storugns, Gotland, Sweden
10	PSP	2450	Massive limestone	Reefoidal facies and mosaic calcite cement	Eocene	p.i	Rembang, Java, Indonesia
11	CRM	1895	Silicate-bearing marble	Granoblastic microstructure	Unknown	p.i	Seilles, Belgium
12	CAR	2829	Calcitic marble	Mainly granoblastic microstructure	Lower Liassic	Apuane Metamorphic Complex Marble s.s. formation	Carrara, Italy
13	ZAN	2830	Diagenetic Dolomite	Hipidiotopic to hydriotopic mosaic dolomite	Early Jurassic	Albenza Fm., Zandobbio Dolomite member	Zandobbio, Italy
14	PED	2782	Diagenetic Dolomite	Hipidiotopic mosaic and brecciated dolomite	Upper Triassic	Dolomia Superiore Fm., Dolomia a Megalodon member	Balvano, Italy
15	MME	2112	Diagenetic Dolomite	Xenotopic to hipidiotopic mosaic of dolomite with subordinated fossiliferous wackestone/packstones	Eocene	p.i	Medan Area, North Sumatera, Indonesia



- *Thermal analyses and kinetic parameters*

The thermogravimetric analysis (TG-DTG) by the Nabertherm muffle furnace was repeated thrice on crushed samples (<3.35 mm). In accordance with Cimprogetti's experience the optimum sample mass to test with this device, equipped with a digital balance, is about 100 g. Actually, experiments confirmed that resolution with samples lighter than 40 g is low, because the high sensibility of the apparatus to vibrations. For this reason a moving average on the TG data was used in order to smooth out fluctuations and spikes and consequently avoid "false" peaks in the DTG curve. Moreover samples burning trials were performed on 80 g in the first test, passing to 100 g in the second, and 120 g in the third one. Tests performed on samples weighting more than 120 g were avoided because they didn't maintain the scheduled heating rate, considering the limited heating power of the system. Results from TG-DTG analyses and kinetic parameters are reported in Tab.3.22. The average calcination duration time of pure limestones, i.e. 111 ± 8 min, was higher than that of dolomites, i.e. 107 ± 6 min, but lower than that of marly limestones, i.e. 121 ± 5 min. Moreover the average starting decomposition temperature of dolomites, i.e. 575 ± 4 °C, was lower than that of pure limestones, i.e. 680 ± 40 °C, in accordance to the literature (Boynton, 1982; Oates, 1998; Schwarzkopf, 1994). Obviously, CaCO_3 component of dolomites decomposed at higher temperature, representing dual-stage decomposition.

Tab.3.17 – Results of physical analysis of carbonate rock samples Symbols legend: BET SSA = Specific Surface Area by BET method.

Sample	Unit	1	2	3	4	5	6	7	8	9	10	11	12	13	14	15
Code		598	2743	2001	2004	2828	1880	1990	1991	2462	2450	1895	2829	2830	2777	2112
Name		SCH	INT	SAC	CMI	VER	QSC	IDW1	IDW2	SMA	PSP	CRM	CAR	ZAN	PED	MME
BET SSA	m ² g ⁻¹	4.06	1.38	0.71	0.33	0.55	0.10	0.19	0.11	0.38	0.09	0.05	0.00	0.06	0.10	0.14
Accessible porosity	%	5.65	12.68	22.80	12.77	1.17	1.11	0.37	0.53	0.53	7.39	0.61	0.65	1.27	0.30	0.88
Real density	g cm ⁻³	2.73	2.73	2.72	2.73	2.71	2.71	2.73	2.71	2.71	2.70	2.75	2.71	2.84	2.85	2.85
Bulk density	g cm ⁻³	2.56	2.75	1.95	2.27	2.64	2.66	2.73	2.76	2.62	2.68	2.72	2.70	2.80	2.86	2.84
Total pore volume	mm ³ g ⁻¹	22.06	0.14	116.71	56.21	4.43	4.18	1.36	1.92	2.03	0.54	2.24	2.72	4.54	1.04	3.10
Average pore radius	µm	0.02	0.07	0.27	0.52	0.02	0.04	0.33	0.78	0.06	0.27	0.13	0.38	0.08	0.53	0.14

Tab.3.18 – Results of mineralogical analysis (XRD-QPA) of carbonate rock samples. Symbols legend: Cal = calcite; Dol = dolomite; Qtz = quartz; Ill = illite; Pl = plagioclase; Chl = chlorite; Rt = rutile.

Sample	Unit	1	2	3	4	5	6	7	8	9	10	11	12	13	14	15
Code		598	2743	2001	2004	2829	1880	1990	1991	2462	2450	1895	2828	2830	2777	2112
Name		SCH	INT	SAC	CMI	VER	QSC	IDW1	IDW2	SMA	PSP	CRM	CAR	ZAN	PED	MME
Cal	%	94.0	93.6	99.7	99.6	99.7	99.8	91.1	97.4	93.9	99.8	86.9	98.5	0.2	3.6	3.2
Dol	%							3.6	2.5				0.8	99.5	96.1	96.2
Qtz	%	4.5	5.9	0.5	0.4	0.3	0.2	0.7	0.2	3.3	0.2	4.4	0.2			0.2
Ill	%	1.5						3.8		1.1		6.0	0.5			
Pl	%									0.6		0.4		0.3	0.3	0.4
Chl	%		0.5					0.8		0.7		2.3				
Rt	%									0.3		0.2				
SUM	%	100	100	100	100	100	100	100	100	100	100	100	100	100	100	100

Tab.3.19 – Results of chemical analysis (XRF-WDS) of carbonate rock samples. Symbols legend: IR = Insoluble residue; LSF = lime saturation factor $[\text{CaO}/(2.8*\text{SiO}_2+1.18*\text{Al}_2\text{O}_3+0.65*\text{Fe}_2\text{O}_3)]$; HI = hydraulicity index $[(\text{SiO}_2+\text{Al}_2\text{O}_3)/\text{CaO}]$; CI = Cement index $[(2.8*\text{SiO}_2+1.18*\text{Al}_2\text{O}_3+0.65*\text{Fe}_2\text{O}_3)/(\text{CaO}+1.4*\text{MgO})]$; SR = Silica ratio $(\text{SiO}_2/(\text{Al}_2\text{O}_3+\text{Fe}_2\text{O}_3))$; AR = Alumina iron ratio $(\text{Al}_2\text{O}_3/\text{Fe}_2\text{O}_3)$.

Samples		1	2	3	4	5	6	7	8	9	10	11	12	13	14	15
Code		598	2743	2001	2004	2828	1880	1990	1991	2462	2450	1895	2829	2830	2777	2112
Name	LLD	SCH	INT	SAC	CMI	VER	QSC	IDW1	IDW2	SMA	PSP	CRM	CAR	ZAN	PED	MME
LOI	0.01	40.74	41.34	43.72	43.14	43.18	43.99	42.45	43.52	42.94	44.64	37.43	43.86	47.2	47.6	46.9
SiO ₂	0.01	5.83	6.78	0.07	0.35	1.44	0.10	2.20	0.18	3.08	0.01	5.35	0.06	0.18	0.06	0.33
Al ₂ O ₃	0.01	1.62	0.34	0.04	0.12	0.33	0.03	0.67	0.02	0.82	0.01	1.51	0.04	0.06	0.04	0.15
Fe ₂ O ₃	0.01	0.68	0.19	0.06	0.09	0.22	0.06	0.23	0.10	0.40	0.03	1.13	0.04	0.06	0.05	0.10
CaO	0.01	49.65	51.20	55.30	55.90	54.20	55.40	52.70	55.00	51.65	55.31	52.20	55.10	31.88	31.06	33.60
MgO	0.01	0.65	0.32	0.58	0.28	0.401	0.33	0.82	0.36	0.62	0.15	1.06	0.90	20.97	21.09	18.60
SO ₃	0.01	0.06	0.03	0.04	0.03	0.04	0.03	0.14	0.02	0.04	0.01	0.04	0.03	0.02	0.04	0.03
Na ₂ O	0.01	0.04	0.02	0.00	0.03	0.04	0.01	0.01	0.04	0.02	0.00	0.12	0.01	0.02	0.06	0.036
K ₂ O	0.01	0.33	0.03	0.01	0.03	0.15	0.01	0.18	0.00	0.28	0.00	0.61	0.01	0.03	0.02	0.038
MnO	0.01	0.11	0.02	0.00	0.01	0.03	0.00	0.46	0.51	0.10	0.00	0.01	0.00	0.01	0.00	0.00
BaO	0.01	0.09	0.00	0.05	0.07	0.00	0.05	0.04	0.06	0.00	0.00	0.08	0.00	0.00	0.00	0.05
SrO	0.01	0.12	0.14	0.03	0.01	0.01	0.02	0.02	0.01	0.02	0.00	0.02	0.02	0.00	0.01	0.01
TiO ₂	0.01	0.08	0.07	0.00	0.01	0.03	0.01	0.03	0.01	0.05	0.01	0.10	0.01	0.01	0.01	0.01
P ₂ O ₅	0.01	0.08	0.02	0.12	0.02	0.06	0.01	0.01	0.01	0.02	0.01	0.05	0.01	0.01	0.01	0.01
Cl-	0.01	0.01	0.00	0.00	0.01	0.00	0.01	0.01	0.01	0.10	0.00	0.03	0.00	0.01	0.02	0.03
SUM	-	100	100	100	100	100	100	100	100	100	100	100	100	100	100	100
IR	-	11.10	6.22	0.18	0.53	2.02	0.34	3.39	0.27	3.20	0.08	13.31	0.14	0.22	0.15	0.32
Alkali	-	0.36	0.04	0.02	0.05	0.18	0.02	0.19	0.04	0.30	0.00	0.73	0.02	0.04	0.08	0.07
LSF	-	2.7	2.6	203.6	47.2	11.9	152.8	7.4	94.8	5.2	1078.8	3.0	235.5	52.1	132.4	28.9
HI	-	0.150	0.139	0.002	0.008	0.033	0.002	0.054	0.004	0.076	0.000	0.131	0.002	0.008	0.003	0.014
CI	-	0.368	0.377	0.005	0.021	0.083	0.006	0.131	0.011	0.187	0.001	0.325	0.004	0.010	0.004	0.019
SR	-	2.5	12.9	0.8	1.7	2.6	1.2	2.4	1.5	2.5	0.2	2.0	0.8	1.4	0.6	1.3
AR	-	2.4	1.8	0.6	1.3	1.5	0.6	3.0	0.2	2.1	0.3	1.3	1.1	1.1	0.8	1.4

Tab.3.20 – Petrographic analysis of carbonate rock samples. Symbols legend: MSR = Micrite-to-Sparite ratio, Nd = Not determined.

Sample	Name	Lithofacies	Primary texture and components	Diagenetic or Metamorphic modifications	MSR	References
1	SCH	Greenish to brownish marl/limestone alternations passing to nodular pelagic limestone	Mixed-fossil wackestones mainly composed of coccolithophorids (matrix), calcareous dinoflagellate cysts (calcispheres), planktonic foraminifera (globigerinids) and bioclasts (mainly inoceramid bivalves, echinoderms). Terrigenous impurity represented by fine-grained quartz and clay minerals, i.e. illite. The impurity content is about 11%.	No diagenetic and/or metamorphic features observed on thin section	16.3	Wiese et al. (2004)
2	INT	Condensed grey marl and greenish limestone facies	Mixed-fossil wackestones with planktonic foraminifera (globorotalids). Terrigenous impurity represented by fine-grained quartz and clay minerals, i.e. chamosite. The impurity content is about 7.6%.	No diagenetic and/or metamorphic features observed on thin section	12.0	Towadros (2012)
3	SAC	Yellowish mud-supported fossiliferous and poorly-compacted porous limestone	Wackestone/packstones with large benthonic foraminifera (nummulites), echinoderm plates embedded in a dark fine-grained micritic matrix. Large sub-mm sized primary porosity.	No diagenetic and/or metamorphic features observed on thin section	5.4	Lentini et al. (2014)
4	CMI	Whitish to beige fossiliferous thick to moderately well bedded calcarenite	Packstone/grainstones with benthonic foraminifera (miliolids), bivalves and echinoids. Large mm-sized intraclastic porosity filled in by equant and mosaic sparry-calcite	The primary sediment seems to be recrystallized into neomorphic sparite, during early diagenesis	3.7	Nolan et al. (1990)
5	VER	Red nodular ammonite-bearing pelagic limestone	Wackestone/packstones with planktonic thin-shelled bivalves, ostracods, foraminifera (protoglobigerins) and radiolarians.	Stylolites and solution seams due to pressure solution	5.1	Martire et al. (2006)
6	QSC	Brownish gray mud-supported peloidal limestone	Fossiliferous peloidal wackestone/packstones. Dark micritic kerogen-bearing peloids associated with coated grains and lumps with benthic foraminifera (Miliolids), echinoids and rare bivalves. Intraclastic porosity is filled in by equant calcite mosaics.	Secondary veins filled in by clear equant calcite cement	7.5	Le Blanc (2017)

Table 3.20 (continued)

Sample	Name	Lithofacies	Primary texture and components	Diagenetic or Metamorphic features	MSR	References
7	IDW1	Dark gray to black slightly dolomitic clotted peloidal micrite/microsparite and microbial boundstone associated with black shales	Laminated mudstone/wackestones to packstone/grainstones with clotted peloidal micrite, intraclasts and areas of microbial boundstone. Cloudy radial fibrous banded calcite fans representing primary marine cement associated with dark microbial laminae (herringbone calcite). Fenestrate porosity, locally enlarged by dissolution, is filled by equant drusy mosaic and cm-size poikilotopic calcite cement	Neomorphic microsparite and sparite due to recrystallization of micrite. Fabric-replacive hypidiotopic dolomite and cloudy rhombohedral crystals (200-500 μm) of saddle dolomite with undulose extinction. Cavities are filled by mm-size poikilotopic calcite cement (burial diagenesis). Stylolites and solution seams due to pressure solution. Kerogen soaked along stylolites after the pressure solution. Different cement generations, possibly related to late diagenetic fluids.	11.9	Vola et al. (2017)
8	IDW2	Gray, slightly dolomitic microbial boundstone with clotted peloidal micrite/microsparite laminae and herringbone calcite passing into clotted peloidal packstone/grainstone with subordinate fenestrate microbialites	Alternation of dark gray micrite/microsparite laminae and light fibrous radial calcite laminae (herringbone calcite) and inferred originally aragonitic botryoidal fans. Matrix of micrite to microsparite with peloidal remnants. Microsparite and sparite range in size from 20 microns to 200 μm but mean size is 60-100 μm . Fenestrae with equant or poikilotopic calcite and impregnated by different films of opaque organic carbon	Neomorphic microsparite and sparite due to recrystallization of micrite. Fabric-replacive hypidiotopic dolomite. Sub mm-sized rhombohedral dolomite crystals postdate the mm-size poikilotopic calcite cement in horizontal voids. Stylolites with organic carbon (kerogen) are often associated with partial dolomitization and recrystallization. Few scattered low to high amplitude black stylolites associated with brownish saddle dolomite	4.8	Vola et al. (2017)
9	SMA	Yellowish brown to olive gray massive carbonates, mostly of reefoidal origin, with interbedded siliciclastic sediments. Fossiliferous grain-supported facies locally passing to lacustrine mud-supported ones	Fossiliferous kerogen-rich floatstone/rudstones from different "reef" facies (stromatoporoids) including reef front, reef core, interreef, shoal and back-reef environments, locally passing to packstone-wackestones microfacies. Large mm-sized faunas and bioclasts including conodonts, rugose corals, possible trilobites, brachiopods and bivalves. Intraclastic porosity filled in by equant and poikilotopic calcite cement	Large mm-sized equant and poikilotopic calcite cement filled in intraclastic porosity	1.4	Jeppsson (2008)
10	PSP	White massive coralline mostly encrusting limestone	Massive coralline framestone/rudstones characterized by bryozoan-foraminifera association with encrusting coralline red algae. Primary intraclastic porosity filled in by equant mosaic calcite cement.	No diagenetic and/or metamorphic features observed on thin section	3.5	Nd

High-grade burnt lime products: impact of calcination kinetics on slaking reactivity; sticking tendency and blocks formation at HT (1300°C)

--	--	--	--	--	--	--

Table 3.20 (continued)

Sample	Name	Lithofacies	Primary texture and components	Diagenetic or Metamorphic modifications	MSR	Ref.
11	CRM	Light to medium dark gray silicate-bearing marble	Primary textures and components are completely obliterated by pervasive metamorphic recrystallization. Accessorial minerals: quartz, illite, plagioclase, chlorite, rutile	Granoblastic microstructures with well-defined grain boundaries. Calcite porphyroblasts present twinings and plastic deformations.	0.4	Nd
12	CAR	Fine to medium coarse-grained metalimestone, homogeneously pearl-white colored or with gray tiny spots	Primary textures and components are completely obliterated by pervasive metamorphic recrystallization	Marble microfabric depends on two main tectonic deformation phases. Main granoblastic microstructures with well-defined grain boundaries, straight or slightly curved with no optical evidence of crystal-plastic deformation. Subordinated xenoblastic structures with less defined grain boundaries, sometimes sutured or embayed to lobate. Variable grain-size and appreciable grain orientation.	0.3	Carmignani et al. (2005)
13	ZAN	Pinkish-white meter-thick and sub-meter-thick beds of medium up to coarse-grained dolostones, showing frequent vuggy porosity and peritidal structures, tepee-like pink horizons and fenestral fabrics	Shallow-water carbonates comprising sub-tidal to peritidal peloidal packstones interbedded with ooid-bioclasic grainstones	Primary textures and components are often completely obliterated by pervasive multistage superimposed dolomitization. The first pervasive replacement dolomitization phase is followed by volumetrically less important dolomite cement precipitation phases.	1.3	Ronchi et al. (2010)
14	PED	20-50 cm up to 1 meter thick beds of fine to coarse-grained grayish and whitish most tectonized dolostones	Peloidal-oncoidal and bioclasic-fossiliferous (Gervilleia, Megalodon) packstone/grainstones sometimes well preserved, sometimes perceivable as ghost primary textures.	Primary textures and components are often obliterated by pervasive, probably multistage, dolomitization. Hypidiotopic mosaic dolomite, brownish saddle dolomite, dolomitized breccia-like textures are dominant.	2.4	Scandone (1971)
15	MME	Light gray and brownish dolostones showing peritidal structures and fenestral fabrics	The original peloidal-fossiliferous (forams) wackestone/packstone is sometimes preserved. Typical association presents micritic benthonic foraminifera (milioids)	Multistage dolomitization superimposed to shallow-water carbonates. Non-planar closely packed fine-grained anhedral crystals of xenotopic dolomite associated with rhombohedral crystals of late saddle dolomite replacements.	1.4	Nd

Moreover the average initial decomposition temperature of marly limestones, 558 ± 80 °C, was apparently lower than dolomites, even if this datum is partially influenced by the contemporaneous dehydroxylation of clay minerals. The Arrhenius parameters were extrapolated according to the Fuoss-Salymer-Wilson (FSW) mathematical approach (Fuoss et al., 1964). Other methods are available in the literature (Doyle, 1962; Ozawa, 1965; Flynn and Wall, 1966). Even if the choice of the algebraic expression of reaction affects Arrhenius parameters determination (Georgieva et al., 2013), the apparent activation energy (E_a) and the pre-exponential factor (A) determined by the Nabertherm furnace (Tab.3.22) are fully consistent with data reported by previous Authors (Boynton, 1982; Oates, 1998; Soltan and Serry, 2011; Kiliç, 2013; Alaabed et al., 2014). Results pointed out average (apparent) activation energy of 100.9 ± 2.2 kJmol⁻¹ for pure limestones, 115.6 ± 3.5 kJmol⁻¹ for dolomites, and 84.1 ± 0.4 kJmol⁻¹ for marly limestones. The highest A value reached, i.e. 132.2 kJmol⁻¹, is related to a coarse-grained silicate-bearing granoblastic marble from Belgium (CRM), while the lowest value reached, i.e. 79.8 kJmol⁻¹, is related to a mud-supported marly limestone from Germany (SCH). The activation energy of dolomites was given by the contribution of MgCO₃ and CaCO₃ decompositions, according to the double step reaction proposed in the literature (Oates, 1998). Pre-exponential factors ranged between 1 up to 237 s⁻¹, and the average was 23 ± 59 s⁻¹.

Thermogravimetric and differential thermal analyses (TG-DTA) were repeated on powders using a Netzsch TG/DTA analyzer, at the University of Ferrara. Arrhenius parameters were extrapolated using the previously adopted FSW method (Fuoss et al., 1964). The average activation energy determined by the Netzsch device was 732 ± 137 kJmol⁻¹, while the average pre-exponential factor was $1.6 \cdot 10^{43} \pm 5.5 \cdot 10^{43}$ s⁻¹. Finally the decomposition enthalpy (ΔH) and the heat capacity (C_p) were extrapolated from the differential thermal analysis (DTA) (Tab.3.22). The visual comparison between differential thermogravimetric analyses (DTG) performed by Netzsch analyzer and Nabertherm furnace on a representative sample, i.e. the Carrara marble (CAR), are reported in Fig.3.14. The comparison between kinetic parameters calculated at the inflection point for the same sample is reported in Tab.3.21. Values point out a faster reaction rate for the Netzsch analyzer than for the Nabertherm furnace.

Tab.3.21 – Kinetic parameters of Carrara marble (CAR) calculated according to Fuoss-Salymer-Wilson (FSW) method from TG analyses performed by the Nabertherm TG muffle furnace and the Netzsch TG/DTA analyzer. Symbols legend: E_a = activation energy; A = pre-exponential factor

Det.	Unit	Nabertherm	Netzsch
Time	min	106.5	88
Temperature	°C	1057	899
Mass	%	21.6	7.1
dT/dt	°C min ⁻¹	6	10
dW/dT	% °C ⁻¹	-0.18	-0.49
dW/dt	% min ⁻¹	-1.1	-4.9
E_a	kJmol ⁻¹	121.5	785.9
A	s ⁻¹	48.9	1.17E+33

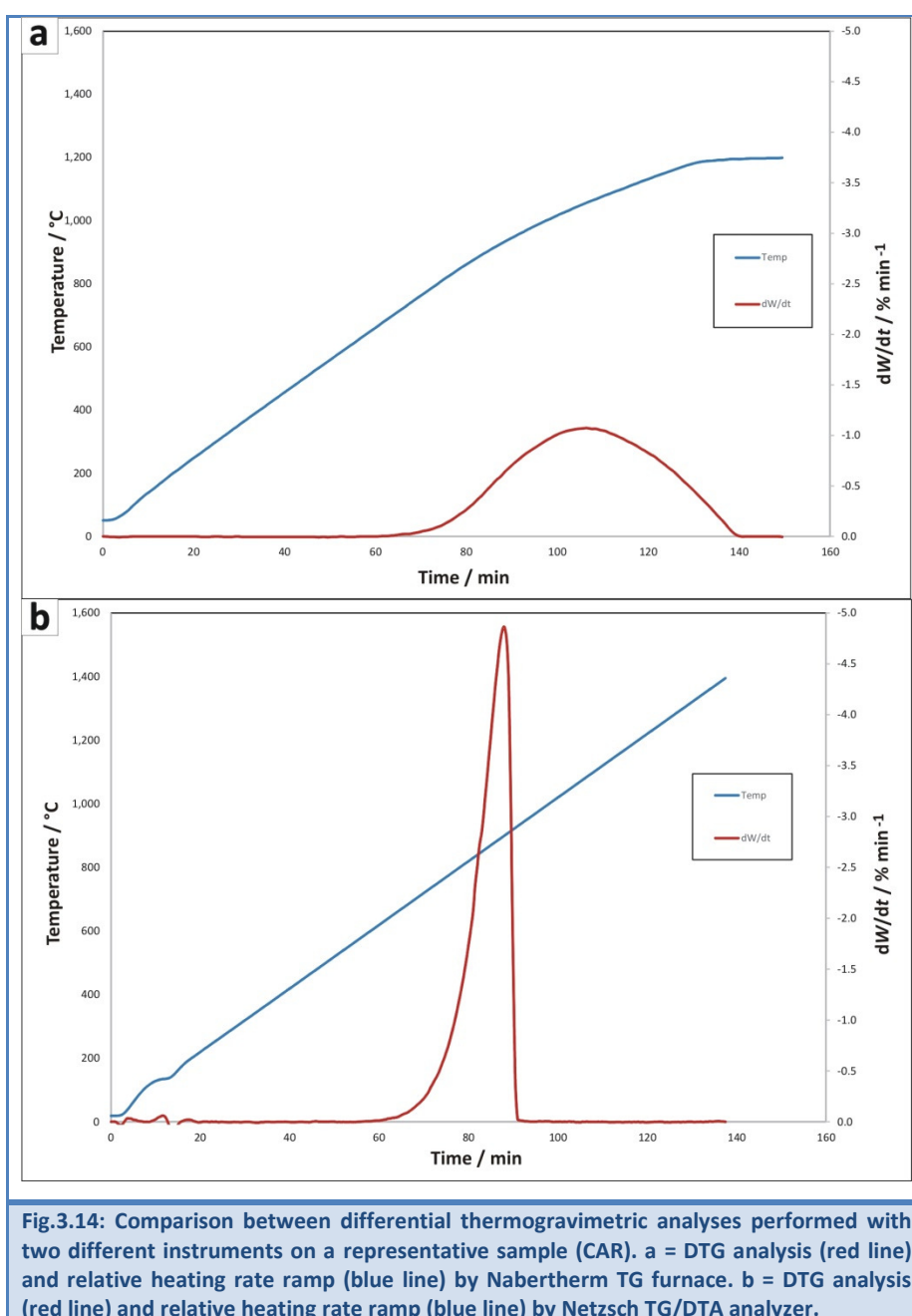
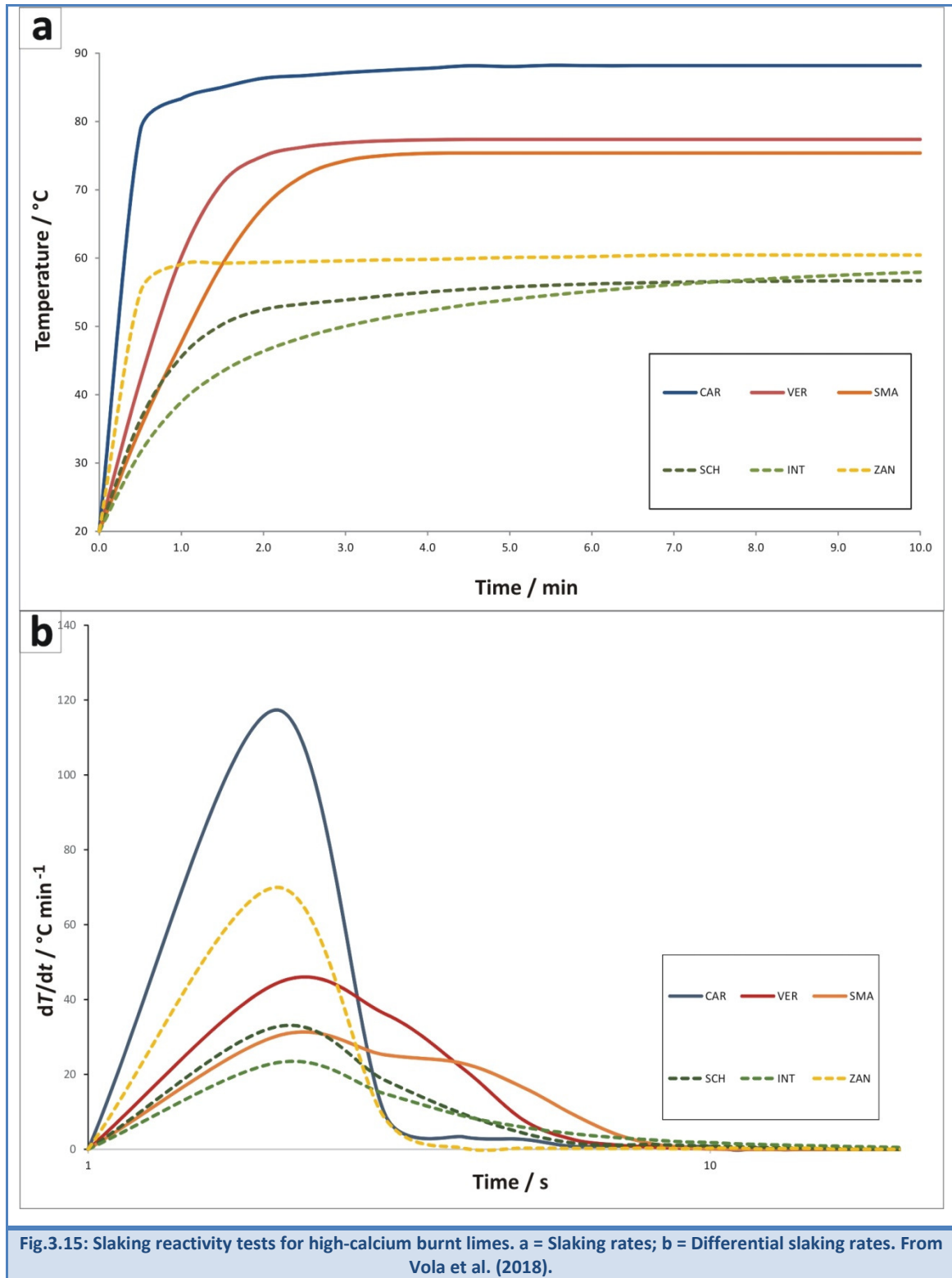


Fig.3.14: Comparison between differential thermogravimetric analyses performed with two different instruments on a representative sample (CAR). a = DTG analysis (red line) and relative heating rate ramp (blue line) by Nabertherm TG furnace. b = DTG analysis (red line) and relative heating rate ramp (blue line) by Netzsch TG/DTA analyzer.

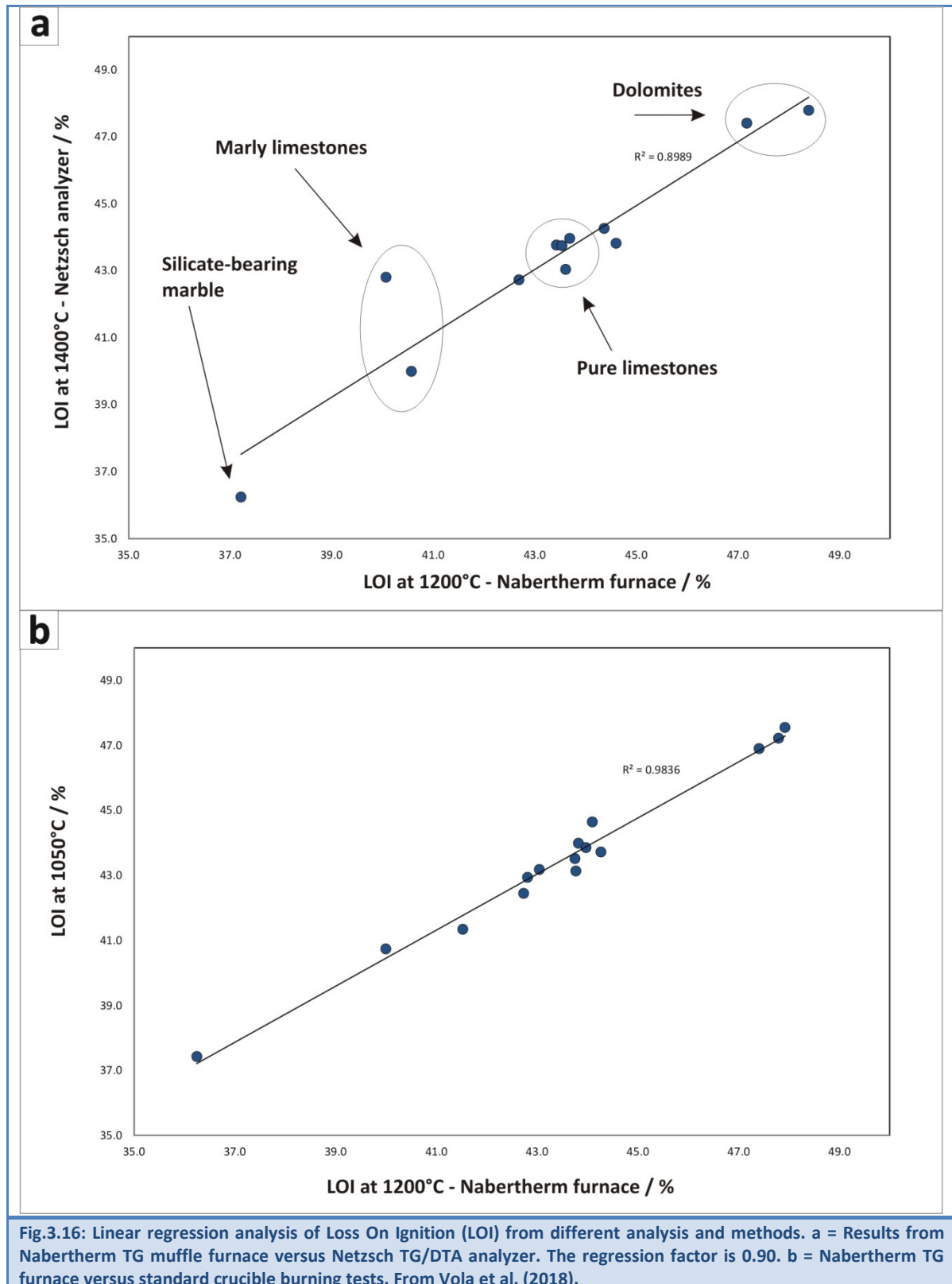


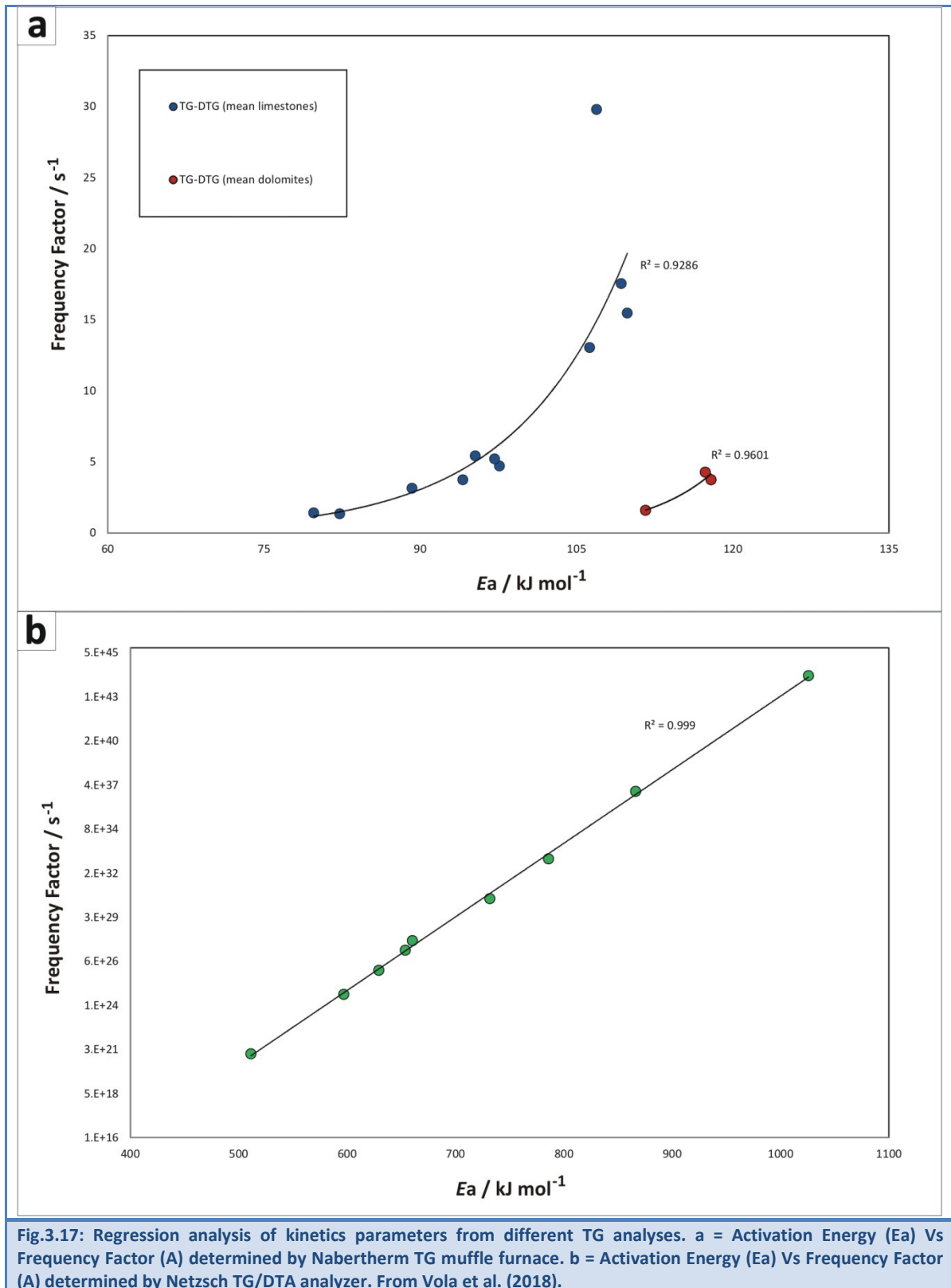
High-grade burnt lime products: impact of calcination kinetics on slaking reactivity; sticking tendency and blocks formation at HT (1300°C)

Chapter 3. Results and Discussion

Tab.3.22 – Measurement conditions and kinetic parameters and extrapolated from Nabertherm TG furnace and Netzsch TG/DTA analyzer. Activation energy and pre-exponential factor extrapolated from TG analyses according to Fuoss-Salymer-Wilson (FSW) method (Fuoss et al., 1964). Symbols legend: E_a = Activation Energy; A = Pre-exponential Factor; Dev. St. = Standard deviation; t = time; T = temperature.

Sample	Unit	1	2	3	4	5	6	7	8	9	10	11	12	13	14	15
code	-	598	2743	2001	2004	2828	1880	1990	1991	2462	2450	2829	1895	2830	2777	2112
name	-	SCH	INT	SAC	CMI	VER	QSC	IDW1	IDW2	SMA	PSP	CAR	CRM	ZAN	PED	MME
Nabertherm TG muffle furnace																
Starting time (t_1)	min	45.5	58.5	67.6	65.6	64.8	63.2	51.3	67.8	55.4	65.9	62.2	65.4	55.5	56.1	47.6
Max time (t_{max})	min	113.0	125.1	131.7	123.6	111.4	118.6	116.5	124.5	109.5	130.4	118.9	96.9	90.4	94.6	83.2
Ending time (t_2)	min	162.3	183.0	193.6	172.6	169.1	167.4	168.5	179.3	161.2	187.8	166.2	125.4	158.5	167.6	155.2
Δt (duration time)	min	116.8	124.5	126.0	107.0	104.3	104.2	117.2	111.5	105.8	121.8	104.0	60.0	103.0	111.5	107.7
Starting T (T_1)	°C	501.3	614.0	687.3	689.0	701.0	699.7	585.0	711.0	647.7	695.0	704.0	729.0	603.0	594.3	528.7
Max T (T_{max})	°C	968.7	974.4	1007.3	1028.3	989.4	1030.0	1018.0	1008.2	999.7	1015.0	1036.1	1011.5	867.7	837.6	810.3
Ending T (T_2)	°C	1157.2	1152.0	1182.3	1183.3	1187.8	1185.2	1187.2	1175.8	1177.2	1178.0	1183.3	1179.0	1145.3	1111.8	1139.7
ΔT (range)	°C	655.8	538.0	495.0	494.3	486.8	485.5	602.2	464.8	529.5	483.0	479.3	450.0	542.3	517.5	611.0
E_a (80g)	kJ mol ⁻¹	77.5	89.6	101.1	92.5	94.1	78.5	104.0	95.5	99.9	105.3	114.3	132.2	129.7	108.5	108.6
E_a (100g)	kJ mol ⁻¹	74.1	96.8	115.7	89.3	98.0	89.2	104.6	108.9	90.4	98.4	106.3	Nd	110.3	121.8	117.6
E_a (120g)	kJ mol ⁻¹	87.8	81.2	112.8	100.5	100.7	79.1	119.4	116.4	95.6	87.8	98.2	Nd	112.1	104.5	127.6
Mean	kJ mol ⁻¹	79.8	89.2	109.9	94.1	97.6	82.3	109.3	106.9	95.3	97.2	106.3	132.2	117.4	111.6	117.9
Dev.St.	kJ mol ⁻¹	7.2	7.8	7.7	5.7	3.3	6.0	8.7	10.6	4.8	8.8	8.1	-	10.7	9.1	9.5
A (80g)	s ⁻¹	1.3	2.9	6.2	3.6	4.3	1.1	11.1	4.8	9.7	9.9	25.4	236.6	10.5	0.9	2.2
A (100g)	s ⁻¹	0.7	5.5	23.7	1.9	4.1	2.1	9.1	57.7	2.5	4.2	9.7	Nd	0.8	3.5	3.0
A (120g)	s ⁻¹	2.3	1.0	16.5	5.7	5.7	0.9	32.5	26.9	4.1	1.6	4.1	Nd	1.5	0.4	6.0
Mean	s ⁻¹	1.4	3.1	15.5	3.7	4.7	1.4	17.6	29.8	5.4	5.2	13.0	236.6	4.3	1.6	3.7
Dev.St.	s ⁻¹	0.8	2.3	8.8	1.9	0.8	0.6	13.0	26.6	3.8	4.3	11.0	-	5.4	1.6	2.0
Netzsch TG/DTA analyzer																
E_a (90mg)	kJ mol ⁻¹	660.3	910.8	866.3	1026.0	597.0	511.2	629.3	731.8	653.7	585.1	785.9	712.8	799.6	811.8	804.3
A (90mg)	s ⁻¹	1.1E+28	8.9E+38	1.6E+37	1.9E+44	5.9E+24	1.4E+21	1.8E+26	4.3E+30	3.0E+27	4.5E+23	1.2E+33	1.1E+30	6.5E+25	1.8E+28	1.5E+26
Decomposition	mVs	898.6	910.6	905.4	907.1	916	917.2	915.5	924.4	909.6	944.4	923.6	927			
Enthalpy (ΔH)	mVs mg ⁻¹	-17961	-14083	-18890	-19993	-20159	-23883	-21682	-25645	-20535	-22571	-24605	-26081	-16042	-13445	-26695
Specific heat	mVs K ⁻¹	-196	-163	-229.4	-242.5	-216.8	-284.6	-239.2	-269.2	-229.4	-168.5	-282.9	-262.4	-203	-113.96	-219
capacity (ΔC_p)	mVs g ⁻¹ K ⁻¹	0.0320	0.0465	0.0864	0.0471	0.0061	0.0357	0.0263	0.0009	0.0269	0.0742	0.1064	0.0466	0.1	0.0382	0.2





Tab.3.23 – Slaking reactivity of quicklimes burnt at 1200 °C. Symbols legend: MHR (1200 °C) = Max Heating Rate according to modified ASTM C110; MHR (1150-1250°C) = Max Heating Rate according to EN 459-2 (average); ND = Not Determined; NR = Not Reached.

Sample	Unit	1	2	3	4	5	6	7	8	9	10	11	12	13	14	15
Code		598	2743	2001	2004	2829	1880	1990	1991	1992	2450	1895	2828	2830	1777	2112
Name	-	SCH	INT	SAC	CMI	VER	QSC	IDW1	IDW2	SMA	PSP	CRM	CAR	ZAN	PED	MME
$\Delta T_{30^\circ\text{C}} (t_{50})$	min	1.94	2.99	0.57	0.83	0.72	0.80	1.50	0.71	1.10	0.40	ND	0.26	0.43	0.94	0.40
$\Delta T_{30^\circ\text{C}} (t_{50})$	s	116.5	179.6	34.1	49.7	43.1	48.0	90.0	42.7	66.1	23.9	ND	15.3	25.7	56.7	23.8
$\Delta T_{40^\circ\text{C}} (t_{60})$	min	NR	NR	0.82	1.90	1.00	1.51	2.12	1.69	1.55	0.83	ND	0.34	4.72	NR	NR
$\Delta T_{40^\circ\text{C}} (t_{60})$	s	NR	NR	59.2	234.0	59.7	67.1	127.3	101.3	93.2	49.6	ND	20.5	0.5	NR	NR
T_{max}	°C	56.7	59.2	79.9	71.4	77.4	74.6	68.95	74.5	75.4	72.4	ND	88.2	61.2	55.2	56.9
$T_{\text{max}} t_{\text{max}}^{-1}$	°C min ⁻¹	6.0	3.2	9.4	6.3	17.2	5.7	11.5	4.0	16.8	8.5	ND	19.6	6.4	22.1	5.7
MHR (1200 °C)	°C min ⁻¹	32.6	23.0	54.5	48.2	44.2	45.2	31.7	53.0	30.1	75.2	ND	93.6	69.9	66.4	75.8
MHR (1150-1250 °C)	°C min ⁻¹	16.8	13.6	36.7	45.5	25.6	36.1	23.7	17.1	17.1	58.4	ND	37.7	91.6	57.5	39.1

Tab.3.24 – Physical-chemical-mineralogical analyses of limes burnt at 1200 °C. Symbols legend: BET SSA =Specific Surface Area; ALI = Available Lime Index; ND = Not Determined.

Sample	Unit	1	2	3	4	5	6	7	8	9	10	11	12	13	14	15
Code	-	598	2743	2001	2004	2829	1880	1990	1991	1992	2450	1895	2828	2830	1777	2112
Name	-	SCH	INT	SAC	CMI	VER	QSC	IDW1	IDW2	SMA	PSP	CRM	CAR	ZAN	PED	MME
Real density	g cm ⁻³	3.20	3.26	3.28	3.25	3.21	3.28	3.30	3.27	3.22	3.27	3.18	3.21	3.19	3.30	3.25
BET SSA	m ² g ⁻¹	0.32	0.47	0.35	0.48	0.49	0.37	0.29	0.33	0.29	0.50	0.39	0.72	3.00	1.77	1.97
ALI	%	Nd	Nd	96.8	95.8	92.0	96.4	Nd	Nd	87.4	95.9	ND	96.8	Nd	Nd	Nd
Lime (CaO)	%	56.0	67.6	99.3	99.2	89.5	100	85.7	89.9	89.2	100	ND	98.2	65.1	59.8	57.9
Periclase (MgO)	%		0.2	0.6				0.2	0.3	0.2		ND	1.3	35.0	40.2	39.0
Calcite (CaCO ₃)	%											ND	0.5			
Larnite (Ca ₂ SiO ₄)	%	29.8	28.8			9.1		10.0	1.4	8.6		ND				
Hatrurite (Ca ₃ SiO ₅)	%	1.0			0.2					0.2		ND				
Tricalcium Aluminate (Ca ₃ Al ₂ O ₆)	%	4.9			0.8					0.7		ND				
Brownmillerite (Ca ₂ (Al,Fe) ₂ O ₅)	%	8.0	3.6			1.5				1.1		ND				3.2
Ca ₂ (MnO ₄)	%							1.8	2.9			ND				
Ca ₃ (SiO ₄)O	%							0.6	5.9			ND				
Gehlenite Ca ₂ Al(AlSi)O ₇	%							1.5				ND				
Portlandite Ca(OH) ₂	%	<0.5	<0.5	<0.5	<0.5	<0.5	<0.5	<0.5	<0.5	<0.5	<0.5	<0.5	<0.5	<0.5	<0.5	<0.5

High-grade burnt lime products: impact of calcination kinetics on slaking reactivity; sticking tendency and blocks formation at HT (1300°C)

- *Burnt limes characterization*

Burnt limes from the TG-DTG analysis by Nabertherm furnace were pulverized to perform the slaking reactivity, according to the modified American test (ASTM C110, 2016) (Fig.3.15). Quicklime reactivity was reported in terms of temperature rise ($\Delta T_{30^\circ\text{C}}$ or t_{50} and $\Delta T_{40^\circ\text{C}}$ or t_{60}), maximum slaking temperature (T_{max}), heating rate at the maximum slaking temperature ($^\circ\text{C min}^{-1}$) and, finally, the maximum heating rate ($^\circ\text{C min}^{-1}$) (Tab.3.23). The reactivity was high for high-calcium limes, i.e. $t_{60} = 1.3 \pm 0.6$ min and $T_{\text{max}} = 75.9 \pm 5.6$ $^\circ\text{C}$, and very high for magnesium-rich limes, i.e. $t_{50} = 0.6 \pm 0.3$ $^\circ\text{C}$ and $T_{\text{max}} = 57.8 \pm 3.1$ $^\circ\text{C}$. Conversely, hydraulic limes presented medium-low reactivity, i.e. $t_{50} = 2.5 \pm 0.7$ min and $T_{\text{max}} = 57.9 \pm 1.8$ $^\circ\text{C}$, according to their low available lime and relatively high impurity content. These results are consistent with average results from slaking tests performed at 1150 $^\circ\text{C}$ and 1250 $^\circ\text{C}$ in conformity to the European test (UNI-EN 459-2, 2010) (Tab.3.23). The residual material from TG-DTG analysis was adopted to perform the ALI, the real density, the BET specific surface area measurements and the quantitative phase analysis (XRD-QPA) (

Tab.3.24). The ALI, determined just on high-calcium limes, was $94.4 \pm 3.5\%$; the average BET surface area 0.43 ± 0.1 m^2g^{-1} , and the average real density 3.28 ± 0.1 g/cm^{-3} , respectively. These values are consistent with ones reported in the literature for limes burnt at high temperatures (Eades and Sandberg, 1970). The XRD-QPA analysis pointed out the following fundamental mineral phases: lime (CaO) in calcitic quicklimes; lime (CaO) plus periclase (MgO) in magnesium-rich ones. Cementitious mineral phases were detected as subordinated constituents, reaching a maximum content in feebly up to moderately hydraulic limes (VER, IDW1, SMA). These samples presented about 8-10% of larnite (Ca_2SiO_4), while hatrurite (Ca_3SiO_5), tricalcium aluminate ($\text{Ca}_3\text{Al}_2\text{O}_6$) and brownmillerite ($\text{Ca}_2(\text{Al,Fe})_2\text{O}_5$) were always $<1\%$. Moreover, South African samples from Neoproterozoic limestone (IDW1 and IDW2) presented some manganese compounds, i.e. $\text{Ca}_2(\text{MnO}_4)$ and $\text{Ca}_3(\text{SiO}_4)\text{O}$, plus gehlenite $\text{Ca}_2\text{Al}(\text{AlSi})\text{O}_7$, as already reported in the literature (Vola et al., 2017). Finally, eminently hydraulic limes pointed out the presence of lime (CaO) and larnite (Ca_2SiO_4) as main mineral phases, associated with hatrurite (Ca_3SiO_5), tri-calcium aluminate ($\text{Ca}_3\text{Al}_2\text{O}_6$) and brownmillerite ($\text{Ca}_2(\text{Al,Fe})_2\text{O}_5$) as subordinated mineral constituents. Traces of portlandite ($\text{Ca}(\text{OH})_2$) were always observed (Tab.3.24).

3.3.13 Discussion

- *Nabertherm method validation*

Initially, Ignition Losses (LOI) determined by the Nabertherm TG muffle furnace at 1200 °C were plotted against LOI determined by the Netzsch TG-DTA analyzer at 1400 °C (Fig.3.16a). Subsequently, ignition losses (LOI) determined by Nabertherm TG muffle furnace were plotted against LOI from burning tests on crucible at 1050°C. The linear regression analysis confirms an acceptable accuracy and data reproducibility (regression factors are 0.89 and 0.99, respectively). Conversely, kinetic parameters, extrapolated according to Fuoss-Salymer-Wilson (FSW) method (Fuoss et al., 1964), were considerably different. In particular the average activation energy (E_a) extrapolated from the Netzsch analyzer was one order of magnitude larger than the equivalent parameter from the Nabertherm furnace, while the pre-exponential or frequency factor (A) was several orders of magnitude larger compared to its analog. Both sets of kinetic parameters (E_a and A) are correlated, attesting the FSW method was correctly applied (Fig.3.17a-b). Calcination duration times and frequency factors also fit well by exponential regression analysis (Fig.3.18). For instance, in this specific case-study, the large scattering of the kinetic data between different devices is mainly dependent to the following factors:

1. the sample mass, i.e. the differential mass factor is about 2000 times;
2. the particle-size distribution, i.e. the differential size factor is about 200 times;
3. the thermal conductivity and the heat flow (differential factors are not known, but wide).

Moreover results are also affected by the FSW mathematical approach, which requires the heating rate be strictly linear and is based on the determination of the inflection point from a single TG analysis (Fuoss et al., 1964). According to this method, samples having very steep TG curves, i.e. ones from Netzsch analyzer, presented larger activation energies than samples having smooth TG curves, i.e. ones from Nabertherm furnace. The enhanced factors represent the most critical issues of the FSW method. Considering that kinetic values from Nabertherm furnace are consistent with ones from the literature (Boynton 1982; Oates, 1998; Soltan and Serry, 2011; Kiliç, 2013; Alaabed et al., 2014), it is possible to conclude that the FSW method is suitable for the first device, while more accurate results by Netzsch analyzer could be obtained adopting other methods,

based on a different mathematical approach (Doyle, 1962; Ozawa, 1965; Flynn and Wall, 1966).

- *LOI relevance*

Though the LOI is an easily detectable parameter; it allows distinguishing between pure and impure carbonates, because reflecting the total amount of carbonate minerals. The highest values, i.e. $LOI \approx 47\%$, are related to the calcination of pure dolomites, while pure limestones pointed out $LOI \approx 44\%$. Conversely, the lowest value, i.e. LOI of 36.8% , was related to the calcination of an impure silicate-bearing marble (CRM). Other two samples presenting an “anomalous” low ignition loss were identified to be marly limestones (SCH and INT), according to their chemical, mineralogical and petrographic compositions (Tab.3.18, Tab.3.20, and Fig.3.16a). The presence of non-carbonate impurities, such as organic matter, sulfates, and clay minerals can be detected by thermogravimetry. However, overlapping reactions make critical the quantitative determination of these compounds in a polycrystalline matrix. For this reason supplementary analytical techniques such as Wavelength Dispersive X-ray Fluorescence Spectroscopy (XRF-WDS), Quantitative Phase Analysis by X-ray Powder Diffraction (XRD-QPA), and Optical Polarized Microscopy (OPM), were adopted to complete the characterization of raw materials.

- *Burnability of carbonate rocks*

Considering the same experimental calcination conditions, particle-size distribution and mass, differences in calcination rates must be related to intrinsic or geological features of carbonate rocks, including chemical and mineralogical compositions, depositional textures and diagenetic or metamorphic modifications. Main differences in burnability between high-calcium, hydraulic and dolomitic limes can be visualized by means of TG-DTG plots on 5 representative samples (Fig.3.19). Effectively, more details between similar samples can be appreciated by the statistical analysis of kinetic parameters plotted against the micrite to sparite ratio (MSR). The regression analysis pointed out the inverse logarithmic correlation between the MSR and the activation energy (Fig.3.20a), and straight logarithmic correlation between the MSR and the calcination duration time (Fig.3.20b). This fact means that mud-supported or microcrystalline and marly limestones generally presented lower activation energies and higher calcination duration times;

conversely crystalline carbonates, constituted by grain-supported limestones with dominant equant or poikilotopic calcite cement, hypidiotopic dolomites and idiomorphic marbles, presented higher activation energies and lower calcination duration times. Results are consistent with ones recently obtained on different lithofacies of the Neoproterozoic limestone from the Transvaal Supergroup, South Africa (Vola et al., 2017).

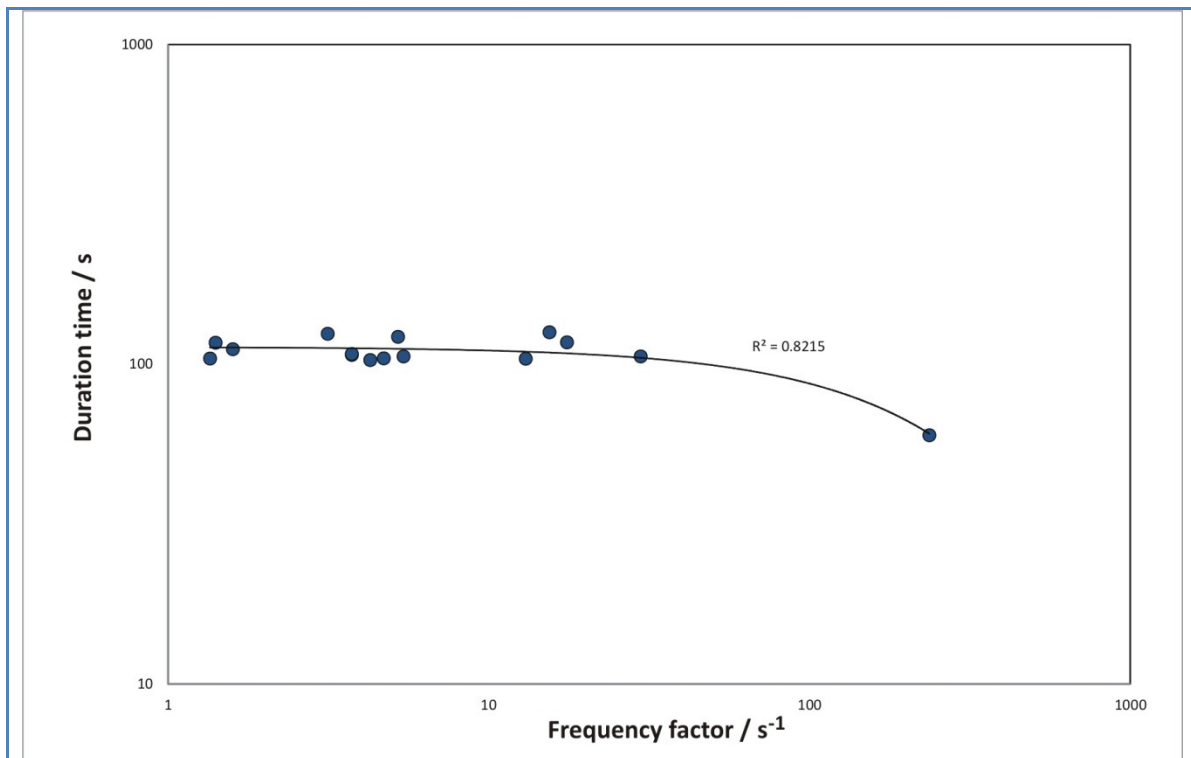
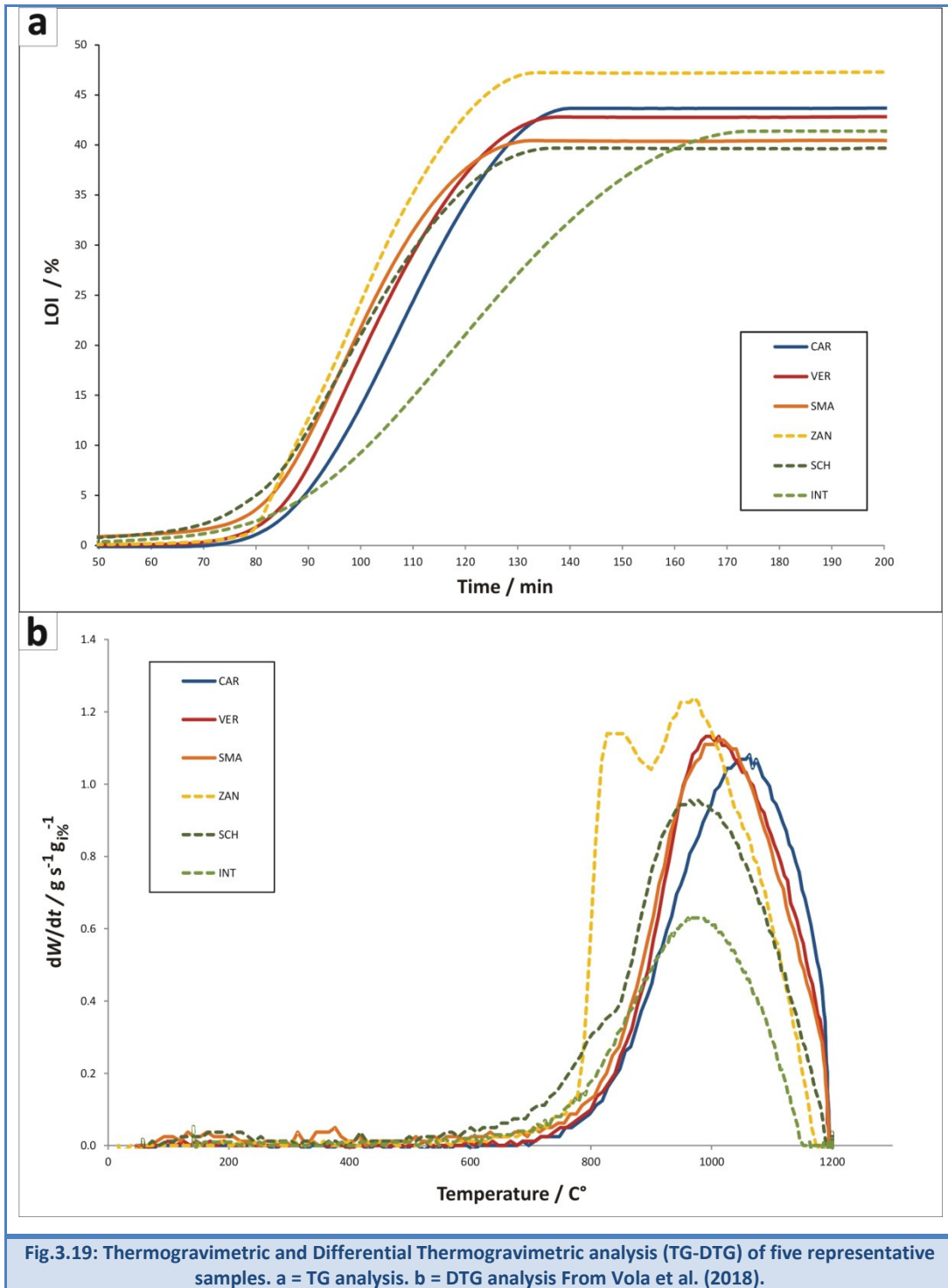
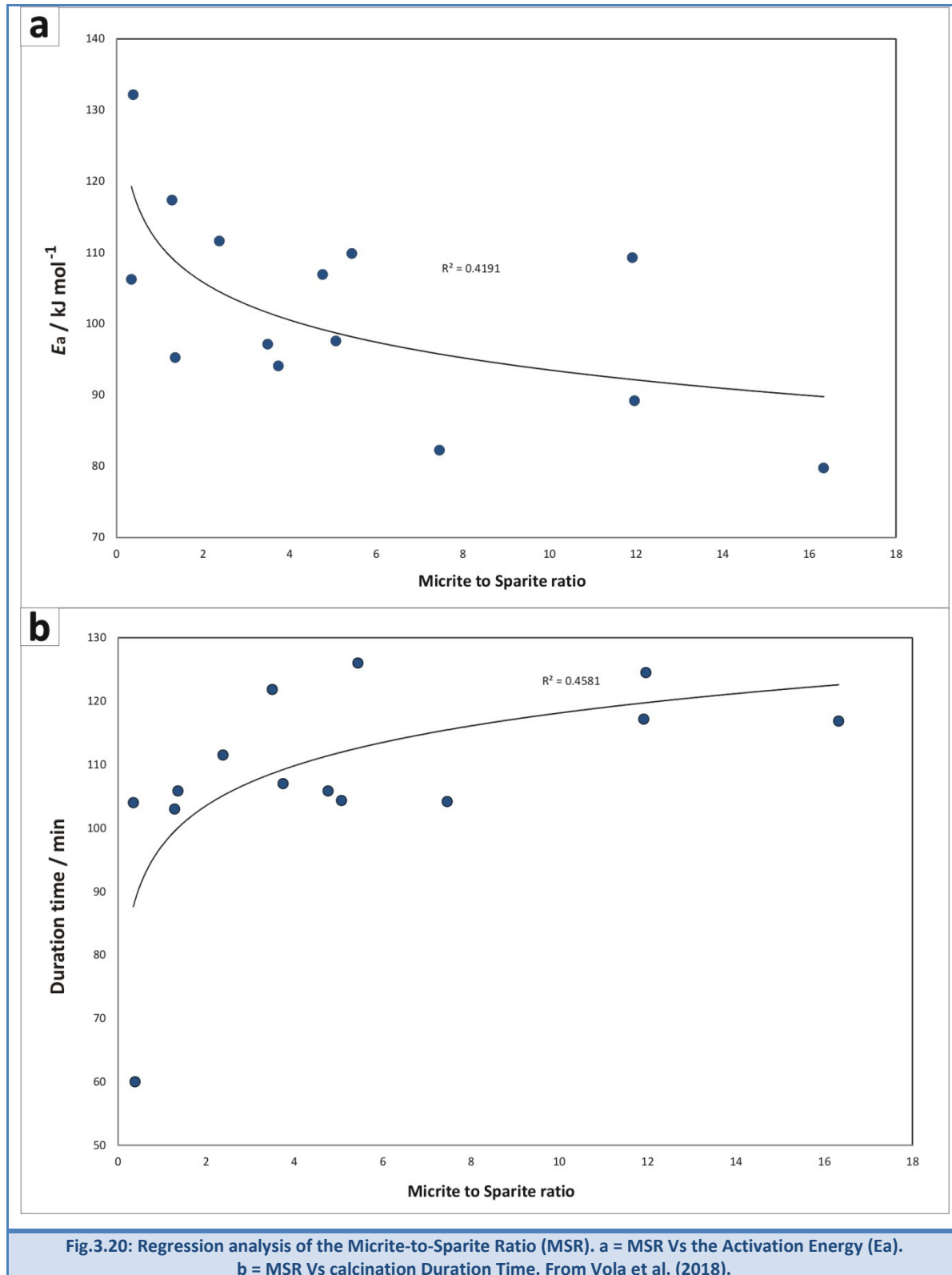


Fig.3.18: Regression analysis of Frequency Factor (A) Vs calcination duration time. TG-DTG analyses performed by Nabertherm furnace. From Vola et al. (2018).





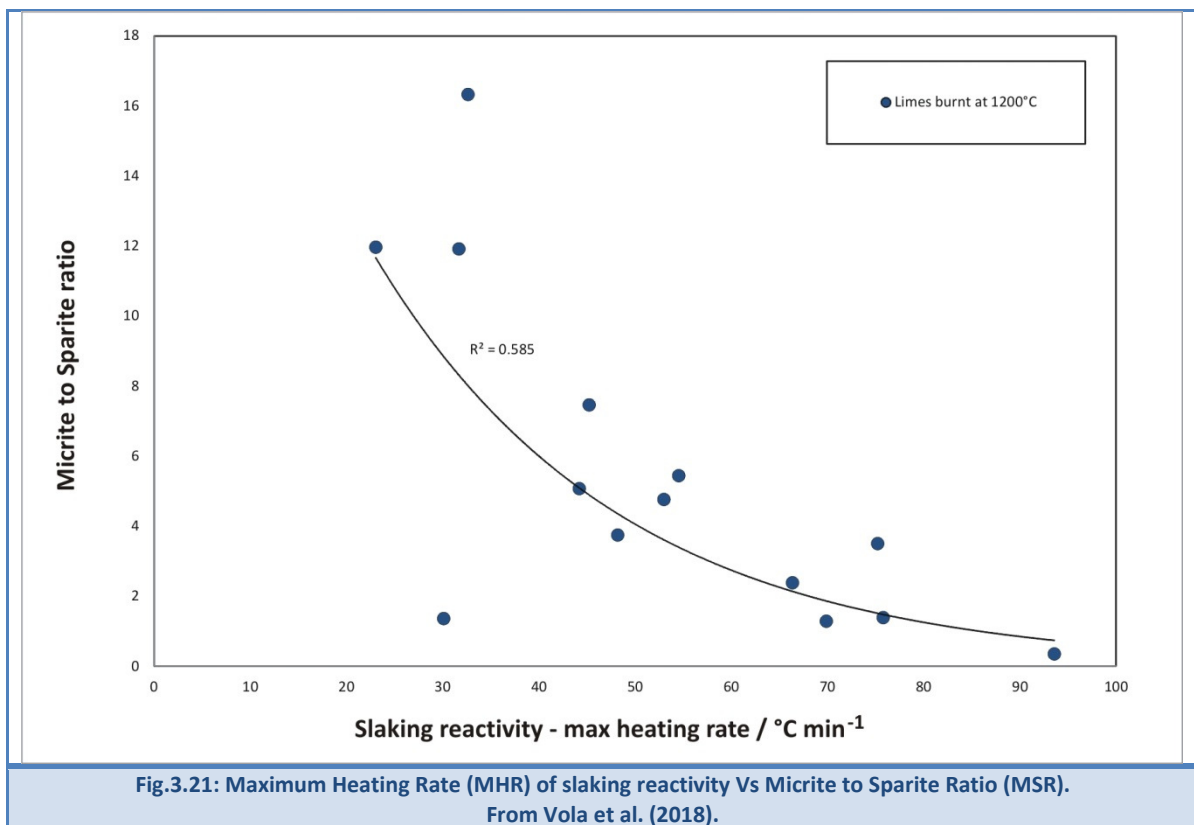


Fig.3.21: Maximum Heating Rate (MHR) of slaking reactivity Vs Micrite to Sparite Ratio (MSR). From Vola et al. (2018).

- *Impact of intrinsic features and derived properties on quicklime reactivity*

A significant result of this research study is represented by the linear correlation between the slaking reactivity of burnt limes and the intrinsic or geological features of carbonate rocks, i.e. either the activation energy (E_a), or the micrite to sparite ratio (MSR). In particular Fig.3.21 highlights the inverse logarithmic correlation between the slaking reactivity maximum heating rate and the micrite to sparite ratio (MSR). It is obvious that large differences in chemical and mineralogical composition affect the slaking lime reactivity too (Wright, 1985; Hogewoning et al., 2008; Baziotis et al., 2011; Akande et al., 2016). This fact is particularly evident comparing pure, i.e. high-calcium limes, and impure samples, i.e. hydraulic limes (Fig.3.23a-b). Higher is the impurity content, i.e. the insoluble residue, lower is the temperature rise, and thus the quicklime reactivity. The quality of impurity plays a significant role in the lime mineralogical composition and reactivity, especially at high burning temperatures (Boynton, 1982). For instance halites and other fluxes can promote the formation of liquid phase and the reaction between lime (CaO) and larnite (Ca₂SiO₄) to form hatrurite (Ca₃SiO₅) (Elsen et al., 2011).

Moreover we investigated the impact of derived physical parameters of burnt limes on slaking rates. Indeed Fig.3.22 reports the correlation between the slaking reactivity and

the BET specific surface area. This factor is considered important in the rate of lime slaking, as well as, the fineness (Boynton, 1982). Effectively, the exponential correlation between the Maximum Heating Rate (MHR) of the slaking reactivity and the BET measurements is reported in Fig.3.22. Finally, the inverse correlation between the real density and the BET specific surface area of high-calcium and dolomitic limes is shown in Fig.3.24. Unfortunately, the real density by gas pycnometry didn't show any significant correlation with reactivity parameters. Therefore fundamental parameters controlling increasing/decreasing effects on slaking reactivity are identified to be the calcination rate, the micrite to sparite ratio, and the specific surface area. This last parameter is significant because reflects the specific sintering tendency of the lime and is strictly related to the calcinations conditions, i.e. the maximum heating temperature and, only in a subordinate way, the retention time. According to the literature (Eades and Sandberg, 1970; Borgwardt and Bruce, 1986; Commandré et al., 2007) none of these parameters is sufficient to exactly predict the quicklime reactivity. However a detailed multidisciplinary analytical characterization allows putting further constraints in selecting the best raw materials and helps in optimizing the process to achieve the target quality with a given material.

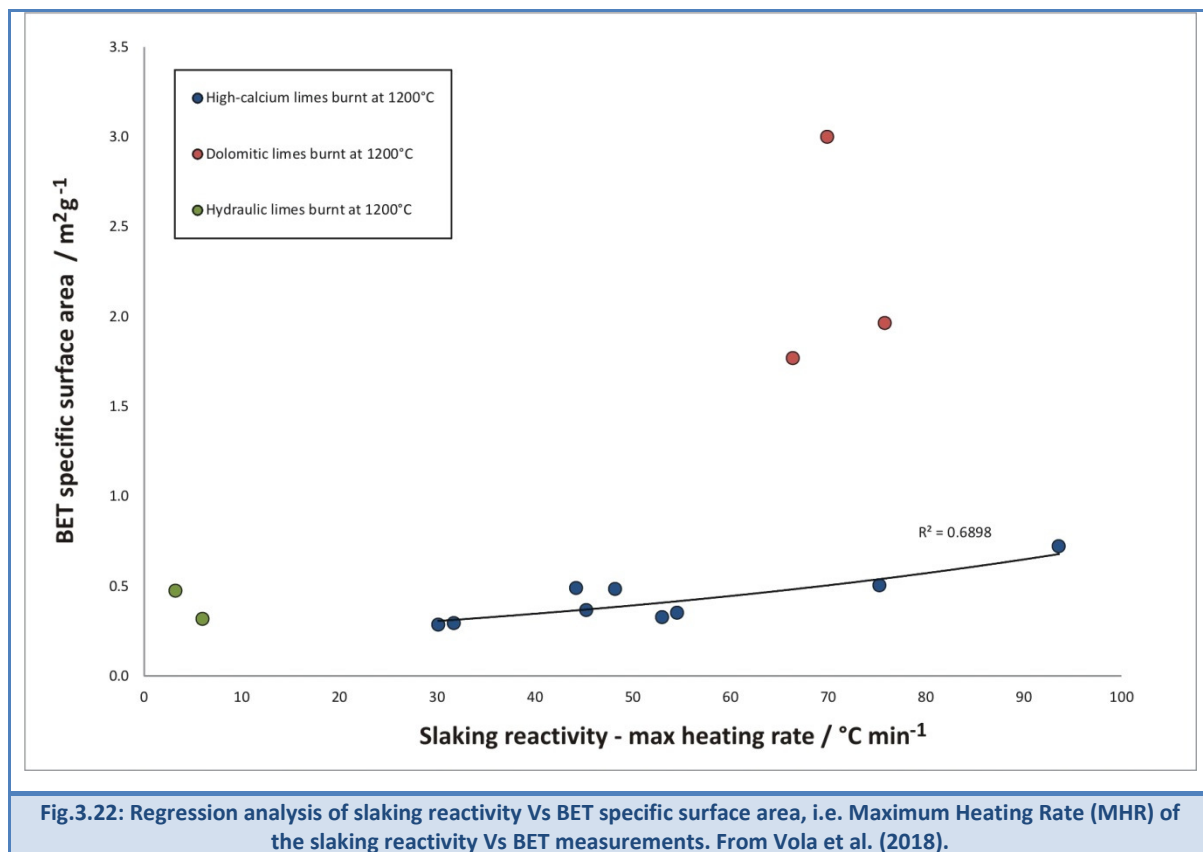


Fig.3.22: Regression analysis of slaking reactivity Vs BET specific surface area, i.e. Maximum Heating Rate (MHR) of the slaking reactivity Vs BET measurements. From Vola et al. (2018).

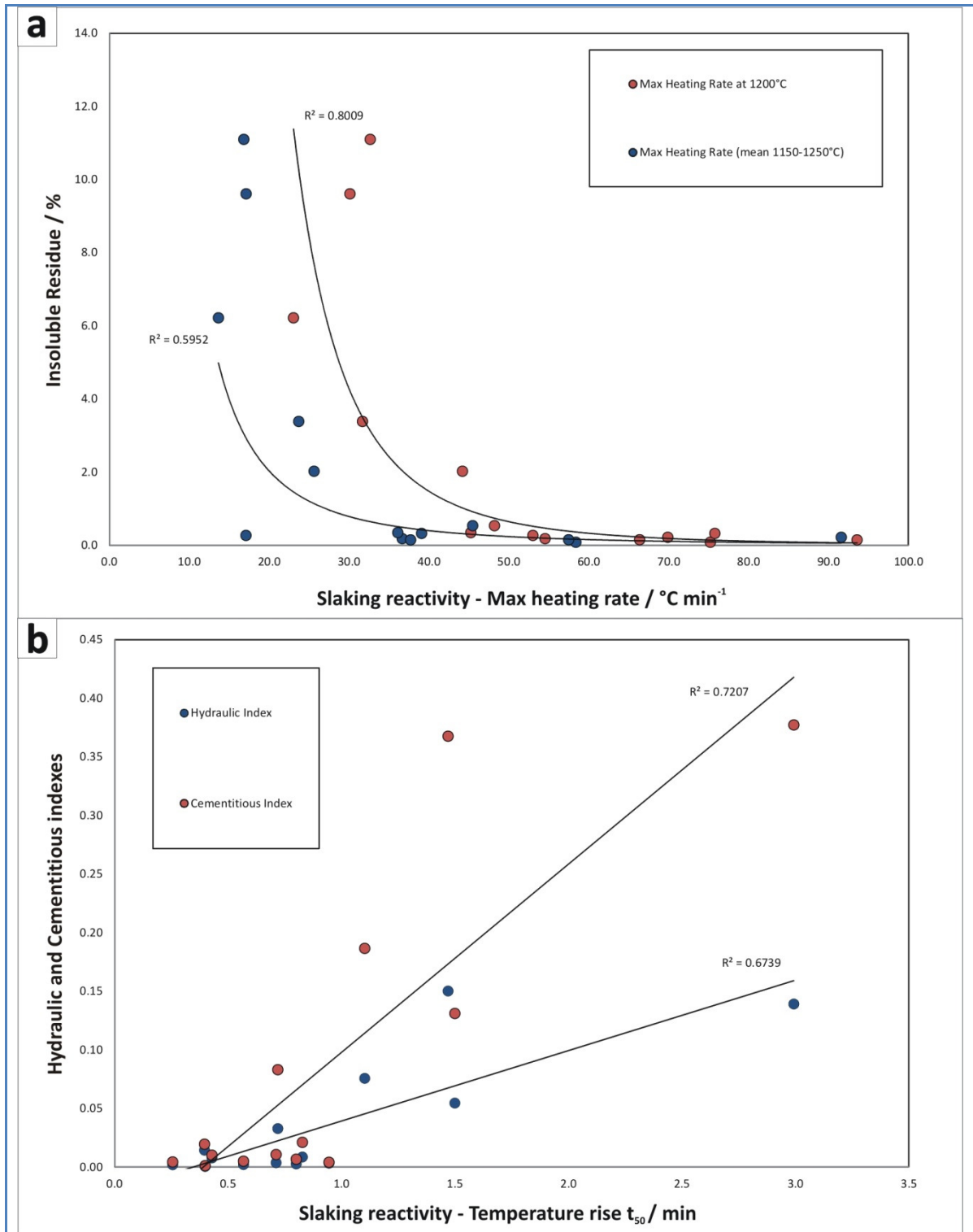


Fig.3.23: Regression analysis of chemical factors Vs slaking reactivity. a = Insoluble Residue Vs Maximum Heating Rate of the slaking reactivity. Double sets of data are plotted: blue points represent reactivity of limes according to the modified American test ASTM C110 (2016); red points represent the average reactivity of lime samples according to the European test EN 459-2. Cementitious and Hydraulic Indexes Vs Slaking reactivity temperature rise (t_{50}). From Vola et al. (2018).

3.3.14 Conclusions

The preliminary result of this work was the validation of TG-DTG analyses performed on massive samples, by means of comparison between the Nabertherm TG furnace and the Netzsch TG-DTA analyzer. Experimental activity allowed reaching the following conclusions:

1. The linear regression analysis between LOI measurements performed by the Nabertherm muffle furnace and the Netzsch analyzer pointed out acceptable data reproducibility (the regression factor is 0.90) (Fig.3.16).
2. The optimum sample mass to test with the Nabertherm furnace is about 80-120 g. Calcination kinetic parameters extrapolated according to Fuoss-Salymer-Wilson (FSW) method by Nabertherm furnace and Netzsch analyzer are not comparable in magnitudes because reaction rates reflect differential samples mass, particle-size distribution, thermal conductivity, and heat flux.
3. The Arrhenius parameters, i.e. the activation energy (E_a) and the pre-exponential or frequency factor (A), extrapolated by Nabertherm furnace on massive samples by the FSW method are fully consistent with data from the literature ($E_{a \text{ mean}} = 103.7 \pm 14.2 \text{ kJmol}^{-1}$; $A \text{ mean} = 23.5 \pm 59.5 \text{ s}^{-1}$).

Subsequently, kinetic parameters by Nabertherm furnace were investigated in order to point out possible relationships between intrinsic or geological features of carbonate rocks, and derived technical properties of burnt lime products. For this purpose it was adopted the so-called “Micrite to Sparite ratio” (MSR), a mineralogical-petrographic factor suitable for distinguishing carbonate rocks burnability. Indeed, the fundamental following correlations were observed:

1. The inverse logarithmic correlation between the MSR and E_a (the regression factor is 0.42) (Fig.3.20a);
2. The logarithmic correlation between the MSR and the calcination duration time (the regression factor is 0.45) (Fig.3.20b);
3. The inverse logarithmic correlation between the Max Heating Rate (MHR) of the slaking reactivity and the MSR (the regression factor is 0.59 for limes burnt at 1200 °C) (Fig.3.21);
4. The inverse potential correlation between the Max Heating Rate (MHR) of the slaking reactivity and the impurity content, i.e. the insoluble residue (regression

factors are 0.81 for limes burnt at 1200 °C, and 0.60 for limes burnt at 1150-1250°C, respectively) (Fig.3.23a);

5. The linear correlation between the slaking reactivity, i.e. t_{50} , and the cementitious/hydraulic indexes (regression factors are 0.72 and 0.67, for HI and CI, respectively) (Fig.3.23b);
6. The exponential correlation between the Maximum Heating Rate (MHR) of the slaking reactivity, and the BET specific surface area (regression factor is 0.69 for high-calcium limes burnt at 1200 °C) (Fig.3.22);
7. The inverse linear correlation between the real density and the BET specific surface area of limes burnt at 1200 °C (regression factors are 0.68 and 0.93 for high-calcium and dolomitic limes, respectively) (Fig.3.24).

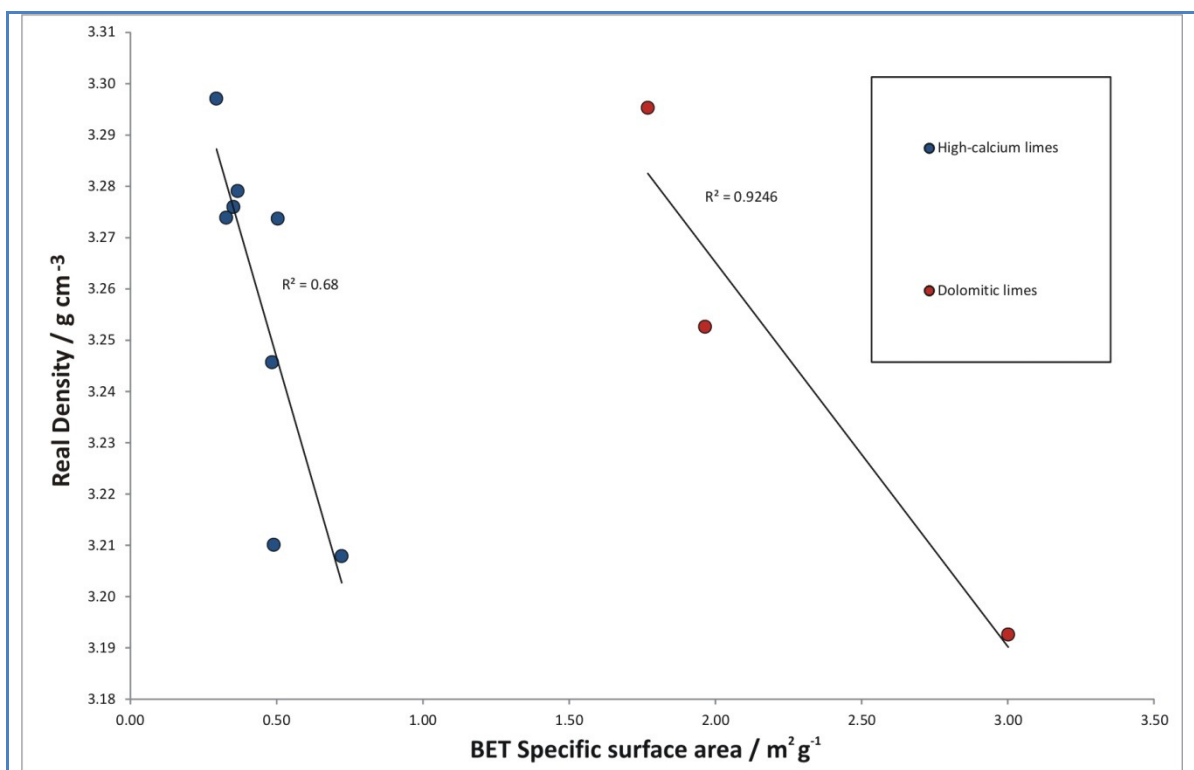


Fig.3.24: Regression analysis of BET specific surface area Vs Real Density by gas pycnometry. From Vola et al. (2018).

3.3.15 Acknowledgements

Authors gratefully acknowledge helpful peer-review of the manuscript by the blind reviewers. We also would like to thank you Prof. Daniele Mazza (PoliTo) for useful suggestions and discussions on kinetics parameters and the FSW method.

3.3.16 Final remarks

The regression analysis between the considered parameters has to be corroborated with statistical assessment test. The correlation coefficient r is assumed as criterion of evaluation of existence of significant correlation between the considered variables. However the correlation coefficient r in general is not sufficiently probative and must be accompanied by the Student's t statistical test. This is particularly necessary when, as for most of the correlations reported, r is less than 0.5. Usually the correlation is considered strong when r is greater than 0.8. The hypothesis that among the variables considered there is an effective correlation is usually verified by means of the following expression:

$$t_{\text{calculated}} > t(v, 1 - \alpha)$$

Where $t(v, 1 - \alpha)$ is the theoretical value deduced from the table of t for v degrees of freedom and $1 - \alpha$ level of significance (risk of not true hypothesis) according to the Student's t -distribution developed by William Sealy Gosset under the pseudonym Student (Student, 1908). Student's t statistical test was then applied to correlations reported into the paper. Results reported in

Tab.3.25 confirmed the validity of the statistical analyses performed.

Tab.3.25 – Student's t statistical test applied to correlation reported into the paper. Symbols legend: 1 = Frequency Factor (A) Vs Duration time (min); 2 = Micrite-to-Sparite Ratio (MSR) Vs Activation Energy (Ea); 3 = Micrite-to-Sparite Ratio (MSR) Vs Frequency Factor (A); 4 = slaking reactivity – Max Heating Rate (MHR) at 1200°C Vs MSR; slaking reactivity - – Max Heating Rate (MHR) at 1200 °C Vs Insoluble Residue (IR); 5 = slaking reactivity - Max Heating Rate (MHR) at 1150-1250°C (average) Vs Insoluble Residue (IR); 7 = slaking reactivity - t50 Vs Hydraulic Index (HI); 8 = slaking reactivity - t50 Vs Cementitious Index (CI); 9 = slaking reactivity - Max Heating Rate (MHR) at 1200°C Vs BET Specific Surface Area (BET-SSA); 10 = BET SSA Vs Real Density; * = the BET value for sample SMA was not considered on this correlation because considered outlayer.

Corrleation no.	1	2	3	4	5	6	7	8	9	10*
Correlation type	exp	log	log	exp	pot	pot	linear	linear	exp	linear
Correlation coefficient - r	-0.91	-0.66	0.67	-0.76	0.86	0.66	0.82	0.85	0.83	-0.82
Linear regression coefficient - R2	0.82	0.44	0.44	0.58	0.74	0.44	0.67	0.72	0.69	0.68
Observations number - N	15.00	15.00	15.00	14.00	14.00	14.00	14.50	14.50	9.00	8.50
Freedom Degree - v	13.00	13.00	13.00	12.00	12.00	12.00	12.50	12.50	7.00	6.50
Calcolated t-Student	-7.73	-3.20	3.22	-4.11	5.88	3.07	5.08	5.68	3.95	-3.72
Significance level - alpha	0.05	0.05	0.05	0.05	0.05	0.05	0.05	0.05	0.05	0.05
Theoretical t-Student (2 tails)	2.16	2.16	2.16	2.18	2.18	2.18	2.18	2.18	2.36	2.45
Correlation check	ok	ok	ok	ok	ok	ok	ok	ok	ok	ok

3.4 Article no. 3. Investigation and prediction of lime agglomeration, blocks formation, sticking tendency and occasional melting by Cimprogetti's Overburning Test method for industrial quicklime production

This article was written in August 2018 by G. Vola with the contribution of G. Brignoli, E. Rodeghero, C. Natali, G. Bianchini and G. Cruciani. The work has been recently submitted to *Construction and Building Materials*, and is still under revision.

3.4.1 Abstract

This study deals with the thermal behaviour characterization of 46 carbonate rocks selected for the industrial manufacture of lime products in vertical shaft kilns worldwide. The so-called "Overburning Test" (OT) method was performed to simulate and predict blocks formation, sticking tendency (ST), and occasional melting at 1300°C, which is ideally considered the highest temperature in lime kilns. Thus high-grade limestones, diagenetic dolomites, granoblastic marbles, and other impure carbonates were selected worldwide. A multidisciplinary analytical approach, including physical-chemical, mineralogical-petrographic, and thermal analyses, was performed to characterize rocks, insoluble residua and derived burnt products. The statistical analysis allowed classifying samples into 4 main groups with wide differences in ST and burnability. The first group (A), consisting of impure carbonates enriched in fluxes, i.e. clays and feldspars, was completely melted. The second group (B), consisting of sporadic impure carbonates, presented high ST. Blocks were mainly constituted by lime (CaO), or lime (CaO) plus periclase (MgO) associated with subordinated cementitious mineral phases. They can be explained by a solid-state sintering process. The third (C) and the fourth (D) groups, deriving from carbonates with scattered impurity content, pointed out medium and low ST. They can be explained by a liquid-phase sintering process or incomplete clinkerization. This study allowed validating the OT method for predicting blockages in lime kilns. Applications span from the evaluation of raw materials suitability for new kilns, to quality control in already working plants. Acceptable ranges, critical limits and practical solutions are discussed according to the technical expertise achieved over the years.

3.4.2 Introduction

The lime agglomeration, blocks formation, and sticking tendency (ST) at high calcination temperature are critical events, occasionally occurring in industrial lime kilns worldwide, which should be avoided at all. They can cause unscheduled shutdowns, damages to the refractory lining, and equipment, such as lances, lime extraction and transport systems. Depending on how severe the problem is, maintenance labor, purchase of lime to make up the difference, and the expense of blocks disposal can bring the cost of a blockage from tens to hundreds of thousands of euros (Tran and Barham, 1991). Different technologies can be affected by similar issues, including rotary, single shaft, and double or Twin Shaft Regenerative (TSR) kilns, representing one of the most significant and unresolved topic in lime technology worldwide (Vola and Sarandrea, 2014). An exhaustive and comprehensive scientific explanation clarifying the mechanism of blocks formation and ST, generally described as “annular concretions” or “annular rings”, is not available in the literature yet. Nevertheless, annular ringing on the refractory walls in long rotary lime kilns were thoroughly investigated by chemical engineers since the end of the 80s of the last century (Tran and Barham, 1991; Tran et al., 1993). Annular concretions and obstructions also occur in cement kilns, but there are no evidences that both phenomena are related, considering the wide difference in chemistry and temperature between kilns and processes (Taylor, 1997; Tran et al., 1993). At least three different types of lime rings have been identified, e.g. “mud-rings”, “mid-kiln rings”, “front-end rings”, occurring at different temperatures and positions along the kiln’s section, and different technical explanations for their formation have been proposed, including recarbonation, sulphation, agglomeration of lime particles in the presence of liquid phase, and possible melting of sodium compounds (Tran, 2006). Obviously, sulphation is more likely to occur in a kiln firing high sulfur content oil (Francey and Tran, 2012). Recently, numerical combustion model was elaborated for counteracting ring formation in rotary kilns for cement production (Pisaroni et al. 2012). This issue can be initially described in terms of “firing” or “sintering”, including both solid-state and liquid-phase sintering processes (De Jonghe and Rahaman, 2003). Moreover, unusual molten of limestone/dolomite occurring in lime kilns, can be investigated considering the wide geological literature on the petrogenesis and evolution of natural carbonate melts and carbonatite magmas (Le Bas, 1981; Bell, 1989; Jones et al., 2013). Considering a practical perspective the blocks formation in TSR kilns is generally linked to several factors or combination of factors, and often related to the poor quality, or impurity content, i.e. the insoluble residue, of raw

materials feeding to the kiln. The impurity content of carbonate rocks is represented by subordinated terrigenous, and/or evaporitic minerals, plus the organic matter, as well (Flügel, 2010; Warren, 2000; Scholle and Ulmer-Scholle, 2003). More rarely, impurity content is also represented by superficial dust, consisting of soil and/or clayey particles lumped on the surface of the aggregate during its storage into the stockpile. The experience indicates that small amount of impurity, e.g. an insoluble residue <1%, could negatively affects the calcination process, promoting the lime agglomeration, leading to serious obstructions or blockages. Moreover, it is well-known that potassium-bearing silicates, such as K-feldspar, illite, and other clay minerals, are commonly used as fluxing agents to form the glassy phase in the ceramic manufacturing and/or in the clinkerization process, by lowering the melting point of the of CaO-SiO₂-Al₂O₃-Fe₂O₃ system (Baumgart et al., 1984; Taylor, 1997). The liquid-phase formation may starts at temperatures between 1250-1350 °C, or even at ~800-900 °C, depending on the presence of halides or other fluxes (Elsen et al. 2011).

More than twenty years ago Cimprogetti's engineers invented the so-called "Overburning test" (OT) method to simulate and predict the lime agglomeration and the ST occurring at 1300°C, which is ideally considered the highest operative temperature in the lime kilns (Vola and Sarandrea, 2014). This practical method for predicting blocks and ST represents a fundamental step forward, which is particularly useful for selecting suitable raw materials, especially for designing and commissioning new kilns. Moreover the same test is periodically required from important lime producers to perform the quality control on raw materials from different quarries or different layers of the same quarry, according to the normal progression of the mining activity (Manocha and Ponchon, 2018). Thus the first aim of this paper was concerned to the technical-scientific validation of the OT method. Subsequently, factors affecting the blocks formation were investigated, as well. For this research activity, 46 carbonate rocks with different compositions and textures/microstructures were selected from several lime producers worldwide. They included mud-supported and grain-supported limestones, diagenetic dolomites, granoblastic marbles, and other impure carbonates. Samples were thoroughly characterized by means of a multidisciplinary analytical approach, including geochemical (XRF-WDS, ICP-MS and EA-IRMS), physical (MIP, BET-N₂, gas pycnometry), diffraction (XRD), microscopic (OPM, SEM-EDS) and thermal analyses (TG-DTG-DTA). Tests were performed on whole-rocks powders, insoluble residua, and lime blocks. The results were

critically discussed in order to provide an evaluation of raw materials suitability for designing and commissioning new kilns and to perform quality control in already working plants.

3.4.3 Test and Experimental Methods

For the experimental details, including sample provenance, physical (BET-N₂, MIP, pycnometry), chemical (XRF-WDS, ICP-MS and EA-IRMS), mineralogical (XRD-QPA, clay mineralogy), microscopic (OPM, SEM-EDS), and thermal analyses (TG-DTG-DTA), plus technical tests, i.e. burning and slaking reactivity tests, readers are requested to refer to Chapter 2 of the present dissertation.

3.4.4 Results

- *Carbonate rocks characterization*

Preliminary geological information on samples provenance, stratigraphic position, and synthetic lithological-petrographic features, including the Micrite-to-Sparite ratio (MSR), are reported in Tab.3.28. Polarized micrographs representing the most significant rock fabrics are shown in Fig.3.25 and Fig.3.26. Unfortunately, source deposits and rock units are not always available, because not revealed by sample providers. The MSR mineralogical-petrographic parameter allows investigating relationships between raw materials and derived burnt limes characteristics. The MSR ranges between 0.3-33 for limestones, between 0.5-10.6 for dolomites, and between 0.4-16.3 for impure carbonates, respectively. From the petrographic point of view mud-supported limestones and marly limestones always present higher values of MSR than grain-supported limestones, diagenetic dolomites and granoblastic marbles (Vola et al., 2018). Chemical (XRF-WDS, ICP-MS, EA-IRMS), physical (MIP, BET, pycnometry), mineralogical (XRD-QPA) and thermal (TG-DTG-DTA) analyses are reported in Tab.3.29, Tab.3.30, Tab.3.31, and Tab.3.32. According to analyses results, carbonate rocks were classified in 3 main groups: 1) high-grade, slightly impure limestones, represented by 24 samples, 2) high-grade and slightly impure dolomites, represented by 16 samples, and 3) impure carbonates, represented by 6 samples, including 3 marly limestones, 2 marly dolomites, and 1 silicate-bearing marble.

Tab.3.26 – Overburning test (OT) method: results, i.e. lime blocks mass values, and related Sticking Tendency (ST)

Block mass (g)	ST (%)	ST class	ST group
≈42	Max	Melted (A)	A
>20	>47.6	very high (B1)	B
18-20	42.9 – 47.6	high (B2)	
16-18	38.1 – 42.9	medium-high (B3)	
14-16	33.3 – 38.1	medium (C1)	C
12-14	28.6 – 33.3	medium-low (C2)	
10-12	23.8 – 28.6	low (D1)	D
<10	<23.8	no ST (D2)	

Tab.3.27 – Elemental Analysis coupled with Isotope Ratio Mass Spectrometry (EA-IRMS). Symbols legend: TC = Total Carbon, TOC = Total Organic Carbon, ND = Not Determined

No.	Code	Name	TC	$\delta^{13}\text{C}$ TC	TOC
			(%)	(‰)	(%)
-	-	-			
1	2001	SAC	12.64	-0.69	0.05
2	2004	CMI	11.63	-0.96	Nd
3	2005	CAL	11.04	3.01	0.11
4	1818	CNG	12.30	0.59	Nd
5	1854	ISP-1	11.25	-1.51	Nd
6	1849	HOS-1	11.19	1.54	0.04
7	1850	HOS-2	11.28	-0.02	Nd
8	1851	HOS-3	12.26	1.86	Nd
9	1852	HOS-4	11.55	1.08	Nd
10	1853	HOS-5	10.71	0.70	Nd
11	2828	VER	11.60	2.10	0.04
12	2829	CAR	11.47	2.35	0.03
13	1990	IDW-1	11.32	-1.60	0.16
14	1991	IDW-2	11.41	-0.33	0.08
15	1880	QSC-1	11.23	3.30	Nd
16	1992	SMA	11.21	1.99	0.20
25	1999	CAL-2	12.53	0.21	Nd
26	1856	ISP-2	13.06	3.59	Nd
27	1867	CRM-1	12.77	3.10	Nd
28	1873	CRM-2	12.62	3.22	Nd
29	2830	ZAN	13.03	4.03	0.06
30	2025	SRI	12.78	1.23	Nd
31	2112	MME	11.91	1.10	0.23
41	598	SCH	10.64	2.22	Nd
44	1895	CRM-3	10.51	3.45	0.03

Tab.3.28 – Geological settings and synthetic petrographic features of carbonate rocks samples. Symbols legend: MSR = micrite-to-sparite ratio; p.i. = proprietary information

Sample	Name	Code	Lithofacies	Texture/Microstructure	MSR	Geological Unit and Stratigraphic position	Provenance
1	SAC	2001	Mud-supported limestone	Wackestone/packstones with benthonic faunas (Nummulites)	5.4	Monti Climiti Fm.Priolo Fm.(?) (Paleocene-Eocene)	Siracusa, Italy
2	CMI	2004	Grain-supported limestone	Packstone/grainstones with benthonic faunas (Miliolids) and neomorphic sparite	3.7	Seeb Fm. (Early Eocene)	Sohar, Oman
3	CAL-1	2005	Mud-supported limestone	fossiliferous kerogen-rich wackestone with planktonic faunas	14.8	p.i.	Monterrey, Nuevo León, Mexico
4	CNG	1818	Granoblastic marble	fine-grained calcitic marble with superimposed mm-sized brownish burial dolomite	3.6	p.i.	Guro-gu, Seoul, South Korea
5	ISP-1	1854	Grain-supported limestone	quite porous, slightly impure limestone with large benthic faunas, i.e. bivalves and red algae, with terrigenous minerals and detrital quartz	33.0	p.i.	Burnpur, West Bengal, India
6	HOS-1	1849	Mud-supported passing to grain-supported limestone	quite porous, peloidal-fossiliferous wackestone/packstone	5.7	p.i.	Mirzaci, Iran
7	HOS-2	1850	Grain-supported limestone	porous, impure, poorly washed, peloidal packstone presenting an early diagenetic dolomitization;	4.3	p.i.	Bakiabad, Iran
8	HOS-3	1851	Grain-supported limestone	quite porous fossiliferous and poorly washed packstone with sporadic large benthic foraminifera	7.9	p.i.	Angoran, Iran
9	HOS-4	1852	Grain-supported limestone	quite porous, impure, fossiliferous packstone constituted by compacted large benthic foraminifera (nummulites), presenting an early diagenetic dolomitization;	5.2	p.i.	Kashigari, Iran

Table 3.28 (continue)

Sample	Name	Code	Lithofacies	Texture/Microstructure	MSR	Geological Unit and Stratigraphic position	Provenance
10	HOS-5	1853	Mud-supported limestone	porous fossiliferous wackestone with sporadic foraminifera and coralline alga, presenting an early diagenetic dolomitization.	29.8	p.i.	Dargaz, Iran
11	VER	2828	Mud-supported limestone	Wackestone/packstones with planktonic faunas (Protoglobigerins, radiolarians)	5.1	Rosso Ammonitico Veronese Fm. (Middle Jurassic)	Valpolicella, Verona, Italy
12	CAR	2829	Calcitic marble	Mainly granoblastic non-oriented calcite microstructure	0.3	Apuane Metamorphic Complex Marble s.s. formation (Lower Liassic)	Marble district Carrara, Italy
13	IDW-1	1990	Microbial limestone	Microbial kerogen-rich boundstone with microsparite	11.9	Uppermost Kogelbeen Fm. or Lower Gamohaam Fm. (Neoproterozoic)	Ouplaas Mine, Daniëlskuil, South Africa
14	IDW-2	1991		Microbial boundstone with poikilotopic calcite	4.8		
15	QSC-1	1880	Mud-supported limestone	Peloidal packstone/wackestones with benthonic faunas (Milioids, echinoids)	7.5	Dammam Fm. (Middle Eocene)	Rawdat Rasid, Qatar
16	SMA	1992	Massive limestone	Fossiliferous kerogen-rich floatstone/rudstones from different reefoidal facies (stromatoporoids)	1.4	Lower Wenlock Hangvar Fm. (Silurian)	Storugns, Gotland, Sweden
17	PSP-1	2450	Massive limestone	Massive coralline framestone/rudstones characterized by bryozoan-foraminifera association with encrusting coralline red algae.	7.7	p.i.	Karawang quarry, Rembang, Java, Indonesia
18	PSP-2	2451			6.1		
19	CRM-d	2665	bioclastic, mainly grain-supported limestone	Fossiliferous porous rudstone/grainstone with large benthic faunas, i.e. bivalves, gastropods, echinoids, and rare forams, passing to a poorly washed packstone/wackestone	3.1	p.i.	Seilles, Belgium
20	CRM-w	2666			2.5		
21	PTL-1a	2701	Mud-supported passing to grain-supported limestone	Fossiliferous-peloidal wackestone/packstones passing to grainstones	3.5	Casper Fm. (Lower Permian and Upper and Middle Pennsylvanian)	Jonathon Quarry Laramie Wyoming, USA
22	PTL-1b	2701			3.7		

Table 3.28 (continue)

Sample	Name	Code	Lithofacies	Texture/Microstructure	MSR	Geological Unit and Stratigraphic position	Provenance
23	PTL-2	2702	Mud-supported passing to grain-supported limestone	Fossiliferous-peloidal wackestone/packstones passing to grainstones	3.8	Casper Fm. (Lower Permian and Upper and Middle Pennsylvanian)	Jonathon Quarry Laramie Wyoming, USA
24	DOC	2887	grain-supported limestone	Peloidal-fossiliferous grainstone, constituted by sub mm-sized rounded micritic grains, green algae, echinos, bryozoa, and other benthonic faunas. Equant calcite cement filled in intraparticles porosity	6.2	p.i.	San Cristobal, Rep. Dominicana
25	CAL-2	2005	Diagenetic Dolomite	fine and medium-grained xenotopica to hypidiotopic kerogen-rich dolomite superimposed to an ooidal packstone/grainstone	4.4	p.i.	Monterrey, Nuevo León, Mexico
26	ISP-2	1856	Diagenetic Dolomite	fine-grained peloidal packstone dolomitized. Sporadic large mm- sized brownish twinned dolomite	4.3	p.i	Burnpur, West Bengal, India
27	CRM-1	1867	Dolomitic marble	Fine-grained xenomorphic to hypidiomorphic kerogen-rich dolomitic marble with rare recrystallized ghostly fossils	2.4	p.i	Seilles, Belgium
28	CRM-2	1873	Dolomitic marble	Fine-grained xenomorphic to hypidiomorphic kerogen-rich dolomitic marble with rare recrystallized ghostly fossils	2.5	p.i	Seilles, Belgium
29	ZAN	2830	Diagenetic Dolomite	coarse-grained, mainly hydrotopic, mosaic dolomite	1.3	Albenza Fm., Zandobbio Dolomite Member (Early Jurassic)	Zandobbio, Italy

Table 3.28 (continue)

Sample	Name	Code	Lithofacies	Texture/Microstructure	MSR	Geological Unit and Stratigraphic position	Provenance
30	SRI	2025	Dolomitic marble	Coarse-grained non-oriented granoblastic microstructure. Large mm-sized dolomitic marble with rounded boundaries.	0.5	p.i	Subang Jaya, Selangor, Malaysia
31	MME	2112	Diagenetic Dolomite	Xenotopic to hipidiotopic mosaic dolomite passing to subordinated fossiliferous, formanifera-rich, wackestone/packstones	1.4	p.i	Medan Area, North Sumatera, Indonesia
32	INTP	1735	Diagenetic Dolomite	Coarse-grained mosaic brownish dolomite with straight grain-boundaries and mm-sized vugs filled in by poikilotopic calcite	1.7	p.i	Dnepropetrovsk, Ukraine
33	SAL	2019	Diagenetic Dolomite	Fine-grained xenotopic dolomite superimposed to fossiliferous-peloidal limestone or breccia-like sediments	12.5	p.i	Campiglia Marittima, Italy
34	QSC-2	1881	Diagenetic Dolomite	Fine to medium-grained brecciated and zoned brownish rhombohedral dolomite	4.3	p.i	Qatar
35	USI	2309	Diagenetic Dolomite	Coarse-grained mosaic brownish dolomite with straight grain-boundaries	2.9	p.i	Kuwait
36	MON	2667	Dolomitic marble	medium up to coarse-grained granoblastic non-oriented microstructure. Sporadic mm-sized rhombohedral dolomite	3.6	p.i	India
37	ESH	2668	Dolomitic marble	medium-grained granoblastic, non-oriented microstructure. Sporadic mm-sized porosity filled in by large mosaic rhombohedral dolomite	5.9	p.i	India
38	JGM	2669	Dolomitic marble	fine-grained granoblastic and oriented microstructure. Mosaic of twinned brownish dolomite with lobate boundaries	3.9	p.i	Bhutan
39	UNI-1	2762	Diagenetic Dolomite	Hypidiotopic mosaic dolomite with ghostly peloids	10.6	Dolomia Principale Fm. (Upper Triassic)	Casnigo, Bergamo Italy

Table 3.28 (continue)

Sample	Name	Code	Lithofacies	Texture/Microstructure	MSR	Geological Unit and Stratigraphic position	Provenance
40	PED	2782	Diagenetic Dolomite	Hypidiotopic mosaic and brecciated dolomite	2.4	Dolomia Superiore Fm., Dolomia a Megalodon Member (Upper Triassic)	Balvano, Italy
41	SCH	598	Mud-supported Marly limestone	Wackestones with planktonic faunas. Terrigenous impurity represented by fine-grained quartz and clay minerals	16.3	Planerkalk Group Munsterland Cretaceous Basin (Cenomanian-Turonian)	Lienen, Germany
42	INT	2743	Mud-supported Marly limestone	Wackestones with planktonic faunas. Terrigenous impurity represented by fine-grained quartz and clay minerals	12.0	El Haria Fm. (Paleocene)	Thala, Tunisie
43	TAS	2904	Calcareous Marl	Wackestones with planktonic faunas. Terrigenous impurity represented by fine-grained quartz, feldspars, micas and clay minerals	27.5	Scaglia Rossa Fm. (Upper Cretaceous)	Tassullo, Italy
44	CRM-3	1895	Calcitic impure marble	coarse-grained granoblastic and oriented microstructure with calcite, K-feldspar, plagioclase and muscovite	0.4	p.i	Seilles, Belgium
45	UNI-2	2217	Marl (50%) and Dolomite (50%)	Nd	Nd	Calcare di Zu Fm. and Argillite di Riva di Solto Fm. (Upper Triassic)	Lecco, Italy
46	UNI-3	2261	Dolomitic Marl	Wackestones with planktonic faunas. Terrigenous impurity represented by fine-grained quartz, feldspars, micas and clay minerals	38.9	Argillite di Riva di Solto Fm. (Upper Triassic)	Lecco, Italy

Tab.3.29 – Chemical analysis (XRF-WDS) of carbonate rock samples

No	Code	Name	LOI	SiO ₂	Al ₂ O ₃	Fe ₂ O ₃	CaO	MgO	SO ₃	Na ₂ O	K ₂ O	MnO	BaO	SrO	TiO ₂	P ₂ O ₅	Cl-
-	-	-	(%)	(%)	(%)	(%)	(%)	(%)	(%)	(%)	(%)	(%)	(%)	(%)	(%)	(%)	(%)
-	-	LLD	0.01	0.01	0.01	0.01	0.01	0.01	0.01	0.01	0.01	0.01	0.01	0.01	0.01	0.01	0.01
1	2001	SAC	43.72	0.07	0.04	0.06	55.30	0.58	0.04	0.00	0.01	0.00	0.05	0.03	0.00	0.12	0.00
2	2004	CMI	43.14	0.35	0.12	0.09	55.90	0.28	0.03	0.03	0.03	0.01	0.07	0.01	0.01	0.02	0.01
3	2005	CAL-1	43.31	0.51	0.08	0.06	55.40	0.47	0.06	0.01	0.03	0.01	0.05	0.03	0.01	0.05	0.01
4	1818	CNG	43.42	0.13	0.07	0.06	55.30	0.93	0.02	0.01	0.02	0.02	0.04	0.02	0.00	0.01	0.00
5	1854	ISP-1	42.99	2.25	0.30	0.21	53.60	0.67	0.03	0.00	0.02	0.01	0.04	0.03	0.04	0.01	0.01
6	1849	HOS-1	43.89	0.22	0.08	0.10	55.10	0.44	0.03	0.02	0.02	0.01	0.08	0.03	0.01	0.01	0.01
7	1850	HOS-2	42.48	1.94	0.29	0.29	50.85	2.29	0.66	0.16	0.08	0.01	0.10	1.02	0.02	0.02	0.09
8	1851	HOS-3	43.82	0.20	0.07	0.10	55.30	0.44	0.03	0.04	0.02	0.01	0.05	0.03	0.01	0.01	0.02
9	1852	HOS-4	43.16	3.32	0.69	0.55	47.65	3.95	0.08	0.09	0.14	0.01	0.03	0.09	0.04	0.12	0.02
10	1853	HOS-5	43.48	1.69	0.36	0.23	50.23	3.46	0.18	0.11	0.14	0.01	0.00	0.06	0.02	0.02	0.07
11	2828	VER	43.18	1.44	0.33	0.22	54.20	0.40	0.04	0.04	0.15	0.03	0.00	0.01	0.03	0.06	0.00
12	2829	CAR	43.86	0.06	0.04	0.04	55.10	0.90	0.03	0.01	0.01	0.00	0.00	0.02	0.01	0.01	0.00
13	1990	IDW-1	42.45	2.20	0.67	0.23	52.70	0.82	0.14	0.01	0.18	0.46	0.04	0.02	0.03	0.01	0.01
14	1991	IDW-2	43.52	0.18	0.02	0.10	55.00	0.36	0.02	0.04	0.00	0.51	0.06	0.01	0.01	0.01	0.01
15	1880	QSC-1	43.99	0.10	0.03	0.06	55.40	0.33	0.03	0.01	0.01	0.00	0.05	0.02	0.01	0.01	0.01
16	1992	SMA	42.81	3.08	0.82	0.40	51.65	0.62	0.04	0.02	0.28	0.10	0.00	0.02	0.05	0.02	0.10
17	2450	PSP-1	44.64	0.01	0.01	0.03	55.31	0.15	0.01	0.00	0.00	0.00	0.00	0.00	0.01	0.01	0.00
18	2451	PSP-2	44.13	0.05	0.05	0.04	55.25	0.22	0.01	0.01	0.01	0.00	0.00	0.00	0.03	0.01	0.00
19	2665	CRM-D	42.63	1.18	0.25	0.21	55.10	0.34	0.02	0.03	0.02	0.00	0.00	0.03	0.02	0.11	<0.01
20	2666	CRM-W	42.72	1.14	0.25	0.24	55.00	0.29	0.02	0.00	0.02	0.00	0.00	0.03	0.02	0.11	<0.01
21	2701	PTL-1a	43.75	0.28	0.05	0.07	55.40	0.24	0.03	0.00	0.02	0.01	0.00	0.04	0.03	0.01	<0.01
22	2701	PTL-1b	43.56	0.50	0.10	0.07	55.30	0.21	0.03	0.00	0.02	0.01	0.00	0.00	0.03	0.01	<0.01
23	2702	PTL-2	43.87	0.09	0.04	0.06	55.40	0.38	0.02	0.00	0.01	0.01	0.00	0.03	0.03	0.01	<0.01
24	2887	DOC	43.30	0.53	0.02	0.04	55.70	0.28	0.02	0.01	0.00	0.01	0.00	0.02	0.12	0.00	<0.01
25	1999	CAL-2	46.25	0.34	0.14	0.14	36.85	16.35	0.05	0.05	0.06	0.03	0.04	0.01	0.01	0.01	0.05
26	1856	ISP-2	47.34	0.05	0.02	0.20	30.64	21.23	0.20	0.00	0.02	0.03	0.00	0.01	0.00	0.02	0.01
27	1867	CRM-1	46.80	1.48	0.20	0.17	29.81	21.38	0.01	0.06	0.15	0.01	0.00	0.00	0.02	0.00	0.12
28	1873	CRM-2	47.77	0.64	0.15	0.12	31.50	19.40	0.04	0.06	0.11	0.01	0.08	0.01	0.01	0.00	0.17
29	2830	ZAN	47.22	0.18	0.06	0.06	31.88	20.97	0.02	0.02	0.03	0.01	0.00	0.00	0.01	0.01	0.01
30	2025	SRI	46.78	0.39	0.16	0.33	35.90	16.10	0.01	0.02	0.02	0.07	0.07	0.02	0.01	0.01	0.01

High-grade burnt lime products: impact of calcination kinetics on slaking reactivity;
sticking tendency and blocks formation at HT (1300°C)

Table 3.29 (continue)

No	Code	Name	LOI	SiO ₂	Al ₂ O ₃	Fe ₂ O ₃	CaO	MgO	SO ₃	Na ₂ O	K ₂ O	MnO	BaO	SrO	TiO ₂	P ₂ O ₅	Cl-
-	-	-	(%)	(%)	(%)	(%)	(%)	(%)	(%)	(%)	(%)	(%)	(%)	(%)	(%)	(%)	(%)
31	2112	MME	46.90	0.33	0.15	0.10	33.60	18.60	0.03	0.04	0.04	0.00	0.05	0.01	0.01	0.01	0.03
32	1735	INTP	46.77	0.33	0.11	0.25	36.40	15.80	0.03	0.05	0.04	0.03	0.00	0.03	0.01	0.01	0.01
33	2019	SAL	47.65	0.11	0.05	0.07	33.60	18.30	0.02	0.06	0.03	0.01	0.00	0.01	0.01	0.00	0.02
34	1881	QSC-2	47.38	0.68	0.04	0.11	34.40	17.20	0.03	0.04	0.02	0.02	0.00	0.01	0.01	0.00	0.02
35	2309	USI	47.64	0.20	0.07	0.12	31.78	19.85	0.19	0.00	0.03	0.01	0.05	0.01	0.02	0.01	0.02
36	2667	MON	47.10	1.32	0.25	0.19	31.80	18.70	0.03	0.15	0.07	0.01	0.00	0.00	0.06	0.02	0.07
37	2668	ESH	46.55	0.81	0.06	0.10	30.41	21.86	0.02	0.09	0.02	0.01	0.00	0.00	0.04	0.00	0.05
38	2669	JGM	47.11	0.75	0.27	0.35	31.40	20.30	0.02	0.05	0.02	0.05	0.00	0.01	0.02	0.02	0.05
39	2762	UNI-1	46.60	1.23	0.42	0.14	30.40	20.91	0.03	0.06	0.13	0.00	0.00	0.01	0.01	0.03	0.02
40	2777	PED	47.55	0.06	0.04	0.05	31.06	21.09	0.04	0.06	0.02	0.00	0.00	0.01	0.01	0.01	0.02
41	598	SCH	40.74	5.83	1.62	0.68	49.65	0.65	0.06	0.04	0.33	0.11	0.09	0.12	0.08	0.08	0.01
42	2743	INT	41.34	6.78	0.34	0.19	51.20	0.32	0.03	0.02	0.03	0.02	0.00	0.14	0.07	0.02	0.00
43	2904	TAS	32.79	18.03	3.64	2.16	40.08	1.64	0.04	0.20	1.00	0.06	0.00	0.10	0.05	0.23	0.00
44	1895	CRM-3	37.43	5.35	1.51	1.13	52.20	1.06	0.04	0.12	0.61	0.01	0.08	0.02	0.10	0.05	0.03
45	2217	UNI-2	31.60	21.22	4.68	1.66	28.67	10.30	0.82	0.19	1.16	0.02	0.00	0.08	0.01	0.34	0.01
46	2761	UNI-3	16.45	41.30	12.00	3.75	14.52	5.80	1.77	0.48	2.77	0.04	0.00	0.09	0.79	0.04	0.00

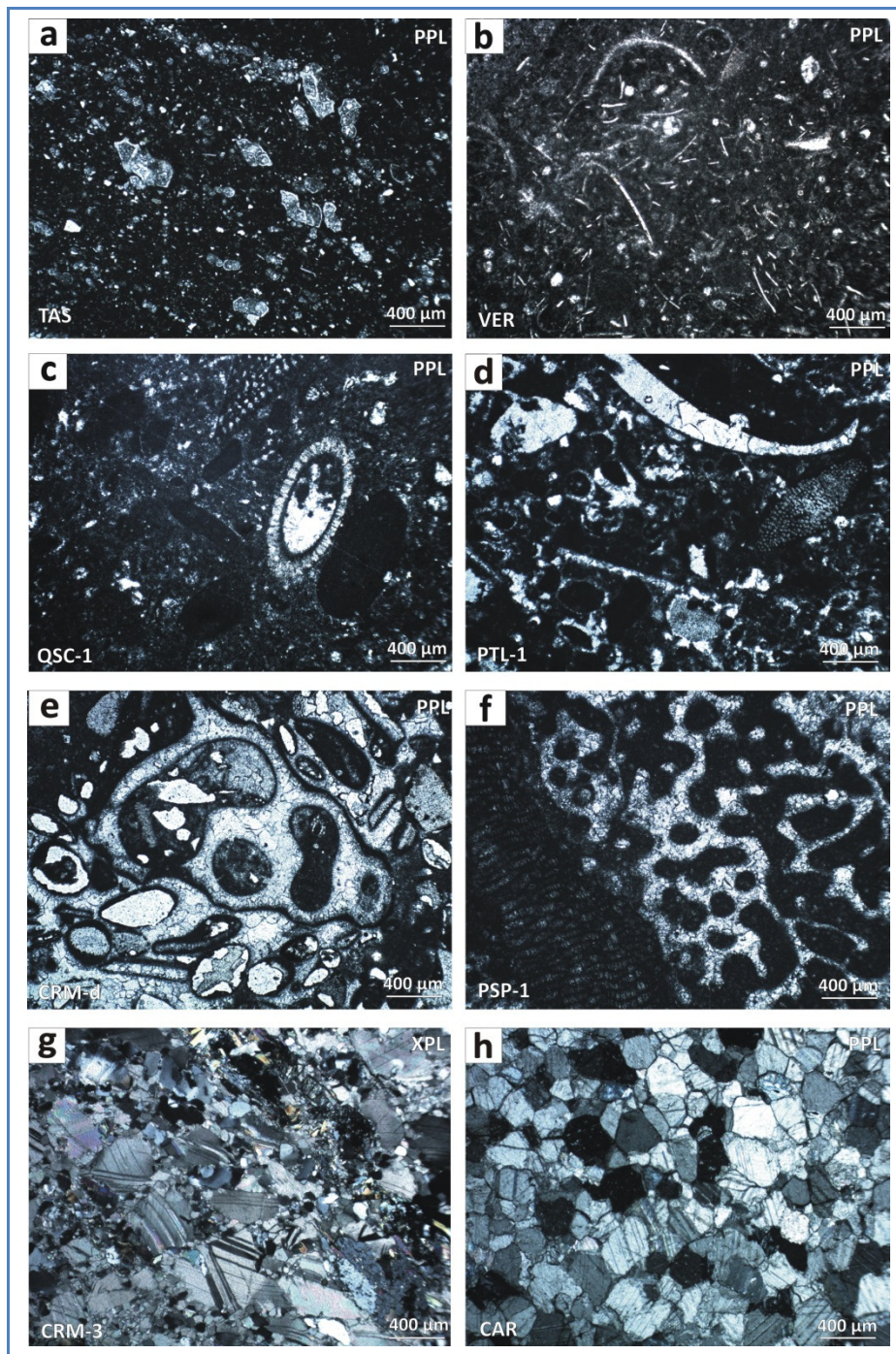


Fig.3.25: Petrographic analysis of fundamental textural and diagenetic/metamorphic features of limestones, marly limestones and calcitic marbles. a = mud-supported calcareous marl with planktonic foraminifera (mainly *Globotruncana*) scattered within dark micritic matrix. Terrigenous impurity is represented by μm -sized quartz and clay minerals dispersed within the calcareous matrix (TAS). b = mud-supported limestone, namely wackestone to packstone, with planktonic thin-shelled bivalves, ostracods, foraminifera (*Protoglobigerins*) and radiolarians (VER). c = mainly mud-supported limestone, namely fossiliferous-peloidal wackestone to packstone with benthonic faunas (*Milioids*, echinoids) (QSC-1). d = grain-supported limestone, namely poorly washed peloidal-fossiliferous packstone with benthonic faunas (bivalves, echinoids) (PTL-1). e = fossiliferous and porous grainstone with large mm-sized gastropods, bivalves and echinoids. Mosaic calcite fillings intraclastic porosity (CRM-d). f = Coralline-encrusting framestone/rudstones characterized by bryozoan–foraminifera–red algae association. g = Plastically deformed, idiomorphic twinned calcite in silicate-bearing granoblastic marble (CRM). 3h Idiomorphic twinned calcite in medium to coarse-grained granoblastic marble with well-defined grain boundaries, straight or slightly curved without optical evidence of crystal-plastic deformation (CAR). PPL/XPL = Plane/Crossed Polarized Light microscopy.

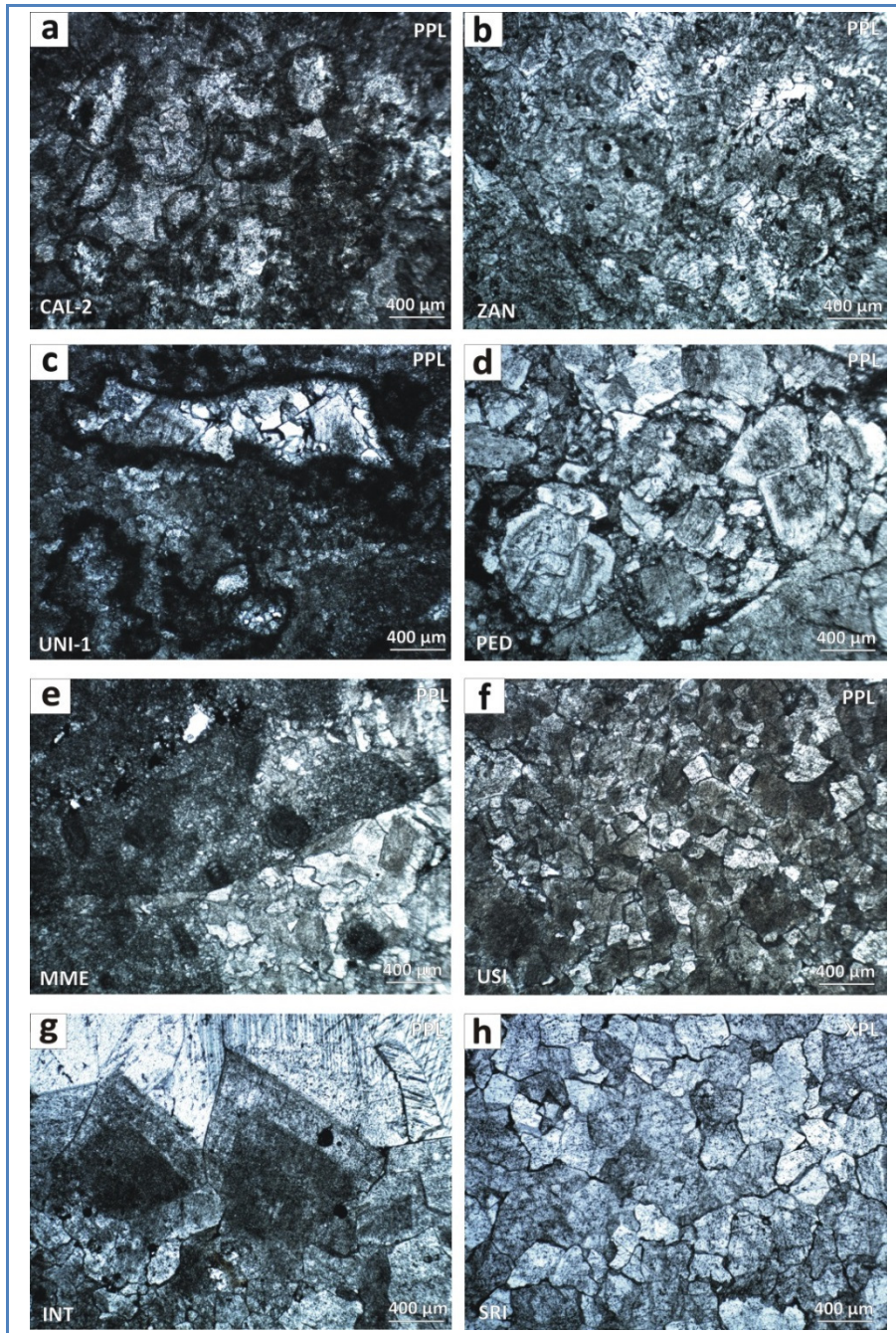


Fig.3.26: Petrographic analysis of fundamental diagenetic/metamorphic features of dolomites and dolomitic marbles. a = Hypidiotopic kerogen-rich diagenetic dolomite, superimposed to an ooidal-fossiliferous packstone to grainstone (CAL-2). b = Hypidiotopic to hydiotopic mosaic burial dolomite superimposed to peritidal peloidal packstones interbedded with ooidal-bioclastic grainstones (ZAN). c = Xenotopic to hypidiotopic mosaic burial dolomite superimposed to microbial packstones (UNI-1). d = Hypidiotopic to hydiotopic fabric passing to dolomitized breccia-like microstructures in a mostly tectonized dolomite-rock (PED). e = Hydiotopic mosaic laterally passing to xenotopic dolomite superimposed to a fossiliferous peritidal wackestone, with well-preserved benthonic foraminifera (Milioids) (MME). f = Hydiotopic mosaic of brownish burial dolomite superimposed to ooidal-peloidal, almost completely obliterated, limestone (USI). g = Hydiotopic mosaic of burial dolomite laterally passing to large (mm-sized) zoned rhombohedral dolomite. Large (cm-sized) cavities with mosaic calcite cement fillings. h = Coarse-grained dolomitic marble with interlobate grain boundaries without any grains orientation (SRI). PPL = Plane Polarized Light microscopy.

Tab.3.30 – X-rays diffraction (XRD-QPA) analysis on rock samples. Symbols legend: Cal = calcite; Dol = dolomite, Qtz = quartz, Ms = muscovite/illite, Sme = smectites, Kln = kaolinite, Chl = chlorite, Ply = Paligorskyte, Srp = Serpentine group, Gt = Goethite, Kfs = K-feldspar, Pl = Plagioclase, Rtl = Rutile, Py = Pyrite, Gp = Gypsum, Anh = Anhydrite, Cel = Celestine, Sp = Sphalerite, Fl = fluorite, Svn = Svanbergite, Ap = apatite, Tr = traces (<0.5%)

No	Code	name	Cal	Dol	Qtz	Ms	Sme	Kln	Chl	Ply	Srp	Gt	Kfs	Pl	Rtl	Py	Gp	Anh	Cel	Sp	Fl	Svn	Ap
			(%)	(%)	(%)	(%)	(%)	(%)	(%)	(%)	(%)	(%)	(%)	(%)	(%)	(%)	(%)	(%)	(%)	(%)	(%)	(%)	(%)
1	2001	SAC	99.8		Tr	Tr	Tr	Tr															
2	2004	CMI	99.5		Tr	0.3						Tr											
3	2005	CAL	97.4	1.8	0.1	0.6						Tr			Tr								
4	1818	CNG	96.1	3.6	Tr	Tr		Tr	Tr				Tr								Tr		
5	1854	ISP-1	95.7	0.7	1.6	Tr	0.9			0.4		0.1		0.5	Tr								
6	1849	HOS-1	99.6		0.2	Tr	Tr					Tr	0.0										
7	1850	HOS-2	87.7	9.6	0.3	0.5				0.2		0.2	0.3	0.3			Tr	0.4	0.2				
8	1851	HOS-3	99.3	0.4	0.0	0.2	Tr	Tr	Tr			Tr	Tr										
9	1852	HOS-4	85.1	12.0	0.3	1.9	Tr	Tr	Tr				0.4	Tr									
10	1853	HOS-5	85.8	11.9	0.5	1.0		Tr	Tr				Tr	0.8									
11	2830	VER	98.0		0.2	1.1	Tr					0.3	0.4										
12	2829	CAR	99.1	0.8	Tr	Tr							Tr	Tr		Tr							
13	1990	IDW-1	96.4	0.3	0.8	1.5			0.4				0.4			0.2							
14	1991	IDW-2	97.3	2.5	0.2	Tr			Tr							Tr							
15	1880	QSC-1	99.7		Tr	Tr	Tr						Tr			Tr							
16	1992	SMA	95.1		1.5	2.0	0.3	Tr	0.9			Tr	Tr	Tr									
17	2450	PSP-1	99.9		Tr		Tr				Tr												
18	2451	PSP-2	99.9		Tr		Tr	Tr			Tr		Tr	Tr									
19	2665	CRM-D	98.6		1.1	Tr	0.2	Tr															
20	2666	CRM-W	97.4		2.1	0.4	Tr	Tr											Tr				
21	2701	PTL-1a	99.0		0.9	Tr							Tr										Tr
22	2701	PTL-1b	98.6		0.9	0.3	Tr						Tr										Tr
23	2702	PTL-2	99.5		0.4	Tr	Tr	Tr					Tr										
24	2887	DOC	99.2		0.7	Tr				Tr													

Table 3.30 (continue)

No	Code	name	Cal	Dol	Qtz	Ms	Sme	Kln	Chl	Ply	Srp	Gt	Kfs	Pl	Rtl	Py	Gp	Anh	Cel	Sp	Fl	Svn	Ap
		(%)	(%)	(%)	(%)	(%)	(%)	(%)	(%)	(%)	(%)	(%)	(%)	(%)	(%)	(%)	(%)	(%)	(%)	(%)	(%)	(%)	(%)
25	1999	CAL-2	23.8	75.7	Tr	0.2	Tr		Tr			Tr	Tr	Tr		Tr							
26	1856	ISP-2	0.5	98.7	Tr	Tr	Tr		Tr			Tr	Tr	Tr									
27	1867	CRM-1		98.2	0.9	0.4							0.4	Tr		Tr							
28	1873	CRM-2		98.9	Tr	0.4	Tr		Tr			Tr	0.2	Tr									
29	2830	ZAN	0.2	99.5		Tr	Tr					Tr	0.3										
30	2025	SRI	4.3	94.0	0.3	0.4	Tr	Tr	0.7				0.5	Tr									
31	2112	MME	3.2	96.2	0.2	0.2	Tr	Tr					0.4	Tr									
32	1735	INTP	2.9	96.7	0.2	0.2						0.2	Tr	0.2	Tr								
33	2019	SAL	2.0	97.8		0.2																	
34	1881	QSC-2	4.1	94.6	0.9	Tr							Tr					Tr					
35	2309	USI	3.2	96.8	Tr	Tr	Tr	Tr					Tr		Tr								
36	2667	MON	0.3	98.7	0.8	0.3	Tr	Tr	Tr					Tr									
37	2668	ESH		99.0	1.0	Tr	Tr	Tr	Tr														
38	2669	JGM		98.7	Tr	Tr		Tr	0.7			Tr		Tr									
39	2762	UNI-1	0.4	97.8	Tr	0.8	Tr	Tr	Tr					Tr	Tr						Tr		Tr
40	2777	PED	1.3	98.6	Tr	Tr	Tr		Tr					Tr									
41	598	SCH	88.9		2.9	5.5	Tr	1.2	0.3			0.4		0.6	0.3								
42	2743	INT	93.8		4.9	0.7		0.3					Tr	Tr									
43	2904	TAS	66.9	5.3	11.2	13.1	0.6				0.4		2.1	0.4									
44	1895	CRM-3	86.8		4.3	3.8			1.1				2.7	1.3									
45	2217	UNI-2	20.8	59.0	10.4	6.3		1.6					0.7	0.8		0.6							
46	2761	UNI-3	8.0	30.6	20.9	17.7		0.3	0.7			11.6	2.4	7.5		0.6							

Tab.3.31 – Physical analysis on carbonate rocks by mercury intrusion porosimetry (MIP) and nitrogen absorption (BET-N₂). Symbols legend: BET SSA = specific surface area by BET method; Av Pore diameter/radius = average pore diameter/radius

No	Code	Name	Dust (%)	Moisture (105 °C)	Capillary porosity	BET SSA (m ² /g)	Real Density (g/cm ³)	Accessible Porosity (%)	Apparent density (g/cm ³)	Pore volume (mm ³ /g)	Av Pore diameter (µm)	Av Pore radius (µm)
-	-	-	(%)	(%)	(%)	(m ² /g)	(g/cm ³)	(%)	(g/cm ³)	(mm ³ /g)	(µm)	(µm)
1	2001	SAC	<0.1	0.14	12.92	0.71	2.72	22.80	2.53	116.71	0.54	0.27
2	2004	CMI	<0.1	0.08	5.47	0.33	2.73	12.77	2.61	56.21	1.04	0.52
3	2005	CAL	<0.1	0.07	0.28	0.16	2.72	0.12	2.76	0.45	1.22	0.61
4	1818	CNG	<0.1	0.13	0.27	0.04	2.73	0.48	2.73	1.76	0.26	0.13
5	1854	ISP-1	<0.1	0.24	4.43	2.46	2.73	13.69	2.68	59.09	0.42	0.21
6	1849	HOS-1	0.4	0.18	4.90	0.30	2.72	15.58	2.66	69.49	0.98	0.49
7	1850	HOS-2	2.1	0.26	6.80	1.82	2.79	17.83	2.46	88.17	0.46	0.23
8	1851	HOS-3	<0.1	0.14	4.60	0.38	2.72	12.36	2.65	53.18	0.80	0.40
9	1852	HOS-4	2.2	0.30	6.00	2.22	2.73	15.97	2.66	71.51	0.16	0.08
10	1853	HOS-5	0.7	0.19	8.00	1.75	2.75	18.39	2.67	84.55	0.32	0.16
11	2828	VER	<0.1	0.18	1.89	0.55	2.71	1.17	2.67	4.43	0.04	0.02
12	2829	CAR	<0.1	0.04	0.35	0.00	2.71	0.65	2.71	2.72	0.76	0.38
13	1990	IDW-1	<0.1	0.13	4.13	0.19	2.73	0.37	2.74	1.36	0.66	0.33
14	1991	IDW-2	<0.1	0.08	4.13	0.11	2.71	0.53	2.78	1.92	1.56	0.78
15	1880	QSC-1	<0.1	0.07	0.80	0.10	2.71	1.11	2.69	4.18	0.08	0.04
16	1992	SMA	<0.1	0.24	0.90	0.38	2.71	0.53	2.63	2.03	0.12	0.06
17	2450	PSP-1	<0.1	0.08	6.73	0.09	2.70	7.39	2.68	27.42	0.54	0.27
18	2451	PSP-2	<0.1	0.04	3.81	0.17	2.71	6.85	2.69	29.67	0.42	0.21
19	2665	CRM-d	<0.1	0.10	4.26	0.93	2.73	16.42	2.72	72.24	0.55	0.28
20	2666	CRM-w	<0.1	1.40	4.09	0.93	2.72	16.65	2.78	71.91	0.53	0.27
21	2701	PTL-1a	0.3	0.05	0.87	0.08	2.71	2.24	2.70	8.48	0.16	0.08
22	2701	PTL-1b	Nd	0.06	Nd	0.07	2.71	2.27	2.74	8.47	0.21	0.11
23	2702	PTL-2	<0.1	0.05	0.84	0.07	2.71	1.28	2.70	4.79	0.31	0.16
24	2887	DOC	<0.1	0.11	3.80	0.42	2.72	5.76	2.69	22.74	0.17	0.09
25	1999	CAL-2	<0.1	0.09	0.76	0.17	2.83	1.16	2.84	4.13	0.16	0.08
26	1856	ISP-2	<0.1	0.12	0.33	0.10	2.86	0.77	2.85	2.73	4.34	2.17
27	1867	CRM-1	<0.1	0.15	0.60	0.18	2.86	0.27	2.91	0.94	0.74	0.37

Tab. 3.31 (continue)

No	Code	Name	Dust	Moisture (105 °C)	Capillary porosity	BET SSA	Real Density	Accessible Porosity	Apparent Density	Pore volume	Av. Pore diameter	Av. Pore radius
28	1873	CRM-2	<0.1	0.17	0.26	0.22	2.86	Nd	Nd	Nd	Nd	Nd
29	2830	ZAN	<0.1	0.08	1.48	0.06	2.84	1.27	2.84	4.54	0.16	0.08
30	2025	SRI	<0.1	0.23	0.70	0.15	2.84	0.91	2.83	4.23	0.58	0.29
31	2112	MME	<0.1	0.09	0.97	0.14	2.85	0.88	2.87	3.10	0.28	0.14
32	1735	INTP	<0.1	0.08	0.60	0.13	2.83	2.51	2.85	9.04	0.25	0.13
33	2019	SAL	<0.1	0.05	0.60	0.06	2.86	1.13	2.91	3.91	0.06	0.03
34	1881	QSC-2	<0.1	0.07	0.40	0.03	2.84	0.50	2.82	1.79	1.24	0.62
35	2309	USI	<0.1	0.08	0.42	0.14	2.84	1.04	2.89	3.64	1.66	0.83
36	2667	MON	<0.1	0.07	0.86	0.06	2.86	0.34	2.87	1.17	0.74	0.37
37	2668	ESH	<0.1	0.11	0.23	0.00	2.84	0.32	2.88	1.12	0.99	0.50
38	2669	JGM	<0.1	0.05	0.26	0.02	2.86	0.17	2.92	0.57	5.72	2.86
39	2762	UNI-1	<0.1	0.05	0.73	0.31	2.86	0.94	2.85	3.32	0.27	0.14
40	2777	PED	<0.1	0.07	0.50	0.10	2.85	0.30	2.87	1.04	1.05	0.53
41	598	SCH	<0.1	0.56	0.78	4.06	2.73	5.65	2.61	22.06	0.04	0.02
42	2743	INT	<0.1	0.12	4.40	1.38	2.73	12.68	2.75	52.82	0.14	0.07
43	2904	TAS	<0.1	0.87	Nd	2.59	2.71	Nd	Nd	Nd	Nd	Nd
44	1895	CRM-3	<0.1	0.10	2.23	0.05	2.75	0.61	2.74	2.24	0.26	0.13
45	2217	UNI-2	<0.1	0.33	Nd	Nd	Nd	Nd	Nd	Nd	Nd	Nd
46	2761	UNI-3	<0.1	1.27	Nd	3.57	2.74	2.54	2.72	9.56	0.06	0.03

Tab.3.32 – Thermal analysis (TG-DTG-DTA) of carbonate rock samples. Symbols legend: Cal = calcination; LOI = Loss on Ignition; Nd not determined yet; Tot. = Total.

No.	Code	Name	LOI 25-200	LOI 230-550	LOI 400-700	LOI Cal.	LOI Tot.	Cal On-set	Cal End-set	Cal On-set	Cal End	Cal Δt
-	-	-	(°C)	(°C)	(°C)	(%)	(%)	(°C)	(°C)	(min)	(min)	(min)
1	2001	SAC	0.17	1.02	-	37.00	44.53	792.5	905.4	77.3	88.5	11.0
2	2004	CMI	0.12	0.01	-	37.54	43.54	794.0	907.0	77.4	88.7	11.0
3	2005	CAL-1	0.21	0.01	-	38.58	43.56	791.0	926.6	77.0	90.7	13.0
4	1818	CNG	0.18	0.03	-	40.28	47.71	810.0	925.0	79.0	90.6	11.0
5	1854	ISP-1	0.32	0.10	-	35.60	42.49	801.0	909.0	78.0	89	11.0
6	1849	HOS-1	0.14	0.03	-	36.47	43.61	799.0	905.0	78.0	88.6	10.6
7	1850	HOS-2	0.59	0.29	-	35.83	49.38	788.8	907.0	77.0	88.0	10.0
8	1851	HOS-3	0.22	0.05	0.32	46.27	46.69	816.2	915.0	79.7	89.6	10.0
9	1852	HOS-4	0.27	0.16	1.30	41.55	42.81	799.8	918.9	78.0	89.9	11.0
10	1853	HOS-5	0.40	0.32	2.21	40.84	43.61	807.0	906.0	78.8	88.7	10.0
11	2828	VER	0.26	0.11	-	42.32	43.81	805.0	916.0	78.0	89.7	11.0
12	2829	CAR	0.10	0.07	-	40.20	43.75	775.0	923.0	75.8	90.4	15.0
13	1990	IDW-1	0.13	0.04	-	39.23	43.62	790.0	924.0	77.0	90.0	13.0
14	1991	IDW-2	0.22	0.01	-	36.30	42.87	799.0	915.0	78.0	89.5	11.5
15	1880	QSC-1	0.42	0.63	-	36.70	44.61	791.0	917.0	77.0	89.7	12.7
16	1992	SMA	0.3	0.58	-	34.37	40.33	786.0	909.0	76.0	89.0	13.0
17	2450	PSP-1	0.13	-	0.57	36.10	43.95	810.0	918.0	79.0	89.9	10.9
18	2451	PSP-2	0.16	0.03	0.60	35.45	44.11	813.8	914.2	79.5	89.5	10.0
19	2665	CRM-d	0.33	0.30	0.72	35.18	43.06	812.2	917.3	79.3	89.8	10.5
20	2666	CRM-w	Nd	Nd	Nd	Nd	Nd	Nd	Nd	Nd	Nd	Nd
21	2701	PTL-1a	0.16	0.08	0.64	36.36	43.61	804.7	915.1	78.5	89.6	11.1
22	2701	PTL-1b	0.17	-	0.53	36.15	43.33	806.5	916.7	78.7	89.7	11.0
23	2702	PTL-2	0.12	0.03	0.48	36.15	43.76	811.3	918.4	79.2	89.9	10.7
24	2887	DOC	0.18	0.05	0.49	34.20	43.31	823.3	924.9	80.4	90.5	10.1
25	1999	CAL-2	0.15	0.84	2.90	27.44	47.79	817.0	903.0	79.8	88.4	8.6
26	1856	ISP-2	0.10	0.05	-	23.76	46.82	837.6	914.4	81.8	89.5	7.7
27	1867	CRM-1	0.29	1.01	-	22.74	47.62	825.4	884.5	80.6	86.5	5.9
28	1873	CRM-2	0.20	1.36	-	27.16	47.58	798.8	894.5	79.0	87.5	8.5
29	2830	ZAN	0.14	0.89	-	24.30	47.85	818	890.7	79.8	87.1	7.3
30	2025	SRI	0.09	0.15	1.16	Nd	46.43	Nd	Nd	Nd	Nd	Nd
31	2112	MME	0.08	0.38	1.82	24.37	47.18	826.9	911	80.8	89.2	8.4
32	1735	INTP	0.21	0.50	2.39	39.92	47.19	781.2	912.2	76.2	89.3	13.1
33	2019	SAL	0.18	0.55	2.26	16.61	47.99	830.3	897.1	81	87.8	6.8
34	1881	QSC-2	0.16	0.30	1.74	42.11	46.87	763	900.9	74.4	88.2	13.8
35	2309	USI	0.25	0.42	2.09	41.60	47.39	770.2	908.9	75.1	89.0	13.9
36	2667	MON	0.16	0.97	2.98	35.61	47.52	789.3	895.2	77.0	87.6	10.6
37	2668	ESH	0.19	0.79	3.48	23.88	46.88	815.9	901.0	79.7	88.2	8.5
38	2669	JGM	0.17	0.35	1.64	25.83	46.51	794.2	894.3	77.6	87.5	9.9
39	2762	UNI-1	0.14	0.31	-	39.95	47.07	792.2	909.0	77.3	89.0	11.7
40	2782	PED	0.19	0.60	2.90	26.18	48.09	817.6	910.6	79.8	89.1	9.3
41	598	SCH	0.90	0.82	2.79	31.14	40.57	785.7	897.7	76.6	87.8	11.2
42	2743	INT	0.26	0.30	1.10	32	41.51	815.3	910.2	79.6	89.2	9.6
43	2904	TAS	Nd	Nd	Nd	Nd	Nd	Nd	Nd	Nd	Nd	Nd
44	1895	CRM-3	0.14	0.04	-	32.09	36.95	789.4	925.3	77.0	90.6	13.6
45	2217	UNI-2	1.02	1.21	3.74	19.25	-	786.3	889.0	76.7	87.0	10.3
46	2761	UNI-3	Nd	Nd	Nd	Nd	Nd	Nd	Nd	Nd	Nd	Nd

Chapter 3. Results and Discussion

Furthermore, burnability moduli from the cement industry, i.e. the Lime Saturation Factor (LSF), the Silica Ratio (SR), the Alumina to iron Ratio (AR), the potential Liquid Phase at 1338°C (LP at 1338 °C), and the Burnability Factor (BF), were calculated from the bulk-rock chemistry. They are defined according to the literature (Taylor, 1997; Ghizdavet, 2016), as follow:

$LSF = CaO / (2.8 \cdot SiO_2 + 1.2 \cdot Al_2O_3 + 0.65 \cdot Fe_2O_3)$		[I]
$SR = SiO_2 / (Al_2O_3 + Fe_2O_3)$		[II]
$AR = (Al_2O_3 / Fe_2O_3)$		[III]
$LP_{at\ 1338^\circ C} = 6.10 \cdot Fe_2O_3 + MgO^* + K_2O + Na_2O$	$\langle AR \leq 1.38 \rangle$	[IV]
$LP_{at\ 1338^\circ C} = 8.20 \cdot Al_2O_3 - 5.22 \cdot Fe_2O_3 + MgO^* + K_2O + Na_2O$	$\langle AR \geq 1.38 \rangle$	[V]
$BF = LSF + 10 SR - 3 \cdot (MgO + A_{eq})$		[VI]

Where (*MgO) denotes an upper limit of 2.0% to the term for MgO and A_{eq} represents the alkali equivalent, corresponding to $(Na_2O + 0.659 \cdot K_2O)$ according to Taylor (1997).

The LSF for high-grade limestones, dolomites, and impure carbonates ranges between 4.5-1078 (average 114.9), 6.6-132.4 (38.5), and 0.1-3.0 (1.6), respectively. The SR for high-grade limestones, dolomites, and impure carbonates ranges between 0.2-8.2 (2.3), 0.2-5.1 (1.9), 2.0-12.9 (4.4), respectively. The AR for high-grade limestones, dolomites, and impure carbonates ranges between 0.2-3.0 (average 1.1), 0.1-3.1 (0.9), and 1.3-3.2 (2.2), respectively. The LP at 1338 °C for high-grade limestones, dolomites, and impure carbonates ranges between 0.04-7.0 (average 1.6), 15.5-22.4 (19.6), and 1.6-33.7 (14.6), respectively. Finally, the burning factor for high-grade limestones, dolomites, and impure carbonates ranges between 18.9-1080.6 (average 134.9), -37.1-75.2 (-0.04), and 0.1-130.4 (33.4), respectively. Burnability moduli are reported in Tab.3.33.

Tab.3.33 – Insoluble Residue and cement industry moduli according to Taylor (1997). Symbols Legend: IR (%) = insoluble residua (averaged values); IC (%) = impurity content, i.e. $[Al_2O_3+Fe_2O_3+SO_3+TiO_2+P_2O_5]$; A_{eq} = alkali content $(Na_2O + 0.65*K_2O)$; LSF = Lime Saturation Factor $[CaO/(2.8*SiO_2+1.18*Al_2O_3+0.65*Fe_2O_3)]$; HI = Hydraulic index $[(SiO_2+Al_2O_3)/CaO]$; CI cement index = $[(2.8*SiO_2+1.18*Al_2O_3+0.65*Fe_2O_3)/(CaO+1.4*MgO)]$; SR = Silica Ratio $(SiO_2/(Al_2O_3+Fe_2O_3))$; AR = Alumina Iron ratio (Fe_2O_3/Al_2O_3) ; BF = burnability factor $[LSF + 10 SR - 3(MgO+ AE + SO_3)]$; LP1338°C = potential Liquid phase at 1338°C for AR < 1.38 $(8.2*Al_2O_3 - 5.22*Fe_2O_3 + MgO + K_2O + N_2O + SO_3)$; LP1338°C = potential Liquid phase at 1338°C for AR > 1.38 $(6.1* Fe_2O_3 + MgO + K_2O + N_2O + SO_3)$, Nd = not determined.

No	Code	Name	IR	IC	A_{eq}	HI	CI	LSF	SR	AR	LP _{1338°C} (AR > 1.38)	LP _{1338°C} (AR < 1.38)	LP _{1338°C} (final)	BF
			(%)	(%)	-	-	-	-	-	-	-	-	-	-
1	2001	SAC	0.18	0.25	0.01	0.00	0.00	203.65	0.75	0.61	0.99	0.63	0.63	209.37
2	2004	CMI	0.53	0.26	0.04	0.01	0.02	47.20	1.71	1.31	0.90	0.86	0.86	63.37
3	2005	CAL-1	0.86	0.26	0.02	0.01	0.03	35.22	3.67	1.37	0.92	0.92	0.92	70.44
4	1818	CNG	0.31	0.16	0.02	0.00	0.01	111.12	0.99	1.16	1.35	1.24	1.24	118.19
5	1854	ISP-1	3.65	0.58	0.02	0.05	0.12	7.90	4.42	1.39	2.02	2.04	2.02	50.01
6	1849	HOS-1	0.40	0.22	0.03	0.01	0.01	70.62	1.26	0.77	1.12	0.62	0.62	81.79
7	1850	HOS-2	2.46	1.27	0.21	0.04	0.11	8.54	3.40	1.00	4.93	4.04	4.04	35.01
8	1851	HOS-3	0.46	0.21	0.05	0.00	0.01	79.53	1.21	0.68	1.12	0.56	0.56	90.22
9	1852	HOS-4	3.21	1.48	0.17	0.08	0.20	4.55	2.67	1.25	7.61	7.04	7.04	18.92
10	1853	HOS-5	2.55	0.81	0.20	0.04	0.10	9.44	2.87	1.61	5.25	5.68	5.25	27.20
11	2828	VER	2.02	0.67	0.13	0.03	0.08	11.89	2.61	1.52	1.96	2.20	1.96	36.37
12	2829	CAR	0.14	0.12	0.01	0.00	0.00	235.50	0.80	1.11	1.15	1.07	1.07	240.75
13	1990	IDW-1	3.39	1.07	0.13	0.05	0.13	7.43	2.45	2.97	2.52	5.47	2.52	29.06
14	1991	IDW-2	0.25	0.15	0.04	0.00	0.01	94.77	1.47	0.18	1.04	0.04	0.04	108.23
15	1880	QSC-1	0.34	0.13	0.02	0.00	0.01	152.80	1.17	0.57	0.72	0.35	0.35	163.48
16	1992	SMA	3.20	1.32	0.20	0.08	0.19	5.25	2.52	2.08	3.38	5.65	3.38	28.00
17	2450	PSP-1	0.08	0.06	0.00	0.00	0.00	1078.80	0.23	0.33	0.32	0.09	0.09	1080.64
18	2451	PSP-2	0.15	0.12	0.01	0.00	0.00	261.17	0.59	1.22	0.47	0.42	0.42	266.33
19	2665	CRM-D	1.42	0.60	0.04	0.03	0.07	14.73	2.60	1.19	1.67	1.34	1.34	39.62
20	2666	CRM-W	2.78	0.64	0.02	0.03	0.07	15.12	2.32	1.08	1.77	1.18	1.18	37.42
21	2701	PTL-1a	1.07	0.18	0.01	0.01	0.02	62.90	2.45	0.73	0.69	0.34	0.34	86.61
22	2701	PTL-1b	1.44	0.23	0.01	0.01	0.03	35.80	3.00	1.43	0.67	0.70	0.67	65.12
23	2702	PTL-2	0.66	0.16	0.01	0.00	0.01	165.98	0.96	0.71	0.75	0.45	0.45	174.39
24	2887	DOC	0.83	0.20	0.01	0.01	0.03	36.50	8.22	0.52	0.57	0.27	0.27	117.81
25	1999	CAL-2	0.57	0.34	0.09	0.01	0.02	30.55	1.20	0.97	17.38	16.90	16.90	-6.75
26	1856	ISP-2	0.21	0.43	0.01	0.00	0.00	112.81	0.21	0.08	22.64	20.57	20.57	51.20

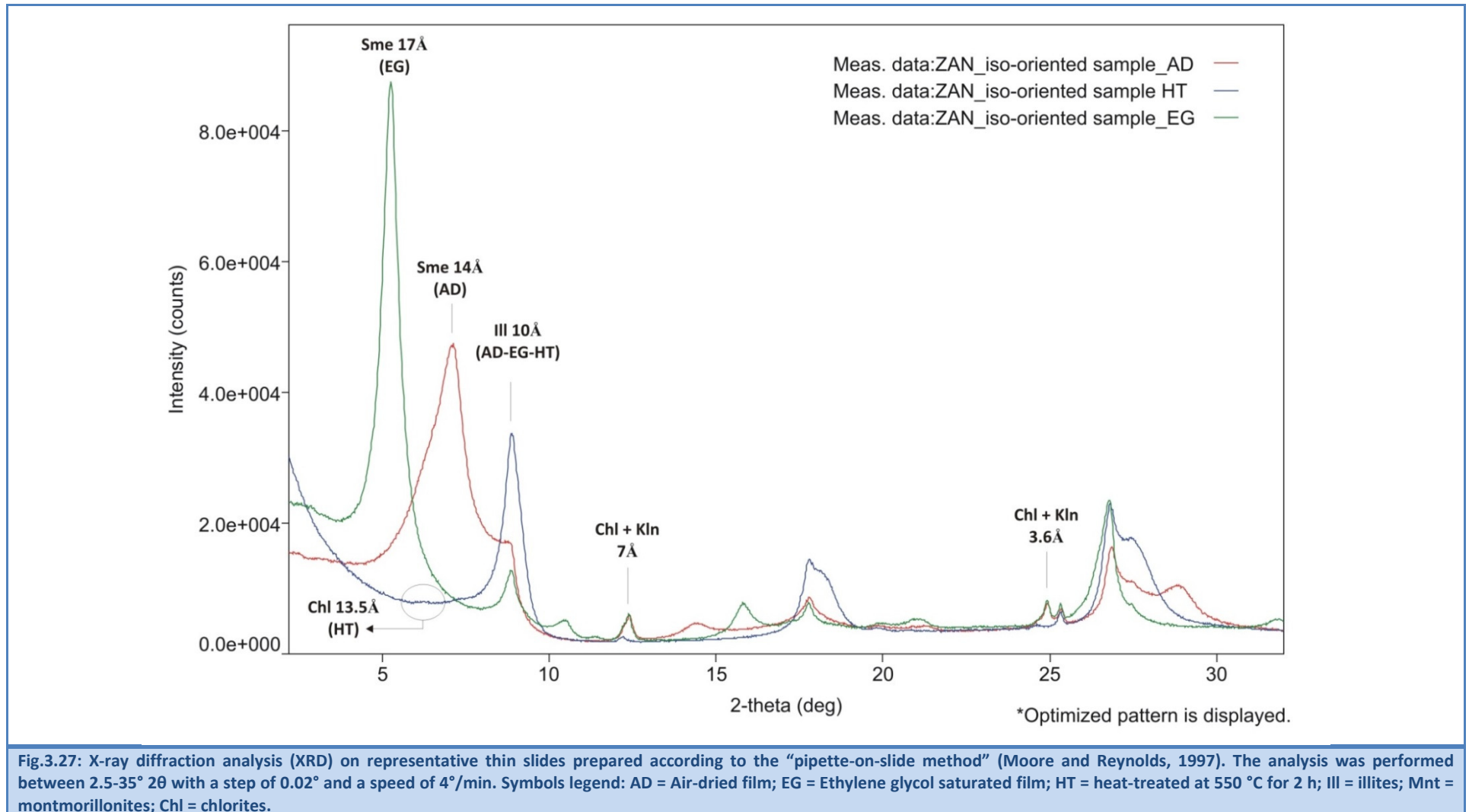
High-grade burnt lime products: impact of calcination kinetics on slaking reactivity;
sticking tendency and blocks formation at HT (1300°C)

Tab. 3.33 (continue)

No	Code	Name	IR	IC	A _{eq}	HI	CI	LSF	SR	AR	LP _{1338°C} (AR > 1.38)	LP _{1338°C} (AR < 1.38)	LP _{1338°C} (final)	BF
27	1867	CRM-1	1.74	0.41	0.16	0.06	0.08	6.62	3.95	1.17	22.65	22.35	22.35	-18.48
28	1873	CRM-2	0.88	0.32	0.13	0.02	0.03	15.39	2.41	1.20	20.35	20.17	20.17	-19.08
29	2830	ZAN	0.22	0.16	0.03	0.01	0.01	52.11	1.45	1.05	21.40	21.24	21.24	3.55
30	2025	SRI	1.18	0.52	0.03	0.02	0.03	24.01	0.81	0.49	18.13	15.75	15.75	-16.27
31	2112	MME	0.32	0.30	0.06	0.01	0.02	28.93	1.32	1.43	19.33	19.37	19.33	-13.90
32	1735	INTP	0.47	0.41	0.08	0.01	0.02	29.88	0.91	0.44	17.46	15.53	15.53	-8.65
33	2019	SAL	0.15	0.16	0.07	0.00	0.01	82.88	0.88	0.69	18.84	18.44	18.44	36.54
34	1881	QSC-2	0.87	0.19	0.04	0.02	0.03	16.96	4.78	0.36	17.92	17.04	17.04	13.06
35	2309	USI	0.18	0.41	0.02	0.01	0.01	44.37	1.03	0.57	20.82	20.02	20.02	-4.94
36	2667	MON	1.52	0.55	0.20	0.05	0.07	7.71	2.99	1.33	20.11	20.03	20.03	-19.13
37	2668	ESH	1.15	0.23	0.10	0.03	0.04	12.66	5.09	0.56	22.61	21.93	21.93	-2.29
38	2669	JGM	0.88	0.68	0.06	0.03	0.04	11.84	1.21	0.78	22.51	20.79	20.79	-37.09
39	2762	UNI-1	1.10	0.63	0.14	0.05	0.07	7.57	2.19	3.08	21.97	23.88	21.97	-33.68
40	2777	PED	0.15	0.14	0.07	0.00	0.00	132.36	0.64	0.80	21.50	21.27	21.27	75.24
41	598	SCH	11.10	2.51	0.25	0.15	0.37	2.66	2.54	2.37	5.22	10.77	5.22	25.35
42	2743	INT	6.22	0.65	0.03	0.14	0.38	2.63	12.89	1.77	1.56	2.16	1.56	130.41
43	2904	TAS	28.75	6.11	0.86	0.54	1.32	0.71	3.11	1.69	16.04	21.46	16.04	24.33
44	1895	CRM-3	13.31	2.83	0.52	0.13	0.32	2.98	2.03	1.34	8.70	8.34	8.34	18.52
45	2217	UNI-2	30.3	7.52	0.96	0.90	1.53	0.43	3.35	2.82	22.60	42.22	22.60	0.10
46	2761	UNI-3	62.9	18.35	2.31	3.67	5.81	0.11	2.62	3.20	33.72	89.64	33.72	1.98

Tab.3.34 – Clay minerals identification on air-dried (AD), ethylene glycol (EG) saturated, and heated-treated (HT) at 550 °C films according to the pipette-on-slide method (More and Reynolds, 1997). Symbols legend: Ill = illites; Sme = smectites; Kln = kaolinites; Chl = chlorites, ML = mixed layers (I-S illite-smectite, I-V illite-vermiculite); Srp = serpentine group; Ply = paligorskites; Tlc = talc; Sep = sepiolite; √√√ = 75-100%; √√ = 50-75%; √ = 25-50%; √ <25%; Tr = traces (<1%), Nd = Not determined because too small amount of sample.

No.	Code	Name	Ill	Sme	Kln	Chl	I-S	I-V	Srp	Ply	Tlc	Sep	Notes
1	2001	SAC	√√		√√	Tr	√√*	-	-	-	-	-	* Sme rich
2	2004	CMI	√	√√√	Tr		-	-	-	-	-	-	
3	2005	CAL-1	√√√	√	√	√	-	-	-	-	-	-	
4	1818	CNG	√√√	-	-	Tr	-	-	-	-	Tr (?)	Tr	
5	1854	ISP-1	-	√√√	Tr	-	-	-	-	√√	-	-	
6	1849	HOS-1	√	√√√	√	Tr	-	-	-	-	-	-	
7	1850	HOS-2	-	-	√	-	√√	-	-	√√√	-	-	
8	1851	HOS-3	√	-	√√	Tr	√√	-	-		-	-	
9	1852	HOS-4	√√√	√√	√	√√	-	-	-	-	-	-	
10	1853	HOS-5	√√	-	-	√	√	-	-	√√	-	-	
11	2828	VER	√√	-	-	-	-	√√√	-	-	-	-	
12	2829	CAR	√√√	√					√				
13	1990	IDW-1	√√√			√√							
14	1991	IDW-2	√√			√√							
15	1880	QSC-1	√√	√√									
16	1992	SMA	√√√	√√	√	√√							
17	2450	PSP-1	√√√	√√	√√	√			√√				
18	2451	PSP-2	√√√	√	√√	√√			√√				
19	2665	CRM-D	√	√√√	√√	-	-	-	-	-	-	-	
20	2666	CRM-W	√√	√	√								
21	2701	PTL-1a	√√√	√√	√	-	-	-	-	-	-	-	
22	2701	PTL-1b	√√	√√√	-	-	-	-	-	-	-	-	
23	2702	PTL-2	√√	√	√								
24	2887	DOC	√							√√			
25	2005	CAL-2	√√√	√	-	√	-	-	-	-	-	-	
26	1856	ISP-2	√√	√√		√√√							
27	1867	CRM-1	√√√										
28	1873	CRM-2	√√√	√√		√√							
29	2830	ZAN	√√	√√√	Tr	√	-	-	-	-	-	-	
30	2025	SRI	√√√	√	√	√√√							
31	2112	MME	√√√	√√	√√	√				√			
32	1735	INTP	√√√		√√								
33	2019	SAL	Nd	Nd	Nd	Nd	Nd	Nd	Nd	Nd	Nd		
34	1881	QSC-2	√	√	√								
35	2309	USI	√√√	√√	√√								
36	2667	MON	√√√	√√	√	√√							
37	2668	ESH	√√	√	√	√√							
38	2669	JGM	√√		√√	√√√					√		
39	2762	UNI-1	√√√	√	√	√√							
40	2777	PED	√√√	√√		√√							
41	598	SCH	√√√	√	√√	√√							
42	2743	INT	√√		√√								
43	2904	TAS	√√	-	-	√	√√*		-	-	-		* Ill rich
44	1895	CRM-3	√√√			√√							
45	2217	UNI-2	√√√	√	√	√√							
46	2761	UNI-3	√√√	√	√	√							



Tab.3.35 – Quantitative-phase analysis by X-ray diffraction (XRD-QPA) on insoluble residua. Symbols legend: Ill-Ms = illite-muscovite; Mnt = montmorillonite; Kln = kaolinite; Chl = chlorites; Srp = serpentine group; Ply = palygorskite; Tlc = talc; Qtz = quartz; Pl = plagioclase; Kfs = K-feldspar; Gt = goethite; Px = pyroxene; Amp = amphibole; Grt = grossular; Gbs = Gibbsite; Mag = magnetite; Hem = hematite; Py = pyrite; Anh = Anhydrite; Gp = gypsum; Bas = bassanite; And = Andalusite; Ky = kyanite; Cls = Celestine; Fl = fluorite; Gn = galena; Sp = Sphalerite; Cpr = cuprite; Rt = rutile; Ant = anatase; Ttn = titanite; Svb = svambergite; * = possible overestimation of illite because illite-smectites (I-S), or illite-vermiculites (I-V) mixed-layers are present into the mixtures.

No.	Code	Ill-Ms	Mnt	Kln	Chl	Srp	Ply	Tlc	Qtz	Pl	Kfs	Gt	Px	Amp	Grt	Gbs	Mag-Hem	Py	Anh	Gp-Bas	And-Ky	Cls	Fl	Gn	Sp	Cpr	Rt-Ant	Ttn	Svb
-	-	(%)	(%)	(%)	(%)	(%)	(%)	(%)	(%)	(%)	(%)	(%)	(%)	(%)	(%)	(%)	(%)	(%)	(%)	(%)	(%)	(%)	(%)	(%)	(%)	(%)	(%)	(%)	
1	2001	69.0*	12.7	3.3	-	-	-	-	8.2	1.5	2.5	0.6	-	-	-	-	1.9	0.3	-	-	-	-	-	-	-	-	-	0.2	-
2	2004	5.2	57.9	-	-	-	-	-	10.9	-	6.7	18.8	-	-	-	-	-	-	-	-	-	-	-	-	-	-	0.5	-	-
3	2005	72.2	-	6.3	1.3	-	-	-	7.5	1.5	0.3	7.0	-	-	-	-	-	3.0	0.8	-	-	-	0.1	-	-	-	-	-	-
4	1818	10.7	-	0.5	-	3.0	-	1.6	19.3	-	10.9	0.2	-	-	-	0.2	0.2	1.2	-	-	-	-	2.8	1.5	0.5	0.6	1.6	-	-
5	1854	2.1	23.6	-	-	-	10.7	-	44.7	13.4	1.2	3.3	-	-	-	-	-	-	-	-	-	-	-	-	-	-	0.5	-	-
6	1849	56.0*	7.0	6.7	-	-	-	-	0.8	-	2.4	21.7	-	-	-	-	4.4	-	-	-	-	-	-	-	-	-	1.0	-	-
7	1850	20.4*	-	-	-	-	9.8	-	12.5	14.0	12.2	9.0	-	-	-	-	-	-	16.3	5.7	-	-	-	-	-	-	-	-	-
8	1851	36.0	1.5	5.9	4.4	-	-	-	1.6	1.0	10.7	12.7	-	-	-	-	20.1	-	-	-	-	-	-	-	-	-	6.0	-	-
9	1852	59.4	3.0	0.7	2.4	-	-	-	10.4	11.8	3.6	0.2	-	-	-	-	8.6	-	-	-	-	-	-	-	-	-	-	-	-
10	1853	36.9*	-	1.4	4.2	-	1.7	-	15.9	0.4	29.8	-	-	-	-	-	2.3	-	-	-	-	6.0	-	-	-	-	1.8	-	-
11	2828	55.5*	1.4	-	-	-	-	-	11.5	0.2	17.8	14.0	-	-	-	-	-	-	-	-	-	-	-	-	-	-	-	-	-
12	2829	40.3	0.3	-	-	0.3	-	-	23.9	8.8	8.9	9.2	2.3	0.5	-	-	-	4.1	-	-	-	-	1.6	-	-	-	-	-	-
13	1990	44.8	-	-	11.5	-	-	-	23.1	-	11.9	-	-	-	-	-	2.0	5.3	-	-	-	-	-	-	-	-	1.5	-	-
14	1991	10.1	-	-	4.2	-	-	-	68.2	-	0.7	1.1	-	-	-	0.2	-	15.4	-	-	-	-	-	-	-	-	-	-	-
15	1880	20.3	11.6	-	-	-	-	-	42.3	0.5	22.0	0.7	-	-	-	0.9	-	1.6	-	-	-	-	-	-	-	-	-	-	-
16	1992	40.6	6.6	1.3	18.0	-	-	-	30.6	0.4	0.3	1.9	-	-	-	-	0.3	-	-	-	-	-	-	-	-	-	-	-	-
17	2450	35.0	5.8	17.2	1.0	18.0	-	-	3.2	1.9	1.0	4.9	-	-	-	-	9.0	-	-	-	-	-	-	-	-	-	2.9	-	-
18	2451	54.8	1.5	7.2	6.4	7.2	-	-	2.1	12.1	5.2	3.0	-	-	-	-	-	-	-	-	-	-	-	-	-	-	0.4	-	-
19	2665	1.4	13.9	6.3	-	-	-	-	78.0	-	-	0.3	-	-	-	-	-	-	-	-	-	-	-	-	-	-	-	-	-
20	2666	12.6	0.9	3.0	-	-	-	-	74.8	-	-	1.5	-	-	-	-	7.3	-	-	-	-	-	-	-	-	-	-	-	-
21	2701	7.9	0.3	-	-	-	-	-	81.0	0.4	7.1	0.3	-	-	-	-	-	-	-	-	-	0.5	-	-	-	-	-	-	2.3
22	2701	22.7	0.5	-	-	-	-	-	64.9	1.1	7.9	0.5	-	-	-	-	-	-	-	-	-	0.2	-	-	-	-	-	-	2.3
23	2702	14.8	1.1	0.8	-	-	-	-	55.9	11.9	3.0	0.8	-	1.9	-	0.5	2.3	-	-	-	1.4	0.4	-	-	-	-	-	-	5.2
24	2887	0.6	-	-	-	-	8.2	-	90.5	-	-	0.7	-	-	-	-	-	-	-	-	-	-	-	-	-	-	-	-	-
25	1999	42.0	1.0	-	11.0	-	-	-	7.0	13.0	13.0	9.0	-	-	-	-	-	3.0	-	1.0	-	-	-	-	-	-	-	-	-
26	1856	6.2	12.8	-	38.6	-	-	-	13.6	10.2	2.1	5.6	6.2	-	-	-	-	0.3	3.6	-	-	-	0.5	-	-	-	0.5	-	-

High-grade burnt lime products: impact of calcination kinetics on slaking reactivity; sticking tendency and blocks formation at HT (1300°C)

Tab. 3.35 (continue)

No.	Code	Ill-Ms	Mnt	Kln	Chl	Srp	Ply	Tlc	Qtz	Pl	Kfs	Gt	Px	Amp	Grt	Gbs	Mag-Hem	Py	Anh	Gp-Bas	And-Ky	Cls	Fl	Gn	Sp	Cpr	Rt-Ant	Ttn	Svb
-	-	(%)	(%)	(%)	(%)	(%)	(%)	(%)	(%)	(%)	(%)	(%)	(%)	(%)	(%)	(%)	(%)	(%)	(%)	(%)	(%)	(%)	(%)	(%)	(%)	(%)	(%)	(%)	(%)
27	1867	22.2	-	-	-	-	-	-	50.1	-	24.8	0.9	-	-	-	-	-	1.8	-	-	0.2	-	-	-	-	-	-	-	-
28	1873	44.6	15.8	-	9.0	-	-	-	8.9	1.4	17.4	1.0	-	-	-	-	-	0.4	1.1	-	-	-	-	-	-	-	0.4	-	-
29	2830	26.9	7.0	1.6	-	-	-	-	2.2	8.0	35.0	1.2	-	-	-	-	16.3	-	-	-	-	-	0.2	-	-	-	1.6	-	-
30	2025	30.1	0.7	1.7	61.4	-	-	-	1.1	-	-	2.3	0.6	-	-	-	0.7	-	-	-	-	-	0.2	-	-	-	0.7	-	-
31	2112	64.0	6.5	3.0	1.1	-	1.8	-	12.0	2.0	0.6	4.5	-	-	-	-	-	0.7	-	-	-	-	-	-	-	-	-	4.2	-
32	1735	47.0	-	3.7	-	-	-	-	9.5	1.0	2.2	33.1	-	-	-	-	2.1	-	-	-	-	-	-	-	-	-	1.6	-	-
34	1881	2.0	0.2	0.3	-	-	-	-	97.4	-	-	-	-	-	-	-	-	-	0.2	-	-	-	-	-	-	-	-	-	-
35	2309	32.0	12.9	4.7	-	-	-	-	18.5	11.0	-	20.2	-	-	-	-	0.7	-	-	-	-	-	-	-	-	-	-	-	-
36	2667	19.5	3.0	0.5	2.9	-	-	-	54.2	-	-	8.1	-	-	-	-	11.5	0.3	-	-	-	-	-	-	-	-	-	-	-
37	2668	5.4	0.7	1.0	1.9	-	-	-	84.9	2.8	0.4	3.0	-	-	-	-	-	-	-	-	-	-	-	-	-	-	-	-	-
38	2669	6.5	-	3.0	74.8	-	-	0.8	10.3	-	-	4.2	-	-	-	-	-	-	-	-	-	-	0.4	-	-	-	-	-	-
39	2762	68.7	0.8	0.7	11.8	-	-	-	8.9	-	3.0	0.6	-	-	-	-	-	-	-	-	-	-	4.5	-	-	-	1.0	-	-
40	2777	15.1	8.3	-	8.3	-	-	-	54.3	7.0	-	-	-	-	-	-	7.0	-	-	-	-	-	-	-	-	-	-	-	-
41	598	50.0	0.2	10.5	2.4	-	-	-	25.7	-	5.1	3.7	-	-	-	-	-	-	-	-	-	-	-	-	-	-	2.4	-	-
42	2743	12.0	-	5.0	-	-	-	-	79.0	3.4	0.4	-	-	-	-	-	-	-	-	-	-	-	-	-	-	-	-	-	-
43	2904	45.6*	2.0	-	-	1.5	-	-	38.9	7.2	1.4	-	-	-	-	-	3.7	-	-	-	-	-	-	-	-	-	-	-	-
44	1895	28.7	-	-	8.6	-	-	-	32.1	20.0	9.5	-	0.7	-	0.3	-	-	-	-	-	-	-	-	-	-	-	-	-	-
45	2217	29.2	1.8	0.5	3.9	-	-	-	49.3	8.4	2.8	0.5	-	-	-	-	-	3.5	0.2	0.2	-	-	-	-	-	-	-	-	-
46	2761	35.3	0.5	0.5	2.1	-	-	-	43.6	10.7	6.3	0.2	-	-	-	-	-	1.0	-	-	-	-	-	-	-	-	-	-	-

- *Insoluble residua and clay minerals characterization*

The identification of clay minerals was performed on air-dried (AD), ethylene glycol (EG)-solvated, and heated-treated (550° C) iso-oriented films, prepared according to the pipette-on-slides method (Moore and Reynolds, 1997). The following fundamental clay mineral groups were identified: 1) illites, 2) smectites, 3) kaolinites, 4) chlorites, 5) mixed-layers (generally irregular illite-smectites, but also illite-vermiculites), 6) serpentine group, and 7) palygorskite. Non-clay minerals recognized in the <2 µm fraction normally are not included in the semi-quantitative analysis on the oriented aggregates, thus the given data refer only to less than 2 µm phyllosilicate groups. Results of the semi-quantitative analysis are reported in Tab.3.34. Representative XRD diffraction patterns of oriented clay minerals (sample ZAN), are reported in Fig.3.27.

Moreover, the quantitative phase analysis (QPA) by the Rietveld method was performed on the whole insoluble residue (IR) after the correct clay mineral identification based on the oriented and treated film analyses. Considering that no structure for illite-smectites (I-S) mixed-layer is available in the literature, this phase was not considered for Rietveld refinements. This fact possibly may cause a systematic increase in the full width at half-maximum intensity (FWHM) of the illite basal peak, leading to an overestimation of the illite, and a misrepresenting of the QPA. In such case the value of illite was highlighted using an asterisk. Results are reported in Tab.3.35.

The following fundamental mineral phases were identified on pure and slightly impure carbonate samples: quartz 0.8-97.4 % (average 31.3 %), micas 0.6-72.2 % (31.2 %), and chlorite 1.0-74.8 % (14.6 %) as fundamental phases; K-feldspar 0.3-35.0 % (8.7 %), palygorskite 1.8-10.7 % (7.6 %), serpentine, i.e. lizardite and antigorite 0.3-18.0 % (7.1 %), smectites 0.2-24.0 % (6.2 %), goethite 0.2-33.1 % (6.0 %), plagioclase 0.2-14.0 % (5.5 %), iron oxides, i.e. magnetite and hematite 0.2-20.1 % (5.7 %), anhydrite 0.2-16.3 % (4.4 %), kaolinite 0.3-17.2 % (3.5 %), pyrite 0.3-15.4 % (2.9 %) as subordinated phases; pyroxenes, i.e. aegirine and diopside, amphiboles, i.e. actinolite and hornblende, talc, svanbergite, andalusite and kyanite polymorphs, gypsum, celestine, bassanite, fluorite, rutile and anatase polymorphs, titanite, galena, sphalerite and cuprite as accessory phases. The following fundamental mineral phases were identified on impure carbonate samples: quartz 25.7-79.0 (average 44.8 %), micas 12.0-50.0 % (33.5 %) plagioclase 3.4-20.0 (9.9 %), K-feldspar 0.4-9.5 % (4.2 %) as fundamental phases; plus chlorite 2.1-8.6 % (4.3 %), kaolinite 0.5-10.5 % (4.1 %), magnetite 0.0-3.7 %, and pyrite 1.0-3.5 % (2.2 %), as

subordinated phases; and goethite, serpentine, smectites, pyroxenes, garnet, anhydrite, gypsum, bassanite, rutile and anatase polymorphs as accessory phases.

- *Overburning Test (OT) and Sticking Tendency (ST) classification*

The “High Temperature Test” or “Overburning Test” method (OT) was performed on each sample 2-4 times to test data repeatability. The average deviation standard of mass values is lower than 2 g. Therefore, the limit of 2 g was adopted to distinguish ST classes. The only exception is represented by mass values falling into the upper and the lower ST classes, whose limits were accordingly not defined (Tab.3.36). Moreover, to facilitate the statistical analysis of data-set, 7 classes were further grouped into 4 main groups, namely A, B, C, and D (Fig.3.28). The group A includes 4 samples completely melted at 1300 °C (OT = 42 g), deriving from impure carbonates (IR > 5%). The group B is constituted by 12 “critical” samples with medium-high (OT = 16-18 g), high (OT = 18-20 g), and very high ST (OT > 20 g), deriving from high-grade or slightly impure limestones, dolomites and calcitic/dolomitic marbles. The group C is constituted by 22 samples, with medium (OT = 14-16 g), medium-low (OT = 12-14 g), and slight ST, deriving from high-grade or slightly impure carbonates. Finally, the group D is represented by 8 samples, without ST (OT < 10g), mostly deriving from mainly pure or slightly impure dolomites, with the only exception of one pure limestone (IDW-1). Results from OT in terms of mass values, and derived ST classification are reported in Tab.3.40, and visualized in Fig.3.28. The average ST measured on 24 high-calcium limestones and calcitic marbles was 15.5 ± 1.1 g, while the average ST measured on 16 dolomites and dolomitic marbles was 10.7 ± 1.6 g. As concerns impure carbonates, 1 marly limestone, 2 marly dolomites, and 1 silicate-bearing marble, were completely melted, pointing out a theoretical ST of 42 g. Conversely, remaining 2 marly limestones pointed out a medium-low ST of 12.9 ± 0.9 g.

Tab.3.36 – Overburning Test (OT) samples mass and Sticking Tendency (ST) classification. Symbols legend: Cal-mrb = calcitic marble, Dol-mrb = dolomitic marble

Sample no.	Lithology	Code	Name	Test-1 (g)	Test-2 (g)	Test-3 (g)	Test-4 (g)	ST (g)	Max (g)	Min (g)	St.Dev. (g)	ST (%)	Class	Notes
1	Lmt	2001	SAC	17.2	18.8	18.1	17.1	17.8	18.8	17.1	0.8	42.4	B3	
2	Lmt	2004	CMI	15.5	15.2	15.0	15.4	15.3	15.5	15.0	0.2	36.3	C1	
3	Lmt	2005	CAL	12.2	-	11.9	11.2	11.8	12.2	11.2	0.5	28.1	D1	
4	Cal-mrb	1818	CNG	18.2	-	15.0	16.9	16.7	18.2	15.0	1.6	39.7	B3	
5	Lmt	1854	ISP-1	18.2	13.7	17.6	16.2	16.4	18.2	13.7	2.0	39.1	B3	decrepiting on cooling
6	Lmt	1849	HOS-1	18.9	17.5	19.5	19.5	18.8	19.5	17.5	1.0	44.9	B2	
7	Lmt	1850	HOS-2	11.4	12.2	10.5	13.6	11.9	13.6	10.5	1.3	28.4	D1	
8	Lmt	1851	HOS-3	17.5	15.5	18.8	18.1	17.5	18.8	15.5	1.4	41.6	B3	
9	Lmt	1852	HOS-4	11.1	11.4	12.7	13.9	12.3	13.9	11.1	1.3	29.2	C2	
10	Lmt	1853	HOS-5	15.0	13.5	12.3	11.7	13.1	15.0	11.7	1.4	31.2	C2	
11	Lmt	2828	VER	15.3	13.4	13.2	13.9	14.0	15.3	13.2	1.0	33.3	C1	
12	Cal-mrb	2829	CAR	15.2	16.0	15.4	14.3	15.2	16.0	14.3	0.7	36.2	C1	
13	Lmt	1990	IDW-1	11.0	10.0	-	7.1	9.4	11.0	7.1	2.1	22.3	D2	
14	Lmt	1991	IDW-2	16.0	15.3	14.7	14.3	15.1	16.0	14.3	0.7	35.9	C1	decrepiting on cooling
15	Lmt	1880	QSC-1	18.4	16.5	18.8	16.1	17.4	18.8	16.1	1.4	41.5	B3	
16	Lmt	1992	SMA	18.2	-	16.2	17.6	17.3	18.2	16.2	1.0	41.2	B3	burning on heating, locally melted, decrepiting on cooling
17	Lmt	2450	PSP-1	15.0	-	14.6	-	14.8	15.0	14.6	0.3	35.2	C1	
18	Lmt	2451	PSP-2	16.1	-	15.7	-	15.9	16.1	15.7	0.3	37.8	C1	
19	Lmt	2665	CRM-d	13.4	13.7	13.9	-	13.7	13.9	13.4	0.2	32.5	C2	decrepiting on cooling
20	Lmt	2666	CRM-w	11.2	11.2	16.7	-	13.0	16.7	11.2	3.2	31.0	C2	decrepiting on cooling
21	Lmt	2701	PTL-1a	18.8	18.1	20.2	-	19.0	20.2	18.1	1.1	45.3	B2	
22	Lmt	2701	PTL-1b	16.6	16.7	16.7	-	16.7	16.7	16.6	0.1	39.7	B3	
23	Lmt	2702	PTL-2	15.7	16.9	-	-	16.3	16.9	15.7	0.8	38.9	B3	
24	Lmt	2887	DOC	23.8	21.6	25.0	-	23.5	25.0	21.6	1.7	55.9	B1	
25	Dol	1999	CAL-2	12.3	11.2	12.5	15.8	12.9	15.8	11.2	2.0	30.8	D1	
26	Dol	1856	ISP-2	13.1	11.9	-	9.7	11.5	13.1	9.7	1.7	27.5	D1	
27	Dol-mrb	1867	CRM-1	14.8	-	-	14.2	14.5	14.8	14.2	0.5	34.5	C1	
28	Dol-mrb	1873	CRM-2	14.5	-	-	16.2	15.4	16.2	14.5	1.2	36.6	C1	

Table 3.36 (continue)

Sample	Lithology	Code	Name	Test-1	Test-2	Test-3	Test-4	ST (g)	Max	Min	St.Dev.	ST (%)	Class	Notes
no.	-	-	-	(g)	(g)	(g)	(g)	(g)	(g)	(g)	(g)	(%)	-	
29	Dol	2830	ZAN	8.7	8.0		7.9	8.2	8.7	7.9	0.4	19.5	D2	
30	Dol-mrb	2025	SRI	16.9	19.2	16.9	15.4	17.1	19.2	15.4	1.5	40.7	B3	
31	Dol	2112	MME	8.7	10.5	-	9.8	9.7	10.5	8.7	0.9	23.0	D2	decrepiting on cooling
32	Dol	1735	INTP	15.6	13.2	-	16.2	15.0	16.2	13.2	1.6	35.7	C1	
33	Dol	2019	SAL	4.2	2.1	7.8	-	4.7	7.8	2.1	2.9	11.2	D2	
34	Dol	1881	QSC-2	5.5	5.5	2.8	6.6	5.1	6.6	2.8	1.6	12.2	D2	
35	Dol	2309	USI	9.9	8.2	-	-	9.0	9.9	8.2	1.2	21.5	D2	
36	Dol-mrb	2667	MON	13.5	11.6	-	-	12.6	13.5	11.6	1.3	29.9	C2	
37	Dol-mrb	2668	ESH	6.2	3.1	-	-	4.6	6.2	3.1	2.2	11.0	D2	
38	Dol-mrb	2669	JGM	14.9	14.8	-	13.8	14.5	14.9	13.8	0.6	34.5	C1	
39	Dol	2762	UNI	9.2	-	-	11.7	10.5	11.7	9.2	1.8	24.9	D1	
40	Dol	2777	PED	2.9	-	-	9.0	5.9	9.0	2.9	4.3	14.1	D2	
41	Marl	598	SCH	12.1	11.6	13.2	11.1	12.0	13.2	11.1	0.9	28.6	D1	cracking on heating
42	Marl	2743	INT	13.0	14.3	14.4	-	13.9	14.4	13.0	0.8	33.1	C2	
43	Marl	2904	TAS	42.0	42.0	42.0	42.0	42.0	42.0	42.0	0.0	100.0	A	burning on heating, completely melted, decrepiting on cooling
44	Mrb	1895	CRM-3	42.0	42.0	42.0	42.0	42.0	42.0	42.0	0.0	100.0	A	completely melted; decrepiting on cooling
45	Marl	2217	UNI	42.0	42.0	42.0	42.0	42.0	42.0	42.0	0.0	100.0	A	completely melted
46	Marl	2761	UNI	42.0	42.0	42.0	42.0	42.0	42.0	42.0	0.0	100.0	A	completely melted

Tab.3.37 – Physical characterization of limes burnt at 1050 °C and blocks burnt at 1300 °C from the OT method. Symbols legend: MDT = mechanical degradation test, DT = drop test, BET SSA = specific surface area by the BET method; DAPD = desorption average pore average, ND = not determined

No.	code	name	finer at 10 mm after MDT	finer at 19 mm after MDT	finer at 19 mm after DT	BET SSA	DAPD	Real Density
			(%)	(%)	(%)	(m ² /g)	(nm)	(g/cm ³)
1	2001	SAC	14.3	Nd	Nd	0.16	13.7	3.31
2	2004	CMI	1.7	Nd	Nd	0.13	12.1	3.31
3	2005	CAL-1	22.8	Nd	Nd	0.11	14.7	3.29
4	1818	CNG	5.1	7.5	Nd	0.04	40.9	3.29
5	1854	ISP-1	3.6	6.5	8.8	0.09	15.4	3.29
6	1849	HOS-1	7.0	8.1	40.0	0.24	48.1	3.29
7	1850	HOS-2	18.2	19.7	51.3	0.25	13.2	3.37
8	1851	HOS-3	8.8	10.8	38.4	0.27	10.1	3.30
9	1852	HOS-4	34.9	38.9	60.2	0.18	14.4	3.30
10	1853	HOS-5	20.1	20.1	17.8	0.31	10.7	3.34
11	2828	VER	4.8	48.6	20.0	0.13	12.8	3.25
12	2829	CAR	57.9	90.7	100	0.24	8.6	3.30
13	1990	IDW-1	9.2	14.3	29.2	0.14	16.2	3.30
14	1991	IDW-2	10.2	12.6	69.3	0.12	13.7	3.32
15	1880	QSC	11.2	17.3	29.9	0.15	11.9	3.27
16	1992	SMA	39.1	58.2	46.6	0.07	21.0	3.26
17	2450	PSP-1	4.9	4.9	9.6	0.83	46.3	3.29
18	2451	PSP-2	3.5	6.8	25.2	0.15	10.6	3.30
19	2665	CRM-D	Nd	Nd	Nd	0.19	10.3	3.27
20	2666	CRM-W	Nd	Nd	Nd	0.22	9.2	3.27
21	2701	PTL-1a	7.2	12.6	18.9	0.16	11.1	3.29
22	2701	PTL-1b	Nd	Nd	Nd	0.12	11.2	3.28
23	2702	PTL-2	7.6	17.4	29.3	0.12	12.1	3.29
24	2887	DOC	6.5	13.5	11.2	0.22	10.0	3.26

High-grade burnt lime products: impact of calcination kinetics on slaking reactivity;
sticking tendency and blocks formation at HT (1300°C)

Tab.3.37 (continue)

No.	code	name	finer at 10 mm after MDT	finer at 19 mm after MDT	finer at 19 mm after DT	BET SSA	DAPD	Real Density
			(%)	(%)	(%)	(m ² /g)	(nm)	(g/cm ³)
25	1999	CAL-2	18.3	Nd	Nd	0.85	6.5	3.42
26	1856	ISP-2	16.0	25.6	83.1	0.87	6.1	3.42
27	1867	CRM-1	Nd	Nd	Nd	1.15	5.6	3.42
28	1873	CRM-2	Nd	Nd	Nd	1.37	5.6	3.44
29	ND	ZAN	4.9	39.8	24.4	2.98	5.5	3.40
30	2025	SRI	20.0	30.2	43.4	0.54	7.1	3.41
31	2112	MME	13.1	37.5	58.0	1.87	5.6	3.43
32	1735	INTP	10.5	11.7	37.0	0.40	8.0	3.42
33	2019	SAL	16.2	30.8	43.4	2.87	5.4	3.42
34	1881	QSC-2	10.9	23.5	36.1	2.76	5.5	3.36
35	2309	USI	17.7	57.2	56.1	4.92	5.4	3.38
36	2667	MON	24.6	34.1	33.1	1.32	6.1	3.42
37	2668	ESH	24.6	33.1	34.1	4.06	5.5	3.40
38	2669	JGM	16.3	36.1	32.9	0.44	7.6	3.43
39	2762	UNI-1	21.1	38.3	55.0	1.59	5.6	3.40
40	2777	PED	42.0	55.0	46.3	4.46	5.2	3.41
41	598	SCH	4.0	9.8	Nd	0.14	14.7	3.23
42	2743	INT	4.9	11.7	6.9	0.15	11.1	3.22
43	2904	TAS	Nd	Nd	Nd	0.53	7.6	3.07
44	1895	CRM-3	Nd	Nd	Nd	0.39	8.8	3.18
45	2217	UNI-2	Nd	Nd	Nd	Nd	Nd	Nd
46	2761	UNI-3	Nd	Nd	Nd	Nd	Nd	Nd

Tab.3.38 – Chemical analysis (XRF-WDS) of lime blocks burnt at 1300 °C

No.	-	1	2	3	4	5	6	7	8	9	10	11	12	13	14	15	16	17	18	19	20	21	22	23
code	-	2001	2004	2005	1818	1854	1849	1850	1851	1852	1853	2828	2829	1990	1991	1880	1992	2450	2451	2665	2666	2701	2701	2702
name	-	SAC	CMI	CAL	CNG	ISP-1	HOS-1	HOS-2	HOS-3	HOS-4	HOS-5	VER	CAR	IDW-1	IDW-2	QSC	SMA	PSP-1	PSP-2	CRM-d	CRM-w	PTL-1a	PTL-1b	PTL-2
SiO ₂	(%)	0.2	0.77	0.13	0.4	2.68	0.32	1.93	0.37	2.03	1.96	1.88	0.22	1.32	0.33	0.36	3.5	0.37	0.02	4.45	4.17	1.23	1.14	0.28
Al ₂ O ₃	(%)	0.1	0.29	0.2	0.11	0.47	0.16	0.42	0.16	0.55	0.56	0.55	0.09	0.49	0.14	0.08	1	0.15	0.02	0.39	0.42	0.09	0.09	0.08
Fe ₂ O ₃	(%)	0.08	0.13	0.14	0.24	0.35	0.19	0.43	0.22	0.57	0.4	0.42	0.08	0.81	0.26	0.08	0.67	0.2	0.03	0.38	0.41	0.1	0.09	0.07
CaO	(%)	98.1	98.3	97.2	96.3	95.8	98.6	85.3	98.5	92.7	92.8	96.2	98.1	94.6	97.2	98.6	93.6	98.6	99.5	94	94.2	98.1	98	99
MgO	(%)	1.02	0.27	0.88	2.58	0.51	0.5	1.54	0.51	3.38	3.95	0.58	1.36	1.33	0.55	0.72	0.71	0.46	0.27	0.46	0.46	0.27	0.43	0.29
SO ₃	(%)	<0.01	<0.01	0.01	<0.01	<0.01	<0.01	3.23	<0.01	0.04	0.03	0.01	<0.01	0.03	<0.01	0.01	0.02	<0.01	<0.01	0.01	0.01	0.01	0.01	<0.01
Na ₂ O	(%)	<0.01	0.07	<0.01	0.05	<0.01	<0.01	<0.01	<0.01	0.08	<0.01	0.1	<0.01	<0.01	<0.01	<0.01	<0.01	0.07	<0.01	<0.01	<0.01	<0.01	<0.01	<0.01
K ₂ O	(%)	0.05	0.05	0.05	0.05	0.05	0.05	0.05	0.06	0.05	0.04	0.05	0.06	0.05	0.05	0.04	0.08	0.05	0.05	0.06	0.07	0.06	0.07	0.05
MnO	(%)	0.03	<0.01	<0.01	0.08	0.04	<0.01	0.03	0.02	0.04	0.03	0.06	<0.01	1.26	1.37	<0.01	0.28	<0.01	<0.01	0.02	<0.01	<0.01	<0.01	0.04
BaO	(%)	<0.01	<0.01	<0.01	<0.01	<0.01	<0.01	<0.01	<0.01	<0.01	<0.01	<0.01	<0.01	<0.01	<0.01	<0.01	<0.01	<0.01	<0.01	<0.01	<0.01	<0.01	<0.01	<0.01
SrO	(%)	0.08	0.05	0.07	0.05	0.07	0.07	6.9	0.07	0.18	0.13	0.03	0.04	0.01	<0.01	0.06	0.06	0.07	0.01	0.07	0.08	0.09	0.09	0.08
TiO ₂	(%)	<0.01	<0.01	<0.01	<0.01	<0.01	<0.01	0.1	<0.01	<0.01	<0.01	<0.01	<0.01	<0.01	<0.01	<0.01	<0.01	<0.01	<0.01	<0.01	<0.01	<0.01	<0.01	<0.01
P ₂ O ₅	(%)	0.26	0.08	0.13	0.06	0.06	0.06	0.07	0.06	0.15	0.06	0.12	0.06	0.05	0.05	0.05	0.06	0.07	0.06	0.18	0.17	0.08	0.08	<0.01
Cl-	(%)	<0.01	<0.01	<0.01	<0.01	<0.01	<0.01	<0.01	<0.01	<0.01	<0.01	0.02	<0.01	<0.01	<0.01	<0.01	<0.01	<0.01	<0.01	<0.01	<0.01	<0.01	<0.01	<0.01

No.	-	24	25	26	27	28	29	30	31	32	33	34	35	36	37	38	39	40	41	42	43	44	45	46
code	-	2887	1999	1856	1867	1873	ND	2025	2112	1735	2019	1881	2309	2667	2668	2669	2762	2777	598	2743	2904	1895	2217	2761
name	-	DOC	CAL-2	ISP-2	CRM-1	CRM-2	ZAN	SRI	MME	INTP	SAL	QSC-2	USI	MON	ESH	JGM	UNI	PED	SCH	INT	TAS	CRM-3	UNI-2	UNI-3
SiO ₂	(%)	2.25	0.91	0.65	1.15	0.05	0.56	0.45	0.35	1.04	0.36	1.94	0.16	2.2	1.73	0.75	0.82	0.53	8.55	8.91	28.9	16	Nd	51.9
Al ₂ O ₃	(%)	0.05	0.28	0.13	0.32	0.2	0.13	0.12	0.14	0.22	0.07	0.06	0.03	0.29	0.05	0.23	0.23	0.03	2.94	0.64	6.13	4.33	Nd	12.7
Fe ₂ O ₃	(%)	0.05	0.19	0.36	0.28	0.18	0.11	0.48	0.16	0.25	0.12	0.12	0.1	0.28	0.16	0.53	0.16	0.06	1.34	0.39	3.38	2.44	Nd	5.04
CaO	(%)	96.5	63.6	58.7	59.4	57.5	60.2	65.1	60	63	59.1	59	61.8	56.6	58.8	58.5	59.1	58.6	85.4	89.1	57.9	74.2	Nd	17.2
MgO	(%)	0.46	34.8	39.9	38.7	41.4	38.8	33.5	39.2	35.2	40.1	38.6	37.8	40.4	39	39.8	39.5	40.6	0.74	0.41	1.9	1.28	Nd	6.06
SO ₃	(%)	0.01	0.01	0.01	0.02	0.01	0.02	<0.01	0.01	0	0.03	0.02	0.02	0.01	0.02	<0.01	0.02	0.02	0.02	0.01	0.03	0.07	Nd	2.08
Na ₂ O	(%)	0.28	<0.01	<0.01	<0.01	<0.01	<0.01	<0.01	<0.01	<0.01	<0.01	<0.01	<0.01	<0.01	<0.01	<0.01	<0.01	<0.01	<0.01	<0.01	0.19	0.16	Nd	0.65
K ₂ O	(%)	0.05	0.06	0.06	0.05	0.06	0.05	0.06	0.06	0.06	0.06	0.07	0.07	0.06	0.06	0.06	0.07	0.06	0.08	0.04	0.72	0.89	Nd	3.2
MnO	(%)	0.03	0.06	0.08	<0.01	0.02	0.02	0.15	0.02	0.06	0.02	0.03	<0.01	0.02	0.03	0.08	<0.01	<0.01	0.32	0.07	0.12	0.02	Nd	0.06
BaO	(%)	<0.01	<0.01	<0.01	<0.01	<0.01	<0.01	<0.01	<0.01	<0.01	<0.01	<0.01	<0.01	<0.01	<0.01	<0.01	<0.01	<0.01	<0.01	<0.01	<0.01	<0.01	<0.01	<0.01
SrO	(%)	0.05	0.02	0.02	0.01	0.02	0.01	0.04	0.02	0.05	0.02	0.02	0.02	0.01	<0.01	0.02	0.02	0.02	0.27	0.3	0.17	0.05	Nd	0.12
TiO ₂	(%)	0.1	<0.01	<0.01	<0.01	<0.01	<0.01	<0.01	<0.01	<0.01	<0.01	<0.01	<0.01	<0.01	<0.01	<0.01	<0.01	<0.01	0.23	<0.01	0.36	0.32	Nd	0.82
P ₂ O ₅	(%)	0.19	0.05	0.07	0.04	0.04	0.05	0.05	0.06	0.04	0.05	0.05	0.06	0.1	0.12	0.07	0.06	0.07	0.14	0.14	0.11	0.15	Nd	0.05
Cl-	(%)	<0.01	<0.01	<0.01	<0.01	0.01	0	<0.01	<0.01	<0.01	<0.01	0	<0.01	0	<0.01	<0.01	<0.01	<0.01	<0.01	0.01	<0.01	<0.01	Nd	0

High-grade burnt lime products: impact of calcination kinetics on slaking reactivity;
sticking tendency and blocks formation at HT (1300°C)

Chapter 3. Results and Discussion

Tab.3.39 – X-ray diffraction Quantitative-phase analysis (XRD-QPA) of lime blocks from the OT method. Symbols legend: Per = periclase, Hat = Hatrurite, Lar = Larnite, Alm = Tricalcium aluminate, Brm = Brownmillerite, Ak-Ge = Akermanite-Gehlenite, Mer = Merwinite, Mag = Magnetite, Hem = Hematite, Fe-Si = Fersilicite, Anh = Anhydrite, Cel = Celestine, Py = pyrite, Qtz = quartz/cristobalite, AP = amorphous phase, Por = portlandite, Tr = traces (<0.5 %).

No.	Code	Name	Lime	Per	Hat	Lar	Alm	Brw	Ak-Ge	Mer	CaMnO ₃	Ca ₂ MnO ₄	Mn ₃ O ₄	Mag	Hem	Fe-Si	Anh	Cel	Py	Cal	Qtz	AP	Por
-	-	-	(%)	(%)	(%)	(%)	(%)	(%)	(%)	(%)	(%)	(%)	(%)	(%)	(%)	(%)	(%)	(%)	(%)	(%)	(%)	(%)	(%)
1	2001	SAC	95.2	-	1.0	0.5	1.6	1.0	-	0.7	-	-	-	-	-	-	-	-	-	-	-	-	Tr
2	2004	CMI	97.8	-	1.5	-	0.2	-	-	0.3	-	-	-	-	-	0.2	-	-	-	-	-	-	Tr
3	2005	CAL	94.9	-	4.2	0.8	-	0.2	-	-	-	-	-	-	-	-	-	-	-	-	-	-	Tr
4	1818	CNG	82.8	3.7	-	0.3	13.0	0.2	-	-	-	-	-	-	-	-	-	-	-	-	-	-	Tr
5	1854	ISP-1	88.2	-	6.3	4.1	0.2	1.1	-	0.2	-	-	-	-	-	0.2	-	-	-	-	-	-	Tr
6	1849	HOS-1	97.4	-	-	0.2	-	0.3	0.3	2.0	-	-	-	-	-	-	-	-	-	-	-	-	Tr
7	1850	HOS-2	86.8	3.5	1.9	1.6	0.2	0.9	-	1.1	-	-	-	-	-	-	2.4	2.0	-	-	-	-	Tr
8	1851	HOS-3	97.2	-	0.9	-	1.8	0.2	-	-	-	-	-	-	-	-	-	-	-	-	-	-	Tr
9	1852	HOS-4	87.7	2.8	7.7	0.5	0.2	1.5	-	-	-	-	-	-	-	-	-	-	-	-	-	-	Tr
10	1853	HOS-5	77.6	3.0	7.5	1.3	2.8	7.7	-	-	-	-	-	-	-	-	-	-	-	-	-	-	Tr
11	2828	VER	87.8	-	8.7	1.4	2.1	-	-	-	-	-	-	-	-	-	-	-	-	-	-	-	Tr
12	2829	CAR	99.7	0.3	-	-	-	-	-	-	-	-	-	-	-	-	-	-	-	-	-	-	Tr
13	1990	IDW-1	78.5	0.2	6.0	6.0	1.6	6.2	-	-	-	-	0.2	-	-	0.5	-	-	0.2	0.6	-	-	Tr
14	1991	IDW-2	95.6	0.2	2.2	-	0.4	-	-	-	0.4	1.1	-	-	-	-	-	-	-	-	-	-	Tr
15	1880	QSC-1	98.5	-	0.2	-	-	1.3	-	-	-	-	-	-	-	-	-	-	-	-	-	-	Tr
16	1992	SMA	83.0	-	9.0	0.7	-	7.0	-	-	-	-	-	-	-	-	-	-	0.3	-	-	-	Tr
17	2450	PSP-1	99.8	-	-	-	0.2	-	-	-	-	-	-	-	-	-	-	-	-	-	-	-	Tr
18	2451	PSP-2	99.6	-	-	-	0.4	-	-	-	-	-	-	-	-	-	-	-	-	-	-	-	Tr
19	2665	CRM-D	75.0	-	10.2	13.2	1.0	0.4	-	-	-	-	-	-	-	0.2	-	-	-	-	-	-	Tr
20	2666	CRM-W	70.4	-	6.6	21.5	0.8	0.2	-	-	-	-	-	-	-	0.6	-	-	-	-	-	-	Tr
21	2701	PTL-1a	82.9	-	1.5	6.5	8.5	0.3	-	-	-	-	-	-	-	-	-	-	-	-	0.3	-	Tr
22	2701	PTL-1b	86.7	-	6.4	4.4	1.2	1.0	-	-	-	-	-	-	-	0.4	-	-	-	-	0.2	-	Tr
23	2702	PTL-2	97.0	-	0.2	1.9	0.2	0.2	-	-	-	-	-	-	-	0.2	-	-	-	-	-	-	Tr
24	2887	DOC	79.3	4.3	2.2	7.0	1.7	3.7	-	-	-	-	-	-	-	1.9	-	-	-	-	-	-	Tr
25	ND	CAL-2	62.5	26.5	4.5	-	3.4	1.3	-	-	-	-	-	-	-	1.1	-	-	-	0.6	-	-	Tr
26	1856	ISP-2	56.4	42.3	0.36	-	-	0.88	-	-	-	-	-	-	-	-	-	-	-	0.4	-	-	Tr
27	1867	CRM-1	52.8	35.7	2.3	3.6	5.5	0.2	-	-	-	-	-	-	-	-	-	-	-	-	-	-	Tr
28	1873	CRM-2	53.1	41.7	1.8	1.4	1.7	0.2	-	-	-	-	-	-	-	0.2	-	-	-	-	-	-	Tr
29	2830	ZAN	56.1	42.0	0.4	-	Tr	1.4	-	-	-	-	-	-	-	-	-	-	-	-	-	-	Tr

Tab.3.39 (continue)

No.	Code	Name	Lime	Per	Hat	Lar	Alm	Brw	Ak-Ge	Mer	CaMnO ₃	Ca ₂ MnO ₄	Mn ₃ O ₄	Mag	Hem	Fe-Si	Anh	Cel	Py	Cal	Qtz	AP	Por	
-	-	-	(%)	(%)	(%)	(%)	(%)	(%)	(%)	(%)	(%)	(%)	(%)	(%)	(%)	(%)	(%)	(%)	(%)	(%)	(%)	(%)	(%)	
30	2025	SRI	61.0	31.9	1.6	2.3		3.1	-	-	-	-	-	-	-	-	-	-	-	-	-	-	-	Tr
31	2112	MME	61.8	35.5	0.3	-	2.1	0.3	-	-	-	-	-	-	-	-	-	-	-	-	-	-	-	Tr
32	1735	INTP	61.5	35.7	0.8	0.5	-	1.3	-	-	-	-	-	-	-	-	-	-	-	-	0.2	-	-	Tr
33	2019	SAL	57.8	36.3	4.0	0.1	-	1.3	-	-	-	-	-	-	-	-	-	-	-	-	0.4	-	-	Tr
34	1881	QSC-2	58.3	34.4	0.3	5.6	1.3	0.2	-	-	-	-	-	-	-	0.2	-	-	-	-	-	-	-	Tr
35	2309	USI	59.0	36.8	2.9	0.6	0.2	0.2	0.3	-	-	-	-	-	-	-	-	-	-	-	-	-	-	Tr
36	2667	MON	52.0	37.4	3.4	1.5	-	5.7	-	-	-	-	-	-	-	-	-	-	-	-	-	-	-	Tr
37	2668	ESH	53.8	37.0	0.2	5.3	-	3.7	-	-	-	-	-	-	-	-	-	-	-	-	-	-	-	Tr
38	2669	JGM	54.6	39.3	4.6	0.9	-	0.7	-	-	-	-	-	-	-	-	-	-	-	-	-	-	-	Tr
39	2762	UNI-1	52.5	40.9	4.1	1.3	0.5	0.3	-	-	-	-	-	-	0.3	0.2	-	-	-	-	-	-	-	Tr
40	2777	PED	61.3	37.5	0.1	0.9	0.2		-	-	-	-	-	-	-	-	-	-	-	-	-	-	-	Tr
41	598	SCH	45.0	0.2	41.4	2.7	8.3	2.5	-	-	-	-	-	-	-	0.2	-	-	-	-	-	-	-	Tr
42	2743	INT	60.2	-	35.3	4.1		0.4	-	-	-	-	-	-	-	-	-	-	-	-	-	-	-	Tr
43	2904	TAS	-	-	1.7	42.6	21.0	0.3	8.1	0.3	-	-	-	-	-	-	-	-	-	-	-	-	26.3	Tr
44	1895	CRM-3	19.3	0.5	7.4	19.5	10.4	16.0	6.7	-	-	-	-	0.4	-	-	-	-	0.7	0.7	1.6	17.0	Tr	
45	2217	UNI-2	Nd	Nd	Nd	Nd	Nd	Nd	Nd	Nd	Nd	Nd	Nd	Nd	Nd	Nd	Nd	Nd	Nd	Nd	Nd	Nd	Nd	Nd
46	2761	UNI-3	-	-	-	-	-	-	-	-	-	-	-	-	-	-	-	-	-	-	-	3.3	96.7	Tr

High-grade burnt lime products: impact of calcination kinetics on slaking reactivity;
sticking tendency and blocks formation at HT (1300°C)

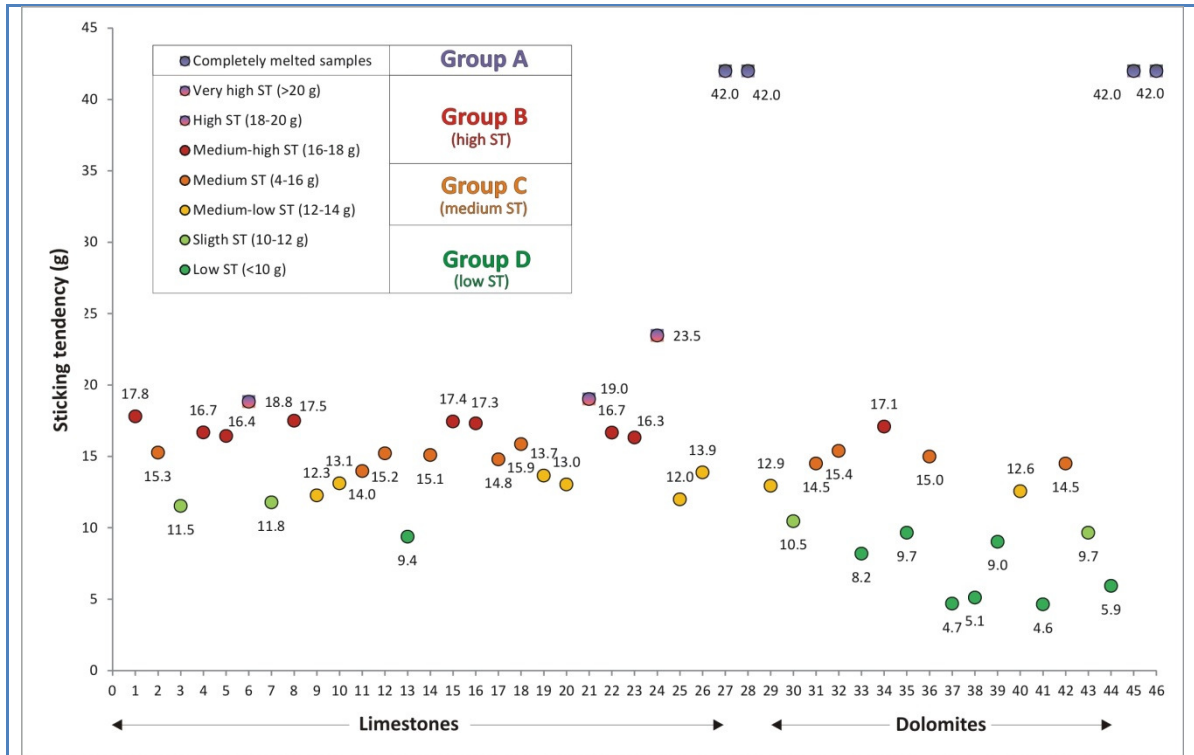


Fig.3.28: Sticking Tendency (ST) classification of 46 analyzed samples.

- *Lime blocks characterization*

Lime blocks from OT can be also characterized by visual aspect, color, physical properties, i.e. hardness, density, BET specific surface area, chemical, and mineralogical analyses (Tab.3.37, Tab.3.38, and Tab.3.39). According to the Munsell geological rock-color chart, lime blocks from high-calcium limestones were white (N9), very pale orange (10YR 8/2), dusky yellow (5Y 6/4), or light brown (5YR 5/6). Conversely, pure dolomitic limes were often pinkish-gray (5YR 8/1). Blocks from slightly impure or marly limestones/dolomites were generally darker, ranging from grayish red (5R 4/2 - 10R 4/2) or pale yellowish brown (10YR 6/2), up to dusky yellowish brown (10YR 2/2), or grayish olive green (5GY 3/2). South African samples from Neoproterozoic limestone, enriched in manganese compounds, were dark greenish gray (5G 4/1). Sometimes lime blocks resulted to be strongly compacted, presenting an anomalous hardness, probably due to the high sintering or overburning tendency. This awareness was achieved observing that the agate mortar was scratched on manual grinding for the XRD analysis. Conversely, lime blocks from high-grade dolomites were generally very soft and easily to crumble. Moreover, some specific samples presented a fast decrepitation on air cooling after the extraction from the muffle furnace. This fact was specifically observed on samples containing orthorhombic

larnite, plus other subordinated cementitious constituents. Finally, melted samples from impure carbonates and/or silicate-bearing marbles, presented characteristic glassy features upon cooling, showing typical mm-sized bubbles and conchoidal fracture (Fig.3.29a).

The physical characterization of lime blocks was performed by means of nitrogen gas intrusion for the BET specific surface area, and by gas pycnometry for the real density determinations. High-calcium limes pointed out a BET area of $0.2 \pm 0.2 \text{ m}^2/\text{g}$, an average pore diameter of $16.6 \pm 11.4 \text{ nm}$ and a real density of $3.3 \pm 0.03 \text{ g/cm}^3$. Conversely, dolomitic limes pointed out a BET area of $2.0 \pm 1.5 \text{ m}^2/\text{g}$, an average pore diameter of $6.0 \pm 0.8 \text{ nm}$ and a real density of $3.4 \pm 0.02 \text{ g/cm}^3$. Blocks from impure carbonates and/or silicate-bearing marbles pointed out BET area of $0.3 \pm 0.2 \text{ m}^2/\text{g}$, average pore diameter of $10.5 \pm 3.1 \text{ nm}$, and real density of $3.2 \pm 0.1 \text{ g/cm}^3$. Results from physical analyses are reported in Tab.3.37.

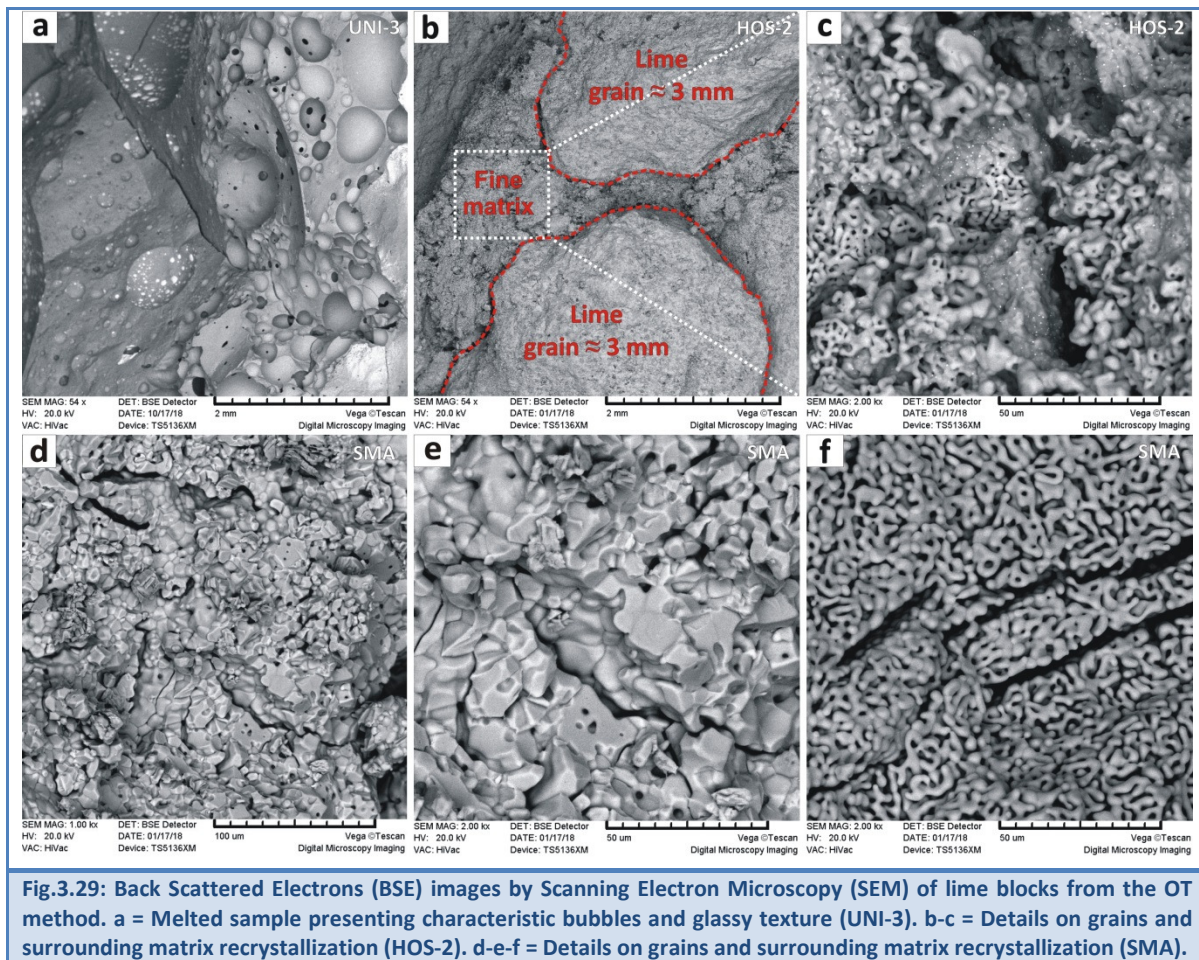


Fig.3.29: Back Scattered Electrons (BSE) images by Scanning Electron Microscopy (SEM) of lime blocks from the OT method. a = Melted sample presenting characteristic bubbles and glassy texture (UNI-3). b-c = Details on grains and surrounding matrix recrystallization (HOS-2). d-e-f = Details on grains and surrounding matrix recrystallization (SMA).

The chemical analysis (XRF-WDS) of lime blocks is reported in Tab.3.38. Some significant BSE micrographs, showing main microstructures observed on a couple of samples (HOS-2 and SMA) by the SEM-EDS are reported in Fig.3.29. The XRD-QPA analysis of lime blocks is reported in Tab.3.39. The Rietveld analysis pointed out lime ($\text{CaO} = 89.1 \pm 8.9\%$), or lime ($\text{CaO} = 57.2 \pm 3.7\%$) plus periclase ($\text{MgO} = 36.9 \pm 4.0\%$), as fundamental constituents in high-calcium and magnesium-rich burnt products, respectively. The following subordinated mineral phases were also identified: larnite ($\text{Ca}_2\text{SiO}_4 = 2.4 \pm 4.1\%$), hatrurite ($\text{Ca}_3\text{SiO}_5 = 2.9 \pm 3.0\%$), tricalcium aluminate ($\text{Ca}_3\text{Al}_2\text{O}_6 = 1.3 \pm 2.5\%$), brownmillerite ($\text{Ca}_2(\text{Al,Fe})_2\text{O}_5 = 1.4 \pm 2.0\%$), merwinite ($\text{Ca}_3\text{Mg}(\text{SiO}_4)_2 = 2.0\%$ max), anhydrite ($\text{CaSO}_4 = 2.4\%$ max), and celestine ($\text{SrSO}_4 = 2.0\%$ max). Moreover, the following accessory mineral phases were observed in traces ($<2\%$): cristobalite (SiO_2), magnetite (FeFe_2O_4), hematite (Fe_2O_3), fersilicite (FeSi), pyrite (Fe_2S), akermanite-gehlenite (solid solution of $\text{Ca}_2\text{Mg}(\text{Si}_2\text{O}_7)$ and $\text{Ca}_2\text{Al}(\text{AlSiO}_7)$), and calcite (CaCO_3). Some manganese compounds (CaMnO_3 , Ca_2MnO_4 , Mn_3O_4) were also identified in South African samples from the Neoproterozoic limestone. Finally, the portlandite ($\text{Ca}(\text{OH})_2$), representing the main significant weathering product, was observed in traces everywhere. Conversely, blocks from impure carbonates pointed out the presence of lime ($\text{CaO} = 25.6 \pm 22.8\%$), and periclase ($\text{MgO} = 15.0 \pm 24.7\%$) as main constituents plus hatrurite ($\text{Ca}_3\text{SiO}_5 = 19.5 \pm 16.0\%$), larnite ($\text{Ca}_2\text{SiO}_4 = 15.5 \pm 15.1\%$), tricalcium aluminate ($\text{Ca}_3\text{Al}_2\text{O}_6 = 6.9 \pm 8.2\%$), brownmillerite ($\text{Ca}_2(\text{Al,Fe})_2\text{O}_5 = 4.0 \pm 6.8\%$), akermanite-gehlenite (solid solution between these end-members: $\text{Ca}_2\text{Mg}(\text{Si}_2\text{O}_7)$ and $\text{Ca}_2\text{Al}(\text{AlSiO}_7) = 3.8 \pm 3.9\%$), calcite ($\text{CaCO}_3 = 2.0 \pm 4.7\%$), and merwinite (max 2.4%). The following accessory mineral phases were determined in traces ($<2\%$): fersilicite, pyrite, magnetite, and cristobalite. Finally, a significant content of amorphous phase ($21.6 \pm 6.6\%$) was determined on a couple of glassy samples (TAS and CRM-3), using an internal standard with the Rietveld method.

3.4.5 Discussion

- *Pressed pellets method (XRF-WDS) validation*

The chemical analyses performed at Cimprogetti by XRF-WDS, was compared to the chemical analysis performed at the University of Ferrara by ICP-MS. This test was carried out on a sub-set of 25 samples on the total 46 whole-rocks selected for this paper. The statistical analysis pointed out the following regression factors for major and minor

elements: magnesium: 0.807, alumina: 0.944 iron: 0.906, sodium: 0.897, potassium: 0.887, titanium: 0.887, manganese: 0.997, strontium: 0.997. Phosphorous and barium are not reported because determined by pre-calibrated standardless analysis. Results confirm an acceptable accuracy and data reproducibility on reported elements for the pressed pellets method performed at Cimprogetti.

- *Impact of chemical and mineralogical compositions on burnability and ST*

The impact of chemical and mineralogical composition on the heating behavior or burnability, and the ST was investigated by means of a thoroughly characterization of carbonate raw materials. Initially, it was considered the possible correlation between the ST and the impurity content, i.e. the insoluble residue (IR). The statistical analysis on calcitic and dolomitic samples pointed out regression factors of 0.47 and 0.77, respectively, attesting an apparent (quite) good fitness between parameters. However, the regression analysis was performed again plotting different ST groups, and melted samples, separately. The result attests no real correlation between ST and IR is present (Fig.3.30). This fact may indicate that the quality of the impurity content, in terms of chemical and mineralogical compositions, could be more important than its quantity for burnt lime products (Boynton, 1982). Indeed, correlations between ST and major, minor, and trace elements were also investigated in order to point out possible interesting trends. Unfortunately, regression factors were always quite low. Therefore, it was investigated the statistical correlation between the ST and moduli from the cement industry, i.e. LSF, SR, AR, LP 1338 °C, and BF (Taylor, 1997). Moreover it was investigated the combination between different moduli, plotting different ST groups, and melted samples, separately. This kind of approach enhanced interesting results. However some indispensable premises to the use of cement moduli must be strictly taken into consideration: 1) the temperature of the overburning test, i.e. 1300 °C, is significantly lower than the temperature of the clinkerization process, i.e. 1450 °C; 2) the calculation of the theoretical LP at 1338 °C for dolomitic materials could be affected by errors, considering that it is declared to be valid for a content of MgO < 2%; 3) cement moduli are suitable for prediction of raw meals burnability, considering homogeneous starting mixtures, and theoretical absence of minor constituents (Telschow, et al. 2012). Effectively, this specific case-study regards carbonate raw materials from the lime industry, i.e. gravel size aggregates, according to the OT method, and not homogeneous raw meals. Moreover subordinated mineral constituents are

present, as well. Finally, dolomitic limes present a content of MgO ranging between 33.5-41.5 %, which is one order of magnitude higher than that expected in standard Portland cements for which the burnability moduli have been formulated.

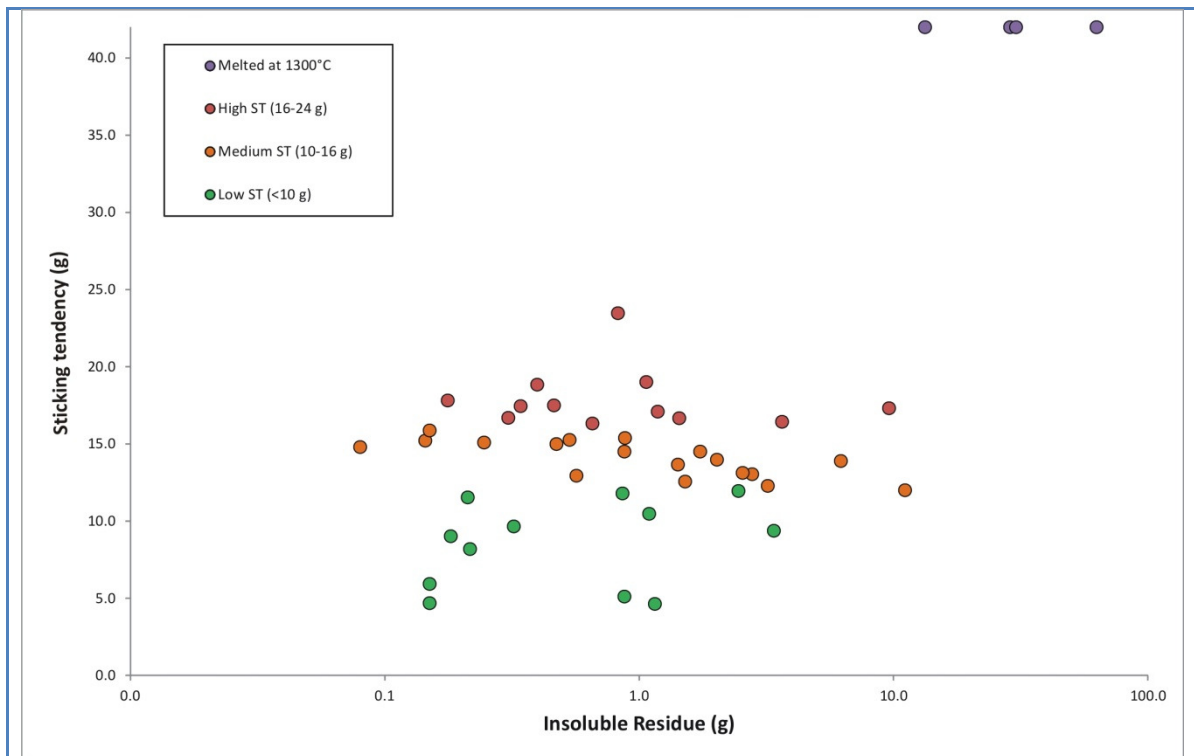


Fig.3.30: Sticking Tendency (ST) Vs Insoluble Residue (IR).

In view of this, main plots are visualized in Fig.3.31, Fig.3.32, Fig.3.33, Fig.3.34, and Fig.3.35. The first one, showing the ST against AR, allows distinguishing 4 main different clusters made of samples with similar lithology and burnability (Fig.3.31). Effectively, the cluster 1 includes impure carbonate rocks melted at 1300 °C, the cluster 2 includes limestones with critical high ST and AR <1, the cluster 3 includes limestones with medium ST and AR between 1-2, finally, the cluster 4 includes dolomites with low ST and AR <1. According to the literature, AR governs the ratio between aluminate and ferrite phases in the clinker, determining the quantity of the liquid phase formed at relatively low temperatures (Taylor, 1997). Especially, the quantity of liquid theoretically passes through a maximum at AR of 1.38 (see the dotted red line in Fig.3.31). The second plot reports the ST against the potential LP at 1338 °C (Fig.3.32).

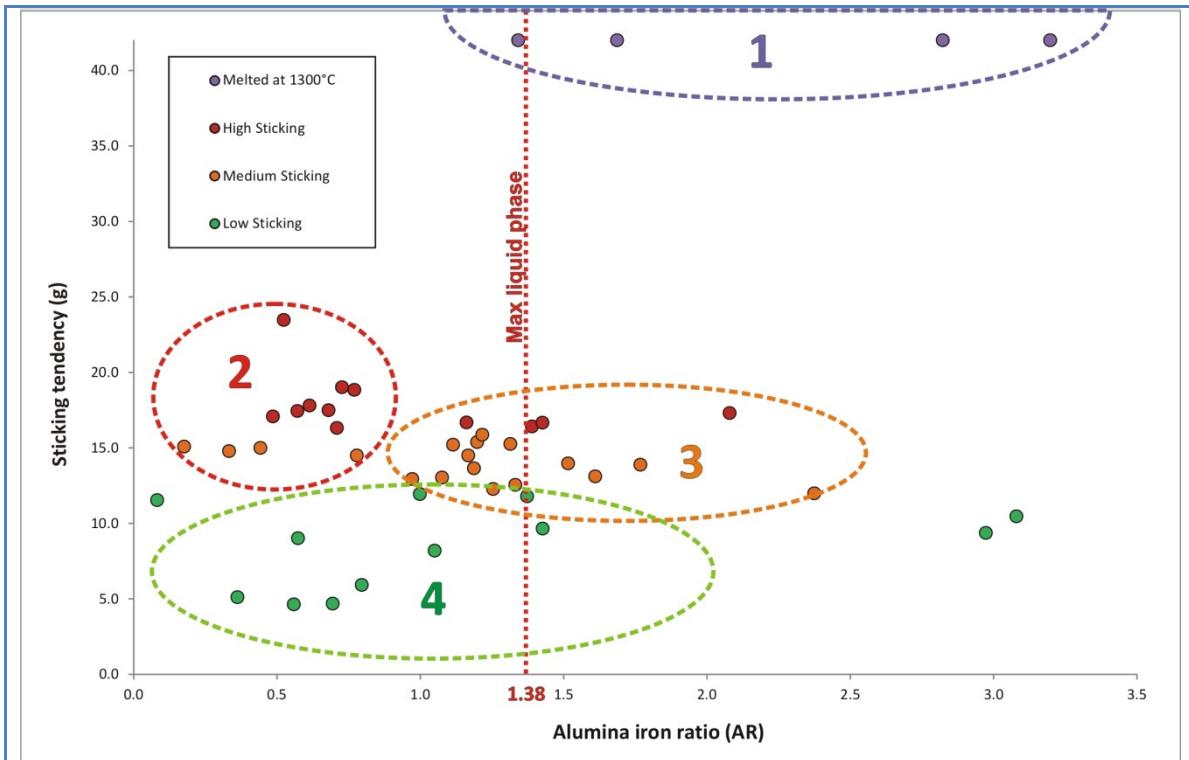


Fig.3.31: Sticking Tendency (ST) Vs Alumina iron Ratio (AR). Symbols legend: 1 = impure carbonates melted at 1300°C; 2 = high ST limestones; 3 = medium ST limestones; 4 = low ST dolomites.

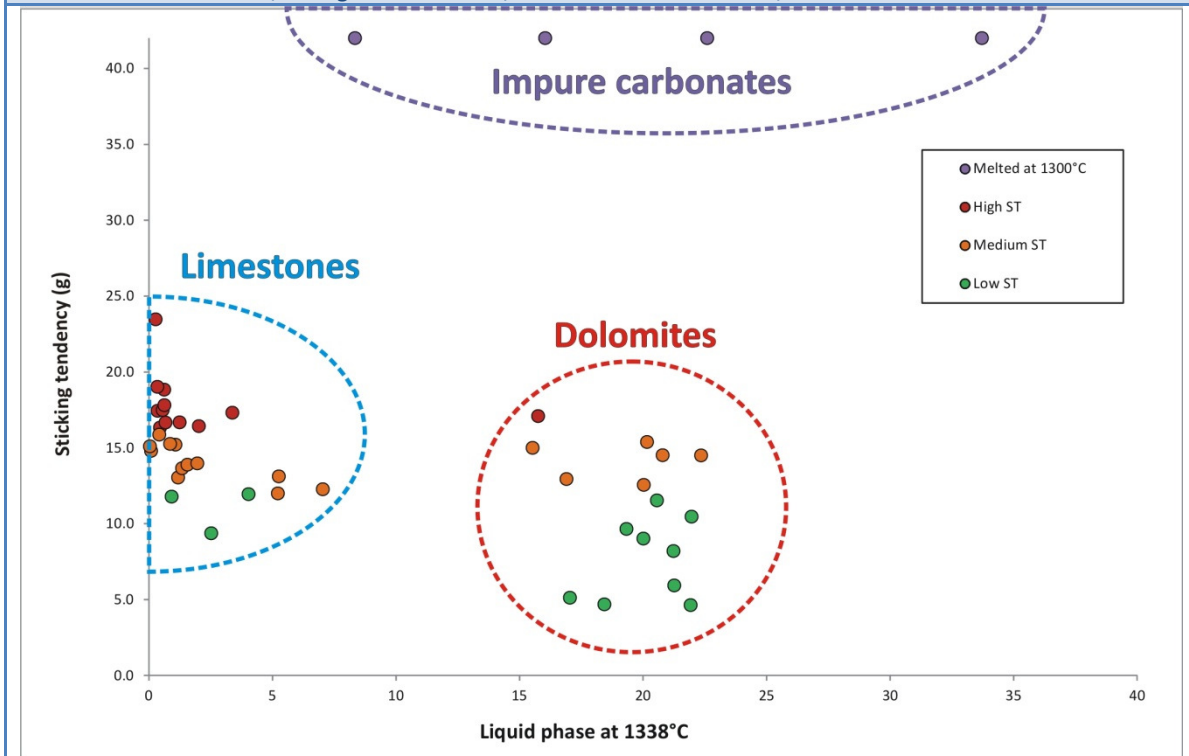


Fig.3.32: Sticking Tendency (ST) Vs potential Liquid Phase at 1338°C (LP)

High-grade burnt lime products: impact of calcination kinetics on slaking reactivity; sticking tendency and blocks formation at HT (1300°C)

Three main clusters are evident: the one on the top includes impure carbonate rocks melted at 1300 °C; the one on right includes dolomites, and the one on the left includes limestones, dolomitic and marly limestones. Combining data sets, it was possible to plot the potential LP calculated at 1338 °C against AR (Fig.3.33). Effectively, previous trends are confirmed, and the following clusters can be identified:

- 1) Impure samples completely melted at 1300 °C, namely group A, are quite dispersed in this plot. The large abundance of fluxing agents directly impact on their burnability. This fact can be visualized plotting alumina (Al_2O_3 %) plus iron (Fe_2O_3 %) against the alkali equivalent (Fig.3.34). The driving process is represented by clay minerals dehydration melting, which is further accentuated by the alkali availability from feldspars decomposition.
- 2) The cluster of high ST, namely group B, is mainly constituted by pure and slightly impure limestones with a theoretical LP at 1338°C between 0.2-1.0 and AR between 0.4-0.8. Blocks with high ST can be explained by a predominant solid-state sintering process, namely “high overburning tendency”, with extremely limited content of ferritic melts, because samples plot on the left of the AR 1.38 dot line (Fig.3.33).
- 3) The cluster of medium ST, namely group C, is mainly constituted by high-grade and slightly impure limestone samples, plus a couple of marly limestones, with theoretical LP between 0.5-1.0, and AR between 1.0 and 2.0. Blocks from cluster 2 can be explained by a predominant liquid-phase sintering, namely “incomplete clinkerization process”, in the presence of some content of aluminate or ferritic melts, because samples are close to the AR 1.38 dot line. This cluster also includes 4 samples with high ST and a couple of samples with low ST (Fig.3.33).
- 4) The cluster of low ST, namely group D, is mainly constituted by dolomitic limes presenting a theoretical high content of LP (>10), and relatively low AR values between 0.1-1.4. The amount of the LP is affected by the large content of magnesium on parameter calculations. This cluster also includes sporadic samples presenting medium and high ST, which should be explained apart. According to the meaning of the liquid factor, dolomitic blocks can be explained in terms of liquid-phase sintering process with dominant ferritic melts, because samples plotted on the left of the AR 1.38 dot line.

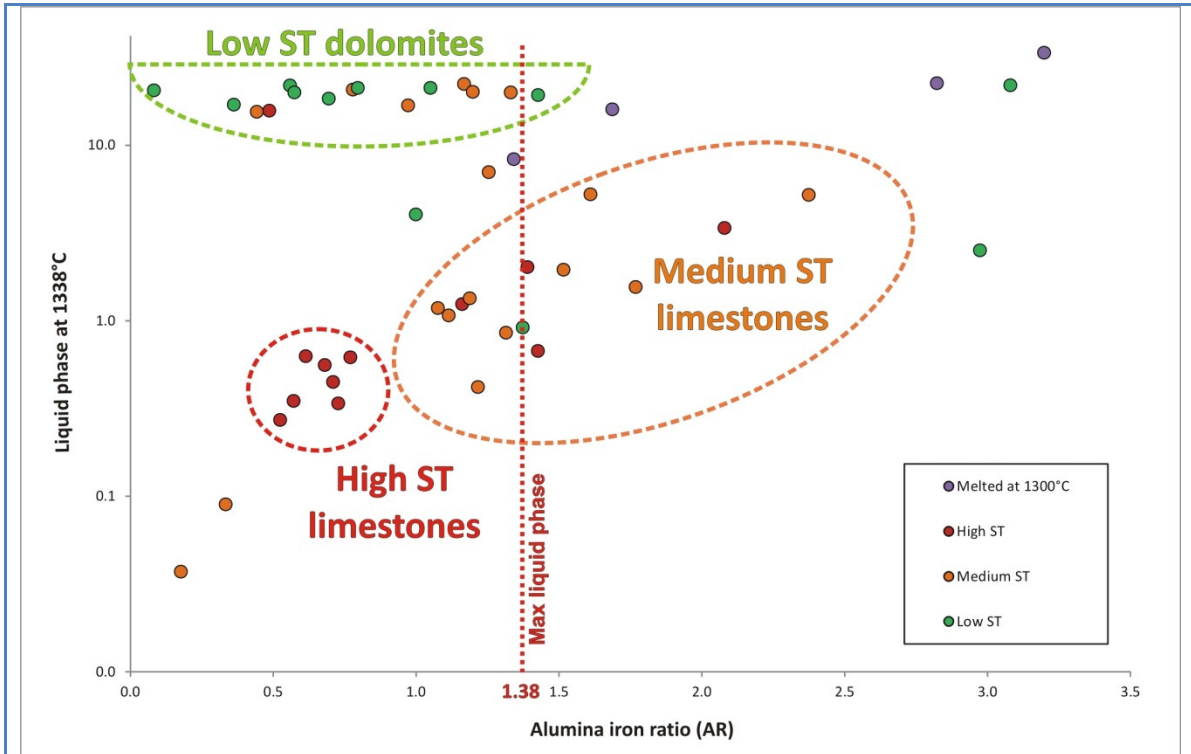


Fig.3.33: potential Liquid Phase at 1338°C (LP) Vs Alumina iron Ratio (AR)

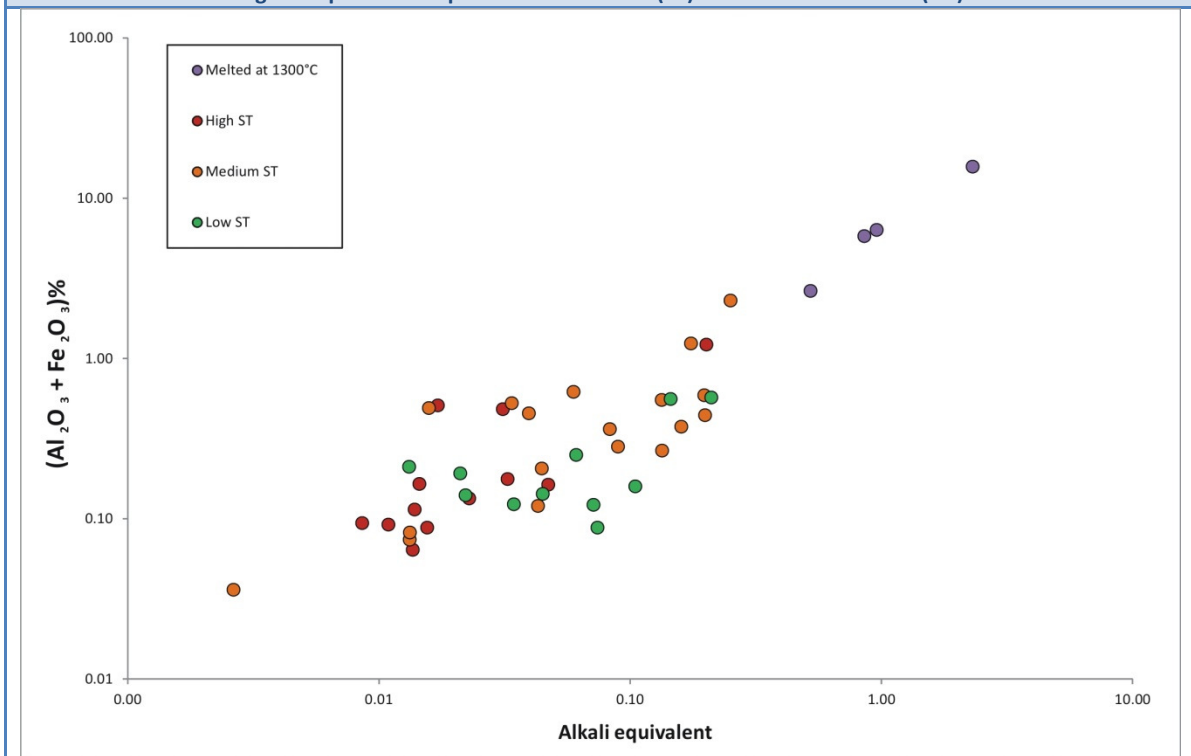


Fig.3.34: Alkali equivalent (A_{eq}) Vs Alumina and Iron summation ($Al_2O_3\% + Fe_2O_3\%$).

High-grade burnt lime products: impact of calcination kinetics on slaking reactivity; sticking tendency and blocks formation at HT (1300°C)

Finally, it was investigated the linear correlation between the LSF and the BF (Fig.3.35). Regression factors for samples presenting medium and high ST were 0.976 and 0.821, respectively. This plot points out that lime blocks with medium and high ST are mainly interested by high overburning tendency, i.e. predominant solid-state sintering process. Different amounts of larnite and hatrurite can be present, essentially depending on the SR values. Indeed, the SR governs the proportion of silicate phases in the system, thus an increase in SR lowers the proportion of liquid at any given temperature in the kiln (Taylor, 1997), making the solid-state sintering or the “overburning tendency” more evident. Moreover, the presence of other subordinated cementitious mineral phases, i.e. aluminates and ferrites, is essentially governed by the AR ratio. Effectively, XRD-QPA analyses performed on lime blocks from different ST groups seem to confirm this theoretical consideration based on cement moduli (Tab.3.39).

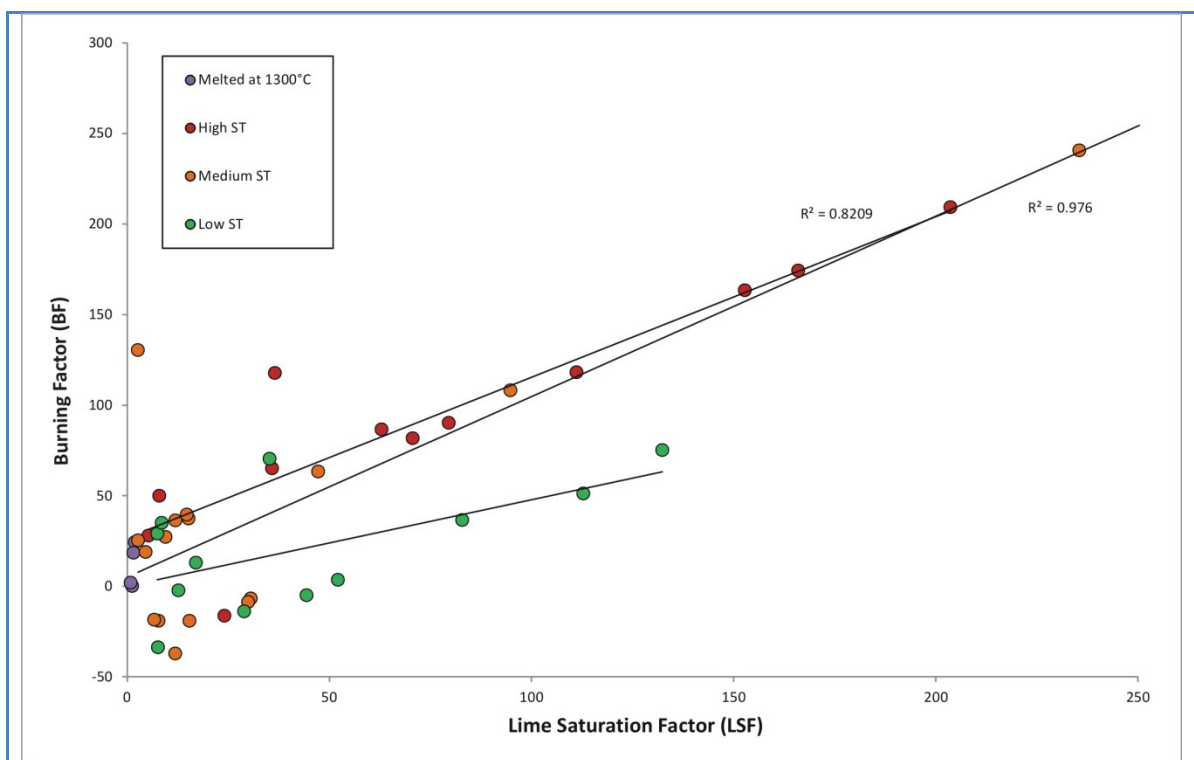


Fig.3.35: Burning Factor (BF) Vs Lime Saturation Factor (LSF).

Especially, subordinated ferrites and aluminates scattered within slightly impure or moderately hydraulic limes attested some secondary sintering reaction took place. According to the proposed interpretation, the impact of clay minerals dehydration and feldspars decomposition on carbonate rocks burnability is essentially limited for high-grade quicklimes, because the low IR content (<1.0 %). Conversely, clay minerals promote higher burnability in impure and slightly impure limestone and dolomites (IR =1-5%) by lowering the melting point of the system, and promoting a liquid-phase sintering process (Baumgart et al., 1984; Taylor, 1997). Effectively, the liquid formation may starts at temperatures >1250 °C or even at ~800-900 °C depending on the presence of halites or other fluxes (Elsen et al. 2011), but a detailed sequence of phases below 1300 °C is not well documented in the literature (Taylor, 1997) (Fig.3.37). A sort of incomplete clinkerization process at 1300 °C was particularly evident for “natural cements” (INT and SCH), and just in a minor way, on moderately hydraulic limes (CRM-d, CRM-w, VER, ISP-1, PTL-1b, SMA, and DOC). On the other hand, impure carbonates (IR > 5%) enriched in clay minerals and feldspars (TAS, CRM-3, UNI-2 and UNI-3), were completely melted at 1300 °C, and typically vitrified on cooling. The glassy or amorphous phase was effectively determined by XRD analysis, as well as, fluidal textures were observed by SEM-EDSX analysis (Fig.3.29a). For instance, contents of clay minerals are reported on Tab.3.34 and Tab.3.35.

As concerns the prevalent low ST of dolomitic limes, it results to be somewhat unclear, and difficult to explain by cement burnability moduli. Effectively, systems containing large concentrations of MgO are not reported in the standard Portland cement chemistry, because the periclase was considered dangerous for cement pastes hydration, thus raw meals were generally designed to contain small proportions of MgO (Taylor, 1997). However concentrations of MgO between 1-5% impact on variable ferrite composition (see Swayze in Taylor, 1997). Moreover, suitable amounts of MgO are reported to have good fluxing effect, because decrease the viscosity of liquid phase, increase the content of liquid phase, and promote the formation of hatrurite at the expense of the free lime (see references in Zhang et al. 2015). An amount of 5% of magnesium oxide is enough to saturate the liquid, which allows the precipitation of periclase into the system (Taylor, 1997). However, MgO contents > 5% are not helpful for the burnability of cement phases. More recently, a review with detailed chemical insights on magnesium-based cements was performed by Walling and Provis (2016). They reported the (CaO, MgO)-Al₂O₃-SiO₂ ternary phase diagram. No

magnesium silicates phases are formed at elevated temperatures akin to those formed in the calcium-rich region of the CaO-Al₂O₃-SiO₂ system, i.e. hatrurite, larnite, and aluminate have no magnesian analogues. This probably impacts on the lower ST of dolomitic limes, as well as, a less pervasive sintering at 1300 °C than high-calcium ones.

- *Impact of rock fabric and lime microstructure on ST*

The statistical analysis pointed out no correlation between MSR and ST, especially for pure limestones. Moreover the SEM-EDS analysis, performed on a high-calcium (HOS-2) and a slightly impure sample (SMA), pointed out completely recrystallized lime microstructures (Fig.3.29). This is consistent with the high temperature and the sufficiently long residence time occurring by means of the OT method. Effectively, several authors reported the progressive obliteration of rocks fabrics, showing the lime recrystallization is a temperature/time-depending process (Eades and Sandberg, 1970; McClellan and Eades, 1970). CaO crystallites coalescence and coarsening were systematically observed on experimental calcines burnt at progressively higher temperatures and retention times by SEM-EDS analysis (Hughes and Corrigan, 2009). Coarse calcite/dolomite crystal-sizes, commonly represented by diagenetic and/or metamorphic microstructures, could facilitate the mechanical degradation and the production of fines at 1050 °C (Vola and Sarandrea, 2015). Results pointed out that dolomitic limes generally present higher BET surface areas than high calcium limes at 1300 °C. This specific physical behavior, as well as the high mechanical degradation, could be linked to a lower ST. Effectively, the statistical analysis pointed out a trend of inverse correlation between the BET surface area of dolomitic limes and the ST, with a regression factor of 0.653. However, the microstructure pointed out a rather limited effect on the ST for the majority of the analyzed samples.

- *Impact of capillary moisture and superficial soil dust on ST*

Both these critical issues are related to the physical properties of samples as received. They were investigated for evaluating possible effects on OT results and ST classification. As a premise, samples are always tested as received from the quarry, avoiding any preliminary washing and drying, because it is convenient to preserve as far as possible the original conditions occurring on the industrial site. Capillary moisture and soil dust, sporadically lumped around the carbonate aggregate, represent a peculiar feature of

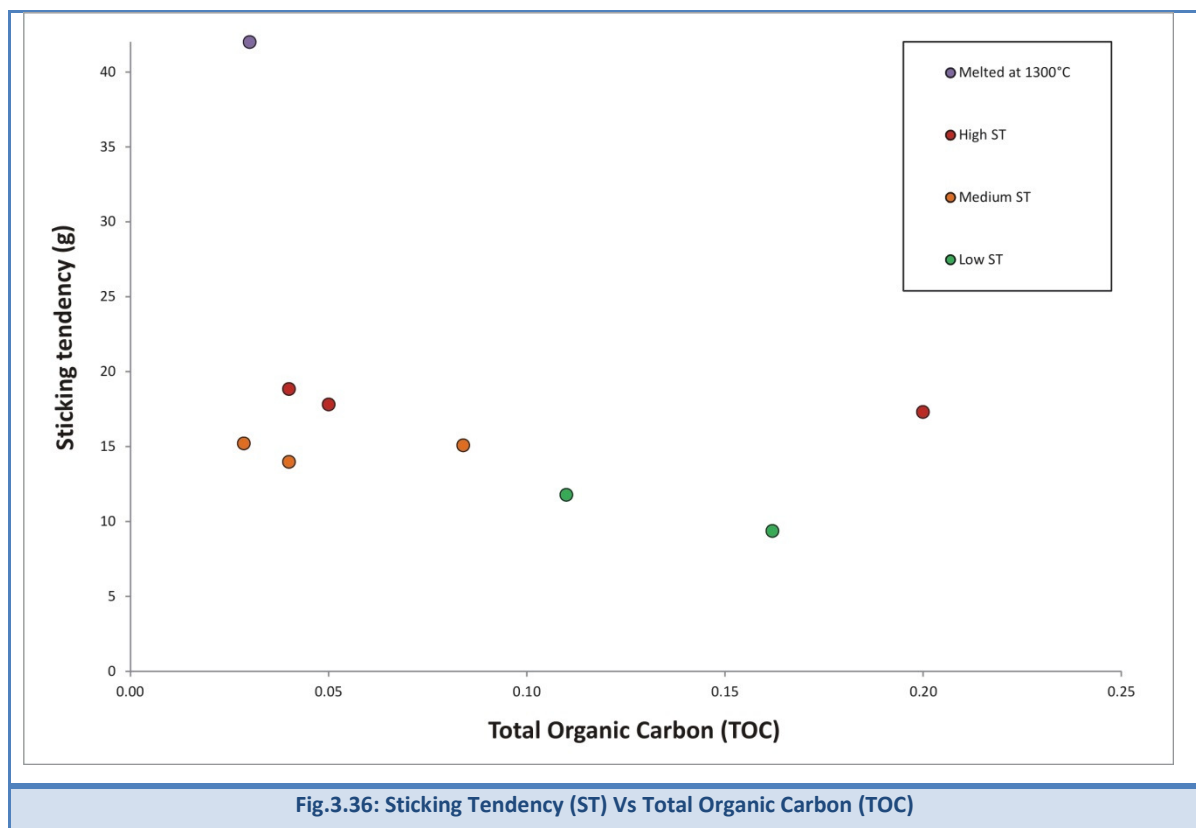
the sample, which is generally misunderstood or underestimated with respect to physical-chemical and mineralogical-petrographic composition of the whole-rock samples. Conversely, laboratory tests demonstrated that both capillary moisture and superficial soil dust impact on the OT, affecting results in the order of ± 2.5 g, i.e. corresponding approximately to one ST class. This fact could be relevant from technical-economical standpoints, especially when the ST is medium or high. Effectively, one order of magnitude up or down in the ST class can be fundamental for optimizing the process and stabilize the kiln, avoiding possible ringing and blockages. Moreover, this difference could play a significant rule on contractual issues, i.e. during the definition of kiln guaranties.

Indeed the impact of free water, or capillary moisture, it was investigated considering a highly porous grain-supported limestone (CRM), presenting a high accessible mercury intrusion porosity (16.5 %). Two aliquots of the same sample were selected: the first one (CRM-d) was preliminary dried at 105°C for a night; the second one (CRM-w) was submerged under water for a night. Then samples were both prepared according to the OT method, and tested in double. Results pointed out that lime blocks from sample with an initial moisture of 1.4 % (CRM-w) were 2.4 g lighter than the same sample previously dried at 105 °C, presenting an initial moisture of 0.1 % (CRM-d) (Tab.3.31). Furthermore, the OT test was repeated 6 months later on the same air-dried sample (CRM-w). In this case result was similar to the one obtained on sample dried at 105 °C (CRM-d). This preliminary investigation pointed out that moisture significantly impacts on OT, by reducing the mass of the lime block of approximately one ST class. However, the moisture benefit can be easily loss if the sample is preliminary dried.

The impact of the superficial soil dust was investigated considering a real case-study. The critical sample we considered (PTL-1a) presented a high ST (19.0 ± 1.1 g) with 0.3 % of superficial dust. An aliquot of the same sample (PTL-1b) was washed and dried at 105 °C for a night, then tested by the OT in double. Results pointed out that lime blocks from “washed” sample were 2.4 g lighter than sample as received. This preliminary investigation pointed out that soil dust content, i.e. clayey particles, could significantly impacts on OT, by increasing the mass of the lime block of approximately one ST class.

- *Impact of organic compounds on ST*

The possible correlation between organic compounds and the ST was investigated too. For this purpose the Total Organic Carbon (TOC) was determined by EA-IRMS on a subset of 9 samples (Tab.3.29). Preliminary results pointed out no correlation between parameters. However results were probably affected by different types of organic compounds, and the limited number of analyzed samples. Especially, Neoproterozoic limestone samples from South Africa (IDW-1, IDW-2), presenting low and medium-low ST, were enriched in thermally-matured kerogen (Vola et al., 2017). Conversely, more recent (in age) samples from Cenozoic deposits, presenting high ST, were enriched in organic matter with low thermal evolution (SAC). Moreover the richest samples in TOC (MME and SMA), presented both a high ST. This topic must be investigated more into details in the early future.



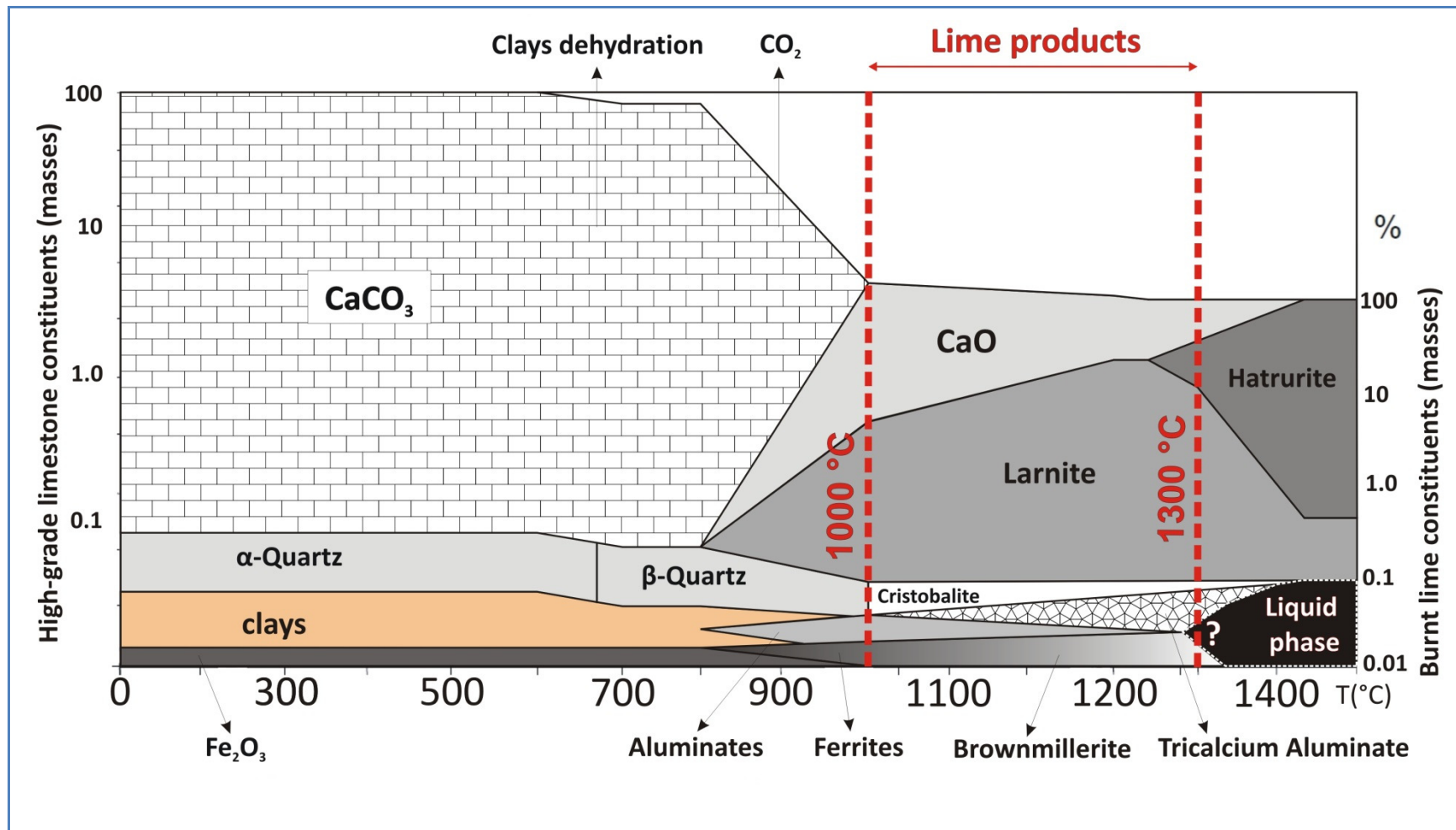


Fig.3.37: Schematic diagram showing the variations in typical phases contents during calcination of a theoretical high-grade limestone with IR ≈ 0.1%. From Portland cement clinker diagram after Taylor (1997), modified.

High-grade burnt lime products: impact of calcination kinetics on slaking reactivity; sticking tendency and blocks formation at HT (1300°C)

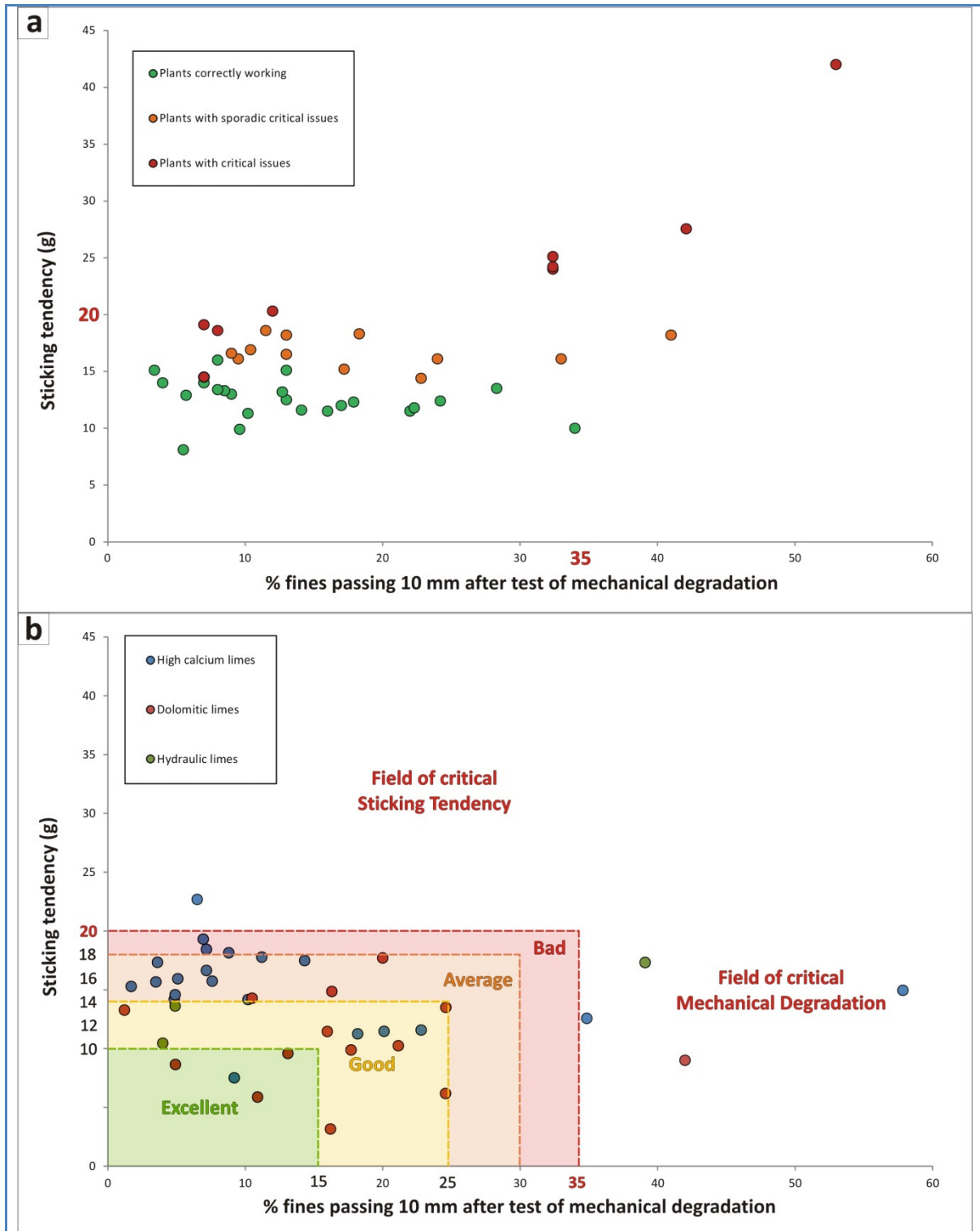


Fig.3.38: Empirical correlation between the Sticking Tendency (ST) and fines passing 10 mm after the Mechanical Degradation (MD) Test according to Vola and Sarandrea (2013). a data-base from historical plants worldwide, i.e. real case-studies. b samples analyzed in this paper, with suitability fields classification.

- *Overburning Test (OT) validation and applications in the lime industry*

The OT was performed on each sample 2-4 times to test data repeatability. The average deviation standard of mass values is lower than 2 g, thus is consistent with the limit adopted for classifying the 7 different classes of ST (Tab.3.26 and Tab.3.40). The OT method was systematically performed by Cimprogetti for characterizing contractual samples for the last ten years, because the great impact on kiln operations. According to experience matured by the company on several plants worldwide, blockages are considered more critical and frequent in the presence of an excess of fines formed during the calcination process. They essentially depend on characteristic thermo-mechanical degradation of quicklime, which is strictly related to textural-microstructural features of the parental carbonate rock (Siegesmund et al., 2000; Shushakova et al., 2013a, 2013b; Vola and Sarandrea, 2015). Considering, their practical importance, ST and fines were empirically correlated (Fig.3.38). Especially, the ST was plotted against fines (<10 mm) determined according the so-called “mechanical degradation” (MD) test on lime pebbles burnt at 1050 °C. This test allows evaluating mechanical behavior of the lime, according to the procedure described by Vola and Sarandrea (2013). Indeed, Cimprogetti’s database of ST and fines from historical plants was plotted in Fig.3.38a. Conversely, case-studies analyzed in this paper were plotted in Fig.3.38b. Acceptable ranges, critical limits, and practical solutions, as well as, guidelines for kilns guaranties were discussed according to the technical expertise matured over the years on several plants worldwide. Especially, ST classes were linked to expected residual CO₂ content of the final burnt product, and additional suggestions were indicated for counteracting the fines excess. They essentially consist in recommending specific coarse-size fraction, i.e. 40-80 or 50-100 mm, for feeding to the kiln (Tab.3.40). It’s significant to point out that important lime producers required to perform the OT method over the years, either for testing new samples from different suppliers or quarries, or from different layers of same quarry, according to the progression of the mining activity (Manocha and Ponchon, 2018).

3.4.6 Conclusions

This study allowed validating the Overburning Test (OT) as a standard method for predicting blockages in lime kilns at high burning temperature. Data reproducibility was tested 2-4 times on 46 samples. The average deviation standard of mass values is lower than 2 g, thus is consistent with the limit adopted for classifying 7 different ST classes (Tab.3.36 and Tab.3.40). 4 main ST groups, presenting large burnability differences, were recognized, and 3 different driving processes identified to explain the above mentioned groups. They are the solid-state sintering, the liquid-phase sintering, and the dehydration melting caused by clay minerals and other fluxes decomposition. The statistical analysis by the regression method allowed pointing out significant trends between the ST and moduli from the cement industry, i.e. Lime Saturation Factor (LSF), Silica Ratio (SR), Alumina to iron Ratio (AR), potential Liquid Phase (LP) at 1338 °C, and Burning Factor (BF). Specific precautions were adopted, considering the application to the lime process. The correlation was performed by plotting different ST groups separately. Therefore, ST groups were explained as follow:

1. The group A includes completely melted samples, deriving from impure carbonates (IR > 5%) enriched in clay minerals, i.e. mostly micas, and feldspars, i.e. plagioclase and K-feldspar, plus other subordinated mineral phases. Clay minerals dehydration and feldspars decomposition facilitate the formation of large melts around 1300 °C. Effectively, the liquid formation may starts at temperatures > 1250 °C or even at ~800-900 °C depending on the presence of halites or other fluxes (Elsen et al. 2011). Melts are well-documented either in cement kiln preheaters, or in rotary lime kiln, and are often related to possible obstructions and condensation of volatiles, which are responsible for the formation of kiln rings and deposits. However, a detailed sequence of phases below 1300 °C is not well documented in the literature (Taylor, 1997) (Fig.3.37).
2. The group B includes high ST samples of classes B1, B2, B3, deriving from pure (IR <1 %) or slightly impure (IR = 1-5 %) limestones, with potential LP at 1338 °C between 0.2-1.0, and AR between 0.4-0.8. Blocks from this group are mainly constituted of lime (CaO), or lime (CaO) plus periclase (MgO), associated with subordinated cementitious mineral phases. The high ST, namely “high overburning tendency”, is related to a predominant solid-state sintering process. According to cement factors, different amounts of larnite and hatrurite can be present, depending

on the SR values. An increase in SR lowers the proportion of liquid at any given temperature in the kiln, and makes the solid-state sintering more evident. Moreover, the presence of limited quantity of ferrites and aluminates is essentially governed by the AR ratio.

3. The group C includes medium ST samples of C1 and C2 classes, deriving from limestones with scattered impurity content, potential LP at 1338 °C between 0.5-10, and AR between 1.0-2.0. Blocks from this group are mainly constituted of lime (CaO), or lime (CaO) plus periclase (MgO), associated with significant contents of larnite, hatrurite, aluminates, and ferrites. These blocks can be essentially explained by means of a liquid-phase sintering process or “incomplete clinkerization process at 1300 °C”, in the presence of some aluminates or ferrites phases.
4. The group D includes low ST samples of D1 and D2 classes, deriving from mostly pure dolomites. This group is characterized by a potential high LP at 1338 °C (>10), and low AR values (0.1-1.4). The amount of LP is governed by the large availability of magnesium on the parameter calculations. The low ST of dolomitic limes is probably related to a liquid-phase sintering process with dominant ferritic melts.

Tab.3.40 – Lime blocks masse values from the OT and ST. The guidelines for new plants commissioning is reported

Block weight (g)	ST (%)	ST class	ST group	Guidelines for plants commissioning	
				Recommended size fractions	Residual CO ₂ Guarantees (%)
≈42	Max	Melted	A	No fractions recommended	Material is rejected
>20	>47.6	very high (B1)	B	A coarse fraction to feed the kiln is warmly recommended, but mechanical degradation of the lime must be low	No guaranty
18-20	42.9 – 47.6	high (B2)		A coarse fraction to feed the kiln is recommended	5.0
16-18	38.1 – 42.9	medium-high (B3)		A coarse fraction to feed the kiln is recommended	3.5
14-16	33.3 – 38.1	medium (C1)	C	A coarse fraction to feed the kiln is recommended	2.5
12-14	28.6 – 33.3	medium-low (C2)		no specific requirements for raw materials	2.0
10-12	23.8 – 28.6	low (C3)			1.0
<10	<23.8	no ST (D)	D		1.0

Applications of the OT method span from the evaluation of raw materials suitability for designing and commissioning new kilns, to the quality control in already working plants. Acceptable ranges, critical limits and practical solutions were discussed according to the technical expertise matured over the years on several plants worldwide. A synthetic table reporting guidelines for kilns guaranties was elaborated, includes the following suggestions:

1. samples washing and drying at 105 °C can be performed to remove soil dust and clayey particles lumped on the surface of the raw aggregate, allowing to the reduction of lime blocks of approximately one ST class (c. 2 g);
2. the sample moisture affects results of approximately one ST class, i.e. higher the moisture, lower the ST;
3. the use of specific coarse-size fraction, i.e. 40-80 mm or 50-100 mm, for feeding to the kiln is warmly recommended for counteracting the formation of fines, which could negatively affect the ST.

3.5 Article no. 4. Factors affecting early sintering and lowering reactivity of quicklimes pebbles burnt at high temperatures (1150-1300 °C)

This paper was written by G. Vola on September 2018 with contributions of M. Mazziere and E. Rodeghero. It represents a synthesis of laboratory research activity performed in 2017-2018. The experimental activity performed for Ms Thesis of one of the authors is included too. The paper has to be finalized for the submission on a scientific journal in the early future.

3.5.1 Abstract

This study deals with thermal behavior characterization and slaking reactivity tests performed on 12 carbonate rocks, essentially high-grade carbonates. Mud-supported and grain-supported limestones, diagenetic dolomites, and crystalline marbles were supplied by different lime producers worldwide in the typical aggregate fractions, i.e. 15-30, 30-60, and 40-80 mm. Standard burning tests at different temperatures, i.e. 1050-1150-1250-1300°C, were performed on samples as received under air conditions in an electric muffle furnace for simulating the calcination process occurring in a Twin Shaft Regenerative (TSR) kiln. Water slaking tests were performed according to the European standard UNI EN 459-2 to achieve the lime reactivity. Mathematical modelling of slaking curves was performed for quantifying hydration rate parameters, by a chemically-controlled shrinking core model equation. The characterization of whole rock powders, and derived burnt lime products was performed by a multidisciplinary analytical approach, including physical-chemical, mineralogical-petrographic, crystallographic, microstructural and thermal analyses. Moreover decomposition kinetics of a subset of representative samples was studied by means of HT-XRD in situ at the ID22 high-resolution powder diffraction beamline at the ESRF, Grenoble, France. The statistical analysis on different data-sets allowed pointing out key-factors controlling the lime slaking reactivity at different burning temperatures. In particular, high-grade, medium- up to coarse-sized crystalline materials, i.e. grain-supported limestones and granoblastic marbles, presented the highest burnability, slaking reactivity, and sintering or overburning tendency at 1250-1300 °C. Conversely, mud-supported limestones and marly limestones, enriched in quartz, clay minerals, and other subordinated non-carbonate impurities, presented the lowest burnability, slaking reactivity and sintering at 1250-1300 °C. Finally, characteristic microstructural features of burnt

limes, including crystallographic lattices, crystallite-size, BET surface area, and real density strongly affect the slaking reactivity too. Results from this research activity put further constraints on suitability of different carbonate rocks for the lime industry.

3.5.2 Introduction

The art of lime burning has been practiced since ancient times. Historically, the soft lime burning process, performed in conventional vertical kilns using traditional fuels, was characterized by low firing temperatures. This allowed obtaining highly porous reactive limes. This is the reason why the lime reactivity was not considered a significant criterion for judging quality and suitability of a lime than chemical purity, almost until the industrial revolution. As industrial and chemical technology developed, lime became an increasingly important component in different reactions and processes (Eades and Sandberg, 1970). Reaction rates of commercial limes became a matter of considerable interest with the introduction of the basic oxygen converter steel furnace (König, et al., 1967; Obst, et al., 1970). The use of quicklime instead of limestone and the rapid acceptance of this technology during the 1960s, caused the definitive substitution of open hearth steelmaking furnaces, and created parallel revolution within the lime industry (Limes and Russell, 1970). The lime reactivity still plays a critical role at different steps of the steelmaking process, and especially to make a good slag facilitating the removal of sulphur and phosphorous, and for providing a safer platform to withstand high intensity arc plasma in the electric arc furnace, and violent reactions in the basic oxygen furnace (Manocha & Ponchon, 2018). The lime reactivity is a topic of great interest in several other industrial sectors including chemical, mining, agricultural, geotechnical, pharmaceutical, environmental, food & beverage, water treatment, where the quicklime is used as fluxing and leaching agent for removing impurities, for acids neutralization, pH stabilization, and flue gas desulfurization (Boynton, 1982; Oats, 1998). Each sector and country developed different standard methods to evaluate the lime reactivity according to their practice and use. Germans metallurgists evaluated the relationship between the lime reactivity and the slagging time according to the hydrochloric acid coarse grain titration (Wuhrer, 1956; Schlitt and Healy, 1970), which is known by insiders as “Wülfrath test”. Conversely, Americans developed the so-called “crucible test” in order to more closely simulate basic oxygen furnace atmospheres (Limes and Russell, 1970). The lime reactivity in the construction or building sector is evaluated according to the American (ASTM C110,

2016) or European (UNI EN 459-2, 2010) standards tests, which are complementary, and both based on temperature rise, related to a water slaking rate test.

Over the years, physicists, chemists and chemical engineers firstly considered physical-chemical properties of the limestone for solving the critical issue of the lime reactivity. Pioneering studies were performed in the 70s under the auspices of the US National Lime Associations (Eades and Sandberg; 1970; McClellan and Eades, 1970). During the 80s and the 90s of the last century much work was done to evaluate the effect of particle size distribution, calcination kinetics, specific surface area, and impurity content (Borgwardt, 1985; Borgwardt and Bruce, 1986). Several authors adopted linear and multiple regression statistics or factorial analysis to evaluate experimental results (Wright, 1985; Baziotis et al., 2011; Akande et al., 2016). More recently, i.e. over the last ten years, an increasing number of mineralogical, crystallographic and, finally, petrographic studies were performed, to bridge the geological gap. Because limestone and dolomite are naturally occurring materials, their composition and physical properties change between different rock formations, but often within the same deposit, and quarry, depending on age, stratigraphic, paleogeographic and structural settings. These factors, operating at the macroscopic (regional) and mesoscopic (outcrop) scales, deeply affect primary (depositional) textures and secondary (diagenetic/metamorphic) modifications at the microscopic scale. Therefore geoscientists proposed studies based on the microfacies analysis, and the petro-physical and crystallographic characterization of carbonate rocks (Hogewoning, et al., 2008; Lech et al., 2009; Rodriguez-Navarro et al., 2009; Soltan, 2009; Soltan and Serry, 2011; Soltan et al., 2011a, 2011b; Soltan et al., 2012; Vola and Sarandrea, 2013; Alaabed et al., 2014; Vola et al., 2017; 2018). A mineralogical-petrographic approach was recently adopted to evaluate the thermal decomposition and the heating behavior of limestone in the industrial cement clinker manufacture too (Marinoni et al., 2015; Galimberti et al., 2016). From a technological standpoint, a large variety of kilns have been used over the years and around the world for quicklime manufacture. Nowadays, many alternatives at different costs are available with respect to specific applications (Schorcht et al., 2013). However, long rotary with a preheater (PLR) or without (LR), and Twin Shaft Regenerative (TSR) kilns, are generally considered the best technology to achieve to goal of soft-burnt reactive quicklime with different type of fuels (Schorcht et al., 2013). In particular, TSR kilns have the lowest specific energy consumption compared with other types of kilns due to the regenerative process (Hai Do et

al., 2011). Indeed TSR kilns represent the best compromise for lowering costs, reducing the gas emissions, and the environmental impact. According to Cimprogetti's experience, the production of soft-burnt quicklime in TSR kilns firing solid fuels, i.e. coal and petcoke, is critical task. Recently, an emblematic industrial case-study from a South African Neoproterozoic limestone was thoroughly investigated by Vola et al. (2017). Impact of rock fabric, thermal behavior, and carbonate decomposition kinetics on quicklime industrial production and slaking reactivity was investigated by Vola et al. (2018) on calcines burnt at 1200°C.

The main goal of this study is to investigate the burnability of industrial carbonate aggregates supplied in the typical fractions, i.e. 15-30 up to 40-80 mm, considering the typical range of temperatures occurring in a TSR kiln firing solid fuels, i.e. 1150-1300°C. Especially, 12 different carbonate rocks were selected from different industrial producers worldwide. Samples presenting different chemical/mineralogical compositions, and textural/microstructural features, were appositely selected. Therefore a multidisciplinary research activity was carried out to investigate carbonate rocks burnability, and early sintering or overburning tendency. Especially, carbonate decomposition kinetics was investigated by thermal analysis. A subset of representative powdered samples was studied by means of HT-XRD in situ at the ID22 high-resolution powder diffraction beamline at the ESRF, Grenoble, France. The petrographic quantitative analysis was performed adopting the so-called "micrite-to-sparite ratio" (MSR) (Vola et al., 2018). Quantitative phase, crystallite-size, and micro-strain analyses of different lime products were performed by whole powder profile fitting by the Rietveld and FP methods. A shrinking core model (SCM) was adopted for modelling experimental wet slaking curves. Finally, the BET specific surface area and the real density of burnt limes were investigated too. The statistical analysis by the regression method was adopted to evaluate correlations between different data-sets and the slaking reactivity. Results put further constraints on suitability of different carbonate rocks for lime manufacture in TSR kilns using solid fuels.

Tab.3.41 – Geological information of carbonate rocks samples. Symbols legend: p. i. = proprietary information

No	Name	Code	Lithofacies	Stratigraphic position	Geological Unit or Formation	Texture/Microstructure	Provenance
1	PSP	2450 2451	Massive limestone	Eocene (?)	Unknown	Reefoidal facies and mosaic calcite cement	Karawang quarry, Rembang, Java, Indonesia
2	IDW1	2452 2453	Microbial limestone	Neoproterozoic	Uppermost Kogelbeen Fm. or Lower Gamohaam Fm.	Microbial boundstone with laminated clotted peloidal micrite, microsparite, and herringbone calcite	Ouplass Mine, Daniëlskuil, S. Africa
3	WOP	245 2455	Mud-supported limestone	Upper Triassic	Dachsteinkalk Fm.	Mudstone/wackestone with rare ostracods	Dürnbach quarry, Waldegg, Austria
4	SMA	2462 2463	Massive limestone	Silurian	Lower Wenlock Hangvar Fm.	Reefoidal facies and mosaic calcite cement	Storugns quarry, Gotland, Sweden
5	EUR	2737 2738	Breccia-like flat-pebbles limestone	Cambrian-Ordovician	Shoshkabalakskaya stratigraphic succession	coated grain peloidal grainstone to packstone and flat pebble rudstone, subordinated wackestone	Ulken-Aktau deposit, Zhanatas, Zhambyl, Kazakhstan
6	CAR	2828	granoblastic marble	Lower Liassic	Apuane Metamorphic Complex Marble s.s. formation	Mainly granoblastic non-oriented calcite microstructure	Carrara marble complex, Carrara, Italy
7	VER	2829	micritic limestone	Middle Jurassic	Rosso Ammonitico Veronese Fm.	Wackestone/packstone with planktonic faunas	Rosso Verona distric, Valpolicella, Verona, Italy
8	PRO	2943	Grain-supported limestone	Unknown	Unknown	Peloidal grainstone with mm-sized brachiopods	Maycopt, Russia
9	ZAN	2830	Diagenetic Dolomite	Early Jurassic	Albenza Fm., Zandobbio Dolomite member	Hypidiotopic to hydriotopic mosaic dolomite	Grena Valley, Zandobbio, Bergamo, Italy
10	PED	2782	Diagenetic tectonized Dolomite	Upper Triassic	Dolomia Superiore Fm., Dolomia a Megalodon member	Hypidiotopic mosaic and brecciated dolomite	La Pedicara quarry, Balvano, Potenza, Italy
11	UNI-1	2761	Diagenetic Dolomite	Upper Triassic	Dolomia Principale Fm.	Hypidiotopic mosaic dolomite with ghostly peloidal texture	Ponte del Costone quarry, Casnigo, Bergamo, Italy
12	MME	2112	Diagenetic Dolomite	Unknown	Unknown	Xenotopic to hypidiotopic mosaic dolomite passing to foraminifera-rich wackestone/packstone	Medan Area, North Sumatera, Indonesia

3.5.3 Test Methods

For the experimental details, including sample provenance, physical (BET, MIP, gas pycnometry), chemical (XRF-WDS), mineralogical (XRD-QPA by the Rietveld method; synchrotron HT-XRD), microscopic (OPM, SEM-EDS), and thermal analyses (TG-DTG-DTA), plus technical tests, i.e. burning and slaking reactivity tests, readers are requested to refer to Chapter 2 of the present dissertation.

3.5.4 Results

- *Carbonate rocks characterization*

Samples were selected from deposits of industrial interest. Preliminary geological information and provenance, stratigraphic position, textural and microstructural features are reported in Tab.3.41. A comprehensive petrographic analysis, including description of depositional textures, diagenetic or metamorphic modifications and the micrite-to-sparite ratio (MSR) is reported in Tab.3.42. High-calcium carbonates include either mud-supported or grain-supported depositional textures. Moreover, some massive limestones, consisting of reefoidal lithofacies, and one calcitic marble, presenting typical granoblastic (metamorphic) microstructure, were considered, as well. Furthermore selected materials cover a wide range in terms of ages, ranging from the Neoproterozoic (2520 Ma) up to the Eocene (34 Ma) times. Dolomitic samples, mostly from Mesozoic formations of the Italian Alpine and Apennine belts, pointed out typical xenotopic up to hydrotopic diagenetic textures. Some breccia-like microstructure was observed too. The most significant rock fabrics are reported in Fig.3.39 and Fig.3.40. Moreover physical, chemical and mineralogical analyses were performed too (Tab.3.43, Tab.3.44 and Tab.3.45)

Tab.3.42 – Petrographic analysis of different carbonate rocks

Sample	Code	Lithofacies	Primary texture and components	Diagenetic or Metamorphic features	MSR	References
PSP	2450 2451	White massive coralline mostly encrusting limestone	Massive coralline framestone/rudstones characterized by bryozoan-foraminifera association with encrusting corallinacean red algae. Primary intraclastic porosity filled in by equant mosaic calcite cement.	No diagenetic and/or metamorphic features observed on thin section	3.5	Nd
IDW	2452 2453	Gray to black slightly dolomitic clotted peloidal micrite and microsparite associated with microbial fenestrate boundstone and black shales.	Laminated mudstone/wackestones to packstone/grainstones with clotted peloidal micrite, intraclasts and areas of microbial boundstone. Cloudy radial fibrous banded calcite fans representing primary marine cement associated with dark microbial laminae (herringbone calcite). Fenestrate porosity, locally enlarged by dissolution, is filled by equant drusy mosaic and cm-size poikilotopic calcite cement	Neomorphic microsparite and sparite due to recrystallization of micrite. Fabric-replacive hypidiotopic dolomite and cloudy rhombohedral crystals (200-500 μm) of saddle dolomite with undulose extinction. Cavities are filled by mm-size poikilotopic calcite cement (burial diagenesis). Stylolites and solution seams due to pressure solution. Kerogen soaked along stylolites after the pressure solution. Different cement generations, possibly related to late diagenetic fluids.	8.4	Vola et al. (2017a)
WOP	2453 2454	Gray to reddish slightly dolo-micritic limestone	mudstone/wackestone with rare ostracods. Poorly washed packstone subordinated.	Tensional fractures filled in by clear mosaic twinned cement. Stylolites and solution seams postdate fractures.	19.9	Krystyn et al. (2009)
SMA	2462 2463	Yellowish brown to olive gray massive carbonates, mostly of reefoidal origin, with interbedded siliciclastic sediments. Fossiliferous grain-supported facies locally passing to lacustrine mud-supported ones	Fossiliferous kerogen-rich floatstone/rudstones from different "reef" facies (stromatoporoids) including reef front, reef core, interreef, shoal and back-reef environments, locally passing to packstone-wackestones microfacies. Large mm-sized faunas and bioclasts including conodonts, rugose corals, possible trilobites, brachiopods and bivalves. Intraclastic porosity filled in by equant and poikilotopic calcite cement	Large mm-sized equant and poikilotopic calcite cement filled in intraclastic porosity	1.4	Jeppsson (2008)
EUR	2737 2738	Gray to reddish and brownish flat-pebble brecciated dolomitic limestone passing to more homogeneous micritic lithofacies	coated grain peloidal grainstone to packstone with sparse millimetre size micritic intraclasts with rectangular shape and by a flat pebble rudstone to packstone/grainstone. Calci-mudstone intraclasts and coated peloidal packstone to wackestone are subordinated.	Burial diagenesis includes sparite blocky and poikilotopic cements, replacive idiotopic to hypidiotopic dolomite and silica replacements. The silicification occurs either in the form of replacive microquartz and chalcedony, or in the form of euhedral bipyramidal crystals of 90-200 μm	Nd	Vola et al. (2017b)

Table 3.42 (continued)

Sample	Code	Lithofacies	Primary texture and components	Diagenetic or Metamorphic features	MSR	References
VER	2828	Red nodular ammonite-bearing pelagic limestone	Wackestone/packstones with planktonic thin-shelled bivalves, ostracods, foraminifera (protoglobigerins) and radiolarians.	Stylolites and solution seams due to pressure solution	5.1	Martire et al. (2006)
CAR	2829	Fine to medium coarse-grained meta-limestone, homogeneously pearl-white colored or with gray tiny spots	Primary textures and components are completely obliterated by pervasive metamorphic recrystallization	Marble microfabric depends on two main tectonic deformation phases. Granoblastic microstructures with well-defined grain boundaries, straight or slightly curved with no optical evidence of crystal-plastic deformation. Subordinated xenoblastic structures with less defined grain boundaries, sometimes sutured or embayed to lobate. Variable grain-size and rare appreciable grain orientation.	0.3	Carmignani et al. (2005)
PRO	2943	Grain-supported limestone	Peloidal grainstone with rare mm-sized brachiopods, and codycean algae	No diagenetic features observed on thin section	4.7	Nd
ZAN	2830	Pinkish-white meter-thick and sub-meter-thick beds of medium up to coarse-grained dolostones, showing frequent vuggy porosity and peritidal structures	Shallow-water carbonates comprising subtidal to peritidal peloidal packstones interbedded with ooid-bioclasic grainstones. Tepee-like horizons and ghost fenestral fabric	Primary textures and components are often completely obliterated by pervasive multistage superimposed dolomitization. The first pervasive replacement dolomitization phase is followed by volumetrically less important dolomite cement precipitation phases.	1.3	Ronchi et al. (2010)
PED	2776 2777	20-50 cm up to 1 meter thick beds of fine to coarse-grained grayish and whitish mostly tectonized dolostones	Peloidal-oncoidal and bioclasic-fossiliferous (Gervilleia, Megalodon) packstone/grainstones sometimes well preserved, sometimes perceivable as ghost primary textures.	Primary textures and components are often obliterated by pervasive, probably multistage, dolomitization. Hypidiotopic mosaic dolomite, brownish saddle dolomite, dolomitized breccia-like textures are dominant.	2.4	Scandone et al. (1971)
UNI-1	2662-A 2662-B	Light and dark gray dolostones showing cements fillings cavities	ghostly peloidal texture	xenotopic up to hipidiotopic diagenetic dolomite with microbially-induced cements fillings cavity	10.6	Gaetani et al. (2012)
MME	2112	Light gray and brownish dolostones showing peritidal structures and fenestral fabrics	The original peloidal-fossiliferous wackestone/packstone is sometimes preserved. Typical association presents benthonic foraminifera (milioids)	Multistage dolomitization superimposed to shallow-water carbonates. Non-planar closely packed fine-grained anhedral crystals of xenotopic dolomite associated with rhombohedral crystals of late saddle dolomite replacements.	1.4	Nd

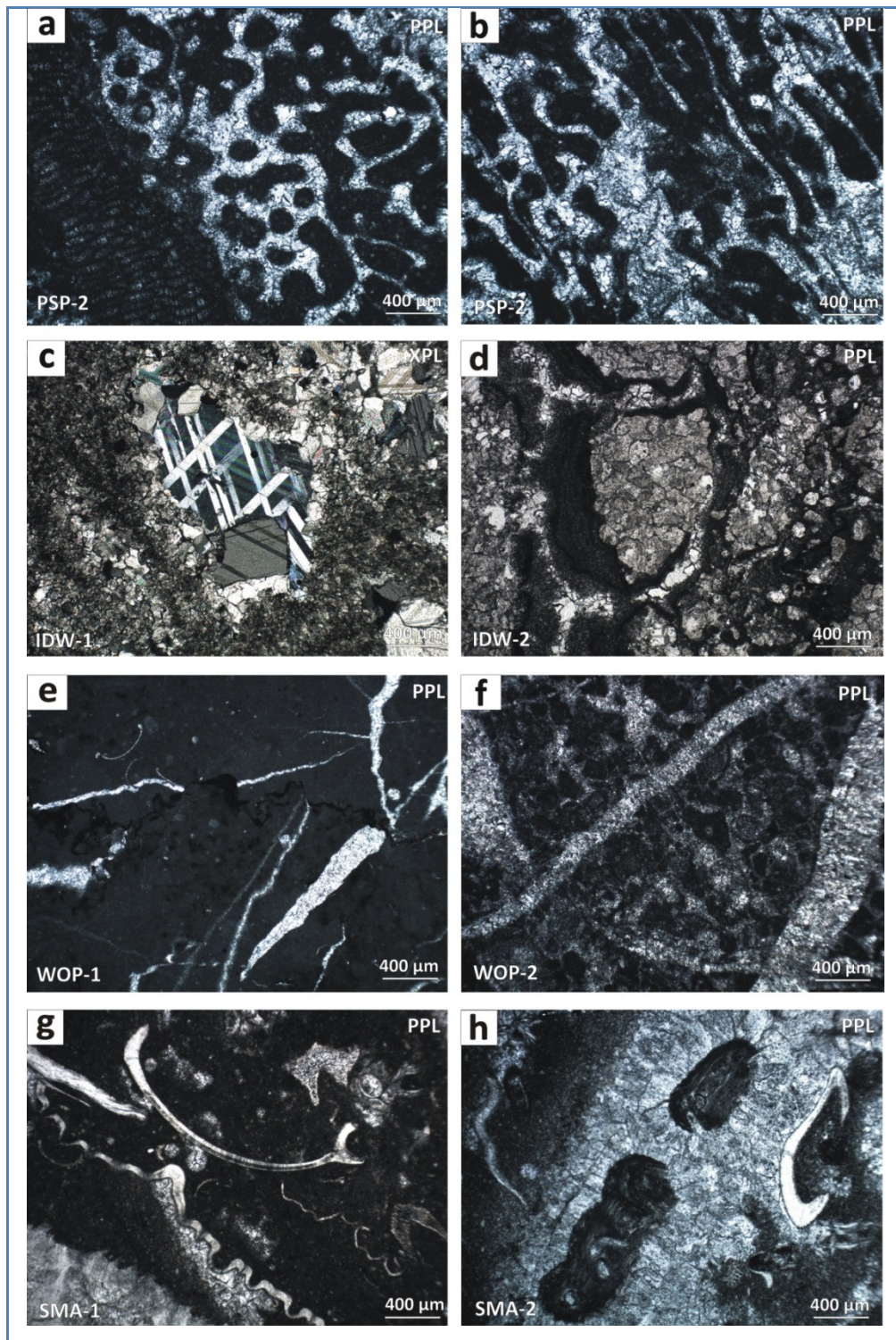


Fig.3.39: Petrographic analysis of significant limestone textures. a-b = framestone/rudstones characterized by bryozoan-foraminifera association with encrusting coralline red algae (Eocene?, PSP). c = twinned poikilotopic calcite cement filled in fenestrate microbialitic boundstone with clotted peloidal recrystallized microsparite. d = clotted peloidal microsparite passing to kerogen-bearing recrystallized microsparite (Neoproterozoic, IDW). e = mudstone/wackestone with rare ostracods with tensional fractures filled in by clear mosaic twinned calcite, and stylolites that postdate fractures (Triassic, WOP). f = Poorly washed peloidal packstone with tensional fractures filled in by twinned mosaic cement (WOP). g-h = Fossiliferous kerogen-rich floatstone/rudstones from different stromatoporoid facies (Silurian, SMA). Large mm-sized faunas and bioclasts including conodonts, rugose corals, possible trilobites, brachiopods and bivalves (Silurian, SMA).

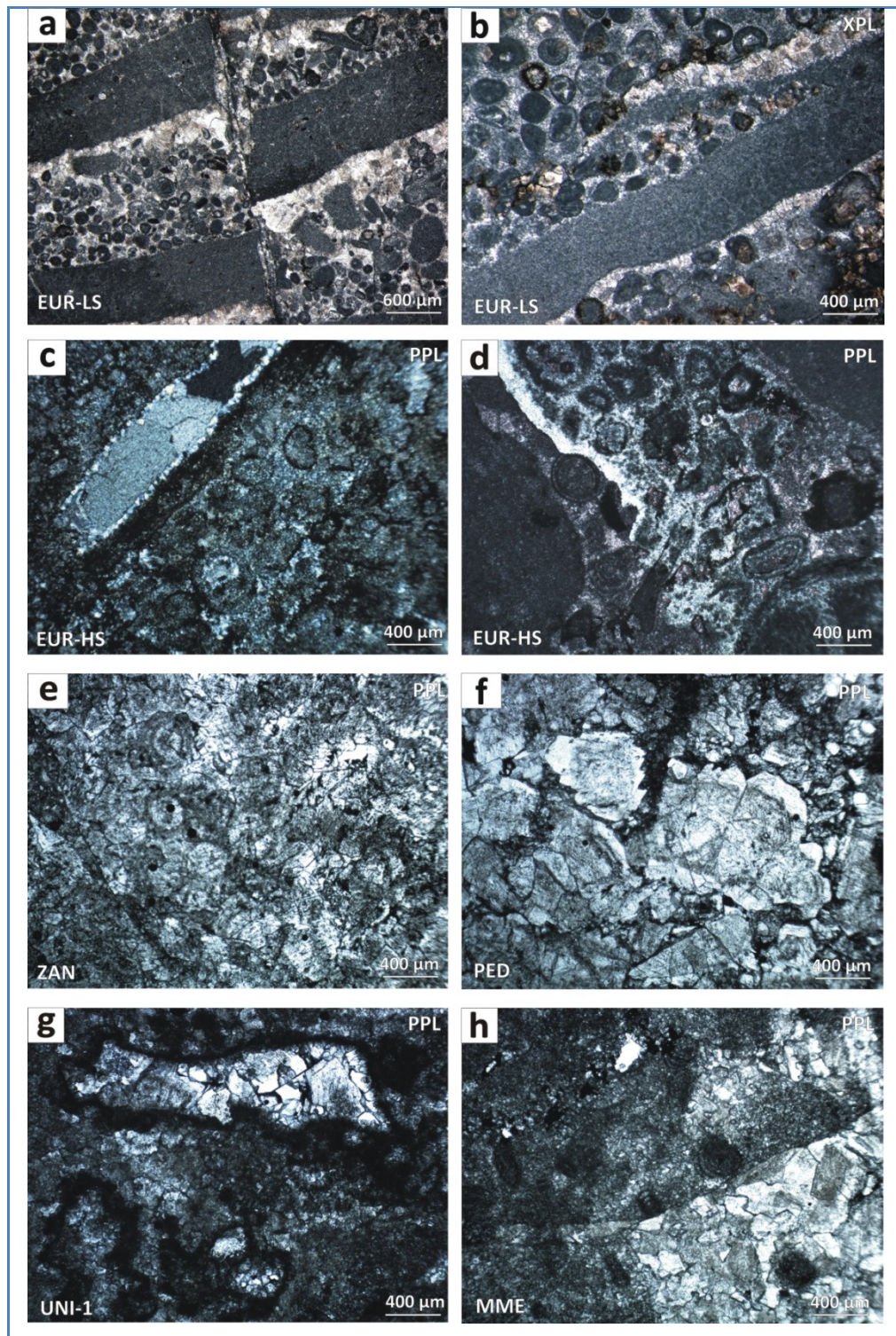


Fig.3.40: Petrographic analysis of significant limestone and dolomite textures. a-b = coated grain peloidal grainstone to packstone with sparse mm-sized micritic intraclasts with rectangular shape (Cambrian-Ordovician, EUR). c-d = The same previous lithofacies locally silicified (EUR). e = dolomitized peloidal packstones (upper Jurassic, ZAN). f = diagenetic breccia-like sediments (upper Triassic, PED). g = xenotopic up to hypidiotopic diagenetic dolomite with microbially-induced cements fillings cavity (upper Triassic, UNI-1); peloidal-fossiliferous wackestone/packstone with benthonic foraminifera with superimposed xenotopic up to idiotopic diagenetic dolomite (MME). Legend: PPL/XPL = plane/crossed polarized light.

Tab.3.43 – Physical analysis on rock samples by mercury intrusion porosimetry (MIP) and gas absorption (BET-N₂)

No	Code	Name	Moisture (105 °C)	BET SSA	Real density	Accessible Porosity	Apparent density	Pore volume	Av. Pore diameter	Av. Pore radius
			(%)	(m ² /g)	(g/cm ³)	(%)	(g/cm ³)	(mm ³ /g)	(μm)	(μm)
1	2450	PSP-1	0.08	0.09	2.70	7.39	2.68	27.42	0.54	0.27
2	2451	PSP-2	0.04	0.17	2.71	6.85	2.69	29.67	0.42	0.21
3	2452	IDW-1	0.11	0.05	2.72	0.41	2.67	1.54	1.60	0.80
4	2453	IDW-2	0.11	0.05	2.72	1.14	2.72	4.24	2.36	1.18
5	2454	WOP-1	0.10	0.15	2.71	1.01	2.70	3.79	0.08	0.04
6	2455	WOP-2	0.10	0.05	2.71	0.55	2.64	2.11	0.20	0.10
7	2462	SMA-1	0.16	0.12	2.71	1.46	2.74	5.42	0.22	0.11
8	2463	SMA-2	0.16	0.11	2.70	1.78	2.66	6.83	0.14	0.07
9	2737	EUR-LS	0.11	0.04	2.76	0.55	2.66	2.09	2.58	1.29
10	2738	EUR-HS	0.10	0.17	2.72	0.69	2.67	2.62	2.67	1.34
11	2828	VER	0.18	0.55	2.71	1.17	2.67	4.43	0.04	0.02
12	2829	CAR	0.03	0.18	2.71	0.65	2.71	2.72	0.76	0.38
13	2941	PRO	0.11	0.60	2.76	13.51	2.63	59.30	0.30	0.15
14	2830	ZAN	0.10	0.06	2.84	1.27	2.84	4.54	0.16	0.08
15	2777	PED	0.07	0.10	2.85	0.30	2.87	1.04	1.05	0.53
16	2762	UNI-1	0.05	0.31	2.86	0.94	2.85	3.32	0.27	0.14
17	2112	MME	0.09	0.14	2.85	0.88	2.87	3.10	0.28	0.14

Tab.3.44 – Chemical analysis (XRF-WDS) of limestone samples. Symbols legend: LOI = Loss on Ignition; IR = insoluble residue; A_{eq} = Alkali Equivalent; CI = Cement Index; HI = Hydraulic Index; Nd = Not determined

		1	2	4	3	5	6	7	8
		2450	2451	2452	2453	2454	2455	2462	2463
Det.	Unit	PSP-1	PSP-2	IDW-1	IDW-2	WOP-1	WOP-2	SMA-1	SMA-2
LOI	%	44.64	44.13	43.48	43.76	43.60	43.62	43.01	42.81
SiO ₂	%	0.01	0.05	0.10	0.15	0.82	0.53	1.83	3.08
Al ₂ O ₃	%	0.01	0.05	0.02	0.03	0.31	0.21	0.53	0.82
Fe ₂ O ₃	%	0.03	0.04	0.16	0.17	0.14	0.11	0.26	0.40
CaO	%	55.31	55.25	54.90	54.70	54.20	54.60	53.20	51.65
MgO	%	0.15	0.22	0.27	0.30	0.70	0.68	0.53	0.62
Na ₂ O	%	0.01	0.01	<0.01	0.03	0.08	0.03	0.01	0.04
K ₂ O	%	<0.01	0.01	<0.01	0.01	0.10	0.06	0.19	0.02
SO ₃	%	<0.01	0.01	0.05	0.06	0.03	0.03	0.05	0.28
MnO	%	<0.01	<0.01	0.50	0.53	0.01	0.00	0.08	0.10
SrO	%	<0.01	<0.01	<0.01	<0.01	0.02	0.02	0.02	<0.01
P ₂ O ₅	%	<0.01	<0.01	0.04	<0.01	0.02	0.01	0.01	0.02
TiO ₂	%	0.01	0.03	<0.01	0.01	0.02	0.01	0.03	0.05
Cl-	%	0.01	0.01	0.01	0.01	0.02	0.01	0.01	0.02
SUM	%	100.2	99.8	99.5	99.7	100.1	99.9	99.8	99.9
IR	%	0.08	0.15	Nd	0.96	1.81	Nd	3.20	Nd
A _{eq}	%	0.01	0.01	0.00	0.03	0.15	0.08	0.13	0.06
HI	%	0.00	0.00	0.00	0.00	0.02	0.01	0.04	0.08
CI	%	0.24	0.49	0.68	0.87	3.61	2.66	6.45	10.40

Tab 3.44 (continue)

		9	10	11	12	13	14	15	16	17
		2737	2738	2828	2829	2943	2830	2777	2762	2112
Det.	Unit	EUR-LS	EUR-HS	VER	CAR	PRO	ZAN	PED	UNI-1	MME
LOI	%	45.00	42.92	43.18	43.86	44.11	47.2	47.55	46.60	46.90
SiO ₂	%	0.05	1.82	1.44	0.06	0.16	0.2	0.06	1.23	0.33
Al ₂ O ₃	%	0.01	0.36	0.33	0.04	0.08	0.1	0.04	0.42	0.15
Fe ₂ O ₃	%	0.02	0.20	0.22	0.04	0.06	0.1	0.05	0.14	0.10
CaO	%	49.50	53.50	54.20	55.10	55.00	31.9	31.06	30.40	33.60
MgO	%	5.29	1.08	0.40	0.90	0.41	21.0	21.09	20.91	18.60
Na ₂ O	%	0.01	0.01	0.04	0.03	0.08	0.0	0.04	0.03	0.03
K ₂ O	%	0.03	0.12	0.04	0.01	0.01	0.0	0.06	0.06	0.04
SO ₃	%	0.05	0.02	0.15	0.01	0.01	0.0	0.02	0.13	0.04
MnO	%	0.01	0.01	0.03	<0.01	0.01	0.0	<0.01	<0.01	<0.01
SrO	%	0.01	0.03	<0.01	<0.01	<0.01	<0.01	<0.01	<0.01	0.05
P ₂ O ₅	%	0.01	0.09	0.01	0.02	0.01	0.0	0.01	0.01	0.01
TiO ₂	%	0.06	0.02	0.03	0.01	0.01	0.0	0.01	0.01	0.01
SUM	%	100.1	100.2	99.9	100.1	100.1	100.5	100.0	100.0	99.9
Cl-	%	0.02	0.00	0.06	0.01	<0.01	0.0	0.005	0.03	0.01
IR	%	Nd	Nd	2.02	0.14	Nd	1.14	2.14	3.14	4.14
A _{eq}	%	0.03	0.09	0.06	0.03	0.09	0.03	0.07	0.07	0.05
HI	%	0.00	0.04	0.03	0.00	0.00	0.01	0.00	0.05	0.01
CI	%	7.56	6.99	4.95	1.46	1.11	29.93	29.72	33.17	27.13

Tab.3.45 – Quantitative-phase analysis by Rietveld method (XRD-QPA) on whole-rock carbonate samples. Symbols legend: Cal=calcite; Dol = dolomite; Ank = ankerite; Qtz = quartz; Ill = illites; Sme = smectites; Chl = chlorites; Kfs = K-feldspar; Pl = plagioclase; Gt = Goethite; Nd = Not determined; Tr = Traces (<0.5 %)

no.	Code	Name	Cal	Dol	Ank	Qtz	Ill	Sme	Chl	Kfs	Pl	Gt
-	-		(Wt.%)	(Wt.%)	(Wt.%)	(Wt.%)	(Wt.%)	(Wt.%)	(Wt.%)	(Wt.%)	(Wt.%)	(Wt.%)
1	2450	PSP-1	100.0	-	-	-	-	-	-	-	-	-
2	2451	PSP-2	99.8	-	-	0.2	-	-	-	-	-	-
3	2452	IDW-1	99.2	0.5	-	0.3	-	-	-	-	-	-
4	2453	IDW-2	97.3	2.5	-	0.2	Tr	-	-	-	-	-
5	2454	WOP-1	96.8	2.8	-	-	0.3	-	-	-	-	-
6	2455	WOP-2	99.8	-	-	0.2	-	-	-	-	-	-
7	2462	SMA-1	95.0	-	-	1.5	2.0	0.3	0.9	-	-	Tr
8	2463	SMA-2	95.1	-	-	1.3	0.7	-	2.9	-	-	-
9	2737	EUR-LS	76.0	23.0	1.0	Tr	-	-	-	-	-	-
10	2738	EUR-HS	93.5	5.6	Tr	0.9	-	-	-	-	-	-
11	2828	VER	98.0	-	-	0.2	1.1	-	-	0.4	-	0.3
12	2829	CAR	99.1	0.8	-	-	0.1	-	-	-	-	-
13	2943	PRO	98.0	1.8	-	-	-	-	-	0.2	-	-
14	2830	ZAN	0.5	99.5	-	-	-	-	-	-	Tr	-
15	2777	PED	1.3	98.3	-	-	-	-	-	-	Tr	-
16	2762	UNI-1	0.4	94.7	-	-	4.5	-	-	-	-	-
17	2112	MME	3.2	96.2	-	0.2	-	-	-	-	Tr	--

- *Thermal analyses and calcination kinetics*

The burnability of carbonate rocks was investigated by means of Netzsch TG/DTA analyzer. Fundamental kinetics parameters, including starting/ending calcination times/temperatures, total calcination time, as well as, mass losses in different ranges of temperature, and total ignition loss are reported in Tab.3.46. Plots on a subset of 4 significant samples are shown in Fig.3.41. They allow evaluating main differences in calcination rates, and amount of available carbonate minerals. Especially, the TG plot as a function of the time pointed out that the highest decomposition rate for sample PSP, and the lowest for sample IDW, under the same experimental conditions.

Tab.3.46 – Thermal analysis (TG-DTA) of rock samples. Symbols legend: Cal = calcination; Nd = Not determined

No.	Code	Name	LOI 25-200	LOI 230-550	LOI 400-700	LOI Cal.	LOI	Cal. On-set	Cal. End-set	Cal. On-set	Cal. End-set	Cal. Δt
			(°C)	(°C)	(°C)	(%)	(%)	(°C)	(°C)	(min)	(min)	(min)
1	2450	PSP-1	0.13	-	0.57	36.10	43.95	810.0	918.0	79.0	89.9	10.9
2	2451	PSP-2	0.16	0.03	0.60	35.45	44.11	813.8	914.2	79.5	89.5	10.0
3	1990	IDW-1	0.13	0.04	-	39.23	43.62	790.0	924.0	77.0	90.0	13.0
4	1991	IDW-2	0.22	0.01	-	36.30	42.87	799.0	915.0	78.0	89.5	11.5
5	2454	WOP-1	0.16	0.09	0.67	35.95	43.64	805.4	908.3	78.6	88.9	10.3
6	2455	WOP-2	Nd	Nd	Nd	Nd	Nd	Nd	Nd	Nd	Nd	Nd
7	2462	SMA-1	0.30	0.58	-	34.37	40.33	786	909	76	89	13.0
8	2463	SMA-2	Nd	Nd	Nd	Nd	Nd	Nd	Nd	Nd	Nd	Nd
9	2737	EUR-LS	Nd	Nd	Nd	Nd	Nd	Nd	Nd	Nd	Nd	Nd
10	2738	EUR-HS	Nd	Nd	Nd	Nd	Nd	Nd	Nd	Nd	Nd	Nd
11	2828	VER	0.26	0.11	-	42.32	43.81	805.0	916.0	78.0	89.7	11.0
12	2829	CAR	0.10	0.07	-	40.20	43.75	775.0	923.0	75.8	90.4	15.0
13	2943	PRO	Nd	Nd	Nd	Nd	Nd	Nd	Nd	Nd	Nd	Nd
14	2830	ZAN	0.14	0.89	-	41.29	47.85	776.7	890.7	75.7	87.1	11.4
15	2782	PED	0.19	0.60	2.90	40.49	48.09	778.5	910.6	75.9	89.1	13.2
16	2762	UNI	0.14	0.31	-	39.95	47.07	792.2	909.0	77.3	89.0	11.7
17	2112	MME	0.08	0.38	1.82	25.10	47.18	821.0	911.0	80.2	89.2	9.0

Tab.3.47 – Kinetics decomposition parameters by in-situ HT-XRD analysis

No	Code	Name	T_i	T_{50}	T_f	$\Delta t (T_i-T_f)$	$\Delta t (T_{50}-T_f)$
-	-	-	(min)	(min)	(min)	(min)	(min)
1	2450	PSP-1	72.5	125.0	177.5	105.0	52.5
4	2453	IDW-2	47.0	108.0	145.0	98.0	37.0
5	2454	WOP-1	50.0	86.0	95.0	45.0	9.0
7	2462	SMA-1	60.0	105.0	140.0	80.0	35.0
14	2830	ZAN	60.0	95.0	110.0	50.0	15.0

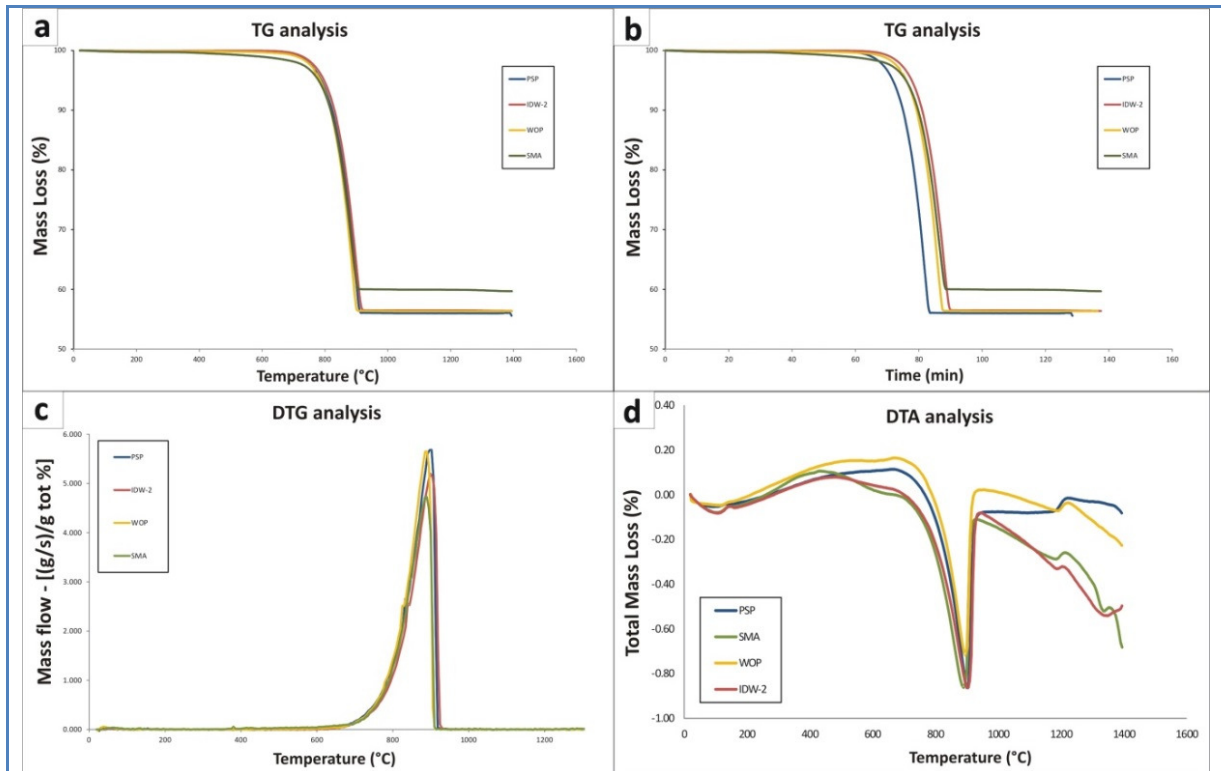


Fig.3.41: Thermal analysis (TG-DTG-DTA) by Netzsch analyzer. a = TG analysis as a function of temperature (°C); b = TG analysis as a function of time (min); c = DTG analysis as a function of temperature (°C); d = DTA analysis as a function of temperature (°C).

- *In-situ high temperature XRD analyses and calcination kinetics*

Isothermal and non-isothermal in-situ HT-XRD analyses were performed at the European Synchrotron Radiation Facility (ESRF), Grenoble, on a subset of 5 samples (PSP-1, IDW-2, WOP-1, SMA-1, and ZAN). Calcite and dolomite kinetics decomposition, as well as, the CaO crystallization was measured according to the procedure described in Chapter 2 (see Paragraph 2.2.13). Moreover the weight % of each phase in the system was determined step-by-step during the experiments. Results are graphically displayed in Fig.3.42. Finally, CaO crystallographic lattices, crystallite-size, and microstrain were determined. Moreover kinetics parameters, including starting calcination time (T_i), final calcination time (T_f), calcination duration time ($T_f - T_i$), half time for calcite decomposition/lime crystallization (T_{50}), are reported in Tab.3.47.

• *Burnt lime characterization*

Chemical (XRF-WDS), mineralogical (XRD-QPA) and crystallographic analyses of burnt limes at different temperatures were carried out. In particular, the quantitative phase analysis (QPA) was performed by Rietveld method, while the CaO lattice parameters, the crystallite-size and the microstrain by the Fundamental Parameters (FP) method. Results are reported in Tab.3.48, Tab.3.49, and Tab.3.50. The physical characterization of burnt limes was performed by nitrogen gas adsorption for the determination of the BET specific surface area, and by elium gas pycnometry for the real density determination. Results are reported in Tab.3.50, as well.

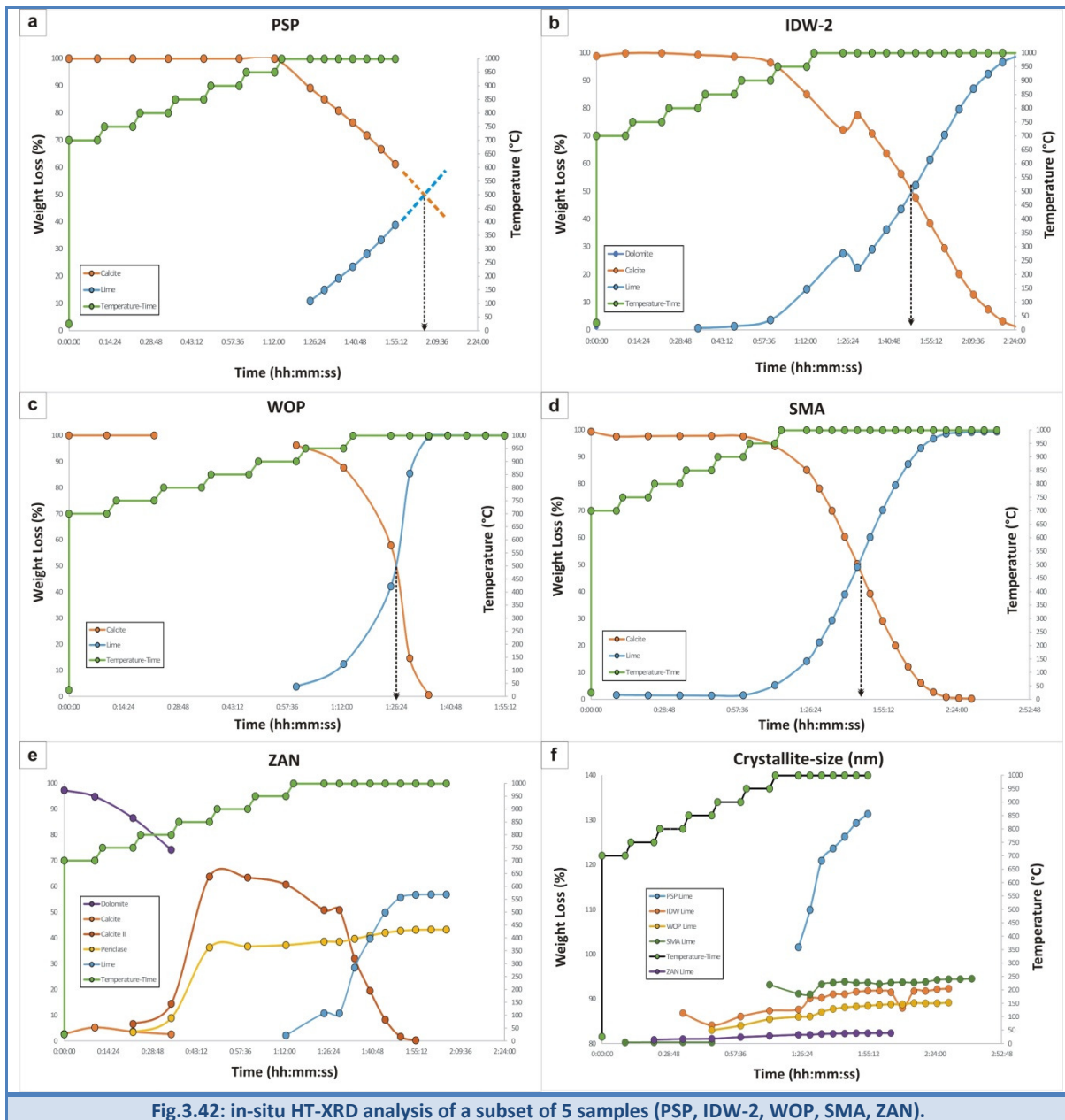


Fig.3.42: in-situ HT-XRD analysis of a subset of 5 samples (PSP, IDW-2, WOP, SMA, ZAN).

High-grade burnt lime products: impact of calcination kinetics on slaking reactivity; sticking tendency and blocks formation at HT (1300°C)

- *Slaking reactivity*

The slaking test for lime reactivity was performed on samples burnt at different temperatures according to the European standard UNI EN 459-2. The ΔT 40 °C or t_{60} , the maximum heating rate, the maximum slaking temperature (T_{max}), were determined on high-calcium limes. The ΔT 30 °C or t_{50} , the maximum heating rate, and the maximum slaking temperature (T_{max}), were determined on dolomitic limes, as well. Results are reported in Tab.3.51. Slaking tests for samples PSP, IDW, WOP, SMA, EUR, PED, and UNI were repeated in double, because two different size-fractions or lithofacies were analyzed, while a single determination was carried out on samples CAR, VER, ZAN, MME, because just one size or lithofacies was available. The Fig.3.43 shows wet slaking and differential wet slaking plots of 4 representative samples burnt at different temperatures. The t_{60} for high-calcium limes ranges between 0.3-2.5 min (mean 1.2 min) for limes burnt at 1050 °C, 0.4-13.9 min (mean 4.1 min) for limes burnt at 1150 °C, 1.7-21.5 min (mean 7.3 min) for limes burnt at 1200 °C, and 1.6-25.2 min (mean 10.1 min) for limes burnt at 1250°C. The T_{max} for high-calcium limes ranges between 69.7-85.5 °C (mean 75.6 °C) for limes burnt at 1050 °C, 63.7-81.3 °C (mean 71.9 °C) for limes burnt at 1150°C, 62.1-75.8 °C (mean 69.9 °C) for limes burnt at 1200 °C, 63.0-78.6 °C (mean 68.3 °C) for limes burnt at 1250 °C. The t_{50} for dolomitic limes ranges between 0.3-0.8 min (mean 0.6 min) for limes burnt at 1050°C, 0.5-1.2 min (mean 0.8 min) for limes burnt at 1150 °C, 0.5-2.8 min (mean 1.5 min) for limes burnt at 1250 °C. The T_{max} for dolomitic limes ranges between 54.6-56.8 °C for limes burnt at 1050 °C, 54.4-56.7 °C for limes burnt at 1150 °C, 53.6-55.2 °C for limes burnt at 1250 °C. Especially, sample PSP presented the highest reactivity at 1050 °C for high-calcium quicklimes ($t_{60} = 0.3$ min, $T_{max} = 85.5$ °C, HR = 129 C°/min), while SMA the lowest, at the same burning temperature ($t_{60} = 2.5$ min, $T_{max} = 70.6$ °C, HR = 24.6 C°/min). Conversely, sample PRO presented the highest reactivity at 1250 °C ($t_{60} = 1.6$ min, $T_{max} = 78.6$ °C, HR = 27.9 °C/min), and sample IDW-2 the lowest at the same temperature ($t_{60} = 25.2$ min, $T_{max} = 63.3$ °C, HR = 9.2 °C/min).

As concerns dolomitic limes, the sample ZAN presented the highest reactivity at 1050 °C ($t_{50} = 0.33$ min, HR = 126.2 °C/min), while the sample PED the lowest at the same temperature ($t_{50} = 0.83$ min, $T_{max} = 55.3$ °C, HR = 61.3 °C/min). Moreover sample ZAN presented the highest reactivity at 1250 °C ($t_{50} = 0.52$ min, $T_{max} = 55.9$ °C, HR = 69.9 °C/min), and the sample PED the lowest at the same temperature ($t_{50} = 2.79$ min). The fitting of wet slaking curves by means of the shrinking core model (SMC) is reported in

Fig.3.44 and Fig.3.45. The equation for spherical particles under reaction control was adopted, according to the literature (Liddell, 2005). The angular coefficient, i.e. slope, and the y-intercept values for the linearized slaking curves are reported in Tab.3.51.

Tab.3.48 – Chemical analysis (XRF-WDS) of limes burnt at different temperatures. Symbols legend: Nd = Not determined yet; Tr = traces (<0.5%)

Code		2450				2451				2452				2453			
		PSP-1				PSP-2				IDW-1				IDW-2			
		1050	1150	1200	1250	1050	1150	1200	1250	1050	1150	1200	1250	1050	1150	1200	1250
LOI	%	Tr	Tr	Tr	Tr	Tr	Tr	Tr	Tr	Tr	Tr	Tr	Tr	Tr	Tr	Tr	Tr
SiO ₂	%	0.08	0.05	0.04	0.13	0.04	0.17	0.16	0.18	0.10	0.11	0.05	0.38	0.12	0.12	0.30	0.18
Al ₂ O ₃	%	0.04	0.03	0.05	0.08	0.03	0.11	0.11	0.12	0.03	0.04	0.02	0.03	0.03	0.03	0.03	0.03
Fe ₂ O ₃	%	<0.01	<0.01	0.03	0.04	<0.01	0.09	0.07	0.08	0.22	0.21	0.41	0.32	0.24	0.26	0.23	0.27
CaO	%	99.50	99.50	99.40	99.30	99.50	99.10	99.2	99.10	97.20	97.70	94.00	96.60	97.20	96.90	96.70	96.80
MgO	%	0.26	0.25	0.31	0.26	0.27	0.36	0.32	0.35	0.87	0.50	3.58	1.07	0.76	0.97	1.25	0.93
Na ₂ O	%	<0.01	<0.01	<0.01	<0.01	<0.01	<0.01	<0.01	<0.01	<0.01	<0.01	<0.01	<0.01	<0.01	<0.01	<0.01	<0.01
K ₂ O	%	0.07	0.05	0.06	0.06	0.06	0.07	0.07	0.05	0.06	0.05	0.05	0.07	0.05	0.05	0.05	0.05
SO ₃	%	<0.01	0.01	0.01	<0.01	0.01	0.01	0.01	0.01	0.06	0.04	0.02	0.01	0.04	0.03	0.05	0.01
MnO	%	<0.01	<0.01	<0.01	<0.01	<0.01	<0.01	<0.01	<0.01	1.39	1.29	1.68	1.42	1.48	1.50	1.36	1.44
SrO	%	0.01	0.01	0.02	0.02	0.02	0.02	0.02	0.02	0.01	<0.01	<0.01	0.01	0.01	0.01	0.01	0.01
P ₂ O ₅	%	0.07	0.07	0.08	0.06	0.07	0.08	0.08	0.09	0.05	0.05	0.05	0.05	0.05	0.05	0.05	0.05
TiO ₂	%	<0.01	<0.01	<0.01	<0.01	<0.01	<0.01	<0.01	<0.01	<0.01	<0.01	0.10	<0.01	<0.01	<0.01	<0.01	<0.01
Cl-	%	<0.01	0.01	<0.01	<0.01	<0.01	<0.01	<0.01	<0.01	0.01	<0.01	<0.01	<0.01	0.01	<0.01	<0.01	<0.01
SUM	%	100	100	100	100	100	100	100	100	100	100	100	100	100	100	100	100

Table 3.48 (continue)

Code		2454					2455					2462				
		WOP-1					WOP-2					SMA-1				
T		1050	1150	1200	1250	1300	1050	1150	1200	1250	1300	1050	1150	1200	1250	1300
LOI	%	Tr	Tr	Tr	Tr	Tr	Tr	Tr	Tr	Tr	Tr	Tr	Tr	Tr	Tr	Tr
SiO ₂	%	1.11	0.93	0.41	0.31	1.02	1.34	0.67	0.42	1.01	0.21	2.00	2.23	2.01	1.00	1.57
Al ₂ O ₃	%	0.57	0.49	0.21	0.17	0.49	0.50	0.34	0.25	0.51	0.11	0.98	0.95	0.83	0.39	0.69
Fe ₂ O ₃	%	0.29	0.22	0.14	0.10	0.21	0.28	0.18	0.14	0.02	0.06	0.55	0.47	0.45	0.28	0.45
CaO	%	95.30	96.70	98.00	98.20	96.20	96.60	95.00	97.80	96.60	97.70	94.90	94.70	95.00	97.10	96.10
MgO	%	2.41	1.24	1.01	0.97	1.80	1.34	3.55	1.13	1.39	1.52	0.74	0.79	0.75	0.82	0.71
Na ₂ O	%	<0.01	<0.01	<0.01	<0.01	<0.01	0.05	<0.01	<0.01	<0.01	<0.01	<0.01	<0.01	<0.01	<0.01	<0.01
K ₂ O	%	0.18	0.12	0.08	0.08	0.06	0.16	0.10	0.07	0.10	0.07	0.27	0.24	0.23	0.07	0.07
SO ₃	%	0.04	0.05	0.04	0.03	0.03	0.04	0.04	0.03	0.04	0.01	0.10	0.18	0.23	0.06	0.04
MnO	%	<0.01	<0.01	<0.01	<0.01	<0.01	<0.01	<0.01	<0.01	<0.01	<0.01	0.22	0.27	0.27	0.17	0.23
SrO	%	0.06	0.05	0.05	0.05	0.05	0.06	0.05	0.05	0.05	0.05	0.05	0.07	0.04	0.05	0.05
P ₂ O ₅	%	0.07	0.07	0.07	0.06	0.05	0.06	0.06	0.06	0.06	0.57	0.06	0.06	0.06	0.07	0.06
TiO ₂	%	<0.01	<0.01	<0.01	<0.01	<0.01	<0.01	<0.01	<0.01	<0.01	<0.01	<0.01	<0.01	<0.01	<0.01	<0.01
Cl-	%	<0.01	<0.01	<0.01	<0.01	<0.01	<0.01	<0.01	<0.01	<0.01	<0.01	<0.01	<0.01	<0.01	<0.01	<0.01
SUM	%	100	100	100	100	100	100	100	100	100	100	100	100	100	100	100

Table 3.48 (continue)

Code	2463					2737				2738				2828			2829			2943				
	SMA-2					EUR-LS				EUR-HS				VER			CAR			PRO				
T	1050	1150	1200	1250	1300	1050	1150	1200	1250	1050	1150	1200	1250	1050	1150	1250	1050	1150	1250	1050	1150	1250		
LOI	%	Tr	Tr	Tr	Tr	Tr	Tr	Tr	Tr	Tr	Tr	Tr	Tr	Tr	Tr	Tr	Tr	Tr	Tr	Tr	Tr	Tr	Tr	
SiO ₂	%	1.53	2.57	0.47	1.84	0.47	0.12	1.17	0.05	0.12	1.27	1.35	1.33	2.45	1.52	1.56	1.33	0.12	0.12	0.15	0.10	0.07	0.14	
Al ₂ O ₃	%	0.68	1.15	0.16	0.76	0.16	0.14	0.24	0.04	0.09	0.26	0.27	0.22	0.46	0.54	0.53	0.43	0.06	0.06	0.07	0.04	0.04	0.06	
Fe ₂ O ₃	%	0.34	0.57	0.17	0.42	0.15	0.09	0.29	0.05	0.04	0.20	0.20	0.18	0.40	0.42	0.43	0.48	0.05	0.06	0.05	0.09	0.13	0.06	
CaO	%	96.00	94.10	98.30	95.50	98.30	98.00	97.00	96.30	93.8	95.60	95.4	92.50	94.50	96.00	96.20	96.00	97.70	97.90	97.30	98.7	96.9	98.9	
MgO	%	0.81	0.86	0.53	0.83	0.56	1.45	0.94	3.41	5.71	2.41	2.42	5.45	1.91	0.92	0.76	1.40	1.76	1.68	1.99	0.76	2.55	0.60	
Na ₂ O	%	<0.01	<0.01	<0.01	<0.01	<0.01	<0.01	<0.01	<0.01	<0.01	<0.01	<0.01	<0.01	<0.01	<0.01	<0.01	<0.01	<0.01	<0.01	<0.01	<0.01	0.05	<0.01	<0.01
K ₂ O	%	0.19	0.28	0.06	0.14	0.07	0.06	0.08	0.05	0.04	0.09	0.07	0.08	0.10	0.20	0.13	0.08	0.07	0.06	0.06	0.05	0.04	0.05	
SO ₃	%	0.10	0.19	0.02	0.01	0.02	0.01	0.03	0.01	0.01	0.02	0.03	0.02	0.01	0.06	0.06	0.04	0.06	0.06	0.04	0.12	0.09	0.08	
MnO	%	0.19	0.19	0.20	0.04	0.18	0.02	0.04	<0.01	0.03	<0.01	0.03	0.03	0.04	0.07	0.06	0.07	<0.01	<0.01	0.02	<0.01	0.03	<0.01	
SrO	%	0.04	0.05	0.05	0.05	0.05	0.04	0.07	0.04	0.04	0.05	0.05	0.05	0.06	0.03	0.03	0.03	0.04	0.05	0.04	0.03	0.03	0.03	
P ₂ O ₅	%	0.06	0.07	0.05	0.05	0.06	0.05	0.12	0.06	0.06	0.11	0.13	0.09	0.10	0.10	0.11	0.10	0.10	0.06	0.06	0.06	0.06	0.06	
TiO ₂	%	<0.01	<0.01	<0.01	<0.01	<0.01	<0.01	<0.01	<0.01	<0.01	<0.01	<0.01	<0.01	<0.01	<0.01	<0.01	<0.01	<0.01	<0.01	<0.01	<0.01	<0.01	<0.01	
Cl-	%	<0.01	<0.01	<0.01	<0.01	<0.01	<0.01	<0.01	<0.01	<0.01	<0.01	<0.01	<0.01	<0.01	<0.01	<0.01	<0.01	<0.01	<0.01	<0.01	<0.01	<0.01	<0.01	
SUM	%	100	100	100	100	100	100	100	100	100	100	100	100	100	100	100	100	100	100	100	100	100	100	

Table 3.48 (Continue)

Code		2830			2776-77						2662 A-B						2112		
		ZAN			PED						UNI-1						MME		
T		1050	1150	1250	1050	1150	1250	1050	1150	1250	1050	1150	1250	1050	1150	1250	1050	1150	1250
LOI	%	Tr	Tr	Tr	Tr	Tr	Tr	Tr	Tr	Tr	Tr	Tr	Tr	Tr	Tr	Tr	Tr	Tr	Tr
SiO ₂	%	0.31	0.38	0.22	0.06	0.04	0.05	0.05	0.06	0.04	0.13	0.25	0.07	0.17	0.31	0.18	0.62	0.18	0.35
Al ₂ O ₃	%	0.31	0.15	0.13	0.05	0.07	0.03	0.04	0.05	0.04	0.05	0.15	0.04	0.07	0.18	0.10	0.28	0.13	0.14
Fe ₂ O ₃	%	0.15	0.01	0.10	0.02	0.05	0.04	0.03	0.05	0.05	0.04	0.10	0.03	0.06	0.9	0.05	0.19	0.13	0.16
CaO	%	61.9	62.0	61.6	60.2	59.3	59.6	61.7	59.0	58.2	61.4	59.3	60.0	61.2	59.4	58.8	59.15	59.3	60.0
MgO	%	37.4	37.2	37.8	39.4	40.3	40.1	38.0	40.6	41.4	38.1	40.0	39.7	38.2	39.8	40.7	39.50	40.1	39.2
Na ₂ O	%	<0.01	<0.01	<0.01	<0.01	<0.01	<0.01	<0.01	<0.01	<0.01	<0.01	<0.01	<0.01	<0.01	<0.01	<0.01	<0.01	<0.01	<0.01
K ₂ O	%	0.08	0.06	0.06	0.06	0.07	0.06	0.07	0.07	0.06	0.07	0.09	0.05	0.06	0.08	0.06	0.07	0.07	0.06
SO ₃	%	0.03	0.02	0.03	0.07	0.07	0.06	0.07	0.06	0.05	0.04	0.06	0.05	0.07	0.06	0.04	0.07	0.04	0.01
MnO	%	0.02	0.02	0.02	<0.01	<0.01	<0.01	<0.01	<0.01	<0.01	<0.01	<0.01	<0.01	<0.01	<0.01	<0.01	<0.01	<0.01	<0.01
SrO	%	0.02	0.01	0.01	0.02	0.03	0.03	0.03	0.02	0.02	0.02	0.02	0.02	0.02	0.03	0.02	0.02	0.02	0.02
P ₂ O ₅	%	0.05	0.05	0.05	0.07	0.07	0.06	0.06	0.06	0.05	0.06	0.04	0.05	0.06	0.06	0.06	0.02	0.06	0.06
TiO ₂	%	<0.01	<0.01	<0.01	<0.01	<0.01	<0.01	<0.01	<0.01	<0.01	<0.01	<0.01	<0.01	<0.01	<0.01	<0.01	<0.01	<0.01	<0.01
Cl-	%	<0.01	<0.01	<0.01	<0.01	<0.01	<0.01	0.01	<0.01	<0.01	0.02	<0.01	<0.01	0.01	<0.01	<0.01	<0.01	0.02	<0.01
SUM	%	100	100	100	100	100	100	100	100	100	100	100	100	100	100	100	100	100	100

High-grade burnt lime products: impact of calcination kinetics on slaking reactivity;
sticking tendency and blocks formation at HT (1300°C)

Chapter 3. Results and Discussion

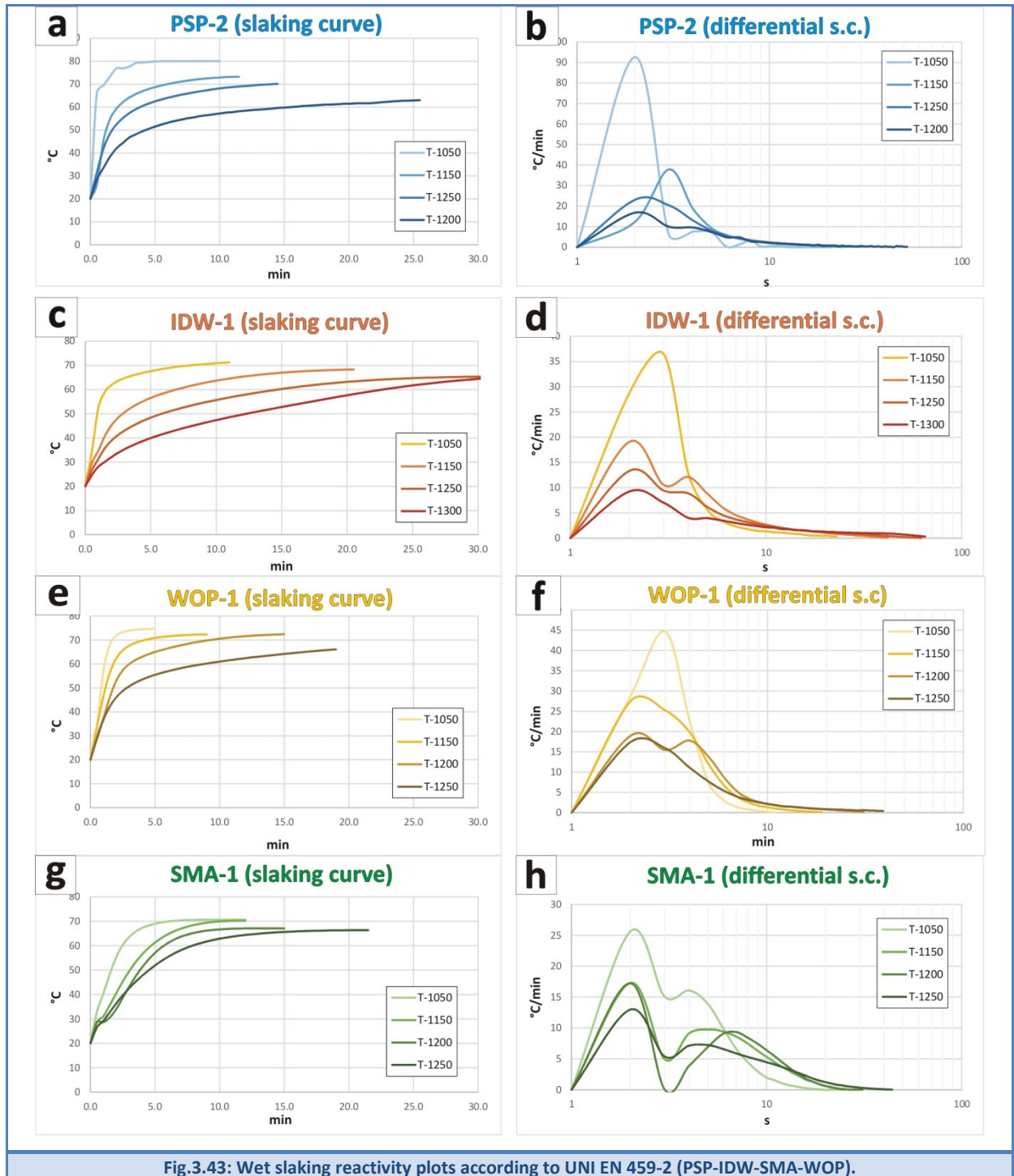
Tab.3.49 – Available Lime Index (ALI) and Quantitative-phase analysis by Rietveld method (XRD-QPA) on burnt limes. Symbols legend: Per = Periclase; Lar = Larnite; Hat = hatrurite; Alm = Aluminates, Fer = Ferrites, Cal = Calcite; Qtz = Quartz; Por = Portlandite; Nd = Not determined; Tr = Traces (<0.5%).

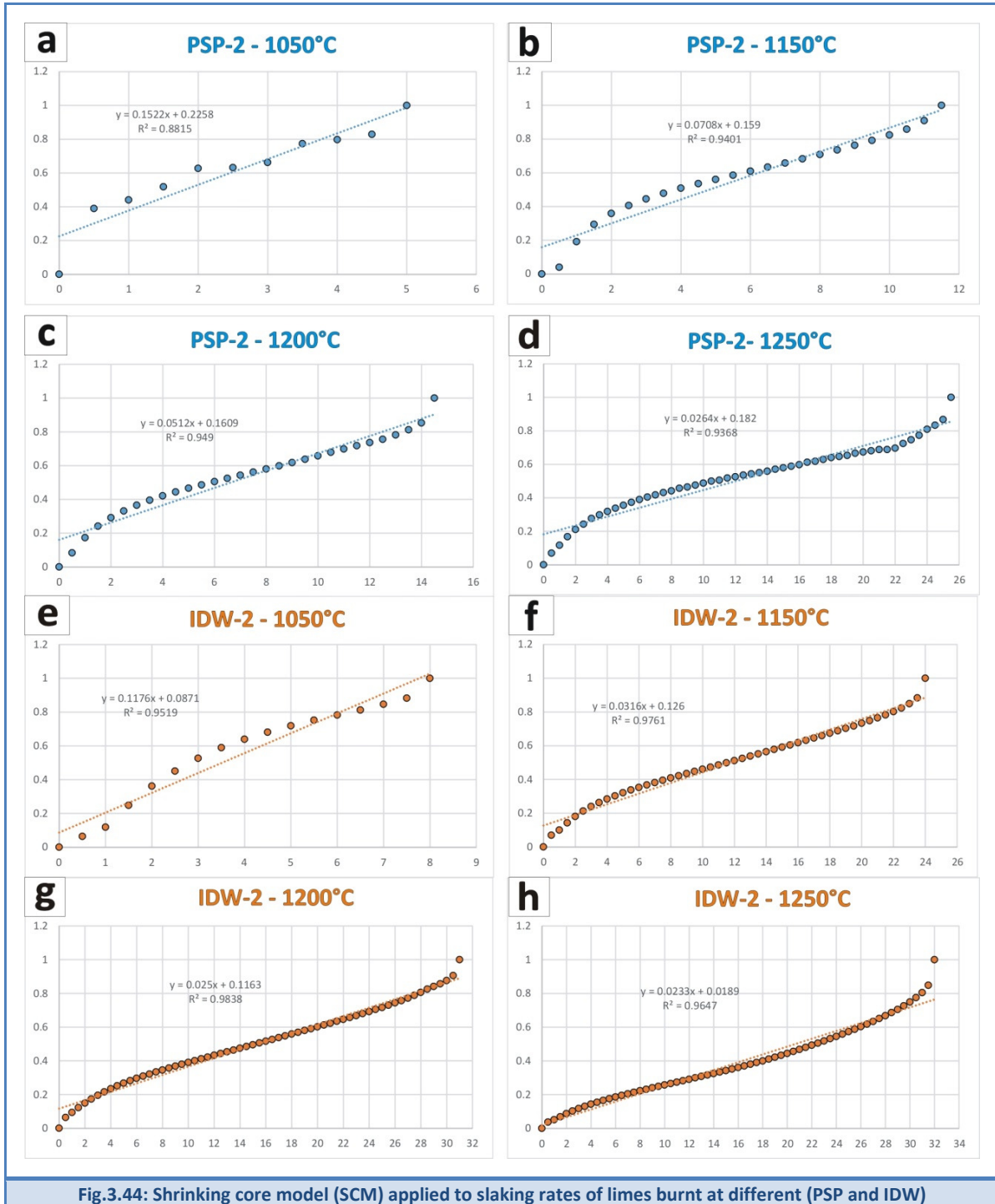
Sample	Codes	T	ALI	Lime	Per	Lar	Hat	Alm	Fer	Cal	Qtz	Ca ₂ MnO ₄	Por
		(°C)	(%)	(%)	(%)	(%)	(%)	(%)	(%)	(%)	(%)	(%)	(%)
PSP-1	2450 FG	1050	97.3	100	Tr	-	-	-	-	-	-	-	Tr
		1150	98.3	100	Tr	Tr	-	Tr	-	-	-	-	Tr
		1200	98.2	100	Tr	-	-	Tr	Tr	-	-	-	Tr
		1250	98.3	99.0	0.3	0.7	Tr	Tr	Tr	-	-	-	Tr
PSP-2	2451 FF	1050	Nd	100	-	-	-	-	Tr	-	-	-	Tr
		1200	Nd	99.1	0.4	-	-	-	-	0.5	-	-	Tr
		1250	Nd	99.0	-	-	-	0.5	-	0.5	-	-	Tr
IDW-1	2452 CF	1050	94.8	95.2	0.5	-	-	Tr	-	-	-	4.4	Tr
		1150	94.6	95.0	-	0.3	Tr	-	Tr	-	-	4.1	Tr
		1200	95.2	94.0	2.7	1.0	-	Tr	-	-	-	2.1	Tr
		1250	93.5	96.6	1.1	Tr	-	0.7	-	-	-	2.5	Tr
IDW-2	2453 FF	1050	Nd	94.9	1.2	2.0	-	Tr	-	Tr	-	3.9	Tr
		1150	Nd	93.0	1.2	1.1	-	-	-	-	-	3.7	Tr
		1200	Nd	89.9	1.3	Tr	3.9	-	Tr	Tr	-	4.8	Tr
		1250	Nd	91.8	1.2	-	3.2	Tr	-	-	-	3.8	Tr
WOP-1	2454 CF	1050	92.9	94.0	2.5	Tr	3.5	Tr	-	Tr	-	-	Tr
		1150	96.2	95.8	1.2	Tr	2.0	1.0	Tr	Tr	-	-	Tr
		1200	97.6	95.9	0.7	2.6	-	0.7	Tr	-	-	-	Tr
		1250	98.3	98.0	0.6	2.0	-	Tr	Tr	-	-	-	Tr
		1300	98.3	94.0	1.6	2.6	1.3	0.5	Tr	-	-	-	Tr
WOP-2	2455 FF	1050	Nd	96.7	1.1	-	0.5	1.8	-	-	-	-	Tr
		1150	Nd	95.0	3.0	1.7	-	0.4	-	-	-	-	Tr
		1200	Nd	97.8	1.2	0.7	-	Tr	Tr	-	-	-	Tr
		1250	Nd	95.0	1.2	1.1	Tr	1.1	-	-	-	-	Tr
		1300	Nd	97.7	1.2	1.2	-	-	-	-	-	-	Tr
SMA-1	2462 CF	1050	91.3	95.0	0.7	3.2	0.2	0.7	0.5	-	-	-	Tr
		1150	91.1	94.7	1.3	0.4	0.2	2.9	0.6	-	-	-	Tr
		1200	91.9	95.0	Tr	3.3	Tr	1.0	Tr	0.5	-	-	Tr
		1250	96.0	97.3	0.4	2.3	-	0.3	-	-	-	-	Tr
		1300	96.7	96.0	0.9	1.9	0.7	0.3	0.3	-	-	-	Tr
SMA-2	2463 FF	1050	Nd	96.0	0.7	2.6	-	0.3	0.4	-	-	-	Tr
		1150	Nd	94.1	0.9	3.3	0.4	0.9	0.3	-	-	-	Tr
		1200	Nd	98.3	0.5	Tr	Tr	1.0	-	-	-	-	Tr
		1250	Nd	95.5	0.8	3.1	Tr	0.9	0.5	-	-	-	Tr
		1300	Nd	98.3	0.6	1.0	0.5	0.4	-	-	-	-	Tr
EUR-LS	2737 LS	1050	Nd	98.0	1.5	-	-	0.5	-	-	-	-	Tr
		1150	Nd	100	Tr	-	-	-	-	-	-	-	Tr
		1200	96.0	96.6	2.5	-	-	0.9	-	-	-	-	Tr
		1250	95.7	94.4	5.6	-	Tr	-	Tr	-	-	-	Tr
EUR-HS	2738 HS	1050	Nd	95.6	1.8	1.4	0.8	-	0.6	-	Tr	-	Tr
		1150	Nd	89.9	1.2	1.1	5.5	1.9	0.4	-	-	-	Tr
		1200	Nd	89.0	3.8	4.5	0.9	1.9	-	-	-	-	Tr
		1250	Nd	84.4	0.6	4.4	2.9	3.1	3.7	-	-	-	Tr
VER	2828	1050	88.7	90.6	Tr	6.6	1.4	1.2	-	-	-	-	Tr
		1150	89.2	89.5	Tr	9.1	-	-	1.5	-	-	-	Tr
		1250	Nd	91.9	1.0	7.1	-	-	-	-	-	-	Tr
CAR	2829	1050	95.9	98.6	1.4	-	-	Tr	-	-	-	-	Tr
		1150	95.3	98.8	1.2	-	-	Tr	-	-	-	-	Tr
		1250	95.2	98.0	1.1	-	-	1.0	-	-	-	-	Tr
PRO	2943	1050	95.6	95.0	0.5	1.2	0.8	2.5	-	-	-	-	Tr
		1150	95.9	96.0	1.8	-	-	1.7	-	-	-	-	Tr
		1250	95.5	96.9	-	-	-	1.8	1.3	-	-	-	Tr

High-grade burnt lime products: impact of calcination kinetics on slaking reactivity; sticking tendency and blocks formation at HT (1300 °C)

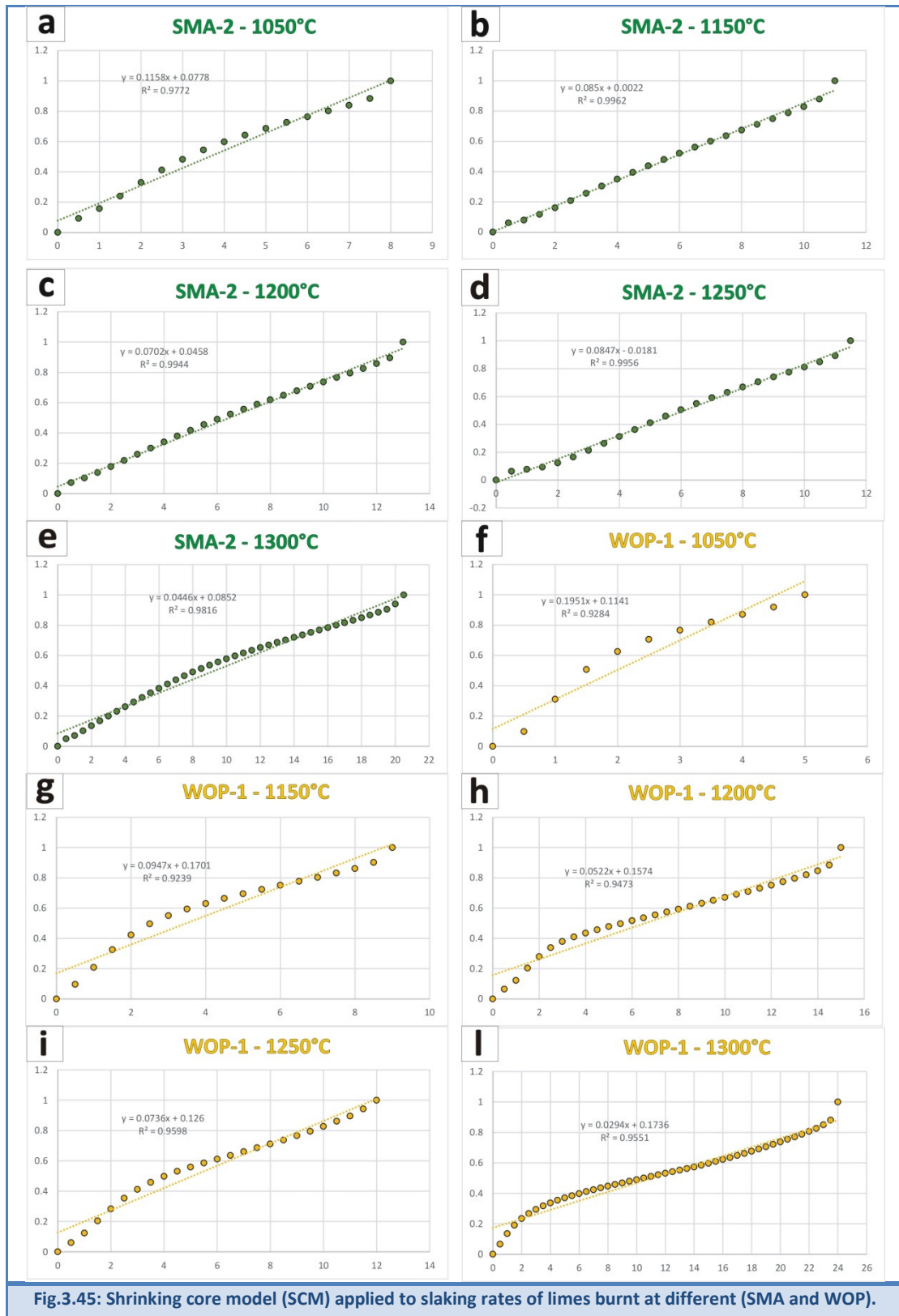
Tab.3.50 – Results from the whole powder profile fitting by FP method. Symbols legend: X-Size = crystallite-size, Er = error; a = lattice parameter; BET SSA = specific surface area by BET method.

Sample	Code	T (°C)	X-Size (Å)	Er (Å)	a (Å)	Strain (%)	Er	BET SSA (m ² /g)	Real Density (g/cm ³)
PSP-1	2450	1050	1773	66	4.8102	0.0506	12	5.49	3.05
		1150	1744	55	4.8107	0.0398	13	3.07	3.10
		1200	1721	48	4.8087	0.0354	11	2.32	3.15
		1250	2003	47	4.8094	0.0201	13	1.56	3.28
PSP-2	2451	1050	2215	96	4.8112	0.0398	15	4.80	3.00
		1150	1968	71	4.8104	0.046	12	3.92	3.10
		1200	2006	136	4.8098	0.0372	19	2.82	3.20
		1250	1706	39	4.8098	0.0249	13	1.86	3.30
IDW-1	2452	1050	1795	58	4.8089	0.0283	15	2.87	3.26
		1150	2074	80	4.8101	0.0462	12	1.66	3.28
		1200	2303	142	4.8086	0.0462	15	1.35	3.32
		1250	2819	142	4.8087	0.0453	13	1.23	3.32
IDW-2	2453	1050	5318	502	4.8104	0.0438	10	2.14	3.24
		1150	2496	124	4.809	0.0467	13	1.52	3.32
		1200	4176	260	4.8091	0.0509	9	1.08	3.32
		1250	4454	313	4.8078	0.0643	9	1.06	3.32
WOP-1	2454	1050	4820	440	4.8104	0.0307	10	1.69	3.21
		1150	2622	137	4.8089	0.0259	11	1.36	3.28
		1200	1834	54	4.8083	0	0	1.11	3.29
		1250	4501	220	4.8068	0.0497	7	1.05	3.29
		1300	4731	355	4.8073	0.0911	11	1.04	3.29
WOP-2	2455	1050	3326	182	4.8094	0.0306	9	1.73	3.24
		1150	3628	200	4.8077	0.0525	9	1.37	3.29
		1200	3053	128	4.8066	0.0689	8	1.32	3.27
		1250	2987	150	4.8071	0.0527	10	1.08	3.30
		1300	2566	99	4.8092	0.078	9	1.02	3.30
SMA-1	2462	1050	3748	235	4.8097	0.0438	11	1.70	3.15
		1150	5289	498	4.8082	0.0473	9	1.38	3.16
		1200	2779	187	4.8087	0.0806	15	1.37	3.20
		1250	5574	371	4.807	0.0569	6	1.66	3.22
		1300	7394	129	4.8066	0.0704	8	0.94	3.30
SMA-2	2463	1050	5049	367	4.8089	0.064	8	1.73	3.06
		1150	3750	243	4.8108	0.0613	10	1.40	3.12
		1200	5941	291	4.8071	0.0794	9	1.21	3.18
		1250	4785	383	4.8073	0.0811	10	1.26	3.22
		1300	2479	83	4.8068	0.0488	8	0.81	3.27
EUR-LS	2737	1050	1726	34	4.8106	0.0118	18	5.41	3.03
		1150	1771	180	4.8077	0.011	9	3.03	3.14
		1200	1783	39	4.8103	0	10	2.59	3.22
		1250	1647	377	4.8093	0.044	7	1.94	3.28
EUR-HS	2738	1050	2712	117	4.8091	0	10	1.91	3.14
		1150	1453	91	4.8088	0.02	6	0.84	3.22
		1200	1707	70	4.8065	0.0367	15	0.54	3.27
		1250	2332	52	4.8082	0	0	0.27	3.30
VER	2828	1050	2002	183	4.8087	0.053	2	1.02	3.19
		1150	1716	67	4.8082	0.1015	12	0.69	3.22
		1250	1161	35	4.8076	0	0	0.63	3.22
CAR	2829	1050	2018	59	4.8086	0.014	2	2.29	3.19
		1150	1662	33	4.8076	0.0236	11	0.85	3.24
		1250	1853	105	4.8071	0.021	3	0.48	3.27
PRO	2943	1050	1601	45	4.8092	0.006	7	1.29	3.29
		1150	1685	84	4.8092	0.047	2	0.53	3.35
		1250	1839	65	4.8096	0.0807	11	0.41	3.35





High-grade burnt lime products: impact of calcination kinetics on slaking reactivity; sticking tendency and blocks formation at HT (1300°C)



Tab.3.51 – Slaking reactivity parameters determined according to European standard UNI EN 459-2

Sample	Code	T	t ₆₀	t ₆₀	T _{max}	t _{max}	t _{max}	Heating Rate (HR)	Max HR	Slope	Y-intercept
		(°C)	(min)	(s)	(°C)	(min)	(s)	(°C/s)	(°C/s)	-	-
PSP -1	2450	1050	0.3	18	85.5	1.0	60	1.43	129.4	1.0000	0.0899
		1150	0.4	24	81.3	8.0	480	0.17	98.2	0.0772	0.4005
		1200	1.7	102	75.8	9.0	540	0.14	42.9	0.0920	0.1483
		1250	7.1	426	69.7	19.0	1140	0.06	18.6	0.0414	0.1041
PSP -2	2451	1050	0.4	24	79.9	5.0	300	0.27	92.6	0.1522	0.2258
		1150	2.1	126	73.2	11.0	660	0.11	37.9	0.0708	0.159
		1200	3.9	234	70.1	14.5	870	0.08	23.1	0.0512	0.1609
		1250	15.5	930	63.0	31.0	1860	0.03	16.8	0.0264	0.1820
IDW-1	2452	1050	1.7	102	71.2	11.0	660	0.11	36.5	0.0643	0.2234
		1150	6.9	414	68.3	20.5	1230	0.06	19.1	0.0382	0.1434
		1200	14.5	870	64.8	29.0	1740	0.04	13.3	0.0263	0.1334
		1250	19.2	1152	63.8	31.0	1860	0.03	9.2	0.0236	0.1192
IDW-2	2453	1050	2.3	138	69.7	8.0	480	0.15	25.9	0.1176	0.0871
		1150	13.9	834	63.7	24.0	1440	0.04	16.1	0.0316	0.1260
		1200	21.5	1290	62.1	31.0	1860	0.03	14.3	0.025	0.1163
		1250	25.2	1512	63.3	32.0	1920	0.03	13.0	0.0233	0.0189
WOP-1	2454	1050	1.3	78	72.8	4.5	270	0.27	38.0	0.1986	0.0981
		1150	2.2	132	72.4	11.0	660	0.11	23.7	0.0785	0.1660
		1200	2.8	168	71.8	14.5	870	0.08	20.1	0.0548	0.1747
		1250	5.3	318	71.7	18.0	1080	0.07	16.2	0.0432	0.1094
		1300	5.3	318	67.9	18.0	1080	0.06	16.2	0.0431	0.1588
WOP-2	2455	1050	1.1	66	74.6	4.5	270	0.28	44.7	0.1951	0.1141
		1150	1.8	108	72.5	11.0	660	0.11	27.5	0.0947	0.1701
		1200	2.8	168	72.0	15.0	900	0.08	19.0	0.0736	0.1574
		1250	3.1	186	72.0	13.0	780	0.09	17.8	0.0522	0.1260
		1300	8.8	528	67.3	24.0	1440	0.05	17.4	0.0294	0.1736
SMA-1	2462	1050	2.5	150	70.6	8.0	480	0.15	25.6	0.1158	0.0778
		1150	4.6	276	70.2	11.0	660	0.11	20.9	0.085	0.0022
		1200	4.6	276	72.0	13.0	780	0.09	17.3	0.0702	0.0458
		1250	5.2	312	68.9	11.5	690	0.10	17.2	0.0847	0.0181
		1300	7.9	474	66.3	19.0	1140	0.06	13.0	0.0446	0.0852
SMA-2	2463	1050	1.8	108	73.5	5.5	330	0.22	24.6	0.1671	0.0509
		1150	3.8	228	69.0	10.0	600	0.12	18.2	0.0958	0.0338
		1200	4.0	240	70.3	10.0	600	0.12	17.8	0.0921	0.0244
		1250	5.0	300	69.9	10.5	630	0.11	15.8	0.0938	-0.0337
		1300	6.0	360	69.5	17.0	1020	0.07	15.3	0.0472	0.1049
EUR-LS	2737	1050	0.3	18	80.5	4.0	240	0.34	115.5	Nd	Nd
		1150	3.3	198	77.8	77.0	4620	0.02	50.3	Nd	Nd
		1200	7.3	439	74.7	25.0	1500	0.05	35.9	Nd	Nd
		1250	10.6	638	71.7	44.5	2670	0.03	18.2	Nd	Nd
EUR-HS	2738	1050	0.5	31	73.3	4.0	240	0.31	80.6	Nd	Nd
		1150	7.3	437	65.8	22.5	1350	0.05	28.1	Nd	Nd
		1200	10.1	604	65.4	26.0	1560	0.04	28.4	Nd	Nd
		1250	14.9	894	63.0	39.0	2340	0.03	18.5	Nd	Nd
VER	2828	1050	1.6	96	74.0	5.2	310	0.24	70.0	Nd	Nd
		1150	1.7	102	71.8	4.5	270	0.27	27.4	Nd	Nd
		1250	3.5	210	70.0	8.5	510	0.14	23.8	Nd	Nd
CAR	2829	1050	0.4	26	81.2	12.5	750	0.11	92.4	Nd	Nd
		1150	2.3	139	75.0	27.5	1650	0.05	47.6	Nd	Nd
		1250	10.8	648	64.7	34.5	2070	0.03	27.8	Nd	Nd
PRO	2943	1050	0.6	39	78.8	5.0	300	0.26	70.9	Nd	Nd
		1150	1.1	69	75.8	12.5	750	0.10	45.3	Nd	Nd
		1250	1.6	98	78.6	8.5	510	0.15	27.9	Nd	Nd

High-grade burnt lime products: impact of calcination kinetics on slaking reactivity; sticking tendency and blocks formation at HT (1300°C)

Table 3.51 (continued)

Sample	Code	T	t ₆₀	t ₆₀	T _{max}	t _{max}	t _{max}	Heating Rate (HR)	Max HR	Slope	Y-intercept
		(°C)	(min)	(s)	(°C)	(min)	(s)	(°C/s)	(°C/s)	Nd	Nd
ZAN	2830	1050	0.33	20	55.3	1.2	70	0.79	126.2	Nd	Nd
		1150	0.48	29	55.7	2.2	130	0.43	98.9	Nd	Nd
		1250	0.52	31	55.9	2	120	0.47	69.9	Nd	Nd
PED-1	2776	1050	0.83	50	54.8	3	180	0.3	61.3	Nd	Nd
		1150	0.69	42	55.8	3.4	205	0.27	52.2	Nd	Nd
		1250	2.79	168	55.3	7	420	0.13	49.7	Nd	Nd
PED-2	2777	1050	0.8	48	55.1	3	180	0.31	65.3	Nd	Nd
		1150	1.09	66	54.9	3.7	220	0.25	52.2	Nd	Nd
		1250	1.09	65	55.8	5.2	310	0.18	49.7	Nd	Nd
UNI-1	2662-A	1050	0.45	27	55.0	1.8	110	0.5	90.1	Nd	Nd
		1150	1.17	70	54.4	5.5	330	0.16	79.6	Nd	Nd
		1250	0.66	39	55.4	4.8	290	0.19	67.9	Nd	Nd
UNI-1	2662-B	1050	0.61	36	54.6	4.7	280	0.19	88.1	Nd	Nd
		1150	0.68	41	54.6	3.2	190	0.29	68.6	Nd	Nd
		1250	2.11	126	53.6	6.8	407	0.13	62.6	Nd	Nd
MME	2112	1050	0.42	25	56.8	2	120	0.47	71.2	Nd	Nd
		1150	0.85	51	56.4	3	180	0.31	51.3	Nd	Nd
		1250	1.29	78	56.2	3.5	210	0.27	26.9	Nd	Nd

3.5.5 Discussion

- *Calcination kinetics and heating behavior by different techniques*

Thermal analyses and kinetic parameters extrapolated by TG/DTA Netzsch analyzer on whole-rock powders (90 mg) were compared with ones from TG/DTG Nabertherm muffle furnace on massive (100 g) granulated (<3.35 mm) samples. Preliminary results on the same sub-set of samples pointed out similar trends, further attesting the validity of the method developed by Vola et al. (2018). Especially, the sample PSP presented the highest calcination duration time, while the sample IDW presented the lowest for both the analyses. At the same time sample SMA resulted to be impure, because the lower LOI with respect to the other samples (Fig.3.41a-b). Further analyses on remaining samples are working in progress on drafting this dissertation.

Moreover decomposition rate was investigated by means of in-situ HT-XRD. Unfortunately, kinetics observed with this technique didn't exactly correspond to those determined by thermal analysis. This is probably related to the different experimental conditions (especially to the different burning T). A comprehensive statistical analysis of different data sets is currently working in progress.

- *Sintering or overburning tendency at high T*

Slaking tests confirmed that burning temperature is one of the most important parameters affecting the reactivity, as already reported in the literature (Boynton, 1982; Oates, 1998). Effectively, an inverse correlation between the slaking reactivity, reported as t_{60}/t_{50} (s), maximum Heating Rate ($^{\circ}\text{C}/\text{min}$), and maximum slaking temperature (T_{max}), and the burning temperature was observed (Fig.3.46, Fig.3.47, and Fig.3.48). In particular, higher is the slope higher is the sintering or overburning tendency (Vola et al., 2017a). Considering the same experimental apparatus and conditions, quite similar particle-size distribution and mass sample, main differences in slaking rates must be related to intrinsic or geological features of carbonate rocks, and derived physical properties of burnt limes. Preliminary considerations on geological parameters allowed grouping calcium carbonates, as follow:

- 1) The group A1 is represented by samples PSP and CAR, presenting the highest reactivity at 1050 $^{\circ}\text{C}$, and a quite low reactivity at 1250 $^{\circ}\text{C}$. These samples pointed out the highest sintering or overburning tendency. Accordingly, they also presented the highest slope in Fig.3.46a. Both samples are high-grade calcium carbonates, constituted by large (mm-sized) sparry-calcite, thus pointed out low values of the micrite-to-sparite ratio (MSR). On the one side PSP is a grain-supported, mainly coralline, limestone, presenting primary intraclastic porosity filled in by equant mosaic cement. On the other CAR is a pure calcitic medium-up to coarse sized marble with typical granoblastic microstructure. The main difference between the two samples is represented by the accessible porosity, which is large for PSP (6.8-7.4%), and quite low for CAR (0.65%). The sample PSP is from an Eocenic deposit (approx. 50 Ma) located in Karawang, Java, Indonesia, but detailed geological information is not available. Conversely, CAR is from the very-well know Lower Liassic (approx. 200 Ma) deposit of the Apuane Metamorphic Complex, Marble s.s. Fm., Carrara, Italy (Carmignani et al., 2005).
- 2) The group B1 is represented by samples PRO and VER, presenting medium-high reactivity at 1050 $^{\circ}\text{C}$, as well as, at 1250 $^{\circ}\text{C}$. These samples pointed out the lowest sintering or overburning tendency. Accordingly, they also presented the lowest slope in Fig.3.46a. Both these samples are mainly constituted by microcrystalline calcite or micrite, but PRO is a high-grade limestone, while VER is slightly impure or marly limestone (the insoluble residue is 2.0%). Especially, PRO is constituted by a peloidal

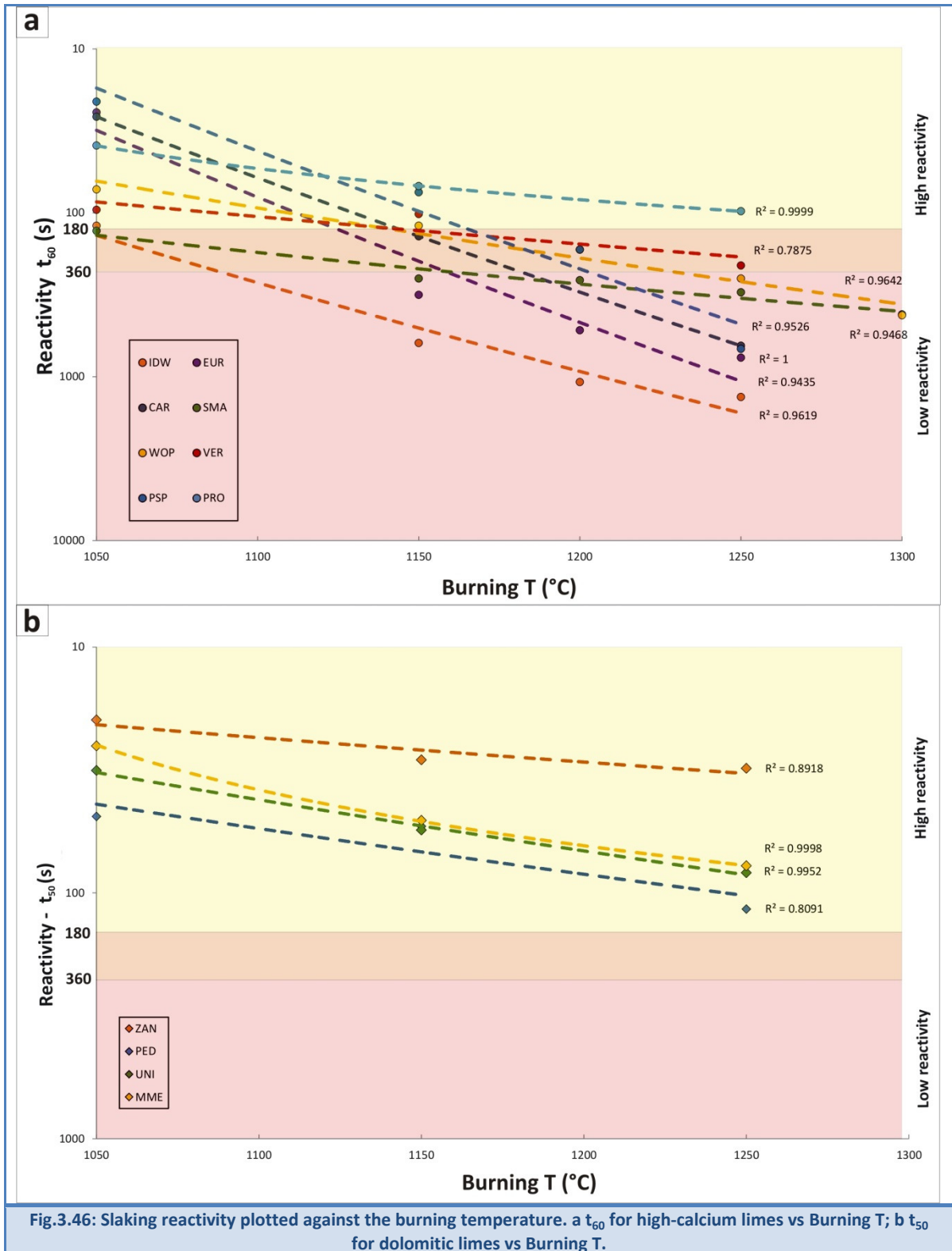
grainstone, with rare large (mm-sized) brachiopods and scarce mosaic cement, while VER is a pelagic wackestone/packstone, enriched in planktonic faunas, presenting some terrigenous minerals, essentially quartz and clay minerals scattered within the micritic matrix. Both samples present a high MSR, ranging between 4.7 (PRO) up to 5.1 (VER). No geological information is available yet for sample PRO. Conversely, VER is from the Middle-Upper Jurassic (160 Ma) Rosso Ammonitico Fm. of the Southern Alps (Martire et al., 2006).

- 3) The group A2 is represented by samples EUR and IDW, presenting medium-low reactivity at 1050 °C, and very low reactivity at 1250 °C. These samples pointed out high sintering or overburning tendency, as well as, the group A1, but the average reactivity is lower. Accordingly, they also presented high slope values in Fig.3.46a. The sample IDW is constituted by microbial boundstone with clotted peloidal micrite associated with large fenestrate porosity filled in by poikilotopic calcite cement. Conversely, the sample EUR is constituted by large (mm-sized) micritic intra-clasts, i.e. flat pebble rudstone, associated with coated grain peloidal grainstone to packstone and subordinated wackestone. Samples are both characterized by long and pervasive diagenetic history, considering they are the oldest materials considered in this study. The first (IDW) is from a Neoproterozoic deposit (2520 Ma) located in Griqualand West, South Africa (Vola et al. 2017a); while the second (EUR) pertains to the Cambrian-Ordovician (approx. 485 Ma) Ulken-Aktau deposit, from Zhanatas, Kazakhstan (Vola et al., 2017b).
- 4) The group B2 is represented by samples WOP and SMA, presenting medium reactivity at 1050 °C, and medium low reactivity at 1250 °C. These samples pointed out low sintering or overburning tendency, as well as, the group B1, but the average reactivity is lower. Accordingly, they also presented a low slope in Fig.3.46a. Both these samples were also studied at 1300 °C to verify low sintering trends. These samples presented quite different textures, because the first (WOP) is mainly constituted by microcrystalline calcite, or mudstone/wackestone, with rare planktonic shells (ostracods), and several tensional fractures filled in by large mosaic cement. Conversely, SMA is mostly constituted by kerogen-rich massive stromatopoidal lithofacies, i.e. floatstone/rudstone with large mm-sized bioclasts, including conodonts, echinoderms, rugose corals, bivalves and brachiopods, which present shells constituted by clear sparry-calcite. Moreover, mosaic cement filled in intra-bioclastic porosity. Indeed the MSR value is very high for WOP (19.9), while is quite

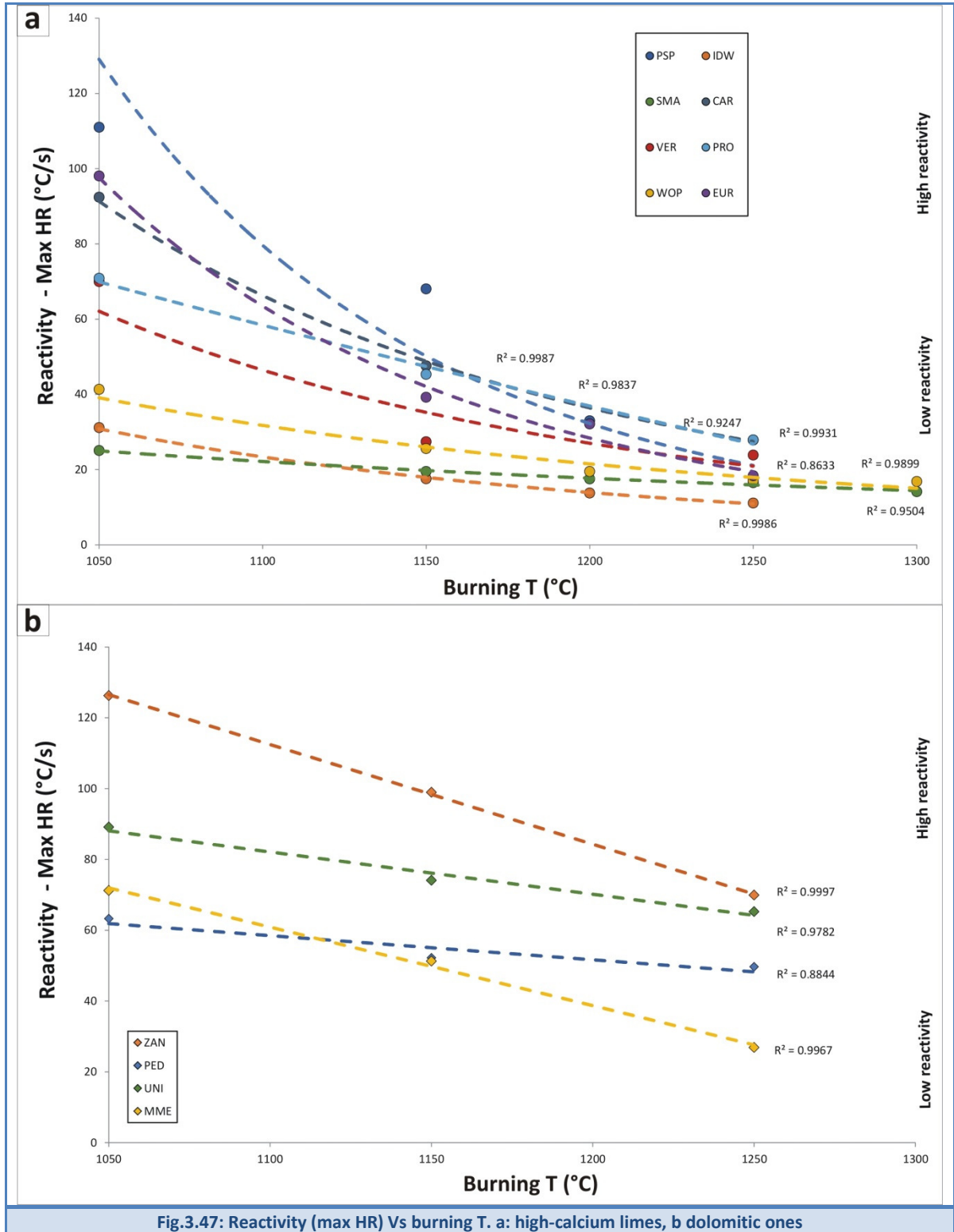
low for SMA (4.1). Both these samples present some impurity content, because their insoluble residue (IR) is 1.8% for WOP, and 3.2% for SMA. Sample WOP is from upper Triassic (Norian-Raethian age, 205 Ma) Dachstein limestone pertaining to the Northern Calcareous Alps (Krystyn et al., 2009); while sample SMA is from Lower Wenlock (Silurian) Fm. (430 Ma) stratigraphic succession of the Gotland island, Sweden (Jeppsson, 2008).

As concerns dolomites, two groups can be distinguished with regards to plots reported in Fig.3.46b, Fig.3.47b, and Fig.3.48b. Both groups are constituted by samples presenting high ΔT 30 °C or t_{50} reactivity, either at 1050 °C or at 1250 °C. This means that investigated Dolomitic limes are lesser extensively affected by sintering or overburning tendency than high-calcium quicklimes. This may be also related to the prevailing low sticking tendency observed on dolomitic limes at high burning temperature (1300 °C) by the so-called Cimprogetti's overburning test (OT) method as reported in Vola et al. (under submission). In particular the first group, is just represented by the sample ZAN, which maintains very high reactivity either at 1050 °C or at 1250 °C, despite the fraction adopted for burning tests (5-15 mm) is finer than fractions adopted for burning the most of the other samples (from 20-40 up to 45-70 mm), with the only exception of sample MME (15-37 mm). The second group includes 3 dolomitic limes, i.e. samples PED, UNI, and MME, presenting a more perceptible lowering of the slaking reactivity at high temperature, as shown in Fig.3.46b, Fig.3.47b. It's significant to point out that the lowering of ΔT 30 °C, or t_{50} (min), and the Maximum Heating Rate (°C/min) are not always associated to the lowering of the maximum T_{max} , as shown in Fig.3.48b. Effectively, samples ZAN and PED pointed out inverse correlation trends, showing higher T_{max} in lime samples burnt at 1150 °C and 1250 °C than in samples burnt at 1050 °C.

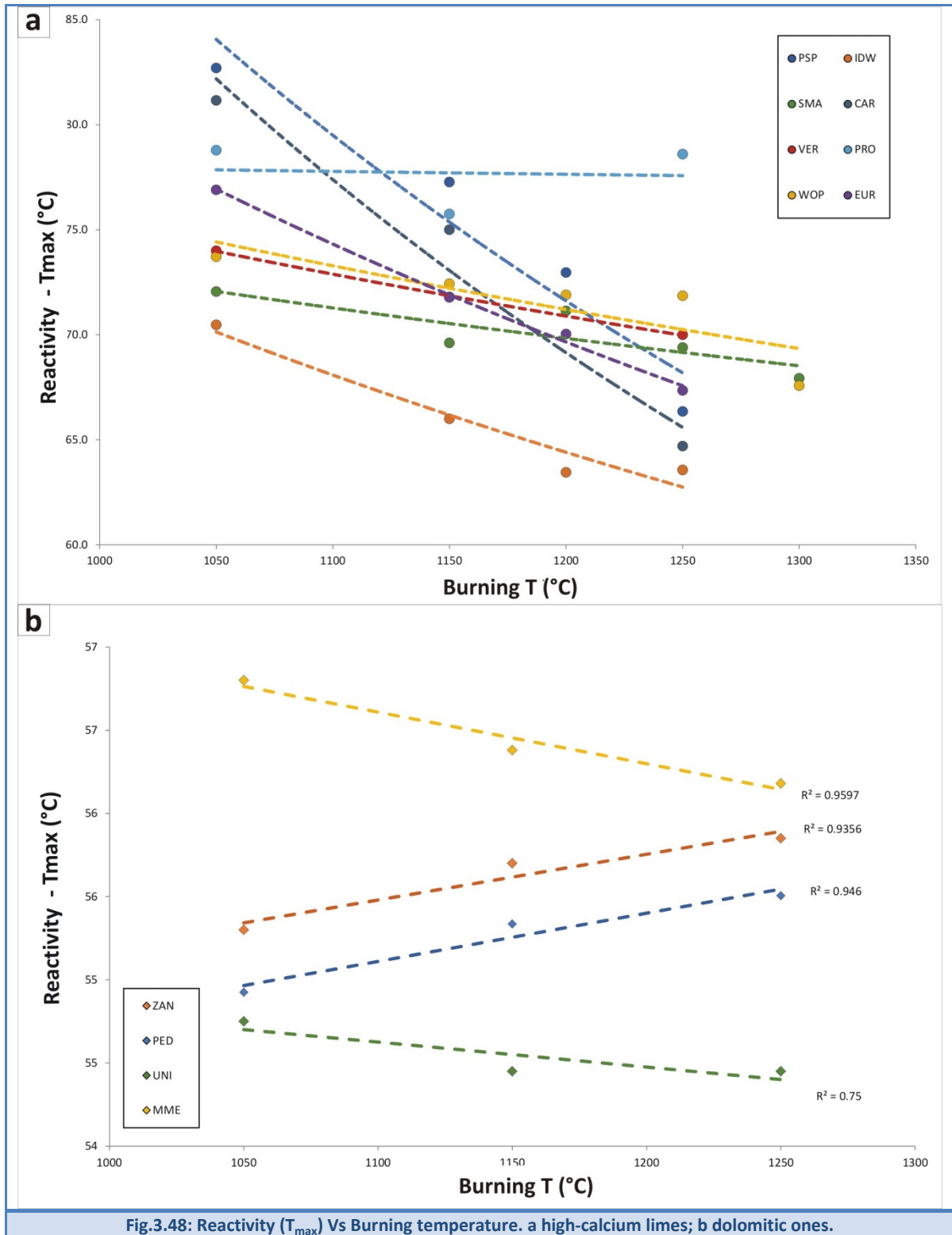
Indeed, the statistical analysis by the regression method was performed to confirm these preliminary observations, and possibly find correlations between different data-sets. The following parameters of burnt limes were plotted against the slaking reactivity: hydration kinetics parameters, CaO lattice parameters, crystallite-size, microstrain, BET SSA and real density. Finally, it was considered the particle-size distribution (PSD) of the quicklime and the slaking water composition.



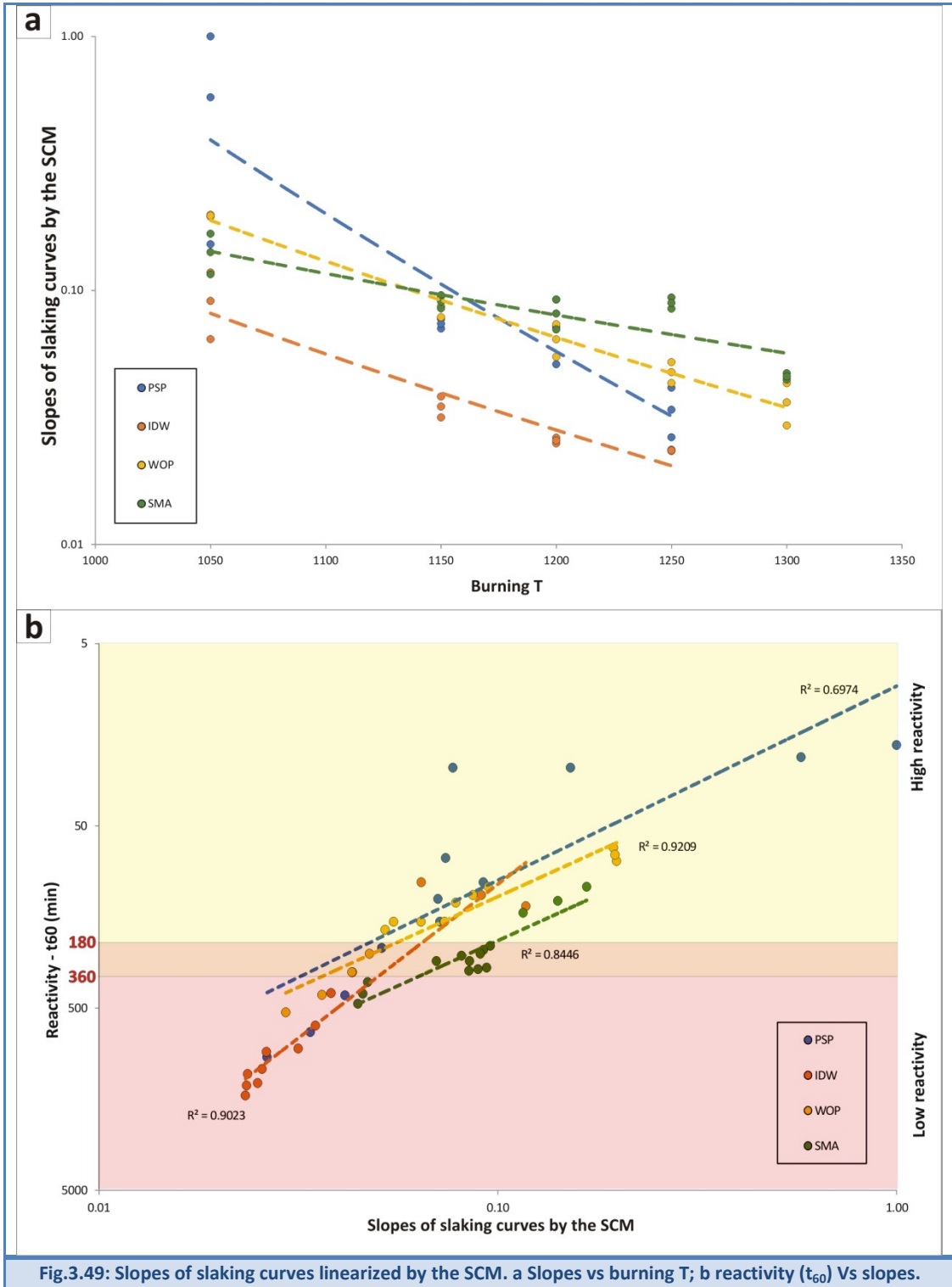
High-grade burnt lime products: impact of calcination kinetics on slaking reactivity; sticking tendency and blocks formation at HT (1300 °C)



High-grade burnt lime products: impact of calcination kinetics on slaking reactivity; sticking tendency and blocks formation at HT (1300°C)



High-grade burnt lime products: impact of calcination kinetics on slaking reactivity; sticking tendency and blocks formation at HT (1300 °C)



High-grade burnt lime products: impact of calcination kinetics on slaking reactivity; sticking tendency and blocks formation at HT (1300°C)

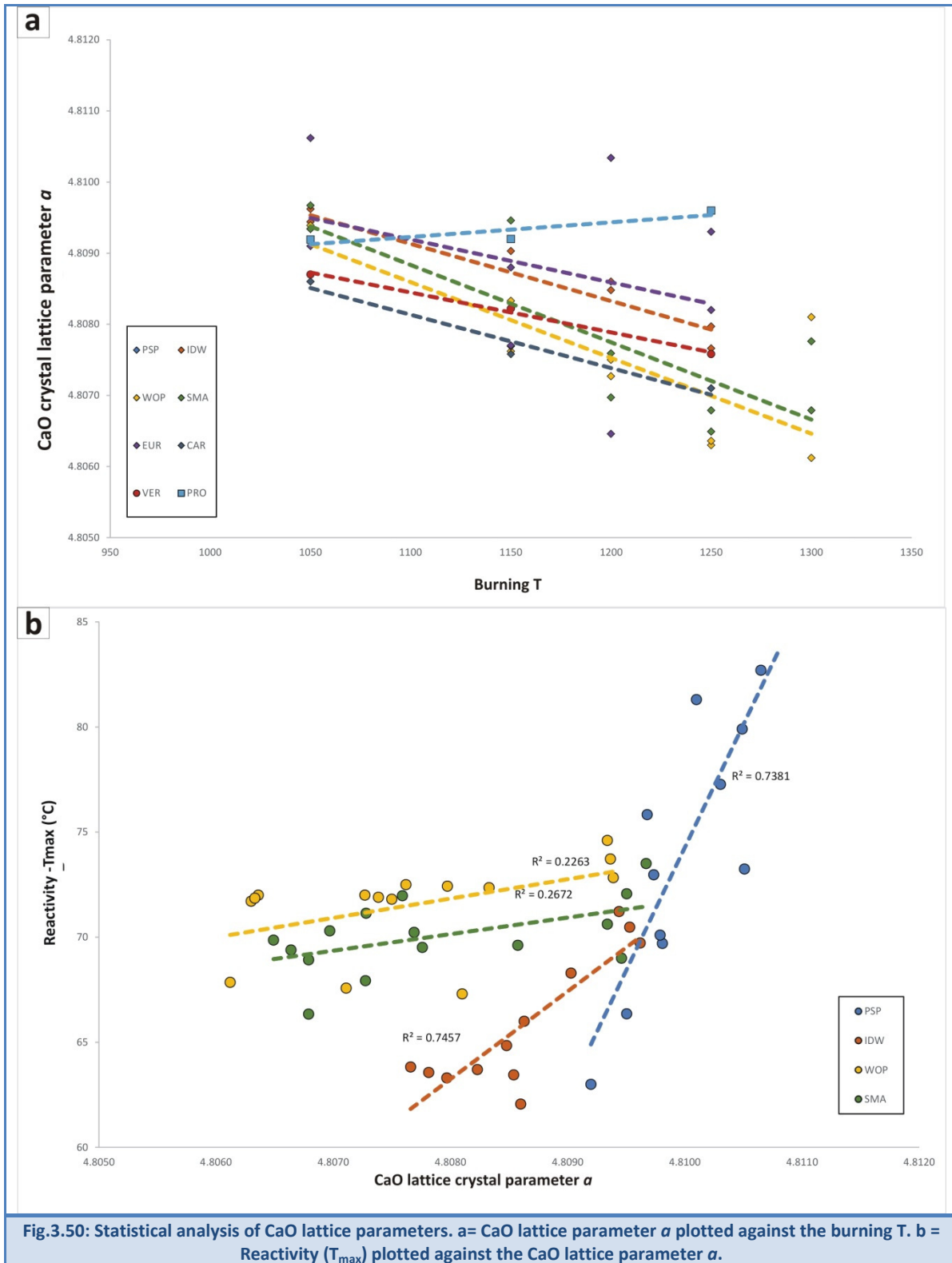


Fig.3.50: Statistical analysis of CaO lattice parameters. a= CaO lattice parameter a plotted against the burning T. b = Reactivity (T_{max}) plotted against the CaO lattice parameter a .

High-grade burnt lime products: impact of calcination kinetics on slaking reactivity; sticking tendency and blocks formation at HT (1300 °C)

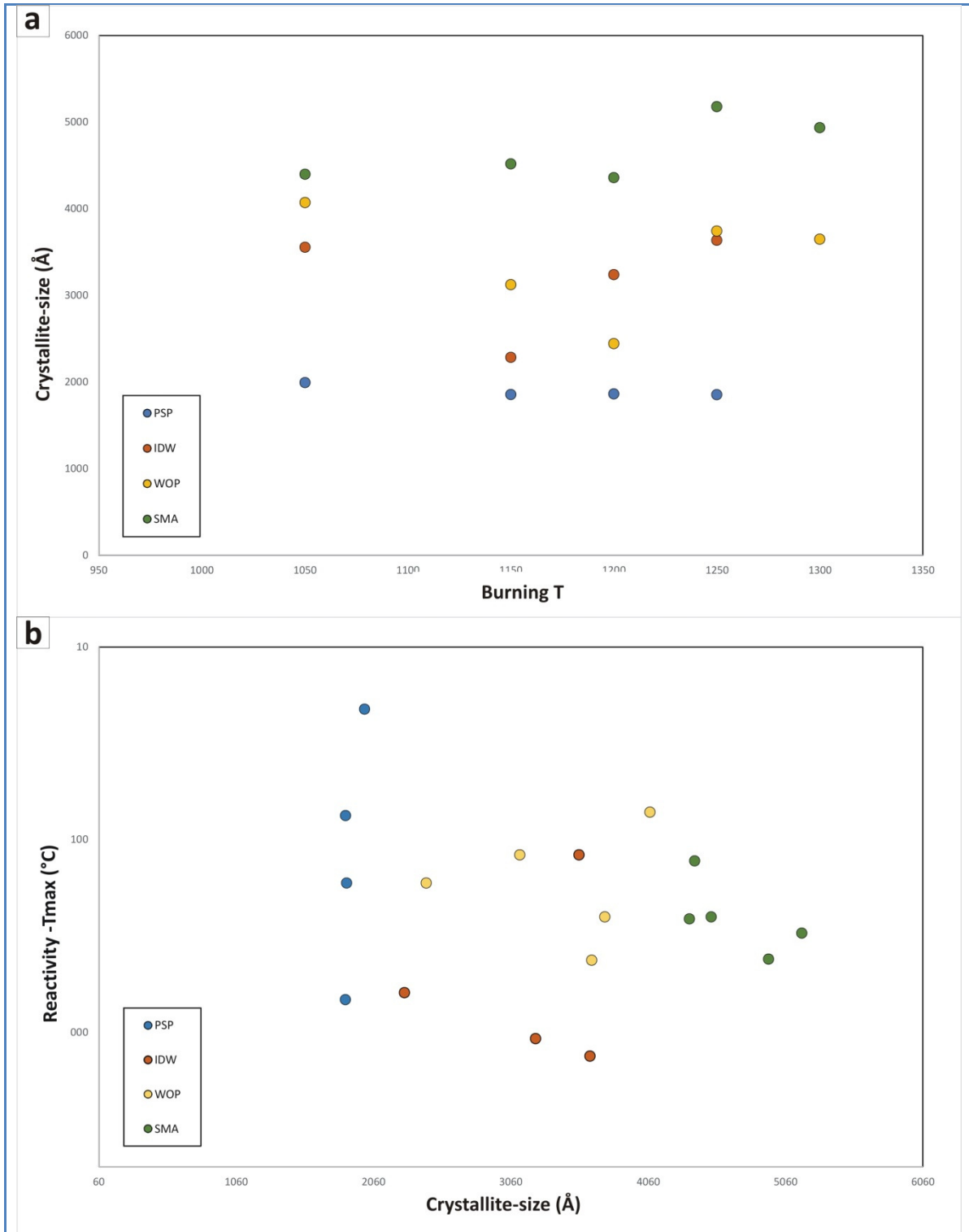


Fig.3.51: Statistical analysis of CaO crystallite-size. a= CaO crystallite-size plotted against the burning T; b= slaking reactivity (T_{max}) plotted against the CaO crystallite-size.

High-grade burnt lime products: impact of calcination kinetics on slaking reactivity; sticking tendency and blocks formation at HT (1300°C)

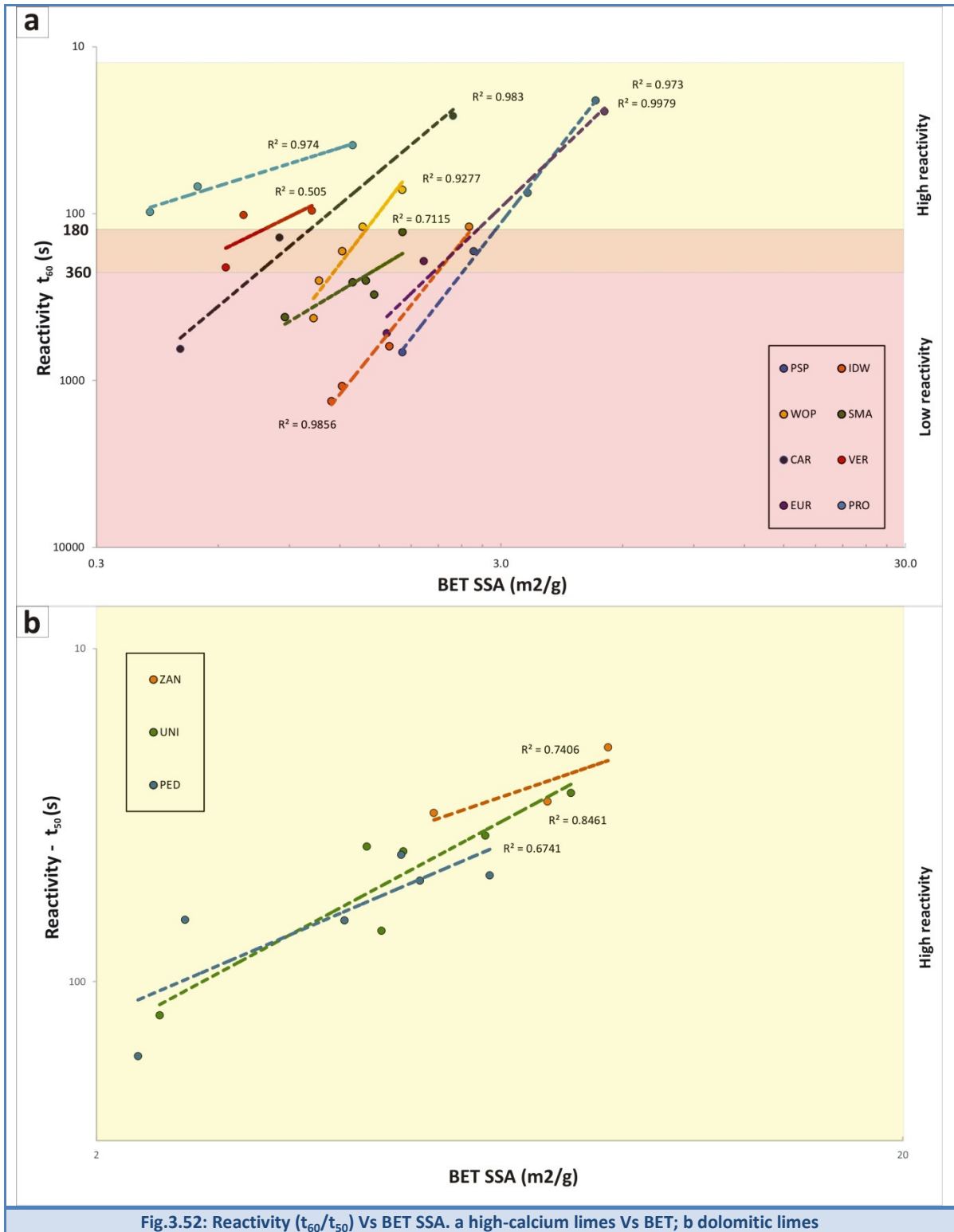
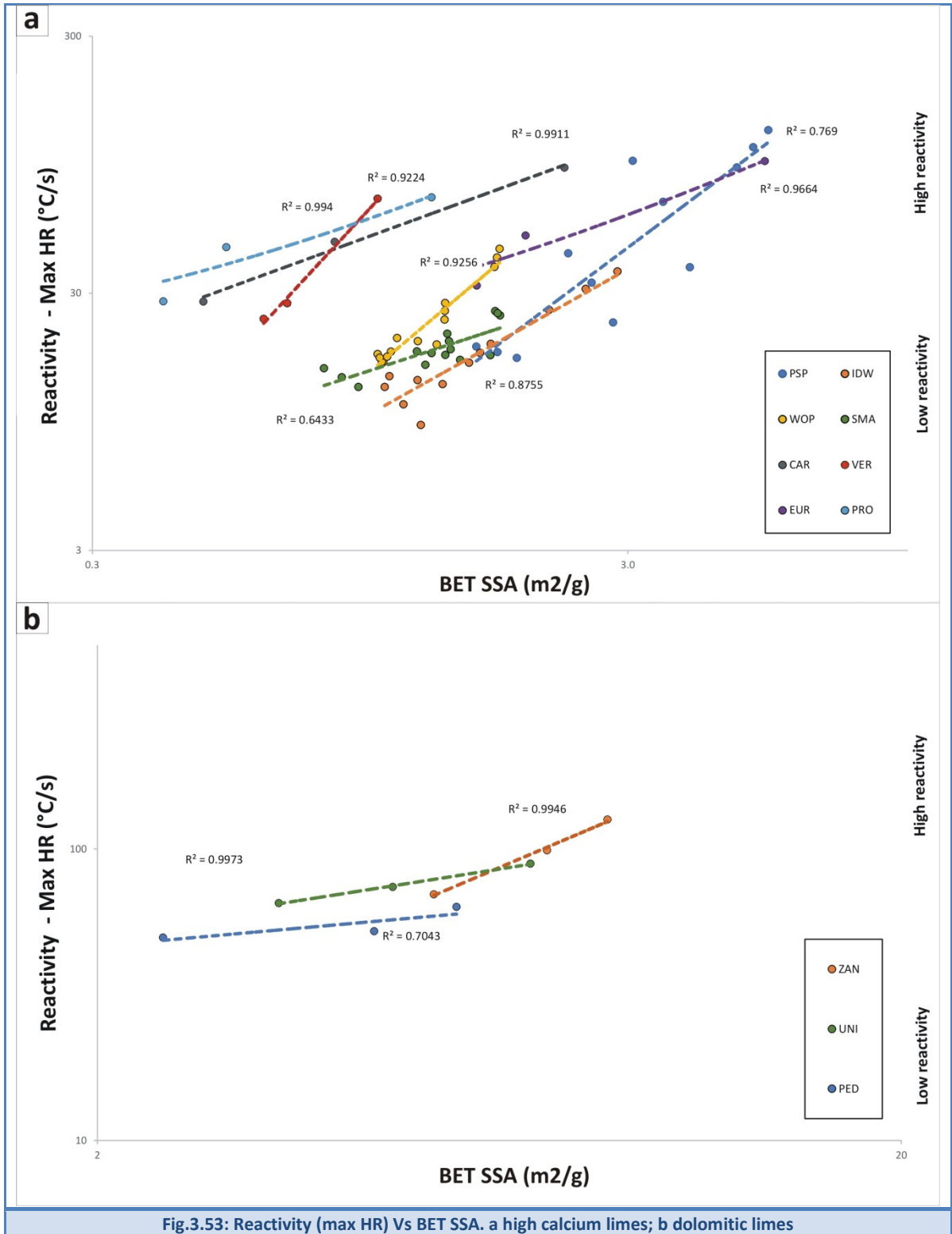


Fig.3.52: Reactivity (t_{60}/t_{50}) Vs BET SSA. a high-calcium limes Vs BET; b dolomitic limes



High-grade burnt lime products: impact of calcination kinetics on slaking reactivity; sticking tendency and blocks formation at HT (1300°C)

- *Impact of hydration kinetics*

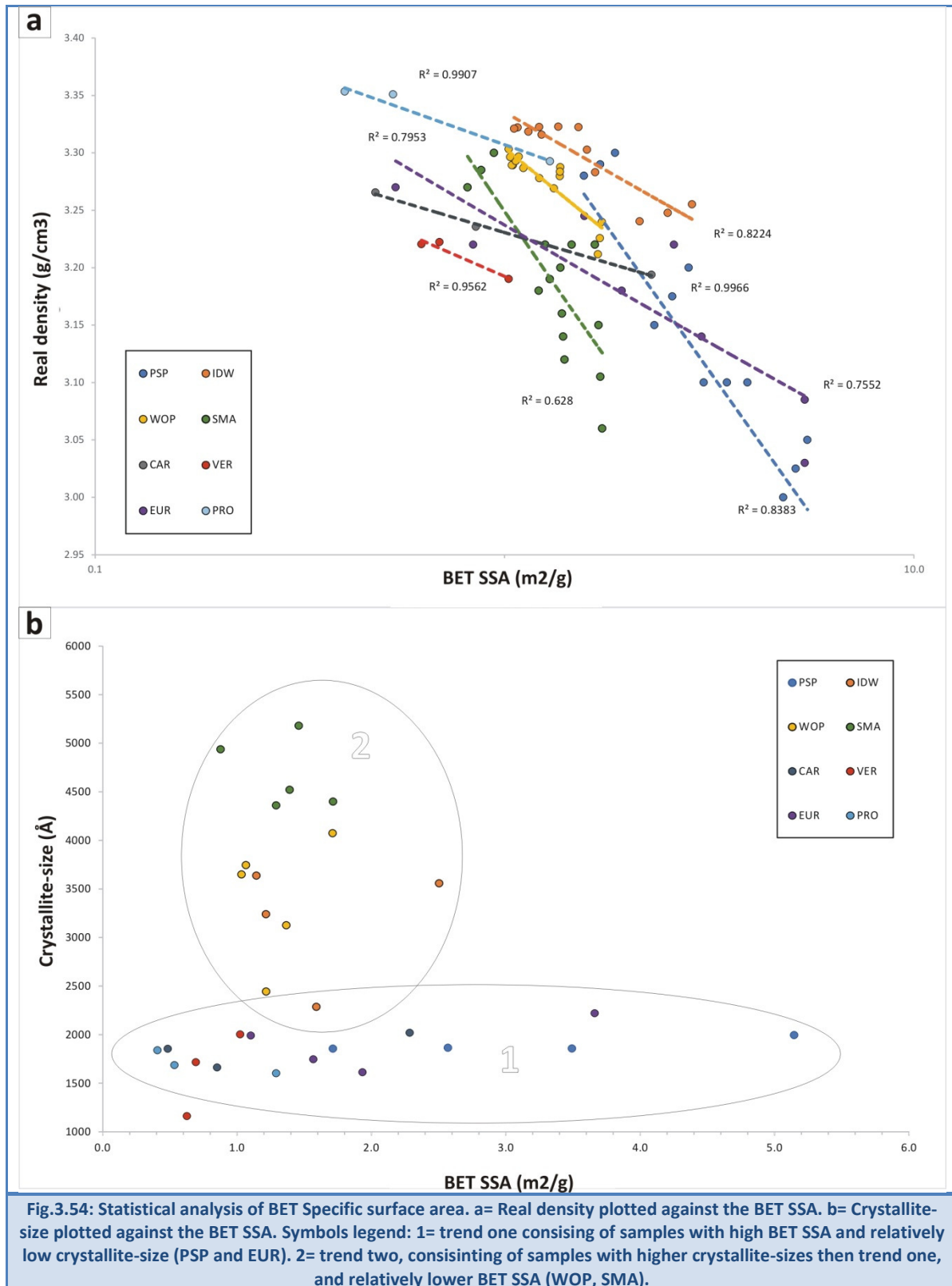
The linearization of the slaking curves by the shrinking core model (SCM) allowed extrapolating angular coefficients or slopes and intercept values. These data were plotted against the burning temperatures and the slaking reactivity, i.e. the ΔT 40 °C, or t_{60} (min) in Fig.3.44 and Fig.3.45. Clearly, higher is the slope, higher is the reactivity. In particular, sample PSP pointed out the highest slaking reactivity, and the highest angular coefficients. Conversely, sample IDW pointed out the lowest slaking reactivity, and lowest angular coefficients. The slope of the linearized slaking curve has a physical meaning, according to the mathematical equation adopted, i.e. the model I, which refers to spherical particles under reaction control (Liddell, 2005).

- *Impact of CaO crystallography, BET SSA and real density*

The main significant crystallographic parameters of the lime samples burnt at different T were plotted against the burning temperatures and the slaking reactivity in Fig.3.50a-b and Fig.3.51a-b. In particular the Fig.3.50a reports the statistical analysis of CaO lattice parameter a , against the burning T, while the Fig.3.50b reports the slaking reactivity (T_{max}) against the CaO lattice parameter a . Results confirmed that CaO crystal lattice parameters are inversely correlated with the temperature, with the only exception of sample PRO, attesting the array of atoms in the crystal structure becomes more regular, defects present are reduced, and the lattices distortion also decreases increasing the burning temperatures. This effect is already reported in the literature (Shi and Li, 2002), and can be also explained by the doping of MgO within CaO cell structure, forming solid solutions. The crystallite-size analysis against the burning temperature is reported in Fig.3.51a; while in Fig.3.51b is plotted the slaking reactivity, i.e. the t_{60} , against the crystallite-size analysis. No clear correlation between crystallite-size and slaking reactivity was observed. Finally, the CaO microstrain analysis against the burning temperature, and the reactivity was considered, as well. Again no correlation was observed between parameters.

Conversely, experiments confirmed that BET specific surface area of quicklime strongly affects the slaking reactivity, as already reported in the literature by several authors (Boynton, 1982, Oates, 1998). Especially, the slaking reactivity, i.e. the t_{60-t50} and the maximum HR, are plotted against the BET specific surface area for both high-calcium and dolomitic limes in Fig.3.53a-b. Sample trends are consistent with expectations, but absolute

values of BET SSA are sometimes surprising. As a matter of fact, the sample PRO, showing the highest reactivity at 1150-1250 °C, presented the lowest BET SSA at the same temperatures, as well. Unexpected results are already reported in the literature (Commandré et al., 2007), and they remained substantially unexplained issues. Moreover the inverse correlation between the BET SSA and the real density by gas pycnometry is plotted in Fig.3.54a. This correlation is consistent with expectations, and is confirmed by previous studies (e.g. Vola et al., 2018). Finally Fig.3.54b reported the CaO crystallite-size analysis, performed on a subset of 4 representative samples, against the BET SSA. This plot allowed pointing out some interesting trends, which are going to be investigated more into details in the early future. Especially, the specific trend (trend one) of highly reactive sample PSP is to be considered. This sample is characterized by high BET SSA, and relatively low crystallite-size values. Standard trends provide crystalline coarsening upon the temperature rise, thus this result sounds rather unexpected. It can be probably explained by a local CO₂ overpressure at high calcination temperature, leading to a partial recarbonation. This preliminary hypothesis is confirmed by the presence of traces of calcite (0.5 %) within the lime samples burnt at 1200-1250 °C (see Tab.3.49). Thus the recarbonation process could acts as inhibitor factor of the slaking reactivity. Moreover, different trend, i.e. trend 2, can be observed for samples WOP and SMA, presenting higher crystallite-sizes and relatively lower BET SSA, than sample PSP. Indeed this second trend is characterized by higher crystalline coarsening, associated with recrystallization and densification at high temperatures. However, the presence of magnesium oxide and/or other silica-alumina impurities, especially in sample SMA, formed a boundary layer between the CaO crystallites, limiting the crystal growth. Therefore these compounds acted as sintering inhibitors with positive relapses on the slaking reactivity, as already reported in the literature (Hogewoning et al., 2008). Fianlly, the sample IDW is chacterized by low BET SSA and intermedite crystallite-size with respect to the other samples. This sample is characterized by the lowest slaking reactivity, and unusual, drastically pronounced sintering tendency between 1150-1250 °C, as already reported by Vola et al. (2017a).



- *Impact of particle size distribution and composition of slaking water*

The impact of these parameters was investigated in order to prevent possible errors occurring on slaking laboratory tests. Actually, possible relapses in industrial applications can be considered too. Experiments pointed out either the particle size distribution (PSD) of the quicklime, or the slaking water composition, strongly affects the lime reactivity. Concerning the PSD, two fractions were initially adopted: < 2 mm grinded quicklime by jaw crusher, and pulverized quicklime from the Herzog annular ring mill. Subsequently, some slaking tests were also performed using powders as received from Herzog mill, and ultrafine powders sieved <90 μm (Fig.3.55). Slaking tests pointed out that finer is the quicklime PSD, higher is the reactivity. The strategy of increasing the fineness can be usefully adopted to raise the reactivity, especially for samples presenting very low BET SSA, e.g. IDW samples. Moreover it's interesting to highlight that sometimes the final slaking temperature resulted to be higher using coarser PSD. In such case the Total Active Slaking Time (TAST) was significantly longer (e.g. slaking test in Fig.3.55c). This result will be investigated more into details in the early future.

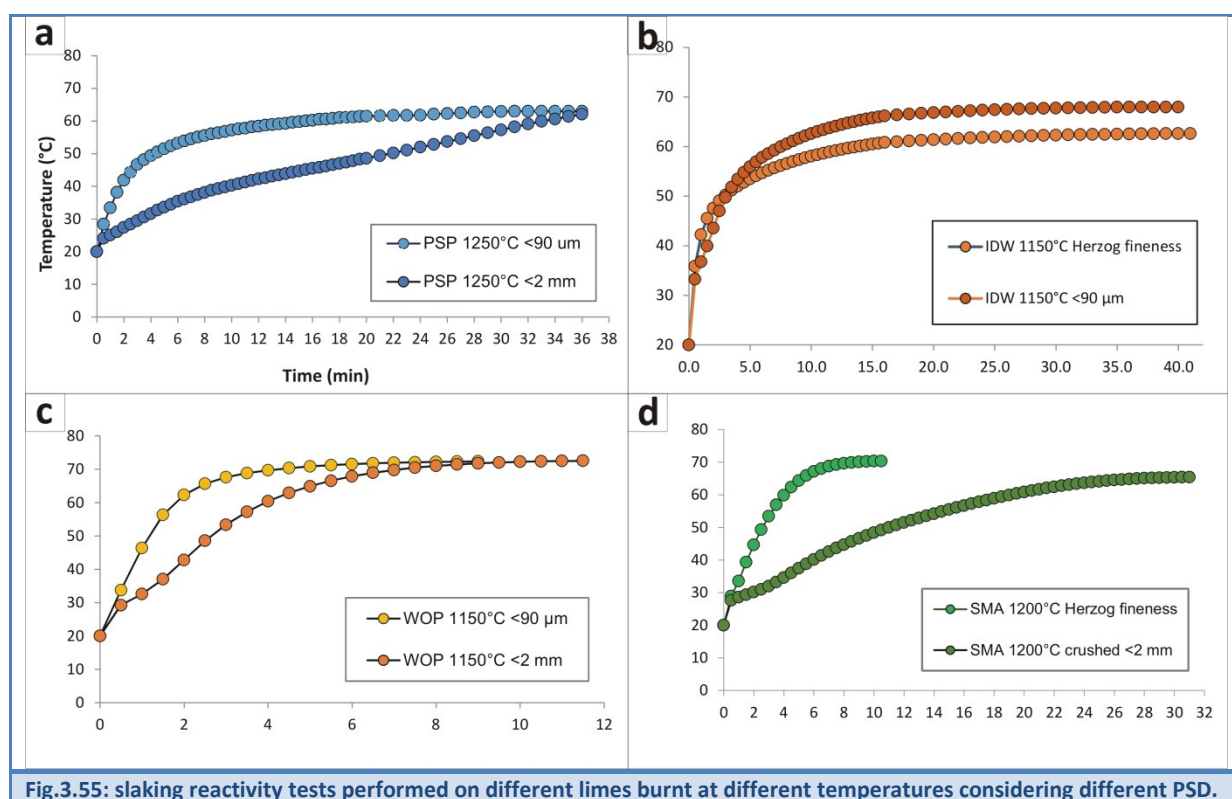


Fig.3.55: slaking reactivity tests performed on different limes burnt at different temperatures considering different PSD.

As concerns the composition of slaking water, a couple of tests were performed using deionized, mineral drinking, and potable water from the water network. Experimental results pointed out a significantly lower reactivity for tests performed using mineral drinking, and potable water from the network than the deionized one. Therefore the use of deionized water (at 20 or 25 °C according to the method adopted) is warmly recommended for laboratory slaking tests. This is necessary in order to avoid possible underestimation of reactivity on preliminary evaluation of new materials for designing, commissioning, or defining guaranties of new kilns and hydration plants. The use of specific substances, i.e. chlorides, is demonstrated to accelerate the slaking reaction, by increasing the dissolution kinetics of the lime into the water (Potgieter et al., 2003; Gallala et al., 2008). From a practical prospecting this indicates that poor hydration plants performance can possibly be rectified by the addition of common salt to the hydration mixture (Potgieter et al., 2003). This can be particularly useful when the lime reactivity is very low, e.g. in the specific South African case-study (see Vola et al. 2017a).

3.5.6 Conclusions

This study allowed investigating carbonate rocks burnability and slaking reactivity in the typical temperatures range of a TSR kiln firing solid fuels (1150-1300 °C). Indeed standard aggregate fractions used for feeding industrial shaft kilns were considered for experimental burnability trials in laboratory. A multidisciplinary analytical approach was performed to carry out the characterization of raw materials and burnt products. Thus the statistical analysis of different data sets was carried out in order to verify possible correlations between different parameters.

A great effort was dedicated to define the kinetics of calcination. TG-DTG analyses from different devices were compared. Preliminary results, confirmed similar trends in calcination rates of a subset of representative samples, according to the method described by Vola et al. (2018). Subsequently, calcination rates from thermal analyses were compared with ones from the in-situ HT-XRD analysis performed at the ESRF (Grenoble). Unfortunately, some of the kinetics observed with this technique didn't match with ones from thermal analyses. This is probably related to the different experimental conditions, including different sample masses, heating rates, and burning temperature. A comprehensive statistical analysis of different data sets is currently working in progress. Moreover some specific tests on a

couple of critical samples, i.e. WOP and PSP, are going to be performed as soon as the beamtime at ESRF will be available again.

The relationship between textural/microstructural features and the slaking reactivity still remain somewhat unclear, and should be investigated more into details. The XRD analysis by the FP method on calcite and dolomite has to be performed in order to verify possible effects on slaking reactivity. Effectively, a recent study performed on the impact of petrography and calcite microstructure on ordinary Portland cement clinker burnability demonstrated how the hatrurite and the larnite are controlled by calcite microstrain at $T < 1300$ °C, thus higher the microstrain, the better the burnability (Galimberti et al., 2016).

The linearization of the lime slaking curves by the shrinking core model (SCM) allowed extrapolating angular coefficients, or slopes, and intercept values. These parameters have a physical meaning because the SCM is a chemical-controlled equation, thus it can be usefully adopted for a preliminary burnability classification of analyzed samples.

The impact of several chemical-physical and mineralogical-crystallographic parameters of the lime was investigated in order to verify possible correlations with the slaking reactivity. XRD refinements by the Rietveld and the FP methods allowed performing quantitative phase, crystallite-size, microstrain analyses and determination of CaO lattices parameters at different burning temperatures. A systematic decrease of CaO cell parameter (a) was observed by increasing the temperature. This effect, already documented in the literature (Shi and Li, 2002), can be essentially explained by the doping of MgO within CaO crystalline structure, forming solid solutions. Neither CaO crystallite-size, nor CaO microstrain pointed out clear correlations with the burning temperature and the reactivity, but further investigations are still working in process.

Conversely, results pointed out that BET SSA strongly affects the slaking reactivity, i.e. higher the BET, higher the reactivity. This trend is confirmed for each single sample, but this law is not valid at all, as shown by the comparison of different samples. Effectively, unexpected results still remain unexplained issue. However, the BET SSA pointed out an inverse correlation with the real density. Moreover, interesting trends can be observed by the statistical analysis of BET SSA against the crystallite-size. Especially, one of the most reactive samples, PSP, pointed out high BET values and relatively low crystallite-sizes. This sample showed significant lowering of the slaking reactivity by increasing the burning temperature, thus was characterized by high sintering or overburning tendency. This was

probably related to the recarbonation process due to a local CO₂ overpressure at high calcination temperature. This was confirmed by the presence of traces of calcite on samples of PSP-2 burnt at 1200-1250 °C (see Tab.3.49). Different trends can be observed for samples WOP and SMA, presenting higher crystallite-sizes and relatively lower BET SSA, than sample PSP. The presence of magnesium oxide and/or other silica-alumina impurities, especially in sample SMA, limited the lime crystal growth at high burning temperatures, acting as sintering inhibitors with positive relapses on the slaking reactivity, according to the literature (Hogewoning et al., 2008).

Finally, quicklime particle size distribution (PSD) and composition of slaking water were examined too. Slaking tests pointed out that finer is the PSD, higher is the reactivity. The strategy of increasing the fineness, by means of harder grinding, can be usefully adopted to raise the reactivity, especially for samples presenting very low BET SSA, e.g. South African (IDW) ones. On the other hand the suitability of this practise must be verified from an industrial point of view. As concerns the composition of the slaking water, experimental results pointed out a significant lowering of the slaking reactivity by using mineral drinking, and potable water from the network with respect to tests performed with deionized water. Therefore the use of deionized water (at 20 or 25 °C according to the adopted method) is warmly recommended for laboratory slaking tests in order to avoid possible underestimation of reactivity on preliminary evaluation of new materials for designing, commissioning, and definition of guaranties for new kilns and hydration plants.

3.6 References

- Akande H.F., Abdulkareem A.S., Kovo A.S., Azeez O.S., and Onifade K.R. (2016) – *Application of factorial analysis for quicklime production from limestone*. Nigerian Journal of Technological Research, 11:2, 16-25, <http://dx.doi.org/10.4314/njtr.v11i2.4>
- Alaabed S., Soltan M.A., Abdelghany O., Amin B.E.M., Tokhi M.E., Khaleel A., Musalim A. (2014) – *United Arab Emirates limestones: impact of petrography on thermal behaviour*. Mineral Petrol, <https://doi.org/10.1007/s00710-014-0329-3>
- Altermann W., and Schopf J.W. (1995) – *Microfossils from the Neoproterozoic Campbell Group, Griqualand West Sequence of the Transvaal Supergroup, and their paleoenvironmental and evolutionary implications*. Precambrian Research, 75, 65-90.
- Altermann W., and Wotherspoon J.Mc.D. (1995) – *The carbonates of the Transvaal and Griqualand West Sequences of the Kaapvaal craton, with special reference to the Lime Acres limestone deposit*. Mineral. Deposita, 30, 124-134, <https://doi.org/10.1007/BF00189341>
- Badenhorst J.J. (1988) – *Limestone and lime*. In: Goldberg I. (ed.) “South Africa's Mineral Industry 1987”, Dept. Mineral and Energy Affairs, Minerals Bureau of South Africa, Johannesburg, 161-163.
- Baumgart W., Dunham A.C., and Amstutz G.C. (Eds.) (1984) – *Process Mineralogy of Ceramic Materials*. Ferdinand Enke Verlag Publishers, Stuttgart, 8-9.
- Baziotis I., Leontakianakos G., Proyer A., Lee H., and Tsimas S. (2011) – *Physico-chemical Properties of Different Carbonate Rocks: Are They Highly Enough to Control Lime Reactivity?* International Journal of Chemistry, <http://dx.doi.org/10.5539/ijc.v3n2p187>
- Bell K. (ed.) (1989) – *Carbonatites: Genesis and Evolution*. London: Unwin Hyman.
- Beruto T.D., Vecchiattini R., and Giordani M. (2002) – *Solid products and rate-limiting step in the thermal half decomposition of natural dolomite in a CO₂ (g) atmosphere*. Thermochemica Acta, 405, 183–194. [https://doi.org/10.1016/S0040-6031\(03\)00190-4](https://doi.org/10.1016/S0040-6031(03)00190-4)
- Beukes N.J. (1980) – *Lithofacies and stratigraphy of the Kuruman and Griquatown iron-formations, northern Cape Province, South Africa*. Trans. Geol. Soc. S. Africa 83, 69–86, https://hdl.handle.net/10520/AJA10120750_1068
- Beukes N.J. (1984) – *Sedimentology of the Kuruman and Griquatown iron-formations, Transvaal Supergroup, Griqualand West, South Africa*. Precambrian Res, 24, 47-84, [https://doi.org/10.1016/0301-9268\(84\)90069-X](https://doi.org/10.1016/0301-9268(84)90069-X)

- Beukes N.J. (1987) – *Facies relations, depositional environments and diagenesis in a major Early Proterozoic stromatolitic carbonate platform to basin sequence, Campbellrand Subgroup, Transvaal Supergroup, Southern Africa*. *Sediment Geol*, 54, 1–46, [https://doi.org/10.1016/0037-0738\(87\)90002-9](https://doi.org/10.1016/0037-0738(87)90002-9)
- Beukes N.J., Klein C., Kaufman A.J., and Hayes J.M. (1990) – *Carbonate petrography, kerogen distribution, and carbon and oxygen isotope variations in an early Proterozoic transition from limestone to iron-formation deposition, Transvaal Supergroup, South Africa*. *Econ Geol*, 85, 663–689, <https://doi.org/10.2113/gsecongeo.85.4.663>
- Bonazzi A., Salvioli Mariani E., and Vernia L. (1984). *Tecniche di determinazione dell'indice di cristallinità dell'illite in campioni di argilla*. *Mineralogica et Petrographica Acta*, 28, 89-99.
- Bonazzi A. (1987) – *Procedure di determinazione e attendibilità dell'indice di cristallinità dell'illite*. In: Ferretti O., and Maffei P. (Eds.) “Procedure di analisi dei materiali argillosi”, Proc. ENEA workshop, 1-2 giugno 1987, S. Teresa, 245-261.
- Borgwardt R.H. (1985) – *Calcination Kinetics and Surface Area of Dispersed Limestone Particles*. *AIChE Journal*, 31, 103, <https://doi.org/10.1002/aic.690310112>
- Borgwardt R.H., and Bruce K.R. (1986) – *Effect of Specific Surface Area on the Reactivity of CaO with SO₂*. *AIChE Journal*, 32:2, 239-246, <https://doi.org/10.1002/aic.690320210>
- Boynton R.S. (1982) – *Chemistry and Technology of Lime and Limestone*. Wiley & Sons, New York, 592 p. ISBN: 978-0-471-02771-3.
- Brignoli G. (2017) – *Procedura di preparazione di provini per l'analisi diffrattometrica di materiali argillosi*. Confidential Report for Cimprogetti, 6 p.
- Brown G, and Brindley GW (1980) – *X-ray diffraction procedures for clay mineral identification*. In: Brindley G.W. and Brown G. (Eds.) “Crystal Structures of Clay Minerals and Their X-ray Identification”, Monograph 5, Mineralogical Society, London, 305-360.
- Button A. (1973) – *The stratigraphic history of the Malmani dolomite in the eastern and north-eastern Transvaal*. *Trans. Geol. Soc. S. Africa*, 76, 29-247, <https://www.wits.ac.za/media/migration/files/cs-38933-fix/migrated-pdf/pdfs-8/EGRU%2073.pdf>
- Carmeuse (2014) – *Idwala South Africa, KFS calcination tests, Stone Committee*. Confidential internal report 1-25.

- Carmignani L, Meccheri M, Primavori P. (2005) – *Marbles and other ornamental stones from the Apuane Alps (northern Tuscany, Italy)*. *Giornale di Geologia Applicata*, <https://doi.org/10.1474/GGA.2005-01.0-23.0023>
- Cheng C., and Specht E. (2006) – *Reaction rate coefficients in decomposition of lumpy limestone of different origin*. *Thermochim Acta*, 449, 8–15, <https://doi.org/10.1016/j.tca.2006.06.001>
- Chilingar G.V. (1960) – *Notes on classification of carbonate rocks on basis of chemical composition*. *J Sediment Res*, 30, 157-158.
- Commandré J.-M., Salvador S., and Nzihou A. (2007) – *Reactivity of laboratory and industrial limes*. *Trans IChemE*, 85:A4, 473–480, <https://doi.org/10.1205/cherd06200>
- Cook R.J. (1992) – *A comparison of methods for the extraction of smectites from calcareous rocks by acid dissolution techniques*. *Clay Minerals*, 27, 73-80, <https://doi.org/10.1180/claymin.1992.027.1.07>
- De Jonghe L.C., and Rahaman M.N. (2003) – *Sintering of Ceramics*. In: Sōmiya S. et al. (Eds.) “Handbook of Advanced Ceramics: Materials, Applications, Processing and Properties”, Elsevier Inc., 1:4, 87–264, <https://doi.org/10.1016/B978-012654640-8/50006-7>
- Doyle C.D. (1962) – *Estimating Isothermal Life from Thermogravimetric Data*, *J. Appl. Polym. Sci.*, 6, 639–42.
- Eades J.L., and Sandberg P.A. (1970) – *Characterization of the properties of commercial lime by surface area measurements and scanning electron microscopy*. *ASTM STP*, 472, 3-24.
- Elsen J., Mertens G., and Snellings R. (2011) – *Portland cement and other calcareous hydraulic binders: History, production and mineralogy*. In: G.E. Christidis (Ed.) “Advances in the characterization of industrial minerals”, *EMU Notes in mineralogy*, London, 9:1, 441-479, <https://doi.org/10.1180/EMU-notes.9.11>
- Emmerich K. (2011) – *Thermal analysis in the characterization and processing of industrial minerals*. In: Christidis G.E. (Ed.) “Advances in the Characterization of Industrial Minerals”, London, EMU, 9:11, 129-170, <https://doi.org/10.1180/EMU-notes.9.5>
- Flügel E. (2010) – *Microfacies of Carbonate Rocks. Analysis, Interpretation and Application*. Springer-Verlag Berlin Heidelberg, 984p. ISBN: 978-3-642-03795-5. <https://doi.org/10.1007/10.1007/978-3-642-03796-2>

- Flynn J.H., and Wall L.A. (1966) – *General Treatment of the Thermogravimetry of Polymers*, Phys. Chem., 70, 487–523.
- Francey S., and Tran H. (2012) – *Impacts of burning high-sulphur fuels in lime kilns*. Journal of Science & Technology for Forest Products and Processes, 2:3, 32-37.
- Frolova E.K. (1959) – *On classification of carbonate rocks of limestone-dolomite-magnesite series*. Novosti Neft Tekhn, Geol, 3, 34-35.
- Fuoss R.M., Salymer I.O., and Wilson H.S. (1964) – *Evaluation of Rate Constants from Thermogravimetric data*. Journal of Polymer Science, A:2, 3147-3151.
- Gaetani M., Sciunnach D, Bini A., and Rossi S. (Eds) (2012) – *Note Illustrative della Carta Geologica D'Italia alla Scala 1:50.000*. ISPRA Istituto Superiore per la Protezione e la Ricerca Ambientale. Regione Lombardia. Foglio 076 Lecco. Servizio Geologico D'Italia; http://www.isprambiente.gov.it/Media/carg/note_illustrative/76_Lecco.pdf
- Galimberti M., Marinoni N., Della Porta G., Marchi M., and Dapiaggi M. (2016) – *Effects of limestone petrography and calcite microstructure on OPC clinker raw meals burnability*. Miner Petrol, <https://doi.org/10.1007/s00710-016-0485-8>
- Gallala W., Gaied M., Tlili A., Montacer M. (2008) – *Factors influencing the reactivity of quicklime*. Proc. Institution of Civil Engineers - Construction Materials, 161:1, February 2008, 25-30, <https://doi.org/10.1680/coma.2008.161.1.25>
- Georgieva V., Vlaev L., and Gyurova K. (2012) – *Non-Isothermal Degradation Kinetics of CaCO₃ from Different Origin*. Journal of Chemistry, Article ID 872981, 2013, <https://doi.org/10.1155/2013/872981>
- Ghizdavet Z. (2016) – *Relationships between burnability indices of the raw mix for clinker production*. Romanian journal of materials, 46:3, 303-312.
- Gonfiantini R, Stichler W, Rozanski K (1993) – *Standards and intercomparison materials distributed by the International Atomic Energy Agency for stable isotope measurements*. In: Stichler W. (Ed.) “Reference and Intercomparison Materials for Stable Isotopes of Light Elements”, IAEA, Vienna, 1993, 13-29.
- Grotzinger J.P. (1989) – *Facies and evolution of Precambrian carbonate depositional system: emergence of the modern platform archetype*. In: Crevello P., Read J.F., Sarg R., and Wilson J. (Eds.) “Controls on carbonate platform and basin development”, Soc Econ Paleont Mineral, 44, 79-106.

- Grotzinger J.P., and James N.P. (2000) – *Precambrian carbonates; evolution of understanding*. In: Grotzinger J.P. and James N.P. (Eds.) “Carbonate Sedimentation and Diagenesis in the Evolving Precambrian World”, SEPM, 67, 3-20.
- Gunasekaran S., and Anbalagan G. (2007) – *Thermal decomposition of natural dolomite*. Bull Mater Sci, 30, 339–344.
- Heaman L.M. (1997) – *Global mafic magmatism at 2.45 Ga: Remnants of an ancient large igneous province?* Geology, 25, 299–302, [https://doi.org/10.1130/0091-7613\(1997\)025<0299:GMMAGR>2.3.CO;2](https://doi.org/10.1130/0091-7613(1997)025<0299:GMMAGR>2.3.CO;2)
- Hogewoning S., Wolter A., and Schmidt S.-O. (2008) – *Dependence of hard burn potential on limestone properties*. ZKG International, 61:6, 54-60 (Part 1); 61:7, 84-93 (Part 2).
- Hughes J.J., and Corrigan M. (2009) – *Microstructural expression of temperature and residence time in laboratory calcined limestone*. Proc. 12th EMABM, Dortmund, 328-334.
- ISO 9277 (2010) – *Determination of the specific surface area of solids by gas adsorption - BET method*. 24 p., <https://www.iso.org/standard/44941.html>
- Jeppsson L. (2008) – *The lower Wenlock Hangvar Formation – a sequence previously split between the Högklint and Slite beds (Silurian, Gotland, Sweden)*, GFF, 130:1, 31-40, <https://doi.org/10.1080/11035890801301031>
- Jones A.P., Genge M., and Carmody L. (2013) – *Carbonate Melts and Carbonatites*, Reviews in Mineralogy & Geochemistry, 75, 289-322, <https://doi.org/10.2138/rmg.2013.75.10>
- Kiliç Ö., and Mesut A. (2006) – *Effects of limestone characteristics properties and calcination temperature on lime quality*. Asian J Chem, 18, 655-606.
- Kiliç Ö. (2013) – *Impact of Physical Properties and Chemical Composition of Limestone on Decomposition Activation Energy*. Asian Journal of Chemistry, 25:14, 8116-8120, <https://doi.org/10.14233/ajchem.2013.15172>
- Kisch H.J. (1991) – *Illite crystallinity: recommendations on sample preparation, X-ray diffraction settings, and interlaboratory samples*. Journal of Metamorphic Geology, 9, 665-670.
- Klein C., and Beukes N.J. (1989) – *Geochemistry and sedimentology of a facies transition from limestone to iron-formation deposition in the early Proterozoic Transvaal Supergroup, South Africa*. Econ Geol, 84, 1733-1742, <https://doi.org/10.2113/gsecongeo.84.7.1733>

- König G., Rellermeyer H., and Obst K.H. (1967) – *Processes Taking Place in the Dissolution of Hard and Soft-Burnt Lime in the Slags from the Basic Oxygen Furnaces*. Stahl und Eisen, 87:18, 1071-1077.
- Krystyn L., Mandl G.W., and Schauer M. (2009) – *Growth and termination of the Upper Triassic platform margin of the Dachstein area (Northern Calcareous Alps, Austria)*. Austrian Journal of Earth Sciences, 102, 23-33.
- Le Bas M.J. (1981) – *Carbonatite magmas*. Mineralogical Magazine, 44, 133–140, <https://doi.org/10.1180/minmag.1981.044.334.02>
- Le Blanc J. (2017) – *A revised guide to the Cenozoic Surface Formations of Qatar, Middle East (excluding the islands)*, <https://sites.google.com/site/leblancjacques/fossilhome>, Accessed 8 Jun 2018.
- Lech R., Wodnicka K., and Pezdich Z. (2009) – *Effect of the limestone fabric on the fabric development in burnt lime*. ZKG International, 6/7, 62, 94-101 (part 1); 8, 62, 63-72 (part 2).
- Lentini F, and Carbone S. (2014) – *Geologia della Sicilia - Geology of Sicily*. Mem. Descr. Carta Geol d'It., 95, 7-414.
- Liddell K.C. (2005) – *Shrinking core models in hydrometallurgy: What students are not being told about the pseudo-steady approximation*. Hydrometallurgy, 79:1-2, 62-68, <https://doi.org/10.1016/j.hydromet.2003.07.011>
- Limes R.W., and Russell R.O. (1970) – *Crucible Test for Lime Reactivity in Slags*. The Reaction Parameters of Lime, ASTM STP 472, 161-172.
- Manocha S. and Ponchon F. (2018) – *Management of Lime in Steel*. Metals, 8, 686, 16p., <https://doi.org/10.3390/met8090686>
- Marinoni N., Allevi S., Marchi M., and Dapiaggi M. (2012) – *A Kinetic Study of Thermal Decomposition of Limestone Using In-Situ High Temperature X-ray Powder Diffraction*. J Am Ceram Soc, 95, 2491-2498, <https://doi.org/10.1111/j.1551-2916.2012.05207.x>
- Marinoni N., Bernasconi A., Della Porta G., Marchi M., and Pavese A. (2015) – *The role of petrography on the thermal decomposition and burnability of limestones used in industrial cement clinker*. Miner Petrol, 109, 719–731, <https://doi.org/10.1007/s00710-015-0398-y>
- Martire L., Clari P., Lozar F., and Pavia G. (2006) – *The Rosso Ammonitico Veronese (Middle-Upper Jurassic of the Trento Plateau): a proposal of lithostratigraphic ordering*

and formalization. Riv. It. Pal. Str. 112:2, 227-250, <https://doi.org/10.13130/2039-4942/6338>

- McClellan G.H., and Eades J.L. (1970) – *The Textural Evolution of Limestone Calcines*. The Reaction Parameters of Lime, ASTM STP, 472, 209-227.
- Miyano T., and Beukes N.J. (1984) – *Phase relations of stilpnomelane, ferri-annite, and riebeckite in very low-grade metamorphosed iron-formations*. S Afr J Geol, 87, 111-124.
- Moore D.M., Reynolds R.C. Jr. (1997) – *X-ray Diffraction and the Identification and Analysis of Clay Minerals*, 2nd edition. Oxford University Press, Oxford, UK, and New York.
- Moropoulou A., Bakolas A., and Aggelakopoulou E. (2001) – *The effects of limestone characteristics and calcinations temperature to the reactivity of the quicklime*. Cem Concr Res, 31, 633-639, [https://doi.org/10.1016/S0008-8846\(00\)00490-7](https://doi.org/10.1016/S0008-8846(00)00490-7)
- Nolan SC, Skelton PW, Clissold BP, Smewing JD. (1990) – *Maastrichtian to early Tertiary stratigraphy and palaeogeography of the Central and Northern Oman*. Geol. Soc. London Sp. Publ., <https://doi.org/10.1144/GSL.SP.1992.049.01.31>
- Oates J.A.H. (1998) – *Lime and Limestone: Chemistry and Technology, Production and Uses*. Weinheim, Germany, WILEY-VCH Verlag GmbH. <https://doi.org/10.1002/9783527612024.ch01>
- Ozawa T. (1965) – *A New Method of Analyzing Thermogravimetric Data*. Bull. Chem. Soc. Jpn., 38, 1881–6.
- Paris G., Adkins J.F., Sessions A.L., Webb S.M., and Fischer W.W. (2014) – *Neoproterozoic carbonate-associated sulfate records positive $\Delta^{33}\text{S}$ anomalies*. Science, 346, 6210, 739-741, <https://doi.org/10.1126/science.1258211>
- Pisaroni M., Sadi R., and Lahaye D. (2012) – *Counteracting ring formation in rotary kilns*. Journal of Mathematics in Industry 2:3, <https://doi.org/10.1186/2190-5983-2-3>
- Potgieter J.H., Potgieter D., De Waal D. (2003) – *An empirical of factors influencing lime slaking. Part II: Lime constituent and water composition*. Water SA, 29:2, 157-160, <http://dx.doi.org/10.4314/wsa.v29i2.4850>
- Rodriguez-Navarro C., Ruiz-Agudo E., Luque A., Navarro A.B., and Ortega-Huertas M. (2009) – *Thermal decomposition of calcite: Mechanisms of formation and textural evolution of CaO nanocrystals*. Am Mineral 94, 578–593. <https://doi.org/10.2138/am.2009.3021>

- Ronchi P, Jadoul F, Ceriani A, Di Giulio A, Scotti P, Ortenzi A, Previde Massara E. (2010) – *Multistage dolomitization and distribution of dolomitized bodies in Early Jurassic carbonate platforms (Southern Alps, Italy)*. *Sedimentology*, 58, 532-565, <https://doi.org/10.1111/j.1365-3091.2010.01174.x>
- Scandone P. (1971) – *Note Illustrative della Carta Geologica d'Italia alla scala 1:100.000. Fogli 199 e 210. Potenza e Lauria*. *Serv Geol d'It.*, 1-71. http://193.206.192.231/carta_geologica_italia/note_illustrative/199.pdf
- Scholle P.A., and Ulmer-Scholle D.S. (2003) – *A Color Guide to the Petrography of Carbonate Rocks: Grains, Textures, Porosity, Diagenesis*, AAPG Memoir 77, 474 p.
- Schwarzkopf F. (1994) – *Lime Burning Technology – a manual for lime plant operators*. 3rd ed., Svedala Industries Kennedy, Van Saun.
- Shi H., Zhao Y., and Li W. (2002) – Effects of temperature on the hydration characteristics of free lime, *Cement & Concrete Research*, 32, 789-793, [https://doi.org/10.1016/S0008-8846\(02\)00714-7](https://doi.org/10.1016/S0008-8846(02)00714-7)
- Shushakova V., Fuller E.R. Jr., and Siegesmund S. (2013a) – *Microcracking in calcite and dolomite marble: microstructural influences and effects on properties*. *Environ. Earth Sci.*, 69:4, 1263-1279, <https://doi.org/10.1007/s12665-012-1995-2>
- Shushakova V., Fuller E.R. Jr., Heidelbach F., Mainprice D., and Siegesmund S. (2013b) – *Marble decay induced by thermal strains: simulations and experiments*. *Environ. Earth Sci.*, 69:4, 1281-1297, <https://doi.org/10.1007/s12665-013-2406-z>
- Siegesmund S., Ullemeyer K., Weiss T., and Tschegg E.K. (2000) – *Physical weathering of marbles caused by anisotropic thermal expansion*. *Int. J. Earth Sci.* 89, 170–182, <https://doi.org/10.1007/s005310050324>
- Soltan A.M.M. (2009) – *Petrographic modelling of Egyptian limestones for quicklime manufacture*. *Arabian Journal of Geosciences*, 4, 803–815. <https://doi.org/10.1007/s12517-009-0095-4>
- Soltan A.M.M., and Serry M.A.-K. (2011) – *Impact of limestone microstructure on calcination activation energy*. *Advances in Applied Ceramics*, 110:7, 409-416, <https://doi.org/10.1179/1743676111Y.0000000042>
- Soltan A.M.M., Kahl W.-A., Hazem M.M., Wendschuh M, and Fischer R.X. (2011) – *Thermal microstructural changes of grain-supported limestones*. *Miner Petrol*, 103, 9-17, <https://doi.org/10.1007/s00710-011-0151-0>

- Soltan A.M.M., Kahl W.-A., Wendschuh M., and Hazem M.M. (2012) – *Microstructure and reactivity of calcined mud supported limestones*. <https://doi.org/10.1179/1743285511Y.0000000024>
- South African Committee for Stratigraphy (SACS) (1980) – *Stratigraphy of South Africa, part 1*, In: Kent L.E. (Ed.) “Litho-stratigraphy of the Republic of South Africa, South West Africa/Namibia, and the Republics of Bophuthaswana, Transkei and Venda”, Handbook Geol. Surv. S. Afr., 8, 1-690.
- Student (Gosset W.S.) (1908) – *The probable error of a mean*. Biometrika, 6, 1–25, <https://doi.org/10.1093/biomet/6.1.1>.
- Sumner D.Y. (1995) – *Facies, paleogeography, and carbonate precipitation on the Archean (2520 Ma) Campbellrand-Malmani Carbonate Platform, Transvaal Supergroup, South Africa*. MIT, Ph.D. 9/1995, 1-514.
- Sumner D.Y. (1997a) – *Carbonate precipitation and oxygen stratification in late Archean seawater as deduced from facies and stratigraphy of the Gamohaam and Frisco formations, Transvaal Supergroup, South Africa*. Am J Sci, 297, 455–487, <https://doi.org/10.2475/ajs.297.5.455>
- Sumner D.Y. (1997b) – *Late Archean calcite-microbe interactions: two morphologically distinct microbial communities that affected calcite nucleation differently*. Palaios, 12, 302–318, <https://doi.org/10.2307/3515333>
- Sumner D.Y., and Bowring S.A. (1996) – *U-Pb geochronologic constraints on deposition of the Campbellrand Subgroup, Transvaal Supergroup, South Africa*. Precambrian Res, 79, 25–36, [https://doi.org/10.1016/0301-9268\(95\)00086-0](https://doi.org/10.1016/0301-9268(95)00086-0)
- Sumner D.Y., and Beukes N.J. (2006) – *Sequence stratigraphic development of the Neoarchean Transvaal carbonate platform, Kaapvaal Craton, South Africa*. S Afr J Geol, 109:1-2, 11-22, <https://doi.org/10.2113/gssajg.109.1-2.11>
- Sumner D.Y., and Grotzinger J.P. (1996) – *Herringbone calcite: petrography and environmental significance*. J Sediment Res, 66, 419-429, <https://doi.org/10.1306/D4268360-2B26-11D7-8648000102C1865D>
- Sumner D.Y., and Grotzinger J.P. (2000) – *Late Archean aragonite precipitation: Petrography, facies associations, and environmental significance*. In: Grotzinger J.P., James N.P. (Eds.) “Carbonate Sedimentation and Diagenesis in the Evolving Precambrian World”, SEPM 67, 123-144.

- Sumner D.Y., and Grotzinger J.P. (2004) – *Implications for Neoproterozoic ocean chemistry from primary carbonate mineralogy of the Campbellrand-Malmani Platform, South Africa*. *Sedimentology*, 51, 1-27, <https://doi.org/10.1111/j.1365-3091.2004.00670.x>
- Taylor H.F.W. (1997) – *Cement Chemistry*. Academic Press, London, 2nd Edition, Thomas Telford Publishing, London, 361, <http://dx.doi.org/10.1680/cc.25929>
- Telschow S., Dam-Johansen K., Jappe Frandsen F., Wedel S., and Theisen K. (2012) – *Clinker Burning Kinetics and Mechanism*. Kgs. Lyngby: Technical University of Denmark (DTU).
- Thorez J. (1976) – *Practical identification of clay minerals*. G. Lelotte Ed., 90 pp.
- Towadros E. E. (2012) – *Geology of North Africa*. London CRC Press/Balkema, 487-488.
- Tran H.N. (2006) – *Lime Kiln Chemistry and Effects on Kiln Operations*. 2006 TAPPI Kraft Recovery Short Course, St. Petersburg, FL, USA.
- Tran H.N., and Barham D. (1991) – *An overview of ring formation in lime kilns*. *Tappi J*, 74:1, 131-136.
- Tran H.N., Mao X., and Barham D. (1993) – *Mechanisms of Ring Formation in Lime Kilns*. *Journal of Pulp and Paper Science*, 19:4, 167-175.
- Veniale F., Setti M., Tortelli M. (1987) – *Influenza delle procedure sui preparati di “polveri” per analisi diffrattometrica RX*. Atti Workshop Procedure di analisi di materiali argillosi, ENEA, S. Teresa, 1-2 giugno, 135-179.
- Vola G., and Sarandrea L. (2013) – *Raw materials characterization for industrial lime manufacturing*. *ZKG International*, 66:5, 62-70.
- Vola G., and Sarandrea L. (2014a) – *Lime reactivity study. Raw material quality, kiln control and influence on lime reactivity in a Twin Shaft Regenerative Kiln (TSR)*. *World Cement*, 45:6, June 2014, 49-55.
- Vola G., and Sarandrea L. (2014b) – *Investigating and predicting blockages*. *World Cement*, October 2014, 85-92.
- Vola G., and Sarandrea L. (2015) – *Investigation and prediction of marble mechanical degradation and dust formation during calcination process in Twin Shaft Regenerative (TSR) kilns*. *Cement International*, 3:13, 42-47.
- Vola G., Sarandrea L., Della Porta G., Cavallo A., Jadoul F., and Cruciani G. (2017a) – *The influence of petrography, mineralogy and chemistry on burnability and reactivity of quicklime produced in Twin Shaft Regenerative (TSR) kilns from Neoproterozoic limestone*

(Transvaal Supergroup, South Africa). Miner Petrol, <https://doi.org/10.1007/s00710-017-0542-y>

- Vola G., Sarandrea L., Della Porta G., and Cruciani G. (2017b) – *Characterization of a Cambrian-Ordovician limestone (Kazakhstan) for the industrial production of quicklime and hydrated lime products*. Proc. AIV-SGI-SIMP-SOGEI 3-7 September 2017, Pisa.
- Vola G., Bresciani P., Rodeghero E., Sarandrea L., and Cruciani G. (2018) – *Impact of rock fabric, thermal behavior, and carbonate decomposition kinetics on quicklime industrial production and slaking reactivity*. Journal of Thermal Analysis and Calorimetry, <https://doi.org/10.1007/s10973-018-7769-7>
- Walraven F., Armstrong R.A., and Kruger F.J. (1990) – *A chronostratigraphic framework for the north-central Kaapvaal craton, the Bushveld Complex and the Vredefort structure*. Tectonophysics, 171, 23-48, [https://doi.org/10.1016/0040-1951\(90\)90088-P](https://doi.org/10.1016/0040-1951(90)90088-P)
- Warren J. (2000) – *Dolomite: occurrence, evolution and economically important associations*. Earth-Science Reviews, 52, 1-81, [https://doi.org/10.1016/S0012-8252\(00\)00022-2](https://doi.org/10.1016/S0012-8252(00)00022-2)
- Walling S.A., and Provis J.L. (2016) – *Magnesia-Based Cements: A Journey of 150 Years, and Cements for the Future?* Chem. Rev. 116, 7, 4170-4204, <https://doi.org/10.1021/acs.chemrev.5b00463>
- Wiese F, Wood CJ, and Kaplan U. (2004) – *20 years of event stratigraphy in NW Germany; advances and open questions*. Acta Geologica Polonica, 54:4, 639-656.
- Wright G. (1995) – *Effect of impurities on lime reactivity*. Ash Grove Cement Company, Rivergate Lime Plant, Confidential Internal Report, 41 p.
- Zhang J., Gong C., Lu L., Wang S., and Hou P. (2015) – *Effect of MgO on the composition and properties of Belite-Barium Calcium Sulphoaluminate cement in the presence of Na₂O and K₂O*. Ceramics – Silikáty, 59:2, 135-144; https://www.irsm.cas.cz/materialy/cs_content/2015/Zhang_CS_2015_0000.pdf



Università degli Studi di Ferrara

UFFICIO DOTTORATI DI RICERCA

AL MAGNIFICO RETTORE
UNIVERSITÀ DEGLI STUDI DI FERRARA
UFFICIO DOTTORATO
Via delle Scienze, n. 41/B – 44121 Ferrara

Richiesta di embargo della tesi di dottorato oltre i 12 mesi (da allegare alla dichiarazione di conformità)			
Nome e cognome del dottorando:	Gabriele Vola		
Corso di dottorato:	Scienze della Terra e del Mare		
Matricola:	058936		
Ciclo:	31		
E-mail per contatti:	gabriele.vola@gmail.com		
Anno dell'esame finale:	2019		
Nome e cognome del Tutore:	Giuseppe Cruciani		
Titolo della tesi:			
High-grade burnt lime products: impact of calcination kinetics on slaking reactivity; sticking tendency and blocks formation at HT (1300 °C)			
Periodo di secretazione:	<input checked="" type="checkbox"/> 18 mesi	<input type="checkbox"/> 24 mesi	<input type="checkbox"/> 36 mesi
Motivo dell'embargo:			
Tesi in corso di pubblicazione	<input checked="" type="checkbox"/>	Tesi già sottoposte a un editore che non consenta l'accesso aperto prima dell'avvenuta pubblicazione	
Motivi di pubblica sicurezza	<input type="checkbox"/>	Quando la tesi può mettere a rischio la sicurezza pubblica e/o nazionale o per motivi di rispetto della Legge vigente	
Tutela della proprietà intellettuale	<input checked="" type="checkbox"/>	Diritto d'autore, brevetti, copyright etc.	
Tesi previo accordo con terze parti	<input type="checkbox"/>	Lavoro prodotto nell'ambito di un progetto di ricerca per il quale sia stato stipulato un accordo con un ente di ricerca esterno o con un ente finanziatore che preveda la divulgazione della tesi solo dopo il completamento dell'intero progetto di ricerca	
Privacy	<input type="checkbox"/>	Qualora la ricerca verta su una o più persone per cui si tema di violare il diritto alla riservatezza	
Descrizione dettagliata della richiesta di secretazione:			
<p>Indicare in modo esaustivo le ragioni per cui si chiede l'embargo, citando gli estremi di eventuali accordi editoriali, contratti commerciali, progetti di ricerca etc. per cui sia richiesta la non accessibilità temporanea ai contenuti del lavoro</p> <p>La presente tesi di dottorato è stata svolta in collaborazione tra l'Università di Ferrara e la società Cimprogetti Srl. I risultati di tale ricerca sono di interesse industriale e si ritiene necessario l'embargo per consentire all'Autore di ultimare la pubblicazione degli articoli in essa contenuti (uno è in corso di revisione, un altro dev'essere finalizzato e inviato ad una rivista scientifica). Il tempo stimato per ultimare i suddetti passaggi è di circa 18 mesi.</p>			
Data:	4 Febbraio 2019		
Firma del dottorando:			
Firma del Tutore:			
Come previsto dal Regolamento in materia di Dottorato di Ricerca dell'Università di Ferrara, che stabilisce l'obbligo di deposito delle tesi di Dottorato nell'archivio istituzionale d'Ateneo ad accesso aperto, la presente istanza dovrà essere sottoposta all'eventuale approvazione da parte del Consiglio di "IUSS Ferrara 1391"			



Università
degli Studi
di Ferrara

Sezioni

Dottorati di ricerca

Il tuo indirizzo e-mail

gabriele.vola@student.unife.it

Oggetto:

Dichiarazione di conformità della tesi di Dottorato

Io sottoscritto Dott. (Cognome e Nome)

Vola Gabriele

Nato a:

San Donato Milanese

Provincia:

Milano

Il giorno:

16 Luglio 1974

Avendo frequentato il Dottorato di Ricerca in:

SCIENZE DELLA TERRA E DEL MARE

Ciclo di Dottorato

31

Titolo della tesi:

High-grade burnt lime products: impact of calcination kinetics on slaking reactivity; sticking tendency and blocks formation at HT (1300 °C)

Titolo della tesi (traduzione):

Prodotti a base di calce viva di alta qualità: impatto della cinetica di calcinazione sulla reattività di spegnimento; tendenza ad incollare e formare blocchi ad alta T (1300 ° C)

Tutore: Prof. (Cognome e Nome)

Cruciani Giuseppe

Settore Scientifico Disciplinare (S.S.D.)

GEO/06

Parole chiave della tesi (max 10):

Produzione di calce viva; reattività di spegnimento; cinetiche di calcinazione; attitudine alla cottura; tendenza ad incollare; Quicklime production; Slaking reactivity; Calcination kinetics; burning attitude; Sticking tendency

Consapevole, dichiara

CONSAPEVOLE: (1) del fatto che in caso di dichiarazioni mendaci, oltre alle sanzioni previste dal codice penale e dalle Leggi speciali per l'ipotesi di falsità in atti ed uso di atti falsi, decade fin dall'inizio e senza necessità di alcuna formalità dai benefici conseguenti al provvedimento emanato sulla base di tali dichiarazioni; (2) dell'obbligo per l'Università di provvedere al deposito di legge delle tesi di dottorato al fine di assicurarne la conservazione e la

consultabilità da parte di terzi; (3) della procedura adottata dall'Università di Ferrara ove si richiede che la tesi sia consegnata dal dottorando in 2 copie, di cui una in formato cartaceo e una in formato pdf non modificabile su idonei supporti (CD-ROM, DVD) secondo le istruzioni pubblicate sul sito : <http://www.unife.it/studenti/dottorato> alla voce ESAME FINALE – disposizioni e modulistica; (4) del fatto che l'Università, sulla base dei dati forniti, archiverà e renderà consultabile in rete il testo completo della tesi di dottorato di cui alla presente dichiarazione attraverso l'Archivio istituzionale ad accesso aperto "EPRINTS.unife.it" oltre che attraverso i Cataloghi delle Biblioteche Nazionali Centrali di Roma e Firenze. DICHIARO SOTTO LA MIA RESPONSABILITA': (1) che la copia della tesi depositata presso l'Università di Ferrara in formato cartaceo è del tutto identica a quella presentata in formato elettronico (CD-ROM, DVD), a quelle da inviare ai Commissari di esame finale e alla copia che produrrà in seduta d'esame finale. Di conseguenza va esclusa qualsiasi responsabilità dell'Ateneo stesso per quanto riguarda eventuali errori, imprecisioni o omissioni nei contenuti della tesi; (2) di prendere atto che la tesi in formato cartaceo è l'unica alla quale farà riferimento l'Università per rilasciare, a mia richiesta, la dichiarazione di conformità di eventuali copie. PER ACCETTAZIONE DI QUANTO SOPRA RIPORTATO

Dichiarazione per embargo

18 mesi


Richiesta motivata embargo

1. Tesi in corso di pubblicazione

Liberatoria consultazione dati Eprints

Consapevole del fatto che attraverso l'Archivio istituzionale ad accesso aperto "EPRINTS.unife.it" saranno comunque accessibili i metadati relativi alla tesi (titolo, autore, abstract, ecc.)

Firma del dottorando

Ferrara, li _____ 4 Febbraio 2019 _____ (data) Firma del Dottorando
_____ Gabriele Vola _____ 

Firma del Tutore

Visto: Il Tutore Si approva Firma del Tutore _____ Giuseppe
Cruciani _____ 